



A University of Sussex PhD thesis

Available online via Sussex Research Online:

<http://sro.sussex.ac.uk/>

This thesis is protected by copyright which belongs to the author.

This thesis cannot be reproduced or quoted extensively from without first obtaining permission in writing from the Author

The content must not be changed in any way or sold commercially in any format or medium without the formal permission of the Author

When referring to this work, full bibliographic details including the author, title, awarding institution and date of the thesis must be given

Please visit Sussex Research Online for more information and further details

Computational Study of the Reactivity of Palladacycles in Catalytic Applications

Sarote Boonseng



Submitted towards fulfilment of the requirement for the degree of

Doctor of Philosophy

School of Life Sciences

University of Sussex

United Kingdom

March 2017

Declaration

I hereby declare that this thesis has not been and will not be submitted in whole or in part to another University for the award of any other degree.

Sarote Boonseng

Abstract

This thesis presents a detailed theoretical/computational analysis using quantum chemistry to investigate the thermochemistry and reaction mechanisms of palladacycles that underpin experimental observations. The thesis begins by establishing a suitable computational methodology for the study of pincer palladacycles. It was found that Density Functional Theory (DFT) was suitable for the accurate reproduction of geometric structures and energetics by comparing a range of commonly used density functionals and basis sets with the X-ray crystal structures of symmetric pincer palladacycles. The detailed electronic structure of several pincer palladacycles was investigated using Complete Active Space Self-Consistent Field method (CASSCF) and it was shown that the dominant configuration was larger than 0.96, indicating that the ground state electronic structure has significant single-reference character. DFT was used to investigate the stability of symmetrical pincer palladacycles, and then by changing the donor ligand, unsymmetrical pincer palladacycles. The pincer palladacycle formation was investigated and it was found that the barrier to C-H activation was dependent on the ligand arm of the pincer that coordinates to PdCl₂. Topological analysis was performed using Quantum Theory of Atoms In Molecules (QTAIM) for determining the strength and nature of the Pd and donor atom interactions, showing that the bond strength depends on the type of donor atom and trans influence in the pincer palladacycles. The mechanism for Pd(0) formation from both symmetrical and unsymmetrical pincer palladacycle pre-catalysts for catalysis in Suzuki-Miyaura carbon-carbon cross-coupling reactions was studied, and then with the introduction of base and the effect of solvent. It was shown that the key steps are transmetallation and reductive elimination processes, and differences in the overall Gibbs free energy and transmetallation barrier provide an explanation for observed catalytic activity. This has been in conjunction with experimental chemists.

Finally, the functionalisation of benzodiazepines was investigated in three conditions; with Pd(II)/Ru(II)-catalysts, with Pd(II)-catalysts and without catalyst. It was found that the Ru(II) photocatalyst with Pd(II)-catalyst is the best condition for functionalisation on benzodiazepines with the lowest energy barrier.

Acknowledgements

Firstly, I would particularly like to express my sincere gratitude to my supervisor Dr Hazel Cox who gave me the opportunity to carry out this research and advised my academic direction. Her friendly guidance helped me throughout my PhD studies and provided important personal development.

Besides my supervisor, I would like to thank my co-supervisor Prof John Spencer for his contributions to the direction and discussion of this thesis along with his kindness. I would also like to thank Prof. Anthony Mcaffery for his helpful discussion in preparing for various presentations throughout my studies.

I would like to thank the Royal Thai Government for providing the full funding for my PhD studies and Mahidol Wittayanusorn School for supporting me throughout my studies. Thanks also go to everyone at the School of Life Sciences, University of Sussex.

I would like to acknowledge the University of Sussex and the EPSRC UK National Service for Computational Chemistry Software (NSCCS) at Imperial College London for computer facilities and IT support.

I would like to thank members of the Cox group: Dr Andrew King, Dr Gavin Roffe, Adam Baskerville, Msugh Targema, Kylie Okolo, Rob Ziolek, Luke Rhodes, Clara Fedullo, Emma Coakley, James Mattock and Patrick Herlihy for providing excellent friendship.

My special thanks go to Dr Gavin Roffe for fruitful collaboration, his kindness and constant support. My special thanks also go to Adam Baskerville for helping me sort out \LaTeX problems and for proofreading my thesis.

I would like to thank all my friends in Sussex for an enjoyable time in the UK including: Dr Shane Lo Fan Hin, Dr Tara Salter, Raysa Khan, James Stubbing, Nutchana Anantakoon (Natt), Dr Jirapas Jongjitwimol (Mai), Dr Pattarapong

Choopanya (Kom), Kiattisak Thepsuriya (Tik), Dr Prapanporn Rattana (Por), Passamol Jaraswit (Yoo), Teeraphan Udomsinkul (Aek), Chuencheewin Yimfuang (Toey), Udomsak Jiragarnkulgasame (Tae), Waruntep Rukchatjaroen (Prio), Wissarut Ketaiam (Bond), Dr Siska Riefelyna, Kunye Li (Troy), Aom, Bank, Colleen, Amber and Kristen. Of particular note is Supojjaneer Sansook (Poj) who has been a good friend for the duration of my time in the UK.

Last but not least, I would like to thank my dad (Hiran), my mum (Supin) and my sister (Sarawalee) for supporting me throughout my life and also to thank my friends at Mahidol Wittayanusorn School.

Abbreviations

CASSCF	Complete active space self-consistent field
CC	Coupled Cluster
CPCM	Conductor-like polarisable continuum model
CI	Configuration Interaction
DC	De-coordination
DFT	Density functional theory
HF	Hartree-Fock
EA	Electron-accepting
ECP	Effective core potential
ED	Electron-donating group
ESI-MS	electrospray ionisation mass spectroscopy
ET	Electron transfer
EWG	Electron withdrawing group
GABA	γ -aminobutyric acid
GGA	Generalised gradient approximation
HGGA	Hybrid generalised gradient approximation
IEF	Integral equation formalism
LDA	Local density approximation
LSDA	Local spin-density approximation
MGGA	Meta generalised gradient approximation
MLCT	Metal-ligand charge transfer
MSE	Mean signed error
MUE	Mean unsigned error
NAO	Natural atomic orbital
NBO	Natural bond orbital

NMR Nuclear magnetic resonance
PCM Polarisable continuum model
PES Potential energy surface
QM Quantum mechanics
QTAIM Quantum theory of atoms in molecules
RE Reductive elimination
RMS Route mean square error
SET Single electron transfer
SDD Stuttgart/Dresden
TDDFT Time-dependent density functional theory
THF Tetrahydrofuran
TM Transmetallation
UV Ultraviolet
ZPVE Zero-point vibrational energy

Contents

1	Introduction and Thesis overview	1
1.1	Introduction to palladacycles and their applications	1
1.2	Computational chemistry	8
1.3	Thesis overview	9
2	Theoretical Background	10
2.1	Introduction	10
2.2	The Schrödinger equation	10
2.3	The Hartree-Fock method	14
2.4	Post-Hartree-Fock approximation	16
2.4.1	Configuration interaction	16
2.4.2	Complete active-space self-consistent field method	18
2.5	Density functional theory (DFT)	19
2.6	Exchange-correlation functionals	21
2.7	Basis set	26
2.7.1	Split-valence basis set	27
2.7.2	Effective core potential (pseudopotentials)	28
2.8	Solvation model	29
2.9	Quantum theory of Atoms in Molecules	29
2.9.1	Critical points	30
2.9.2	Bond strength and the nature of the bond	32
2.9.3	π -character in the single bond	33
2.10	Natural bond orbital (NBO) analysis	34
3	Determining a Method for Pincer Palladacycle Calculations	36

3.1	Introduction	36
3.2	Aim of this work	40
3.3	Computational details	40
3.4	Results and discussion	41
3.4.1	The RMS error in Cartesian coordinates, and the error of interatomic and bond distances, in symmetrical pincer palladacycles	41
3.4.2	The RMS Cartesian coordinates, and the error of interatomic and bond distances of Pd-L	50
3.5	Conclusion	52
4	Pincer Palladacycles Studied Using CASSCF Method	53
4.1	Introduction	53
4.1.1	Electronic structure using CASSCF method	53
4.2	Aims of this work	57
4.3	Computational details	57
4.4	Results and discussion	58
4.4.1	Symmetrical pincer palladacycles	58
4.4.2	Electronic structures of symmetrical pincer palladacycles	66
4.4.3	CASSCF efficiency for optimisation of the pincer structure	66
4.4.4	Unsymmetrical pincer palladacycles	67
4.4.5	Electronic structures of unsymmetrical pincer palladacycles	72
4.5	Conclusion	75
5	Formation Reaction of Pincer Palladacycles	76
5.1	Introduction	76
5.1.1	C-H bond activation	76
5.1.2	C-H bond activation on pincer palladacycles	80
5.1.3	Palladium chloride chemistry	82
5.1.4	<i>Trans</i> influence	82
5.2	Aims of this work	83
5.3	Computational details	84
5.4	Results and discussion	85

5.4.1	Formation reaction of symmetrical pincer palladacycles	88
5.4.2	Formation reaction of unsymmetrical pincer palladacycles	99
5.4.3	Kinetic study	119
5.4.4	The energetic span model for pincer palladacycle formation	120
5.4.5	Nature of bonding in pincer palladacycles	121
5.5	Conclusion	132
6	Formation of the Active Catalyst Pd(0) from Symmetrical and Un-	
	symmetrical Pincer Palladacycles	133
6.1	Introduction	133
6.1.1	Palladium complex (pre)-catalysts	134
6.1.2	DFT study of Palladium catalysis	143
6.2	Aims of this work	147
6.3	Computational details	148
6.4	Results and discussion	149
6.4.1	Base-free Pd(0) formation from symmetrical pincer palladacycles	151
6.4.2	Base-free Pd(0) formation from unsymmetrical pincer pallada- cycles	157
6.4.3	Pd(0) formation reaction in the presence of a base	166
6.4.4	Analysis of reaction energy barriers of PdYCY and PdYCY' pathways to Pd(0) formation in the absence and presence of base	176
6.4.5	Solvation effects on the Pd(0) formation reaction	179
6.4.6	Rationalisation of the catalytic activity by the model Pd(0) formation reactions	180
6.5	Conclusion	187
7	The Functionalisation of Benzodiazepines Using Pd(II)/Ru(II) Cata-	
	lysts: a DFT Study	188
7.1	Introduction	188
7.1.1	Benzodiazepine chemistry	188
7.1.2	[Ru(bpy) ₃] ²⁺ chemistry	200
7.1.3	Electron transfer theory	201
7.2	Aim of this work	206

7.3	Computational details	208
7.4	Results and discussion	210
7.4.1	Reduction potential	210
7.4.2	Mechanism of functionalisation using Pd(II)/Ru(II)-catalysts .	215
7.4.3	Mechanism of functionalisation using Pd(II)-catalyst	224
7.4.4	Mechanism of functionalisation without catalyst	228
7.4.5	Consideration of the role of the catalyst	230
7.5	Conclusion	231
8	Concluding Remarks, Future Direction and Thesis Outcome	232
8.1	Concluding remarks	232
8.2	Future direction	233
8.3	Thesis outcomes	234
	Appendices	255
A		256
B		262

List of Figures

1.1	Palladacycles; a) C-anionic four-electron donor (CY) complex and b) C-anionic six-electron donor.	2
1.2	PCP pincer palladacycles (PdPCP) 1 , 2 , 3 and 4	3
1.3	SCS pincer palladacycles (PdSCS) 5 and 6	3
1.4	Phosphorus donor palladacycles 7 and 8 using in the Suzuki-Miyaura cross-coupling reaction.	4
1.5	Sulfur donor palladacycles 9 , 10 and 11 using in Suzuki-Miyaura cross-coupling reaction.	4
1.6	Nitrogen donor palladacycles 12 used in Suzuki-Miyaura cross-coupling reaction.	5
1.7	P-coordinated NC palladacycles 13 , 14 , 15 , 16 and 17	5
1.8	Oxime palladacycles 18 , 19 , 20 and 21	6
1.9	Palladacycles 22 and 23 applied as catalysts in Suzuki-Miyaura reaction under eco-friendly conditions.	7
1.10	Unsymmetrical NCS 24 pincer palladacycle used in the Suzuki-Miyaura reaction.	7
1.11	Palladacycle 28 with antitumour activity.	8
2.1	Promotion of electrons to get single and double excitations.	17
2.2	(left) Slater functional plot. (right) Gaussian functional plot.	27
2.3	Topology of the electron density (left) and molecular graph (right) for benzene. The NCPs, BCPs and RCPs are shown in the molecular graph as small violet dots, orange dots and yellow dots, respectively.	32
3.1	Structure of a) <i>cis</i> -M(Met)X ₂ and b) <i>cis</i> -M(His)X ₂ where M is Pd and Pt, and X is F, Cl, Br and I.	39

3.2	Symmetrical pincer palladacycle complexes 1 and 2 investigated in this study.	41
3.3	a) Optimised geometry of complex 1 and b) optimised geometry of complex 2 (grey = carbon, white = hydrogen, dark blue = nitrogen, light green = chlorine, dark green = palladium and yellow = sulphur).	42
3.4	RMS error for complex 1 . Optimised structure compared to its X-ray crystal structure using the Quatfit program.	43
3.5	RMS error for complex 2 . Optimised structure compared to its X-ray crystal structure using the Quatfit program.	43
3.6	Average RMS errors for complex 1 and 2 optimised structures compared to their X-ray crystal structures using the Quatfit program.	44
3.7	Interatomic distance MSE and MUE for complex 1 (excluding hydrogen) compared to the X-ray crystal structure varying the method and basis set.	46
3.8	Bonded distance MSE and MUE for complex 1 (excluding hydrogen) compared to the X-ray crystal structure varying the method and basis set.	47
3.9	Interatomic distance MSE and MUE for complex 2 (excluding hydrogen) compared to the X-ray crystal structure varying the method and basis set.	47
3.10	Bond distance MSE and MUE for complex 2 (excluding hydrogen) compared to the X-ray crystal structure varying the method and basis set.	48
3.11	Average bonded and interatomic distance MSE and MUE for PdNCN and PdSCS compared to their X-ray crystal structures.	49
3.12	Average RMS error using the Quatfit program, bond and interatomic distance MSE and MUE for Pd-L bonds of complexes 1 and 2 compared to their X-ray crystal structures.	51
4.1	Model of oxyheme studied by Yamamoto and Kashiwagi <i>via</i> CASSCF.	54
4.2	Structure of a) the cob(I)alamin and b) the interaction of base with cob(I)alamin.	54
4.3	Metal-salen catalysts; a) full salen ligand and b) model for simulation.	55

4.4	Structure of $M(2\text{-thienylpyridine})_2$	56
4.5	<i>trans</i> - $[\text{RuCl}_4(\text{NO})(1\text{H-indazole})]$ structure studied by Freitag and co-workers	57
4.6	Symmetrical and unsymmetrical pincer palladacycles used in this study.	58
4.7	Active space orbitals of PdNCN resulting from CASSCF optimisation calculation and an orbital numbering scheme which is not based on orbital energy. The orbitals in blue and red squares are the active orbitals for CAS(8,8) and CAS(6,6), respectively. The isovalue for representative orbitals is 0.05 (grey = carbon, white = hydrogen, dark green = palladium, light green = chlorine and dark blue = nitrogen).	61
4.8	Active space orbitals of PdSCS resulting from CASSCF optimisation calculation and an orbital numbering scheme which is not based on orbital energy. The orbitals in blue and red squares are the active orbitals for CAS(8,8) and CAS(6,6), respectively. The isovalue for representative orbitals is 0.05 (grey = carbon, white = hydrogen, dark green = palladium, light green = chlorine and yellow = sulphur).	63
4.9	Active space orbitals of PdPCP resulting from CASSCF optimisation calculation and an orbital numbering scheme which is not based on orbital energy. The orbitals in blue and red squares are the active orbitals for CAS(8,8) and CAS(6,6), respectively. The isovalue for representative orbitals is 0.05 (grey = carbon, white = hydrogen, dark green = palladium, light green = chlorine and orange = phosphorus).	65
4.10	Molecular orbitals involved in the excited state configuration of symmetrical pincer palladacycles: a) PdNCN, b) PdSCS and c) PdPCP. Contour plots for isovalue 0.02 leading to clearer plot between Pd-L bond interactions (grey = carbon, white = hydrogen, dark green = palladium, light green = chlorine, dark blue = nitrogen, yellow = sulphur and orange = phosphorus).	68

- 4.11 Active space orbitals of PdNCS resulting from CASSCF optimisation calculation and an orbital numbering scheme which is not based on orbital energy. The orbitals in blue and red squares are the active orbitals for CAS(8,8) and CAS(6,6), respectively. The isovalue for representative orbitals is 0.05 (grey = carbon, white = hydrogen, dark green = palladium, light green = chlorine, dark blue = nitrogen and yellow = sulphur). 70
- 4.12 Active space orbitals of PdSCP resulting from CASSCF optimisation calculation and an orbital numbering scheme which is not based on orbital energy. The orbitals in blue and red squares are the active orbitals for CAS(8,8) and CAS(6,6), respectively. The isovalue for representative orbitals is 0.05 (grey = carbon, white = hydrogen, dark green = palladium, light green = chlorine, yellow = sulphur and orange = phosphorus). 73
- 4.13 Active space orbitals of PdNCP resulting from CASSCF optimisation calculation and an orbital numbering scheme which is not based on orbital energy. The orbitals in blue and red squares are the active orbitals for CAS(8,8) and CAS(6,6), respectively. The isovalue for representative orbitals is 0.05 (grey = carbon, white = hydrogen, dark green = palladium, light green = chlorine, dark blue = nitrogen and orange = phosphorus). 74
- 4.14 Molecular orbitals involved in the excited state configuration of unsymmetrical pincer palladacycles: a) PdNCS, b) PdSCP and c) PdNCP. Contour plots for isovalue 0.02 leading to clearer plot between Pd-L bond interactions (grey = carbon, white = hydrogen, dark green = palladium, light green = chlorine, dark blue = nitrogen, yellow = sulphur and orange = phosphorus). 75
- 5.1 *Trans* influence involves sigma orbitals. The strength of the interaction and bond distance between Pd-X depends on the effect of the ligand L which is situated *trans* to X donor atom. 83
- 5.2 NCN ligand conformer; a) *cis*-form and b) *trans*-form. 87

5.3	Gibbs free energy profile of <i>trans</i> -NCN and <i>cis</i> -NCN pincer ligand in the gas phase.	88
5.4	Gibbs free energy profile for the formation reaction pathway of symmetrical NCN, SCS and PCP pincer palladacycles (PdNCN, PdSCS and PdPCP, respectively).	89
5.5	Optimised geometry of each stationary point along the PdNCN formation reaction pathway (grey = C, white = H, green = Cl, green/blue = Pd and blue = N).	90
5.6	Optimised geometry of each stationary point along the PdSCS formation reaction pathway (grey = C, white = H, green = Cl, green/blue = Pd and yellow = S).	91
5.7	Optimised geometry of each stationary point along the PdPCP formation reaction pathway (grey = C, white = H, green = Cl, green/blue = Pd and orange = P).	92
5.8	Traditional orbital of metal-P interaction. Upper figure is σ donation and π back-donation.	93
5.9	Molecular orbital showing the Pd overlap with the benzene ring; a) Int1N and b) Int1S	94
5.10	Molecular graphs of Int2 ; a) Int2N , b) Int2S and c) Int2P . The BCPs are shown as small blue dots and RCPs are shown as orange dots. In Int2N and Int2S , the HCl position is on the plane of palladium complex leading to have a few interactions between HCl and palladium complex. While, in Int2P , the HCl position is perpendicular to Pd complex leading to more interactions between H ($-\text{CH}_3/-\text{CH}_2-$) and Cl (HCl).	96
5.11	Model formation reaction of palladacycles from PdCl ₂	97
5.12	An unassisted formation reaction pathway for unsymmetrical NCS pincer palladacycle (PdNCS); Path A is N coordination to Pd first and Path B is S coordination to Pd first (Reactant = pincer ligand (YCY') + PdCl ₂ , Int = Intermediate, TS = Transition State and Product = palladacycle (PdYCY') + HCl.	100

- 5.13 Optimised geometry of each stationary point along the PdNCS formation reaction pathway which N coordinates to Pd first (**Path A**) (grey = C, white = H, green = Cl, green/blue = Pd, blue = N and yellow = S). 101
- 5.14 Optimised geometry of each stationary point along the PdNCS formation reaction pathway which S coordinates to Pd first (**Path B**) (grey = C, white = H, green = Cl, green/blue = Pd, blue = N and yellow = S). 102
- 5.15 The formation reaction mechanism profile of PdNCS. **Path A** corresponding to the blue pathway represents the N coordination first to the Pd atom while **Path B** corresponding to the red pathway represents the S coordination first to the Pd atom. 103
- 5.16 Molecular graph of **Int2** for a) **Path A** and b) **Path B**. The BCPs are shown as small blue dots and RCPs are shown as orange dots. . . 104
- 5.17 An unassisted formation reaction pathway for unsymmetrical SCP pincer palladacycle (PdSCP); **Path C** is S coordination to Pd first and **Path D** is P coordination to Pd first (**Reactant** = pincer ligand (YCY') + PdCl₂, **Int** = Intermediate, **TS** = Transition State and **Product** = palladacycle (PdYCY') + HCl. The Me---Pd represents the agostic Pd---H-CH₂ interaction. 108
- 5.18 The formation reaction mechanism profile of PdSCP. **Path C** corresponding to the red pathway represents the S coordination first to the Pd atom, while **Path D** corresponding to the green pathway represents the P coordination first to the Pd atom. 110
- 5.19 Optimised geometry of each stationary point along the PdSCP formation reaction pathway which S coordinates to Pd first (**Path C**) (grey = C, white = H, green = Cl, green/blue = Pd, yellow = S and orange = P). 111
- 5.20 Optimised geometry of each stationary point along the PdSCP formation reaction pathway which P coordinates to Pd first (**Path D**) (grey = C, white = H, green = Cl, green/blue = Pd, yellow = S and orange = P). 112

- 5.21 An unassisted formation reaction pathway for unsymmetrical NCP pincer palladacycle (PdNCP); **Path E** is N coordination to Pd first and **Path F** is P coordination to Pd first (**Reactant** = pincer ligand (YCY') + PdCl₂, **Int** = Intermediate, **TS** = Transition State and **Product** = palladacycle (PdYCY') + HCl. The Me---Pd represents the agostic Pd---H-CH₂ interaction. 114
- 5.22 Optimised geometry of each stationary point along the PdNCP formation reaction pathway which N coordinates to Pd first (**Path E**) (grey = C, white = H, green = Cl, green/blue = Pd, blue = N and orange = P). 115
- 5.23 Optimised geometry of each stationary point along the PdNCP formation reaction pathway which S coordinates to Pd first (**Path F**) (grey = C, white = H, green = Cl, green/blue = Pd, blue = N and orange = P). 116
- 5.24 The formation reaction mechanism profile of PdNCP. **Path E** corresponding to the blue pathway represents the N coordination first to the Pd atom, while **Path F** corresponding to the green pathway represents the P coordination first to the Pd atom. 117
- 5.25 Left hand pictures are shown the molecular graphs and pictures of right hand are shown the contour map of electron density. The bond critical points (BCPs) are shown in blue dots and ring critical points (RCPs) are shown in orange dots; a) PdNCN, b) PdSCS and c) PdPCP. 122
- 5.26 Model palladacycles **I** - **III** studied to investigate *trans* influence. . . 126
- 5.27 Pictures of left hand are shown the molecular graphs and pictures of right hand are shown the contour map of electron density. The BCPs are shown in blue dots and RCPs are shown in orange dots; a) PdNCS, b) PdSCP and c) PdNCP. 129
- 6.1 a) The transmetallation intermediate, [(Phbz)Pd(Ph)(PPh₃)] and b) palladacycles (pre-catalyst), [Pd(Phbz)(R)(PPh₃)]. 140
- 6.2 Transition state of transmetallation reaction between arylboronic acid and palladacyclic complex. 141

6.3	Transition state of reductive elimination studied by Klinkenberg and Hartwig.	142
6.4	Three different T-shape isomers.	145
6.5	Reaction of oxidative addition of PdNCN pincer with a) hypervalent iodonium salts and b) phenyl iodides.	146
6.6	The symmetrical (1-3) and unsymmetrical (4-6) pincer palladacycles used in this study.	147
6.7	Geometrical optimisation of PhB(OH) ₂ conformers i, ii and iii.	151
6.8	The Gibbs free energy profile of symmetrical pincer palladacycles to generate catalytically active Pd(0) species (base-free).	154
6.9	Geometry of the transition state structure for the transmetallation step TS1-2 in the base-free for Pd(0) formation from a) PdNCN, b) PdSCS and c) PdPCP (grey = C, white = H, blue = N, red = O, pink = B, blue/green = Pd, light green = Cl, yellow = S and orange = P). Distances are in angstroms.	155
6.10	Geometry of the transition state structure for the reductive elimination step TS3-4/5 in the base-free for Pd(0) formation from a) PdNCN, b) PdSCS and c) PdPCP (grey = C, white = H, blue = N, blue/green = Pd, yellow = S and orange = P). Distances are in angstroms.	156
6.11	The Pd(0) formation reaction mechanism from PdNCS. The blue pathway shows the route of Pd(0) formation reaction <i>via</i> N de-coordination from Pd at TS1-2 and the red pathway shows the route <i>via</i> S de-coordination from Pd. Route I represents the pathway <i>via</i> breaking the N-Pd bond and route II represents the pathway <i>via</i> breaking S-Pd bond (base-free).	157
6.12	The Pd(0) formation reaction mechanism from PdSCP. The red pathway shows the route of Pd(0) formation reaction <i>via</i> phenyl orientated over S at Int1 and the green pathway shows the route <i>via</i> phenyl orientated over S. Route I represents the pathway <i>via</i> breaking the S-Pd bond and route II represents the pathway <i>via</i> breaking the P-Pd bond (base-free).	158

- 6.13 The Pd(0) formation reaction mechanism from PdNCP. The blue pathway shows the route to Pd(0) formation *via* N de-coordination from Pd at **TS1-2** and the green pathway shows the route *via* P de-coordination from Pd. Route **I** represents the pathway *via* breaking the N-Pd bond and the route **II** represents pathway *via* breaking the P-Pd bond (base-free). 159
- 6.14 Geometry of the transition state structure for the transmetallation step **TS1-2** in the base-free for Pd(0) formation from a) PdNCS, b) PdSCP and c) PdNCP (grey = C, white = H, red = O, pink = B, blue/green = Pd, light green = Cl, blue = N, yellow = S and orange = P). Distances are in angstroms. 165
- 6.15 Geometry of the transition state structure for the reductive elimination step for Pd(0) formation from a) PdNCS, b) PdSCP and c) PdNCP (grey = C, white = H, red = O, pink = B, blue/green = Pd, light green = Cl, blue = N, yellow = S and orange = P). Distances are in angstroms. 166
- 6.16 The Gibbs free energy profile of symmetrical pincer palladacycles to generate catalytically active Pd(0) species in the presence of the base. 169
- 6.17 Geometry of the transition state structure for the transmetallation step **TS3-4** in the presence of the base for the Pd(0) formation from a) PdNCN, b) PdSCS and c) PdPCP (grey = C, white = H, red = O, pink = B, blue/green = Pd, blue = N, yellow = S and orange = P). Distances are in angstroms. 169
- 6.18 Pd(0) formation reaction from unsymmetrical NCS pincer palladacycle (PdNCS) in the presence of the base. 172
- 6.19 Pd(0) formation reaction from unsymmetrical SCP pincer palladacycle (PdSCP) in the presence of the base. 173
- 6.20 Pd(0) formation reaction from unsymmetrical NCP pincer palladacycle (PdNCP) in the presence of the base. 174
- 6.21 The Gibbs free energy profile of unsymmetrical pincer palladacycles to generate catalytically active Pd(0) species in the presence of the base. 175

6.22	Geometry of the transition state structure for the transmetallation step TS3-4 in the presence of the base for the Pd(0) formation from a) PdNCS, b) PdSCP and c) PdNCP (grey = C, white = H, red = O, pink = B, blue/green = Pd, blue = N, yellow = S and orange = P). Distances are in angstroms.	176
6.23	The Gibbs free energy profile of symmetrical and unsymmetrical pincer palladacycles to generate catalytically active Pd(0) species in the presence of the base in toluene solvent.	184
6.24	Pincer palladacycles investigated by Roffe.	186
7.1	Core structure of benzodiazepines where R represents substitutions or side chains on the core structure and γ -aminobutyric acid (GABA), a neurotransmitter.	189
7.2	GABA _A and benzodiazepine receptors on postsynaptic membrane. . .	190
7.3	Benzodiazepine compounds used for psychosedative and tranquilising agents: a) chlorodiazepoxide, b) diazepam, c) oxazepam and d) nitrazepam.	191
7.4	Tris-2,2'-bipyridylruthenium(II) ion.	200
7.5	The Latimer diagram for calculation of excited state redox potential.	202
7.6	Simplified Jablonski diagram.	203
7.7	Electron transfer process diagram of inorganic reaction; a) outer-sphere and b) inner-sphere redox reactions.	204
7.8	Parabolic curves to represent electron transfer from reactant to product.	204
7.9	Born-Haber cycle for calculating the redox Gibbs free energy change.	209
7.10	Gibbs free energy profile of the functionalisation of the benzodiazepine mechanism using Pd(II)/Ru(II)-catalysts. In the reaction mechanism cycle, [Ru ²⁺] and [Ru ³⁺] represent [Ru(bpy) ₃] ²⁺ and [Ru(bpy) ₃] ³⁺ , respectively.	217
7.11	The energy plot by varying the bond distance between Pd and C2 to confirm no transition state between Int4 and Int5 (assuming Pd-C2 is the reaction coordinate). The energies are shown in hartrees.	222
7.12	Molecular plot of HOMO and LUMO of [Ru(bpy) ₃] ²⁺	224
7.13	Gibbs free energy profile of functionalisation using Pd(II)-catalyst.	226

7.14	Gibbs free energy profile of functionalisation without catalyst with an explicit MeOH molecule.	230
8.1	Percentage yield for functionalised-benzodiazepine products using different aryldiazonium salt.	233
A.1	Representation of canonical molecular orbitals of a symmetrical NCN pincer palladacycle resulting from the HF calculation.	256
A.2	Representation of canonical molecular orbitals of a symmetrical SCS pincer palladacycle resulting from the HF calculation.	257
A.3	Representation of canonical molecular orbitals of a symmetrical PCP pincer palladacycle resulting from the HF calculation.	258
A.4	Representation of canonical molecular orbitals of an unsymmetrical NCS pincer palladacycle resulting from the HF calculation.	259
A.5	Representation of canonical molecular orbitals of an unsymmetrical SCP pincer palladacycle resulting from the HF calculation.	260
A.6	Representation of canonical molecular orbitals of an unsymmetrical NCP pincer palladacycle resulting from the HF calculation.	261

List of Schemes

1.1	Example of reaction involving a C-anionic four-electron donor ligand.	2
1.2	Example of reaction involving a C-anionic six-electron donor ligand.	2
1.3	Unsymmetrical NCN' 25 and PCN 26 pincer palladacycles used in the aldol condensation reaction	7
3.1	Formation reaction of pincer palladacycles.	52
5.1	Formation reaction of palladacycle by Cope <i>et al.</i>	77
5.2	C-H bond activation types; i) oxidative addition, ii) electrophilic substitution and iii) multicentred reaction.	77
5.3	Two proposed reaction mechanism pathways: electrophilic aromatic substitution (left hand side) and agostic C-H bond activation (right hand side).	78
5.4	Formation of palladium coordination complex as 14e species, PdX ₂ (D-CH) ₂ .	79
5.5	Pincer palladacycle reaction profile calculated by Davies <i>et al.</i>	79
5.6	Possible formation reaction; i) assisted intramolecular, ii) assisted intermolecular and iii) unassisted mechanism.	80
5.7	Formation reaction mechanism of a pincer palladacycle	81
5.8	Proposed reaction mechanism for C-H bond activation.	82
5.9	An unassisted formation reaction pathway for PdYCY. YCY = Pincer ligand, Int = Intermediate, TS = Transition State and PdYCY = Symmetrical pincer palladacycle.	86
6.1	A traditional Heck coupling reaction, where R is aryl or vinyl and EWG is electron withdrawing group.	134
6.2	General process for the Heck catalytic cycle reaction.	135
6.3	The Heck catalytic cycle reaction proposed by Amatore and Jutand.	135

6.4	A traditional cross-coupling reaction, where Ar is an aryl group and Nu ⁻ is a nucleophile.	136
6.5	General process for cross-coupling reactions	136
6.6	New mechanism for the cross-coupling reactions proposed by Amatore and Jutand.	137
6.7	Suzuki-Miyaura cross-coupling reaction.	138
6.8	General catalytic cycle of Suzuki-Miyaura cross-coupling reaction based on Suzuki proposal.	138
6.9	Reaction of aryl halide with acrylic acid using a palladium catalyst.	138
6.10	Proposed formation mechanism of ligand free palladium in the Heck reaction.	139
6.11	The reaction process for generating the Pd(0) catalyst.	139
6.12	Reductive elimination reaction pathway of palladium complex.	141
6.13	Reductive elimination of arylpalladium cyanide complexes to generate aryl nitrile and Pd(0).	142
6.14	Reductive elimination step of arylpalladium cyanide complexes.	142
6.15	Oxidative addition of aryl halides to Pd(0) complexes study using DFT by Goossen and co-workers. The process involves coordination (step 1), oxidative addition (step 2), C-X bond cleavage (step 3) and isomerisation (step 4).	144
6.16	Pd(0) formation for the pincer palladacycles i) without base and ii) with base.	149
6.17	Proposed mechanism of generation of Pd(0) from pincer palladacycle by phenylboronic acid.	150
6.18	Catalytically active Pd(0) species formation reaction from symmetrical pincer palladacycles.	153
6.19	Catalytically active Pd(0) species formation reaction from unsymmetrical NCS pincer palladacycle (PdNCS).	160
6.20	Catalytically active Pd(0) species formation reaction from unsymmetrical SCP pincer palladacycle (PdSCP).	161
6.21	Catalytically active Pd(0) species formation reaction from unsymmetrical NCP pincer palladacycle (PdNCP).	162

6.22	General mechanism of Pd(0) formation reaction from symmetrical pincer palladacycles with base.	168
6.23	Suzuki-Miyaura cross-coupling reaction tested in order to compare with the calculation data.	180
7.1	Three principal ways for 1,4-benzodiazepine synthesis.	192
7.2	Libraries of 1,4-benzodiazepine proposed by Ellman <i>et al.</i>	193
7.3	Libraries of 1,4-benzodiazepine proposed by Spencer <i>et al.</i>	194
7.4	2-Substituted 5-phenyl-1,4-benzodiazepine derivatives synthesis by Herrero co-workers. a: 1) HCl, EtOAc followed by 2) (Cl ₃ CO) ₂ CO, Et ₃ N, CH ₂ Cl ₂ ; b: 1) HCl, EtOAc followed by 2) α -methoxy- α -(trifluoromethyl)phenylacetic acid chloride	195
7.5	One-pot synthesis of 1,4-benzodiazepine derivative by Wang <i>et al.</i>	196
7.6	One-pot N-deprotection and cyclisation of a 1,4-benzodiazepine derivative by Popp <i>et al.</i> a: di- <i>tert</i> -butyl dicarbonate, THF; b: PPh ₃ , diisopropyl azodicarboxylate, <i>N</i> -(2,2-dimethoxyethyl)-2-nitrobenzenesulfonamide, THF; c: trifluoroacetic acid, triethylsilane, dichloromethane; d: thiophenol, K ₂ CO ₃ , MeCN.	197
7.7	1,4-benzodiazepine derivative synthesis <i>via</i> cyclisation using Pd-catalysis.	198
7.8	Carboamination reaction of saturated 1,4-benzodiazepines using a Pd-catalyst.	198
7.9	Pd-catalysed synthesis of saturated 1,4-benzodiazepines by Rigamonti and co-workers.	198
7.10	Pd-catalyst synthesis of functionalised 1,4-benzodiazepines by Spencer group.	199
7.11	Functionalised chloro-1,4-benzodiazepine using Pd(OAc) ₂ by Spencer group.	199
7.12	Functionalised 1,4-benzodiazepine using Pd(OAc) ₂ and photocatalyst [Ru(bpy) ₃] ²⁺ by Spencer group.	200
7.13	Possible reaction mechanism of functionalisation using Pd(II)/Ru(II)-catalysts.	201
7.14	a) Electron excited-state of tris-2,2'-bipyridylruthenium(II) ion by UV and visible light, b) oxidative quenching and c) reductive quenching.	202

7.15	Model reactions investigated in this study, calculated in methanol solvent.	207
7.16	Possible reaction cycle of functionalisation using Pd(II)/Ru(II)-catalysts used in this work. The dotted line indicates the role of Pd(II) in the absence of the Ru(II)-photocatalyst.	215
7.17	Calculated geometries for C-H bond activation process. The bond distances are given in Å.	218
7.18	Calculated geometries for isomerisation process. The bond distances are shown in Å and bond angles are in degree.	219
7.19	Calculated geometries for single-electron transfer (SET) process. The bond distances are in Å.	221
7.20	Calculated geometries for reductive elimination process. The bond distances are in Å.	223
7.21	Calculated geometries of oxidative addition process of the reaction with Pd(II)-catalyst. The model transition, TS5-6 , is based on the transition structure obtained in the Canty <i>et al.</i> study.	227
7.22	Calculated geometries of functionalisation reaction without catalyst with an explicit MeOH molecule.	229

List of Tables

3.1	Gibbs free energy, ΔG^0 , of complexes 1 , 2 and PdPCP ([ClPd2,6-(Me ₂ PCH ₂) ₂ C ₆ H ₃]) for the formation reaction using ω B97XD/6-311++G(2df,2p) for both PBE/6-31+G(d,p) and ω B97XD/6-31+G(d,p)-optimised geometries.	52
4.1	Occupation number of CAS(n,m) in symmetrical pincer palladacycles (PdYCY), where n is number of electrons and m is number of active orbitals. The configuration interaction (CI) coefficient and weight (w.) of the dominant configuration is also provided. The numbering of orbitals is not based on orbital energy level.	60
4.2	Configuration state function (CSF), configuration interaction (CI) coefficient and its weight of optimised-PdYCY ground state using CASSCF(6,6) and CASSCF(8,8) with 6-31+G(d,p)[SDD]. All configurations with weight > 0.01 are listed.	62
4.3	Bond and interatomic distance MSE and MUE (excluding hydrogens) using PBE and CAS(6,6) with a 6-31+G(d,p)[SDD] basis set, compared to X-ray crystal structure.	67
4.4	Occupation number of CAS(n,m) in unsymmetrical pincer palladacycles (PdYCY'), where n is number of electrons and m is number of active orbitals. The configuration interaction (CI) coefficient and weight (w.) of the dominant configuration state is also provided. The numbering of orbitals is not based on orbital energy level.	69

4.5	Configuration state function (CSF), configuration interaction (CI) coefficient and its weight of optimised-PdYCY' ground state using CASSCF(6,6) and CASSCF(8,8) with 6-31+G(d,p)[SDD]. All configurations with weight > 0.01 are listed.	71
5.1	Key structure data along pathway of PdYCY formation.	98
5.2	Gibbs free energy barrier, ΔG^\ddagger for symmetrical pincer palladacycles in kJ mol^{-1}	98
5.3	Key structure data along pathway of PdNCS formation.	105
5.4	Key structure data along pathway of PdSCP formation.	109
5.5	Key structure data along pathway of PdNCP formation.	118
5.6	Gibbs free energy barrier, ΔG^\ddagger , and rate constant of reaction, k , at the rate-determining step C-H bond activation.	119
5.7	Energetic spans (δE) of PdYCY(Y') formation.	120
5.8	Electron density, $\rho(\mathbf{r})$, calculated using QTAIM analysis, Pd-L interaction (L=Y, C and Cl) in PdYCY, Y=N, S or P	123
5.9	Laplacian, $\nabla^2\rho(\mathbf{r})$, total energy density, $H(\mathbf{r})$, ellipticity, ε and delocalisation index, $\delta(\text{Pd-L})$. All values are in atomic units.	124
5.10	The electron density, $\rho(\mathbf{r})$, from the topological analysis parameters of QTAIM and Pd-Cl bond length <i>trans</i> to donor atom (NCH ₃ in I , SMe in II and PMe ₂ in III).	127
5.11	The topological analysis parameters from QTAIM: electron density $\rho(\mathbf{r})$, Laplacian of the electron density $\nabla^2\rho(\mathbf{r})$, total energy density $H(\mathbf{r})$, ellipticity ε , and delocalisation index $\delta(\text{Pd-L})$ at the bond critical point of Pd-Y(Y') in PdNCS, PdSCP and PdNCP. All values are in atomic units.	130
5.12	The bond distance in compound of symmetrical and unsymmetrical pincer palladacycles.	131
6.1	The label for Pd(0) formation reaction from each pincer type presented in this work, where Y = N, S or P.	150

6.2	The Gibbs free energy barrier, ΔG^\ddagger for the main key steps TM and RE and the total Gibbs free energy of reaction, ΔG_r for pincer palladacycles in gas phase and solvent under base-free conditions. All energies are in kJ mol^{-1}	178
6.3	The Gibbs free energy barrier, ΔG^\ddagger for the main key steps TM and RE and the total Gibbs free energy of reaction, ΔG_r for pincer palladacycles in gas phase and solvent in the presence of a base. All energies are in kJ mol^{-1}	179
6.4	Gibbs free energy barrier (ΔG^\ddagger) and total Gibbs free energy ΔG_r from calculations in this work (with base and toluene solvent). Gibbs free energy values are in kJ mol^{-1}	183
6.5	Gibbs free energy barrier from calculations in the <i>o</i> -xylene solvent and percentage conversion from experiments. Gibbs free energy values are in kJ mol^{-1} . The structure data for 7a to 14 are shown in Figure 6.24.	185
6.6	Energetic spans (δE) of Pd(0) formation from pincer palladacycle in the presence of the base in toluene solvent. Energy values are in kJ mol^{-1}	187
7.1	Comparison of the calculated and experimental data of redox potential for low spin complex $[\text{Ru}(\text{bpy})_3]^{n+}$ in MeCN solvent with different solvation model and molecular cavity.	213
7.2	Comparison of the calculated and experimental data of redox potential for high spin complex $[\text{Ru}(\text{bpy})_3]^{n+}$ in MeCN solvent with different solvation model and molecular cavity.	214
B.1	The relative Gibbs free energy of reaction for PdYCY in gas phase and solvent under the base-free condition.	263
B.2	The relative Gibbs free energy of reaction for PdNCS in gas phase and solvent under the base-free condition.	264
B.3	The relative Gibbs free energy of reaction for PdSCP in gas phase and solvent under the base-free condition.	265
B.4	The relative Gibbs free energy of reaction for PdNCP in gas phase and solvent under the base-free condition.	266

B.5	The relative Gibbs free energy of reaction for PdYCY in gas phase and solvent under the presence of the base.	267
B.6	The relative Gibbs free energy of reaction for PdNCS in gas phase and solvent under the presence of the base.	268
B.7	The relative Gibbs free energy of reaction for PdSCP in gas phase and solvent under the presence of the base.	268
B.8	The relative Gibbs free energy of reaction for PdNCP in gas phase and solvent under the presence of the base.	269

Chapter 1

Introduction and Thesis Overview

1.1 Introduction to palladacycles and their applications

In 1965 Cope and Siekman first reported the synthesis of palladacycles and since their discovery they have been found to have many useful and interesting applications in modern organic chemistry.¹ They play an important role as catalysts in a number of chemical reactions, and are also utilised as intermediates in organic reactions.^{2,3} These palladacycles are also used in nanoscience applications such as gas sensors,⁴ chemical switches⁴ and in medicinal chemistry.⁵

For classification of palladacycles, two broad types exist, depending on how the ligand coordinates to the palladium centre. The first type is the C-anionic four-electron donor ligand (CY) coordinating to the palladium centre and the second type is the C-anionic six-electron donor ligand (YCY) known as a pincer ligand coordinating to the palladium centre, where Y is a two-electron donor ligand (Figure 1.1).⁶ An example of the C-anionic four-electron donor ligand is 1,3-bis(2-pyridyloxy)benzene (Scheme 1.1).⁷ When this reacts with Pd(OAc)₂, a palladacycle is formed as the product. A C-anionic six-electron donor ligand pincer complex may be synthesised by the reaction between *m*-hydroxyphenol and diphenylchlorophosphine with triethylamine in toluene solvent. Palladium chloride is then added in the reaction mixture (Scheme 1.2).⁸

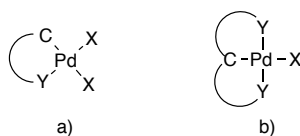
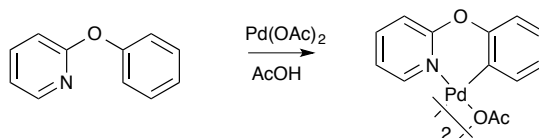
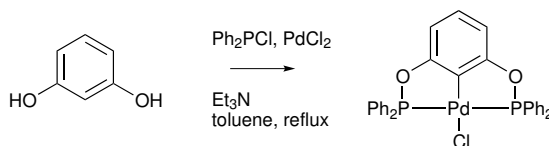


Figure 1.1. Palladacycles; a) C-anionic four-electron donor (CY) complex and b) C-anionic six-electron donor.⁶



Scheme 1.1. Example of reaction involving a C-anionic four-electron donor ligand.⁷



Scheme 1.2. Example of reaction involving a C-anionic six-electron donor ligand.⁸

Many researchers have synthesised palladacycles and modified their structures for catalytic applications. One of the widest applications is in the Heck reaction, which involves the coupling of an α -olefin with an organic halide.⁹ PCP pincer palladacycles, PdPCP **1** and **2** (Figure 1.2) were used to achieve the coupling between iodobenzene and methylacrylate in solvent *N*-methylpyrrolidone and base sodium carbonate.¹⁰

Based on the work of Beller and Zapf,¹¹ the PdPCP **3** (Figure 1.2) was synthesised and used in the coupling of styrene with iodo- and bromobenzene.¹² They observed **3** to be a good catalyst, providing both a high yield and regioselectivity. In addition, this catalyst is inexpensive and stable in air. Moreover, the PdPCP **4** was found to be a stable catalyst when it was introduced in the Heck reaction between methyl acrylate and aryl bromides or iodides (Figure 1.2).¹³

SCS pincer palladacycles (PdSCS) have been found and used in the Heck reaction. It has been shown that PdSCS **5** (Figure 1.3) was successful in catalysing a C-C bond in the coupling of iodobenzene with either styrene or methyl acrylate in dimethylformamide and this catalyst was easily recyclable.¹⁴ Furthermore, in the literature, porous silica, Merrifield resin and poly(norbornene) bound PdSCS **6** (Figure 1.3) acted as pre-catalysts in the Heck coupling reaction between iodobenzene and *n*-butyl acrylate.¹⁵ It has also been shown that supported palladacycles act as

shown to be easily accessible and be highly efficient for the cross-coupling of less reactive chloroaromatic compounds.²⁰

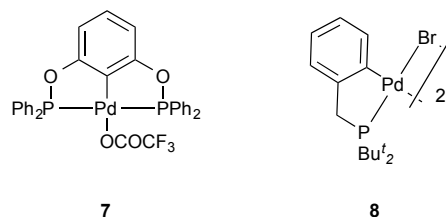


Figure 1.4. Phosphorus donor palladacycles **7** and **8** using in the Suzuki-Miyaura cross-coupling reaction.^{19,20}

Palladacycles containing sulfur donor atoms are also interesting and they have been developed and applied for the Suzuki-Miyaura reaction. For instance, Zim *et al.*²¹ used catalyst precursor sulfur-containing palladacycles **9**, **10** and **11** (Figure 1.5) for cross-coupling using aryl bromides and chlorides. Their investigation showed that these palladacycle complexes gave medium to excellent yields of products.

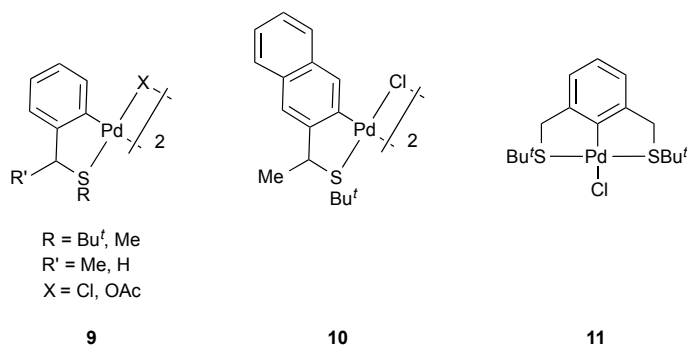


Figure 1.5. Sulfur donor palladacycles **9**, **10** and **11** using in Suzuki-Miyaura cross-coupling reaction.²¹

The pincer NCN palladacycle, PdNCN **12** (Figure 1.6) was tested for the catalytic C-C bond formation of iodobenzenes with phenyl boronic acids. It was showed that **12** worked very well with high yields and gave more than 900,000 of TON and 45,000 h⁻¹ of turnover frequency, TOF (TOF = TON/reaction time (h)).²²

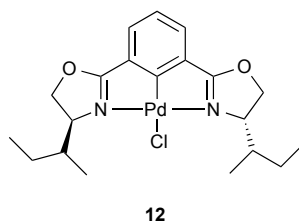


Figure 1.6. Nitrogen donor palladacycles **12** used in Suzuki-Miyaura cross-coupling reaction.²²

In other types of active catalysts, P-coordinated and As-coordinated NC palladacycles are shown in Figure 1.7. The catalytic activity of the P-coordinated NC palladacycle **13** was examined in the Suzuki-Miyaura reaction and showed very high TONs and excellent conversions in cross-coupling between PhB(OH)_2 and a broad range of aryl chlorides.²³ Moreover, the P-coordinated NC palladacycle **14** (Figure 1.7) catalytic precursors were applied to polymer chemistry where they were used for controlled Suzuki cross-coupling polymerisation and gave a very narrow polydispersity index (PDI).²⁴ Varying the ring size of P-coordinated to NC palladacycles **15** (Figure 1.7) in the cross-coupling between aryl bromide and phenylboronic acid showed that the catalytic activity increased with increasing ring size, due to increasing the mobility of the P group.²⁵ In addition, the catalytic activity of the interesting As-coordinated NC palladacycle **16** (Figure 1.7) was investigated by Bedford *et al.*²⁶ and their results showed that As-coordination provided a high TON but medium percentage conversion, compared to the results from P-coordinated NC palladacycles **17** (Figure 1.7) showing both high percentage conversion and TON.

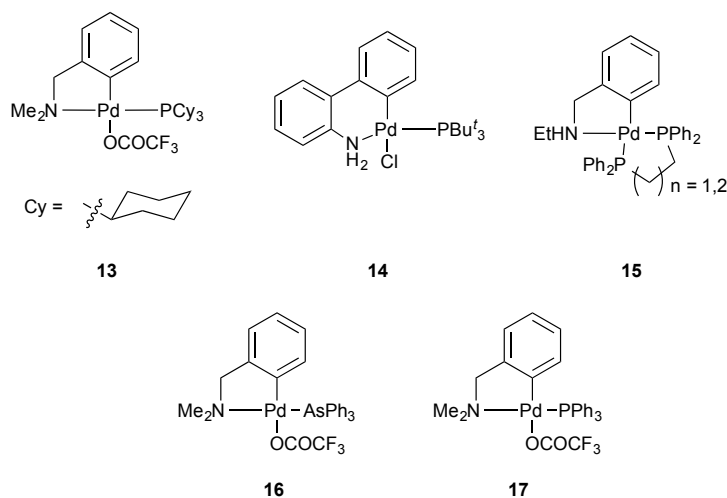


Figure 1.7. P-coordinated NC palladacycles **13**, **14**, **15**, **16** and **17**.^{23–26}

Oxime palladacycles are an interesting type of catalytic or pre-catalytic compound which have an oxime arm (Figure 1.8). They act as catalysts or pre-catalysts in a number of organic reactions. The oxime palladacycles **18**,²⁷ **19**²⁷ (Figure 1.8) catalyst precursors were used for the coupling reaction of aryl, allyl and benzyl bromides and chlorides with phenylboronic acid and the results provided a high TOF.²⁷ An oxime palladacycle has been claimed to form a recyclable catalyst when functionalised on the polymer substrate, **20**. (Figure 1.8) It has been shown that a polymer-supported oxime palladacycle acted as a pre-catalyst and led to the cross-coupling reaction between benzoyl bromide derivatives and phenylboronic acid in DMF-H₂O. Using these pre-catalysts gave excellent percentage yields.²⁸

Some chemists are interested in reactions under eco-friendly conditions. It has been shown that the oxime-derived palladacycle pre-catalyst **21** (Figure 1.8) used for the reaction between benzoyl chloride and phenylboronic acid in the eco-friendly solvent 2-MeTHF is chemically less hazardous. The oxime palladacycle pre-catalysts provided a high catalytic activity with good percentage yield.²⁹ There have also been reports of palladacycles **22** and **23** (Figure 1.9) being applied as a catalyst for the C-C bond formation in Suzuki-Miyaura reactions under eco-friendly condition.^{30,31}

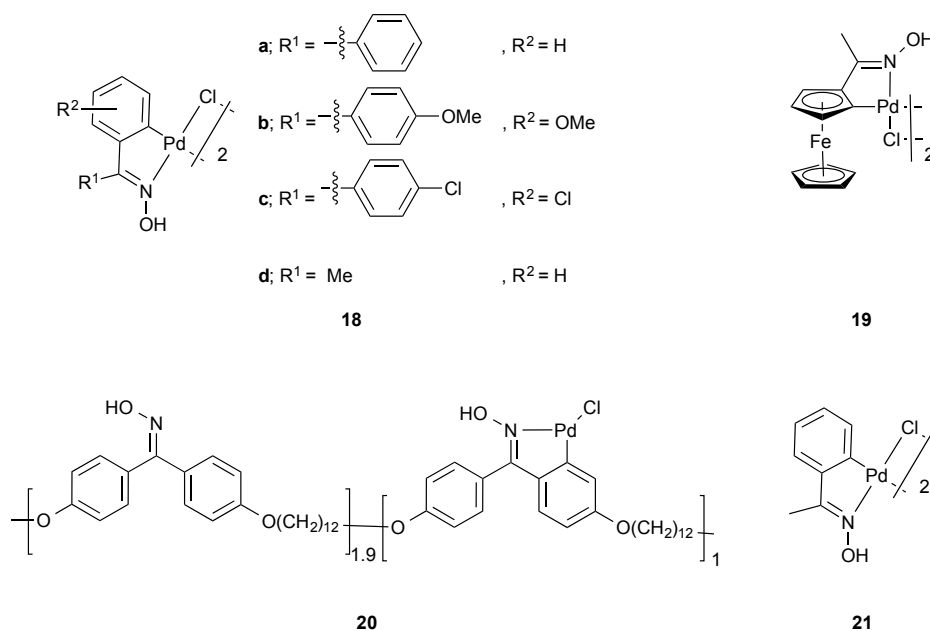


Figure 1.8. Oxime palladacycles **18**, **19**, **20** and **21**.²⁷⁻²⁹

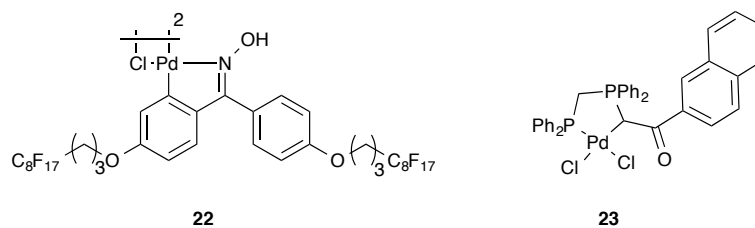


Figure 1.9. Palladacycles **22** and **23** applied as catalysts in Suzuki-Miyaura reaction under eco-friendly conditions.^{30,31}

The other type of pincer palladacycle is the unsymmetrical type which has been synthesised and its catalytic activity tested in the Suzuki-Miyaura reaction.⁶ The unsymmetrical SCN pincer palladacycle **24** (Figure 1.10) was used as a pre-catalyst in this reaction. It provided high percentage conversion when the reaction between 4-bromoanisole and phenylboronic acid in *o*-xylene and base K_2CO_3 was performed.³²

In addition, unsymmetrical pincer palladacycles can be used in catalytic aldol condensation. For example, Roffe *et al.* synthesised novel unsymmetrical NCN' **25** and PCN **26** pincer palladacycles and tested the catalytic aldol condensation of methylisocyanoacetate with benzaldehyde in dichloromethane. These catalysts gave excellent yields (Scheme 1.3).³³

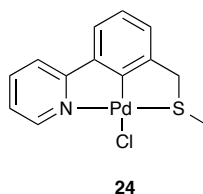
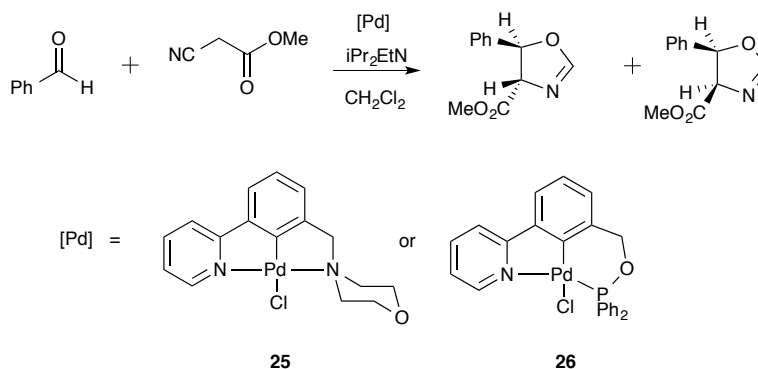


Figure 1.10. Unsymmetrical NCS **24** pincer palladacycle used in the Suzuki-Miyaura reaction.³²



Scheme 1.3. Unsymmetrical NCN' **25** and PCN **26** pincer palladacycles used in the aldol condensation reaction.³³

Palladacycle compounds have also been used in biomedical applications. For example, the palladacycle **28** (Figure 1.11) has been used to stunt the growth of tumours. It showed a high antiproliferative activity against the MDA-MB231 and MCF7 human breast cancer cell lines, with IC_{50} in the range 1-5 μ M where IC_{50} is the inhibition constant. This is the concentration of substance inhibiting biological response by 50 percent.³⁴ In addition, there is an excellent review which provides examples of anti-cancer palladacycles.³⁵

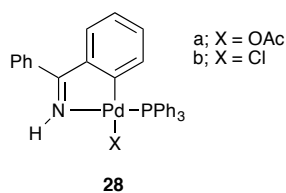


Figure 1.11. Palladacycle **28** with antitumour activity.³⁴

The foregoing literature survey above has discussed the many applications of palladacycles. Their catalytic and biological activities depend upon the types of ligand arms. Understanding the activities, structures and bonding of palladacycles is crucial in the modification and development of such catalysts. Thus theoretical and computational chemistry are major tools for gaining insight into the physical and chemical properties of these important molecules. These methods are used in rationalising the bonding of the complex, understanding the mechanism, and predicting or explaining the observed selectivity from experiment.

1.2 Computational chemistry

Computers are used in nearly every industry, and they have had very wide-reaching effects in science including computational chemistry. Chemists use computers in order to simulate those chemical systems which cannot be observed by experiment. Computational chemistry uses a mathematical description of chemistry, known as theoretical chemistry, which is incorporated in computer programs for solving chemical problems, understanding phenomena or predicting the results of future experiments. Computational chemistry can be divided into two broad types, quantum mechanics based on the Schrödinger equation and molecular mechanics based on Newton's second law.³⁶ Normally, we can use molecular mechanics such as molecular

dynamics or stochastic dynamics for simulation of proteins or very large molecules, whilst for smaller systems, quantum mechanics may be used. In this thesis, we will focus only on quantum mechanics, which is “the correct mathematical description of the behaviour of electrons”.³⁷ In principle, we cannot solve the Schrödinger equation exactly for systems with more than two particles but we can use approximation methods such as *ab initio* methods, semi-empirical and density functional theory (DFT). The key ideas and concepts of approximation methods and some relevant computational chemistry techniques relating with our work will be discussed in theoretical background (Chapter 2).

1.3 Thesis overview

This thesis presents a computational investigation of the structure, bonding and reactivity of some pincer palladacycles and Pd-based catalysts. First, the theoretical background, including concepts of approximation methods, basis sets, quantum theory of Atoms in Molecules (QTAIM) and natural bond orbital (NBO) analysis will be provided in Chapter 2. The methodological requirement for the study of pincer palladacycles is presented in Chapters 3 and 4, in order to secure and validate a suitable methodology for the research in this thesis. Chapter 3 provides a method validation for studying the geometries of pincer palladacycles and Chapter 4 contains a complete active space self-consistent field (CASSCF) method investigation of pincer palladacycles to determine the nature of the electronic structure. Chapter 5 presents an investigation of the formation and stability of symmetrical and unsymmetrical pincer palladacycles (PdYCY and PdYCY', respectively) to determine the role of the donor atoms Y and Y' in their stability. Chapter 6 investigates the formation of the active catalyst Pd(0) from the pincer palladacycle pre-catalysts, and the results are used to provide insight into the desirable properties of an effective catalyst for Suzuki-Miyaura cross-coupling reactions. Chapter 7 focusses on the functionalisation of benzodiazepine using a Pd-catalyst and provides an explanation for the increased reaction yield when a Ru-photocatalyst is presented in the experiment. Finally, Chapter 8 presents the concluding remarks and future direction, and provides the thesis outcomes of my work, including publications, oral presentations and posters.

Chapter 2

Theoretical Background

This chapter provides the theoretical background including the Hartree-Fock method, post-Hartree-Fock method, Density Functional Theory (DFT) method, basis sets, Quantum Theory of Atoms in Molecules (QTAIM) and Natural Bond Orbital (NBO) analysis.

2.1 Introduction

In this thesis, the complete active space self-consistent field (CASSCF) method, which is a post-Hartree-Fock method, is used to study electronic structure and DFT methods are used to investigate structures, reactivities and physical properties. Thus, we introduce some of the basic concepts behind these methods. We start with the Schrödinger equation and Hartree-Fock method which lay the foundation for CASSCF, following which DFT methods will be discussed. Finally, an overview of the basis sets and analysis tools used in this thesis will be presented.

2.2 The Schrödinger equation

Atomic and molecular systems can be described using an eigenvalue equation known as the Schrödinger equation. A wavefunction, Ψ , is a mathematical function which contains all the information of the quantum system. The key piece of information extracted from Schrödinger equation is the energy of the system, thus the main goal for approximating the solution of the Schrödinger equation is to obtain the energy

of the atomic or molecular system. When determining the energy of an atomic or molecular system, quantum mechanics (QM) can be used to predict the behaviour of electrons and nuclei and thus determine the molecular properties. The general form of the non-relativistic, time independent, Schrödinger equation is

$$\hat{H}\psi = E\psi, \quad (2.1)$$

where \hat{H} is the Hamiltonian operator and E is an eigenvalue which, here, is the electronic energy.

The most general form of the Hamiltonian operator represented in atomic units can be written as:

$$\hat{H} = \overbrace{-\frac{1}{2} \sum_{i=1}^N \nabla_i^2 - \frac{1}{2} \sum_{A=1}^M \frac{1}{M_A} \nabla_A^2}^{\text{kinetic terms}} - \overbrace{\sum_{i=1}^N \sum_{A=1}^M \frac{Z_A}{r_{iA}} + \sum_{i=1}^N \sum_{j>i}^N \frac{1}{r_{ij}} + \sum_{A=1}^M \sum_{B>A}^M \frac{Z_A Z_B}{R_{AB}}}^{\text{potential terms}} \quad (2.2)$$

where A and B run over the M nuclei in the system, while i and j run over the N electrons. The nucleus A has a mass equal to M_A which is represented in multiples of the electron mass. Z_A and Z_B are the atomic charge number for nucleus A and B , respectively, and R_{AB} is the distance between nuclei. r_{iA} represents the distance between the electron i and nucleus A and r_{ij} represents the distance between electrons i and j . The first two terms in equation (2.2) represent the system's kinetic energy and last three terms represent the potential energy, which consists of Coulomb attraction and repulsion.³⁸ ∇_q^2 ($q = i$ or A) is the Laplacian operator which is defined as the second derivative of the chosen coordinate system. For example, ∇_q^2 in terms of the Cartesian coordinate system for a three-dimensional space (3D) is

$$\nabla_q^2 = \frac{\partial^2}{\partial x_q^2} + \frac{\partial^2}{\partial y_q^2} + \frac{\partial^2}{\partial z_q^2}. \quad (2.3)$$

The Hamiltonian in equation (2.2) is rarely used directly in computational software, but is simplified using the Born-Oppenheimer approximation.^{36,37} The underlying physical justification of the Born-Oppenheimer approximation is that the nuclei are much heavier than the electrons which move much faster than the nuclei. From the point of view of the electrons, the motion of the nuclei is much less and hence the nuclei can be approximated to be fixed. This situation leads to

the nuclei's kinetic energy being zero and their nuclear-nuclear repulsion potential energy being constant. The molecular geometry can be represented by fixed nuclear coordinates with electrons acting as a cloud of negative charge distributed around the positions of nuclei. A plot of a number of different nuclear geometries for a given system as a function of energy is called a potential energy surface (PES). The minimum energy structure on the PES corresponds to the most stable structure of a given molecule.³⁹⁻⁴¹ In the Born-Oppenheimer approximation, the electronic and nuclear motion are solved separately to simplify calculations and the Hamiltonian operator in equation (2.2) is reduced to the electronic Hamiltonian (\hat{H}_{elec}):

$$\hat{H}_{\text{elec}} = \underbrace{-\frac{1}{2} \sum_{i=1}^N \nabla_i^2}_{\text{kinetic term}} - \underbrace{\sum_{i=1}^N \sum_{A=1}^M \frac{Z_A}{r_{iA}}}_{\text{nuclear-electron attraction}} + \underbrace{\sum_{i=1}^N \sum_{j>i}^N \frac{1}{r_{ij}}}_{\text{electron-electron repulsion}} \quad (2.4)$$

The first term of equation (2.4) is the kinetic operator of the electrons, second term accounts for nuclear-electron attraction and the last term is the electron-electron repulsion. A more compact form of equation (2.4) is

$$\hat{H}_{\text{elec}} = \hat{T} + \hat{V}_{ne} + \hat{V}_{ee} \quad (2.5)$$

where \hat{T} , \hat{V}_{ne} and \hat{V}_{ee} are the kinetic, nuclear-electron attraction and electron-electron repulsion terms, respectively. The solution from \hat{H}_{elec} operating with the electronic wavefunction (Ψ_{elec}) is the electronic energy (E_{elec}). From this point, the total electronic energy can be calculated by adding the E_{nuc} which is the energy from the constant nuclear repulsion term (the last term of the equation (2.2)) to E_{elec} :

$$E_{\text{total}} = E_{\text{elec}} + E_{\text{nuc}}. \quad (2.6)$$

From now, the electronic Hamiltonian and electronic wavefunction are considered and they can be written as $\psi_{\text{elec}} = \psi$ and $\hat{H}_{\text{elec}} = \hat{H}$.³⁸

The exact energy of the hydrogen atom and its exact wavefunction can be calculated due to it being a two particle system and hence solvable analytically. For many-electron wavefunctions, we do not know the exact form of the wavefunction,

hence approximate methods are required to find the approximate wavefunction and energy. Confidence in this approximate energy can be heightened by use of the variational principle. This theorem states that the energy, E from any wavefunction ψ is greater than or equal to the true (exact) energy, $E_0^{(ex)}$, of the ground state, i.e.

$$\frac{\int \psi^* \hat{H} \psi d\tau}{\int \psi^* \psi d\tau} = \frac{\langle \psi | \hat{H} | \psi \rangle}{\langle \psi | \psi \rangle} \geq E_0^{(ex)}. \quad (2.7)$$

where $\langle \psi | \psi \rangle$ is equal to 1 for a normalised function. The wavefunction ψ from equation (2.7) is called the trial wavefunction.³⁸ This theorem can be used to assess the quality of the trial wavefunction: the lower the energy, E , the closer to the true ground-state energy, E_0 , and, it is assumed, the better the trial wavefunction. This trial wavefunction holds all information about the system and has to obey the following fundamental postulate: ψ must be i) continuous, ii) single-valued, iii) finite and iv) antisymmetric to electron exchange.³⁷ The variational principle is also the key mathematical concept for DFT.³⁸ What we need to do in order to find the exact energy of the ground state is to minimise the functional $E[\psi]$ which “*is a function whose argument is itself a function*”³⁸ by searching through all eligible N -electron wavefunctions. The formula for finding $E_0^{(ex)}$ is

$$E_0^{(ex)} = \min_{\psi \rightarrow N} E[\psi] = \min_{\psi \rightarrow N} \langle \psi | \hat{T} + \hat{V}_{ne} + \hat{T}_{ee} | \psi \rangle \quad (2.8)$$

where $\psi \rightarrow N$ indicates that ψ is an allowed N -electron wavefunction. It is not possible to solve equation (2.8) exactly, thus an approximate method is chosen for determining the energy that best approaches $E_0^{(ex)}$.³⁸

2.3 The Hartree-Fock method

We will introduce the Hartree-Fock (HF) method which is the simplest type of *ab initio* calculation (*ab initio* means “from the beginning”).³⁷ It is the fundamental approximation, which can be used to address the many-electron wavefunction problem at a basic level and leads to some higher-level approximate methods such as the CASSCF method. Thus, understanding this approximation will help to understand other approximate methods.

The HF method starts from the Hartree scheme where it is built from one-electron atomic orbitals corrected by electron spin. The electron-electron repulsion term is treated by assuming average field of the other $N - 1$ electrons. In this method, the wavefunctions approximate the N -electrons by a Slater determinant, Ψ , obeying the Pauli exclusion principle:

$$\Psi = \frac{1}{\sqrt{N!}} \begin{vmatrix} \varphi_1(\vec{x}_1) & \varphi_2(\vec{x}_1) & \cdots & \varphi_N(\vec{x}_1) \\ \varphi_1(\vec{x}_2) & \varphi_2(\vec{x}_2) & \cdots & \varphi_N(\vec{x}_2) \\ \vdots & \vdots & \ddots & \vdots \\ \varphi_1(\vec{x}_N) & \varphi_2(\vec{x}_N) & \cdots & \varphi_N(\vec{x}_N) \end{vmatrix} \quad (2.9)$$

where $\varphi(\vec{x})$ is a spinorbital at position x where it is composed of a spatial orbital (ψ) and spin function (α and β). The simpler notation for representing equation (2.9) can be written using only its principal diagonal.⁴² That is

$$\Psi = (1/N!)^{1/2} |\varphi_1(\vec{x}_1)\varphi_2(\vec{x}_2)\cdots\varphi_N(\vec{x}_N)|. \quad (2.10)$$

Roothaan and Hall suggested an idea to use linear combination of atomic orbitals (LCAO) or basis functions, χ to treat electron distribution qualitatively and it is written as:⁴⁰

$$\varphi_i = \sum_{s=i}^m c_{si}\chi_s \quad (2.11)$$

where c are coefficients. The set of basis functions are called the basis set, which is discussed in detail in section 2.7.

Next, we will introduce the HF equation for individual spinorbitals and the

procedure for solving this equation. The HF equation is formed from:

$$\hat{f}_i \varphi_i = \varepsilon_i \varphi_i \quad (2.12)$$

where ε is the eigenvalue and can be physically understood as the orbital energies and φ being satisfied through the minimisation. \hat{f} is the Fock operator defined as:

$$\hat{f}_i = \overbrace{-\frac{1}{2}\nabla_i^2}^{\text{kinetic term}} - \underbrace{\sum_A \frac{Z_A}{r_{iA}}}_{\text{potential term}} + V_{\text{HF}}. \quad (2.13)$$

The first two terms represent the kinetic term and the electron-nuclear interaction (potential term). These terms (kinetic + potential) are known as the one-electron core Hamiltonian or hydrogenic part, $\varepsilon_i^{(0)}$. V_{HF} , which is known as the Hartree-Fock potential, is an average repulsion potential between electron i^{th} and the other $N-1$ electrons. Therefore, in equation (2.13), the complicated two-electron repulsion operator ($1/r_{ij}$) is replaced by V_{HF} , leading to electron-electron repulsion being considered in an average way. V_{HF} consists of i) the Coulomb operator, $\hat{J}_j(\vec{x}_1)$, representing the electron potential due to the average charge distribution of another electron in φ_i and ii) the exchange operator $\hat{K}_j(\vec{x}_1)$ being the correction term which leads to an exchange of the variable in the two spinorbitals.³⁸ V_{HF} is given by:

$$V_{\text{HF}}(\vec{x}_1) = \sum_j^N \left(2\hat{J}_j(\vec{x}_1) - \hat{K}_j(\vec{x}_1) \right). \quad (2.14)$$

The HF equations are solved through the self-consistent field (SCF) procedure which uses an iterative process searching until a convergence criterion is satisfied. When the basis functions, equation (2.11), are substituted in equation (2.12) and then both sides multiplied by $\chi_{s'}^*$ and integrated overall space, we obtain:

$$\sum_{s=i}^m F_{s's} c_{si} = \varepsilon_i \sum_{s=i}^m S_{s's} c_{si} \quad (2.15)$$

$F_{s's}$ and $S_{s's}$ are the Fock and overlap matrix, respectively and can be written as:

$$F_{s's} = \left\langle \chi_{s'} \left| \hat{f}_i \right| \chi_s \right\rangle \quad (2.16)$$

$$S_{s's} = \langle \chi_{s'} | \chi_s \rangle \quad (2.17)$$

Equation (2.15) is known as the Roothaan equation which is a set of simultaneous equations for determining the coefficients. To find an unknown energy, ε_i , initially the spinorbitals are constructed by choosing the set of basis functions and formulating a set of trial coefficients, c_{si} (using equation (2.11)). Next, $F_{s's}$ and $S_{s's}$ are calculated using equation (2.16) and (2.17) then the energy, ε_i is solved using the self-consistent field method. In each iteration, the new sets of c_{si} are calculated until a convergence criterion has been satisfied (either c_{si} or ε_i are the minimal improvement compared to previous iteration).⁴²

2.4 Post-Hartree-Fock approximation

The HF method has no electron correlation and it does not consider the instantaneous Coulomb interaction between electrons. HF considers the interaction between an electron with an average field of other electrons (it does not consider the instantaneous Coulomb interaction between electrons). Thus, the HF method fails to properly account for the electron correlation, leading to errors when calculating molecular properties. The Configuration Interaction (CI), Coupled Cluster (CC) and Complete Active Space Self-Consistent Field (CASSCF) method are procedures to treat electron correlation more precisely. Due to using the CASSCF method for studying electronic structures in this thesis, the CI method, which is the principle of the CASSCF method, will be introduced, after which the CASSCF will be discussed.

2.4.1 Configuration interaction

The configuration interaction (CI) method treats the Hartree-Fock determinant as the ground state then adds other determinants as promotions of electrons from the ground state to unoccupied or virtual orbitals for treating electron correlation.⁴³ Each state of promotion can be defined as single, double *etc.* excitation as shown in Figure 2.1.

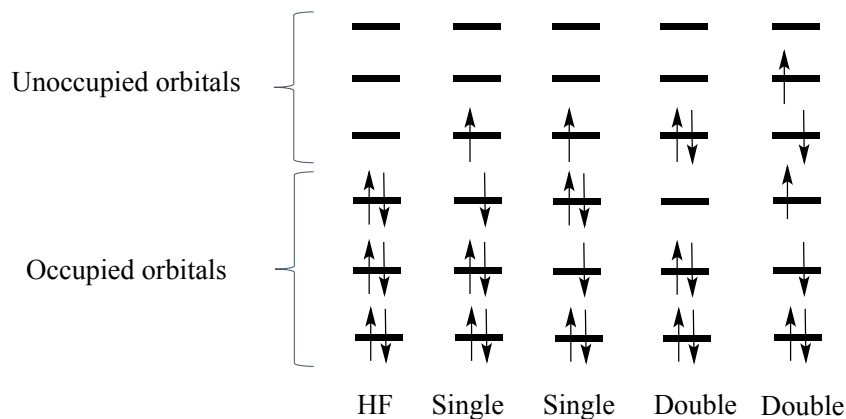


Figure 2.1. Promotion of electrons to get single and double excitations.

Consider the wavefunction with N -electrons in the ground state, which can be written as:

$$\Psi_0 = (1/N!)^{1/2} |\varphi_1(\vec{x}_1)\varphi_2(\vec{x}_2)\cdots\varphi_m(\vec{x}_m)\varphi_n(\vec{x}_n)\cdots\varphi_N(\vec{x}_N)| \quad (2.18)$$

where $\varphi_N(\vec{x}_N)$ is the highest occupied molecular orbital, and $\varphi_m(\vec{x}_m)$ and $\varphi_n(\vec{x}_n)$ are among the occupied spinorbitals. Equation (2.18) can be written in a simpler notation with the normalisation factor implied as:

$$\Psi_0 = \|\varphi_1\varphi_2\cdots\varphi_m\varphi_n\cdots\varphi_N\| \quad (2.19)$$

When an electron is promoted to an excited state, the determinant will be re-written to take account of this excited electron. For example, if one electron from the occupied orbital φ_m is excited to a virtual φ_p , the singly excited determinant can be written as:

$$\Psi_m^p = \|\varphi_1\varphi_2\cdots\varphi_p\varphi_n\cdots\varphi_N\| \quad (2.20)$$

If two electrons have been promoted, one from the occupied orbital φ_m to a virtual φ_p and one from φ_n to φ_q . This can be written as a doubly excited determinant as:

$$\Psi_{mn}^{pq} = \|\varphi_1\varphi_2\cdots\varphi_p\varphi_q\cdots\varphi_N\| \quad (2.21)$$

We can write other possibilities for excited determinants as there are many possibilities to promote the electron from the ground-state to a virtual orbital. Each determinant

is called a configuration state function (CSF).⁴²

The exact ground-state wavefunction can be expressed as a linear combination of basis function (recall equation (2.11)), thus the excited-state determinants can be added to the ground-state determinant as a linear combination of CSFs as well. That is:

$$\Psi_{\text{CI}} = c_0\Psi_0 + \sum_{m,p} c_m^p \Psi_m^p + \sum_{\substack{m<n \\ p<q}} c_{mn}^{pq} \Psi_{mn}^{pq} + \dots = \sum_{J=1}^L C_J \Psi_J \quad (2.22)$$

where c_m^p , c_{mn}^{pq} and C_J represent expansion coefficients. The second term represents singly excited determinants involving one electron excitation; the third term is a doubly excited determinant and so on. The expression represented in equation (2.22) is called the configuration interaction (CI).⁴²

The common kind of CI calculation is classified by the number of electrons simultaneously promoted to virtual orbitals. The CI involving only single excitations is called CIS. Other kinds of CI are CISD involving single and double excitation and CISD(T) involving single, double and perturbative triple excitations. Furthermore, if it involves all possible excitations, it is called full CI.⁴²

2.4.2 Complete active-space self-consistent field method

The CASSCF method is a modified form of the multiconfiguration self-consistent field method (MCSCF). The construction of the wavefunction starts from a linear combination of two or more configurations.

$$\Psi_{\text{MCSCF}} = \sum_{K=1} C_K \Psi_K \quad (2.23)$$

where Ψ_K is the configuration state. The coefficients C_K in equation (2.23) as well as c_{si} in equation (2.11) are optimised, while C_J and c_{si} in equation (2.22) coefficient in CI method are fixed at the Hartree-Fock values. The wavefunctions are themselves optimised by determining the optimal values of coefficients. For determining the optimal value of coefficients, the wavefunctions are divided into three classes:

1. A set of inactive orbitals is doubly occupied in all determinants corresponding to core orbitals.
2. A set of virtual orbitals is unoccupied in all determinants remaining empty

during calculation.

3. A set of active orbitals is all other orbitals which lie between the inactive and virtual orbitals.

The active electrons and the number of active orbitals for calculating the system can be chosen. Only the active electrons are distributed in the active orbitals which is calculated using the full CI procedure. Therefore, the CSFs are built from all possible combinations of active electron promotion in the active orbitals.⁴² For solving the wavefunction, the coefficients C_K are determined variationally using Ψ_K as the trial wavefunction. In each iteration, the set of coefficients is solved continually until self-consistency.

2.5 Density functional theory (DFT)

DFT is another computational methodology which can be used to treat the electron correlation. This method is a technique employed to calculate molecular structures, physical and chemical properties, based on the electron density instead of the wavefunction. It provides good accuracy, compared to semi-empirical methods, and has much lower computational cost, compared to some methods such as Møller-Plesset perturbation, CASSCF and the coupled cluster method.

The two basic theorems behind DFT were proposed by Hohenberg and Kohn where they are known as Hohenberg-Kohn existence and Hohenberg-Kohn variational theorems. The Hohenberg-Kohn existence theorem proved that “*the energy and all other properties of a ground-state molecule are uniquely determined by the ground-state electron probability density*”.⁴³ This proof guarantees that we can get the information of molecular properties from the construction of the electron density of the wavefunction. The Hohenberg-Kohn variational theorem, (c.f. equation (2.7)) but this theorem based on electron density, expresses that the energy from any trial electron density is greater or equal to the true ground state energy. Thus, based on these theorems, the ground-state energy of a molecule can be written as:

$$E[\rho] = T[\rho] + V_{ee}[\rho] + V_{ne}[\rho] \quad (2.24)$$

where $E[\rho]$ is the total electronic energy, $T[\rho]$ is the kinetic energy of the electrons, $V_{ee}[\rho]$ is the electron-electron repulsion energy and $V_{ne}[\rho]$ is the nuclear-electron interaction. The $V_{ee}[\rho]$, consists of the classical Coulomb interaction energy, $J[\rho]$, and the exchange energy, $K[\rho]$. The two classical terms $V_{ne}[\rho]$ and $J[\rho]$ are well treated and they can be calculated exactly *via*:

$$V_{ne}[\rho] = \sum_{A=1}^M \frac{Z_A}{r_{A1}} \rho(\mathbf{r}_1) d\mathbf{r}_1 \quad (2.25)$$

$$J[\rho] = \int \frac{\rho(\mathbf{r}_1)\rho(\mathbf{r}_2)}{r_{12}} d\mathbf{r}_1 d\mathbf{r}_2 \quad (2.26)$$

In consideration of the equation (2.24), the first and second terms are more difficult to deal with since energy terms for the kinetic and some components of the potential have no classical form.⁴⁰ To solve this issue, Kohn and Sham introduced a general equation form to investigate the total electronic energy of the system:

$$E[\rho] = T_S[\rho] + J[\rho] + V_{ne}[\rho] + E_{XC}[\rho] \quad (2.27)$$

$T_S[\rho]$ is the exact kinetic energy of the non-interacting system which can be exactly calculated. E_{XC} is the exchange-correlation energy and it includes unknown terms: the non-classical effects of self-interaction correction, exchange and correlation (contributing to the potential energy of system) and a portion belonging to the kinetic energy. Substituting equation (2.25) and (2.26) in equation (2.27), and expressing the $T_S[\rho]$ term, the more precise equation (2.27) can be written as:

$$E[\rho] = \sum_{i=1}^N \psi_i^{\text{KS}}(\mathbf{r}_1) \nabla_1^2 \psi_i^{\text{KS}}(\mathbf{r}_1) + \int \frac{\rho(\mathbf{r}_1)\rho(\mathbf{r}_2)}{r_{12}} d\mathbf{r}_1 d\mathbf{r}_2 - \sum_{A=1}^M \frac{Z_A}{r_{A1}} \rho(\mathbf{r}_1) d\mathbf{r}_1 + E_{XC}[\rho] \quad (2.28)$$

where, ψ_i^{KS} is the one-electron spatial orbital, and is known as the Kohn-Sham orbital.

Generally, $E_{XC}[\rho]$ is determined by approximate techniques which can be considered to have two separate components: the exchange energy functional, $E_X[\rho]$, and correlation energy functional, $E_C[\rho]$:⁴²

$$E_{XC}[\rho] = E_X[\rho] + E_C[\rho]. \quad (2.29)$$

Kohn and Sham also introduced the set of equations for solving the electron density, which closely follows the form of the Schrödinger equation (see equation (2.1)). The equation is known as the Kohn-Sham equation:⁴²

$$\left\{ -\frac{1}{2}\nabla_1^2 + \int \frac{\rho(\mathbf{r}_2)}{r_{12}} d\mathbf{r}_2 + \sum_{A=1}^M \frac{Z_A}{r_{12}} + v_{XC}(\mathbf{r}_1) \right\} \psi_m^{KS}(\mathbf{r}_1) = \epsilon_m^{KS} \psi_m^{KS}(\mathbf{r}_1) \quad (2.30)$$

where ϵ_m^{KS} is the Kohn-Sham orbital energy and $v_{XC}(\mathbf{r}_1)$ is the exchange-correlation potential defined as:

$$v_{XC}(\mathbf{r}_1) = \frac{\delta E_{XC}[\rho]}{\delta \rho}. \quad (2.31)$$

and the electron density is defined as:

$$\rho(\mathbf{r}) = \sum_{\text{occ}} |\psi_i|^2. \quad (2.32)$$

To solve the Kohn-Sham equation, the trial electron density is generated and the exchange-correlation potential is formulated by using $E_{XC}[\rho]$. Then, the Kohn-Sham equation is solved with an initial set of its orbitals. This procedure is repeated, and each cycle updated with improved electron density until the exchange-correlation and density have both reached the target tolerance set by the program. Next, the main points of some functionals will briefly discussed.

2.6 Exchange-correlation functionals

As mention above, the exchange-correlation functional is unknown, thus the error of calculation depends on the E_{XC} approximation. The challenge is to decrease the error of $E_{XC}[\rho]$ as much as possible by proper selection of exchange and correlation functionals.⁴² Many researchers have developed the approximation form to obtain the good accurate $E_{XC}[\rho]$. There are no systematic ways for improving the quality of $E_{XC}[\rho]$. Thus, the best way to verify the performance of the exchange-correlation functional is to compare the theoretical calculations with experimental results of known systems.

The simplest exchange-correlation functional is the local density approximation (LDA). This functional considers the electron density to be treated as a homogeneous

electron gas to find the exchange-correlation energies:

$$E_{XC}^{\text{LDA}}[\rho] = \int \rho(\mathbf{r}) \varepsilon_{XC}^{\text{LDA}}(\rho(\mathbf{r})) d\mathbf{r}. \quad (2.33)$$

where $\varepsilon_{XC}^{\text{LDA}}(\rho(\mathbf{r}))$ represents the exchange-correlation energy per electron of a uniform electron gas and $\rho(\mathbf{r}) \varepsilon_{XC}^{\text{LDA}}(\rho(\mathbf{r}))$ represents the exchange-correlation energy density.⁴⁴

However, it should be emphasised that the LDA uses the same spatial orbital to fill spin-paired electrons, which means that this approximation will give inaccurate results if the molecule is open-shell. Thus, the local-spin-density approximation (LSDA), which allows the spin-paired electrons to fill in different spatial orbitals, is used.

In addition to the inclusion of electron density as in LSDA, it also takes into account the gradient of the density which is added to the exchange correlation energy given in equation (2.33). As this functional is gradient-corrected, it is named the generalised gradient approximation (GGA):

$$E_{XC}^{\text{GGA}}[\rho_\alpha, \rho_\beta] = \int f(\rho_\alpha(\mathbf{r}), \rho_\beta(\mathbf{r}), \nabla\rho_\alpha(\mathbf{r}), \nabla\rho_\beta(\mathbf{r})) d\mathbf{r} \quad (2.34)$$

where f is a function consisting of densities and the gradients of densities.⁴² There are a variety of exchange-correlation functionals for GGA such as PBE, BP86 and B97D. Functionals have a more complicated mathematical form, thus we will present only the important terms of functionals and refrain from giving their details.

The PBE (Perdew-Burke-Ernzerhof) functional was developed by Perdew *et al.*^{45,46} where it consists of the PBE exchange energy and the PBE correlation energy:

$$E_{XC}^{\text{PBE}}[\rho_\alpha, \rho_\beta] = E_X^{\text{PBE}}[\rho_\alpha, \rho_\beta] + E_C^{\text{PBE}}[\rho_\alpha, \rho_\beta]. \quad (2.35)$$

In short, equation (2.35) can be written as: $E_{XC}^{\text{PBE}}[\rho] = E_X^{\text{PBE}}[\rho] + E_C^{\text{PBE}}[\rho]$. The exchange energy per electron of a uniform electron gas for PBE is written as an enhancement factor ($F(s)$), containing the reduced density gradient ($s(\mathbf{r})$), multiplied by the LSDA exchange energy per electron, $\varepsilon_X^{\text{LSDA}}$:

$$E_X^{\text{PBE}}[\rho] = \int \rho(\mathbf{r}) \varepsilon_X^{\text{PBE}}(\rho(\mathbf{r})) d\mathbf{r} = \int \rho(\mathbf{r}) \varepsilon_X^{\text{LSDA}}(\rho(\mathbf{r})) F(s) d\mathbf{r} \quad (2.36)$$

and

$$s(\mathbf{r}) = \frac{|\nabla\rho(\mathbf{r})|}{2k_F\rho(\mathbf{r})} \quad (2.37)$$

For the correlation part, the PBE correlation energy per electron is calculated from the LSDA correlation energy per electron, $\varepsilon_C^{\text{LSDA}}$, corrected by gradient contribution, $H(t)$:

$$E_C^{\text{PBE}}[\rho] = \int \rho(\mathbf{r})\varepsilon_c^{\text{PBE}}(\rho(\mathbf{r}))d\mathbf{r} = \int \rho(\mathbf{r})[\varepsilon_C^{\text{LSDA}}(\rho(\mathbf{r})) + H(t)]d\mathbf{r} \quad (2.38)$$

The performance of this functional which is improved by adding $F(s(\mathbf{r}))$ and $H(t)$ was tested by the atomisation energy calculation on twenty small molecules compared to experimental data. It was shown that the PBE functional had a mean absolute error less than LSDA, indicating that atomisation energy calculation errors were reduced by using PBE.⁴⁵

The BP86 functional consists of B (sometimes one also finds B88) exchange and P86 correlation functional. The B exchange energy, $E_X^{\text{B}}[\rho]$, is constructed in the form of a correction term, which is added to the LSDA functional:

$$E_X^{\text{B}}[\rho] = E_X^{\text{LSDA}} - \beta \sum \int \rho(\mathbf{r})^{4/3} \frac{x_\sigma^2}{1 + 6\beta x_\sigma^2 \sinh^{-1} x_\sigma^2} d\mathbf{r} \quad (2.39)$$

$$x_\sigma = \frac{|\nabla\rho(\mathbf{r})|}{\rho(\mathbf{r})^{4/3}} \text{ (sometimes one also finds } \frac{|\nabla\rho_\sigma|}{\rho_\sigma^{4/3}} \text{)} \quad (2.40)$$

where β is the constant which is determined by fitting to exact atomic Hartree-Fock data and σ represents the α or β spin.⁴⁷

The P86 correlation is constructed to improve the approximate energy for atoms, molecules and solids for the inhomogeneous electron gas system since E_C^{LSDA} gives serious errors for calculating these systems.⁴⁸ The E_C^{P86} form, proposed by Perdew⁴⁸ in 1986, is built from the LSDA functional with a correction term:

$$E_C^{\text{P86}}[\rho] = E_C^{\text{LSDA}} + \int \frac{d^{-1}e^{-\Phi}C(\rho)|\nabla\rho(\mathbf{r})|^2}{\rho(\mathbf{r})^{4/3}} d\mathbf{r} \quad (2.41)$$

It clearly shows the inclusion of an extra term which has the gradient of the electron density, $\nabla\rho(\mathbf{r})$.

Another example of a GGA functional which is used for validation purposes

in this thesis is B97D. This functional is constructed using the GGA functional introduced in 1997,⁴⁹ and an extension term is added in order to account for van der Waals interactions:

$$E_X^{\text{B97D}}[\rho] = E_X^{\text{B97}}[\rho] + E_C^{\text{B97}}[\rho] + E_{\text{disp}} \quad (2.42)$$

The $E_X^{\text{B97D}}[\rho]$ consists of the γ parameter, chosen to fit the known energy value, and the reduced gradient, x_σ (recall equation (2.40) for x_σ).

$$E_X^{\text{B97}}[\rho] = \sum \int \rho(\mathbf{r}) \varepsilon_X^{\text{LSDA}}(\rho(\mathbf{r})) \frac{\gamma_{X\sigma} x_\sigma^2}{1 + \gamma_{X\sigma} x_\sigma^2} d\mathbf{r}. \quad (2.43)$$

For the B97D correlation energy, $E_C^{\text{B97D}}[\rho]$, opposite spins and parallel spins are calculated separately. For correlation energy with opposite spins:

$$E_{C\alpha\beta}^{\text{B97}}[\rho] = \int \rho_{\alpha,\beta}(\mathbf{r}) \varepsilon_C^{\text{LSDA}}(\rho_\alpha(\mathbf{r}), \rho_\beta(\mathbf{r})) \frac{\gamma_{C\alpha\beta} x_{\text{av}}^2}{1 + \gamma_{C\alpha\beta} x_{\text{av}}^2} d\mathbf{r} \quad (2.44)$$

where $x_{\text{av}}^2 = 1/2(x_\alpha^2 + x_\beta^2)$ and correlation energy with parallel spins:

$$E_{C\sigma\sigma}^{\text{B97}}[\rho] = \sum \int \rho(\mathbf{r}) \varepsilon_C^{\text{LSDA}}(\rho(\mathbf{r})) \frac{\gamma_{C\sigma\sigma} x_\sigma^2}{1 + \gamma_{C\sigma\sigma} x_\sigma^2} d\mathbf{r} \quad (2.45)$$

This functional uses an empirical (scaled) dispersion correction for E_{disp} . It can be written as:

$$E_{\text{disp}} = -s_6 \sum_{i=1}^{N_{\text{atom}}-1} \sum_{j=i+1}^{N_{\text{atom}}} N_{\text{atom}} \frac{C_6}{r_{ij}^6} f_{\text{damp}}(\mathbf{r}_{ij}) \quad (2.46)$$

where s_6 is the scaling factor for this correction term, N_{atom} is the number of atoms in the system, C_6 represent the dispersion coefficient and $f_{\text{damp}}(\mathbf{r}_{ij})$ is called a damping function.

In a further improvement on GGA functionals, inclusion of the second derivative of the electron density (Laplacian of the electron density) or kinetic density energy allows for improved accuracy. This functional name is the meta-generalised gradient approximation functionals (meta-GGA) which is known as third rung of Jacob's ladder. Hence, we can write a meta-GGA in the general form:

$$E_{XC}^{\text{MGGA}}[\rho_\alpha, \rho_\beta] = \int f(\rho_\alpha(\mathbf{r}), \rho_\beta(\mathbf{r}), \nabla\rho_\alpha(\mathbf{r}), \nabla\rho_\beta(\mathbf{r}), \nabla^2\rho_\alpha(\mathbf{r}), \nabla^2\rho_\beta(\mathbf{r})) d\mathbf{r} \quad (2.47)$$

The TPSS functional is one of the meta-GGA functionals and this method includes the reduced Laplacian as a variable which is added in the enhancement factor of the exchange energy. The correlation energy for the TPSS functional consists of the kinetic energy density, $\tau_w(\mathbf{r})$, acting as a correction term.⁵⁰ Another example of a meta-GGA functional, used in the validation calculations in Chapter 3, is M06L which has the spin kinetic energy density included in the exchange part and the opposite spins and parallel spins in the correlation term are treated separately.⁵¹

We now move up Jacob’s ladder of DFT to hybrid-GGA functionals which include contributions from Hartree-Fock theory. The B3LYP functional, which is a popular hybrid, consists of the Becke exchange functional with 3 parameters a , b and c for their linear combination (B3) and the Lee-Yang-Parr (LYP) correlation functional:

$$E_{XC}^{\text{B3LYP}} = (1 - a)E_X^{\text{LSDA}} + aE_X^{\text{HF}} + b\Delta E_X^{\text{B}} + (1 - c)E_C^{\text{LSDA}} + cE_C^{\text{LYP}} \quad (2.48)$$

where a , b and c are 0.20, 0.72 and 0.81, respectively.³⁶

M06 is the hybrid functional which is an improvement from M06L by Truhlar *et al.*⁵² The general form of this functional is given by:

$$E_{XC}^{\text{M06}} = \frac{X}{100}E_X^{\text{HF}} + \left(1 - \frac{X}{100}\right)E_X^{\text{DFT}} + E_C^{\text{DFT}} \quad (2.49)$$

where X is the percentage of Hartree-Fock exchange in the total exchange functional. This functional splits the exchange term into 27 % of Hartree-Fock and 73 % of DFT.

In this work, most of single-point calculations are performed with the hybrid functional ωB97XD . This functional was developed by Head-Gordon *et al.* to improve the ωB97X functional which does not include van der Waals interaction.⁵³ The X of the name ωB97X stands for the use of the $E_X^{\text{SR-HF}}$ functional (SR = short-range). The general equation for ωB97X can be written as:

$$E_{XC}^{\omega\text{B97XD}} = E_X^{\text{LR-HF}} + c_X E_X^{\text{SR-HF}} + E_X^{\text{SR-B97}} + E_C^{\text{B97}} + E_{\text{disp}} \quad (2.50)$$

where there are three exchange terms, one correlation term and one dispersion correction. In the Hartree-Fock exchange term, the long-range (LR) and short-range (SR) operators to partition the Coulomb operator are used. They contain the

parameter ω which defines the range of the operators; this functional has $\omega = 2.0$ Bohr⁻¹ which denotes the distance between long and short range. c_X of the $E_X^{\text{SR-HF}}$ term is the fractional number of short-range operator. As can be seen in equation (2.43), the B97 exchange is modified by replacing the $\varepsilon_X^{\text{LSDA}}(\rho)$ with $\varepsilon_X^{\text{SR-LSDA}}(\rho)$. The $\varepsilon_X^{\text{SR-LSDA}}(\rho)$ includes the ω parameter and if ω is equal to 0, $\varepsilon_X^{\text{SR-LSDA}}(\rho)$ is reduced to $\varepsilon_X^{\text{LSDA}}(\rho)$. ω B97XD includes 100 % HF exchange at long range, while it includes a small fraction of exact HF exchange and B97 exchange at short-range. For correlation energy, E_C^{B97} has the same form as equation (2.44) and (2.45). For E_{disp} , the unscaled dispersion correction is used in this functional (not including s_6 scaling factor). It is given by:

$$E_{\text{disp}} = - \sum_{i=1}^{N_{\text{atom}}-1} \sum_{j=i+1}^{N_{\text{atom}}} \frac{C_6}{r_{ij}^6} f_{\text{damp}}(\mathbf{r}_{ij}) \quad (2.51)$$

2.7 Basis set

The basis set is the set of basis functions. Ideally, one would want to use an infinite basis set, in order to achieve the HF limit, but in practice, an infinite basis set is computationally intractable, therefore the choice of basis set is important as it must provide good accuracy whilst being computationally efficient.⁵⁴ The basis set must not be too small or too big. It should be suitable for describing the molecular problem.

There are two functional forms to be used for a basis set: Slater functions $\exp(-\zeta r)$ and Gaussian functions $\exp(-\xi r^2)$.⁴¹ The Slater function is good for approximating an atomic wavefunction (Figure 2.2), but it requires substantial computer time to conduct all numerical integrations for the molecular system. The Gaussian function, implemented within the Gaussian09 program, is a better choice for evaluating the molecular system as it requires less demanding calculation and thus a lower computation time (Figure 2.2).

The main disadvantage of the Gaussian function is that a single Gaussian is a poor approximation, as it lacks a cusp at the nucleus and the shape of the function at large distance is different from the ideal atomic orbital.^{40,54} For solving this problem, several linear combinations of a single Gaussian function are used to approximate the system. For example, STO-3G uses three Gaussian functions to approximate

a Slater function, and STO-3G represents “Slater-type orbital (approximated by) three Gaussians”.⁴⁰ However, STO-3G is not good enough for research because it is too small.⁴⁰ Therefore, split-valence basis sets, which are used in this work, are more widely adapted in computational research rather than using STO-3G.

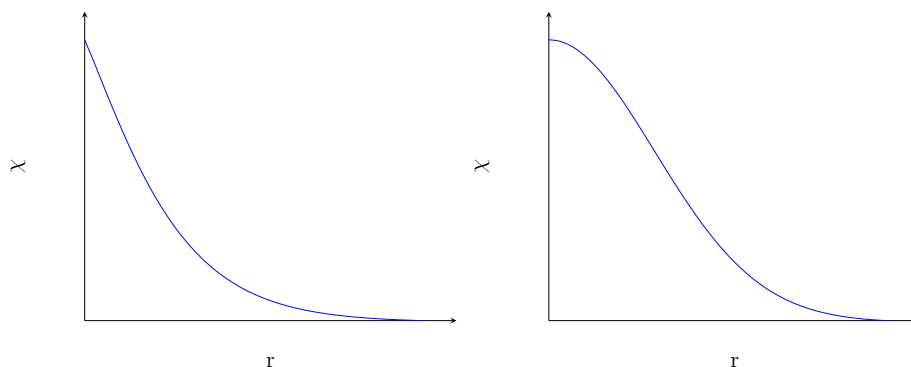


Figure 2.2. (left) Slater functional plot. (right) Gaussian functional plot.

2.7.1 Split-valence basis set

The split-valence basis set was introduced by Pople *et al.*⁵⁵ and also goes by the name Pople basis set. For instance, The 3-21G basis set consists of a core orbital using one basis function, which is composed of three Gaussians (hence the “3”), and the valence orbital splits into an inner shell and an outer shell (hence the “21”) which is known as a double zeta basis set. The inner shell involves two Gaussians and the outer shell involves only one Gaussian. Therefore, CH₄ uses 17 basis functions; each H has a 1s orbital split into 1s’ and 1s’’; C has 1s function for the core electron and 2s, 2p_x, 2p_y and 2p_z orbitals split into eight functions (2s’, 2p_x’, 2p_y’, 2p_z’, 2s’’, 2p_x’’, 2p_y’’, and 2p_z’’). Linear combinations of the 17 basis functions are used to build 17 molecular orbitals. Accuracy can be improved by using a double zeta basis set known as 6-31G which allows one orbital to represent the core orbital where is composed of six Gaussian functions, and the valence orbitals are split into an inner and outer shell, comprised of 3 and 1 Gaussians, respectively. To increase flexibility, the valence orbitals can also split into three parts, with an example being 6-311G, where they are called triple zeta basis sets. Thus, in the case of 6-311G, the H and He atoms for triple zeta have a total of 3 basis functions and the second period of the periodic table have a total of 13 basis functions. The greater flexibility of the basis function

leads to the improvement of the computational result quality. However, adding more additional basis functions results in a more computationally expensive calculation.

Polarisation functions can be used to further improve the basis set and increase flexibility. They allow the valence orbitals to change shape by adding in functions that are one unit of angular momentum higher. For example, p functions are added to hydrogen atoms and d functions are added to C, O, N *etc.* The simple 3-21G basis set becomes 3-21G* (sometimes written as 3-21G(d)) when polarisation functions are added to the non-hydrogen and helium atoms. Polarisation functions can be added to all atoms, including the hydrogen and helium atoms with the basis set referred to as 3-21G** (sometimes written as 3-21G(d,p)). Diffuse functions can be included in the basis set. Adding these functions lead to an expansion of the asymptotic behaviour of the Gaussian, representing the expanding electron cloud. The symbol “+” is added to a Pople basis set to represent the addition of diffuse functions to non-hydrogen atoms and “++” when diffuse functions are added to all atoms.⁴⁰

All calculations in this work are performed using a double zeta Pople basis set for the optimisation of structures on all atoms (except for Pd and Ru) augmented with polarisation and diffuse functions on all non-hydrogen atoms and polarisation functions on the hydrogen atoms. This is a 6-31+G(d,p) basis set. In the single point energy calculation, to obtain the accurate energy the triple zeta Pople basis set is used with added polarisation and diffuse functions (2p for hydrogen atom and 2df for others). This basis set is 6-311++G(2df,2p) and it is used for all atoms except Pd and Ru. The basis set for Pd and Ru will be discussed in the next section.

2.7.2 Effective core potential (pseudopotentials)

There are many electrons in Pd and Ru, hence a large set of functions to describe them is required. In addition, most electrons are in the core shell, which have a small effect on chemical properties. The solution to this problem is to have a combined nuclear-electronic core and treat it as a nuclear point charge. The core electrons can be replaced with an effective potential proposed by Hellmann,⁵⁶ now referred to as the effective core potential (ECP).³⁶ The key for ECP construction is how many electrons are added to the ECP, and in some cases the scalar and/or spin-orbit relativistic effects might be added in the effective potential. The popular ECP

choices, which are widely used, are the Stuttgart/Dresden (SDD)⁵⁷ and Los Alamos National Laboratory double zeta (LanL2DZ)^{58,59} and they were also used for Pd and Ru atoms in this thesis. They consider 28 electrons for Pd and Ru in the core shell and include relativistic treatment. The valence (non-ECP) electrons are treated using a double-zeta basis set.

2.8 Solvation model

Solvent effects can be included in a theoretical calculation on the compound to obtain the results corresponding with experiment. In quantum mechanical calculations, an implicit solvation model is often used in the calculation rather than using an explicit solvation model. One of the implicit solvation models normally used is the polarisable continuum model.⁶⁰ The idea of this solvent model is that a solute molecule is put into the cavity formed by interlocking spheres around the atoms of the solute molecule. At the same time, the molecule in the cavity is treated inside of a continuous dielectric field representing the solvent.⁶⁰ For the Gaussian09 program, one of the popular specific solvation methodologies implemented is the integral equation formalism polarisable continuum model (IEFPCM) which is the default for Gaussian09 and IEFPCM is the synonym for PCM. This model was developed originally by Cancès and Mennucci in 1997.⁶¹⁻⁶³ It is “a reformulation of dielectric polarisable continuum model (DPCM) in terms of the integral equation formalism”.⁶⁴ The solute-solvent interaction is calculated from the interaction of the electrostatic potential of the solute with the polarisation of the dielectric field.⁶⁵ The other popular model is the conductor-like polarisable continuum model (CPCM). It considers the dielectric continuum as a conductor-like continuum. These models provided an accurate approximation to the Gibbs free energy⁶⁴ and they were used in this thesis.

2.9 Quantum theory of Atoms in Molecules

The wavefunction ψ has all the information of the atomic or molecular system considered but we cannot observe it directly. The Quantum Theory of Atoms in Molecules (QTAIM) is a model for extracting the information from ψ . This model

was developed by Bader and co-workers.⁶⁶ The principal concept of the QTAIM is to separate the molecule into basins containing individual atoms with electron density. Then the electron density ($\rho(\mathbf{r})$), which is physically observable, within the molecule is plotted to investigate its topology. Therefore, the view of the molecule is observed as a network of bond paths linking atoms in the molecule.⁶⁶ Chemical bonds and physical properties can be gained from this topology of the electron density.

2.9.1 Critical points

The plotting of the electron density provides information on the electronic structure. Maxima, minima or saddle points in space can be observed by the first derivative of the electron density, $\nabla\rho(\mathbf{r})$. At these points, $\nabla\rho(\mathbf{r})$ are called “critical points”, where the $\nabla\rho(\mathbf{r})$ are equal to zero. For classification between minima, maxima or saddle point, the second derivative of the electron density, $\nabla^2\rho(\mathbf{r})$ which is known as the Laplacian of the density can be used to describe these points. The diagonalisation of the Hessian matrix form, with respect to the x, y, z principal axes, is used to determine the curvature of the density (λ). The diagonal form can be written as:

$$\nabla^2\rho(\mathbf{r}) = \begin{pmatrix} \frac{\partial^2\rho}{\partial x^2} & 0 & 0 \\ 0 & \frac{\partial^2\rho}{\partial y^2} & 0 \\ 0 & 0 & \frac{\partial^2\rho}{\partial z^2} \end{pmatrix} = \begin{pmatrix} \lambda_1 & 0 & 0 \\ 0 & \lambda_2 & 0 \\ 0 & 0 & \lambda_3 \end{pmatrix} \quad (2.52)$$

where, λ_1, λ_2 and λ_3 are the curvature of the density.

The types of critical point are classified by the number of non-zero curvatures of ρ , called rank (ω), and the algebraic sum of the signs of the curvature, called the signature (σ). The symbol for the representation of each critical point can be written as (ω, σ) . Normally, $\omega = 3$ is found for a molecular structure with an equilibrium charge distribution, and each curvature contribution is +1 or -1 depending on positive or negative curvature. Thus, the critical points of the molecule can be divided into four types:⁶⁷

1. The first type is (3,-3). This type has three local maxima which have three negative curvatures. This type refers to the nuclear critical point (NCP).
2. The second type has two negative curvatures (3,-1). This critical point is found

at the saddle points having a maximum of ρ in the plane but the third axis, which is perpendicular to this plane, is a minimum. This point is known as the bond critical point (BCP).

3. The third type concerns two positive curvatures (3,+1), where ρ is a minimum in the plane and the second derivative of ρ is positive along two axes. This point is called the ring critical point (RCP).
4. The last type is known as the cage critical point (CCP) which has three negative curvatures (3,+3). This point is found at the central point of a cage molecular structure.

The Poincaré-Hopf relationship can be applied to confirm that all critical points have been found and identified in an isolated molecule or an infinite crystal. This relationship is given by:

$$n_{\text{NCP}} - n_{\text{BCP}} + n_{\text{RCP}} - n_{\text{CCP}} = \begin{cases} 1 & \text{(Isolated molecules)} \\ 0 & \text{(Infinite crystals)} \end{cases} \quad (2.53)$$

where n is the number of each type of critical point (CP) and $\{n_{\text{NCP}}, n_{\text{BCP}}, n_{\text{RCP}}, n_{\text{CCP}}\}$ is known as the “characteristic set”.⁶⁸ Thus, the Poincaré-Hopf relationship is necessary for proving there are no missing CPs in the calculation of the molecule and the crystal.

The example topology of the electron density and molecular graph of benzene are shown in Figure 2.3. The NCPs (small violet dots) give the maximum of ρ density, whilst the charge distribution between provides the saddle points. All of the saddle points represent BCPs (small orange dots). The centre of the benzene ring gives the point of minimum charge density in this plane which is a RCP. This analysis satisfied the Poincaré-Hopf relationship which has summation of the number CP = 1 ($n_{\text{NCP}} = 12$, $n_{\text{BCP}} = 12$, $n_{\text{RCP}} = 1$ and $n_{\text{CCP}} = 0$).

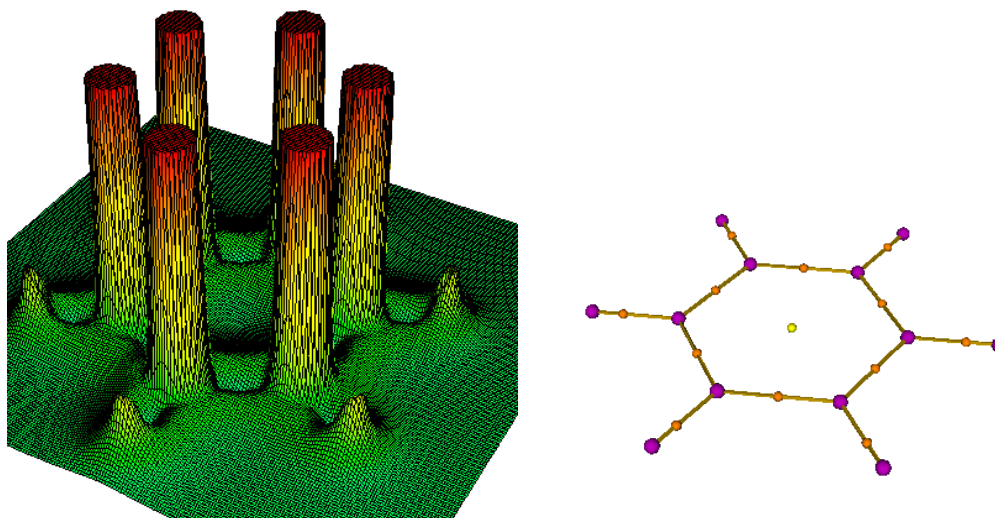


Figure 2.3. Topology of the electron density (left) and molecular graph (right) for benzene. The NCPs, BCPs and RCPs are shown in the molecular graph as small violet dots, orange dots and yellow dots, respectively.

In Figure 2.3 (right), the yellow lines connect to the maximum charge linking between nuclei. This line is defined as the bond path. At the BCP, the intersection is always found between the bond path and atomic surface (the atomic surface is defined as the boundary of the atom basins).⁶⁶ Thus, the bond path and BCP can be used as confirmation of linking between nuclei. However, the bond paths do not necessarily represent chemical bonds, they represent an interaction between the nuclei.⁶⁹ The connecting of bond paths also represent the shape of the molecule and are referred to as a molecular graph.⁶⁸

2.9.2 Bond strength and the nature of the bond

To rationalise the stability of a structure, the topological analysis can be used to investigate the strength and nature of interactions. At the BCP, the value of $\rho(\mathbf{r})$ can be used to characterise the strength of an atomic interaction, reflecting the strength of a bond and the magnitude of $\rho(\mathbf{r})$ can be used to indicate the nature of the bond. When $\rho(\mathbf{r})$ is greater than 0.20 a.u. between atoms they have a shared interaction (covalent bond), and when $\rho(\mathbf{r})$ is less than 0.10 a.u. this indicates a closed-shell interaction (e.g. ionic interaction, van der Waals, hydrogen bond *etc.*).⁶⁸

When considering $\nabla^2\rho(\mathbf{r})$ which is made up from the summation of three

curvatures (recall equation (2.52)), an important indicator for the identification of the regions of the local electronic charge, correspond to the accumulation or depletion at the BCP. If the value of $\nabla^2\rho(\mathbf{r})$ is greater than zero, the density of the electrons at the BCP is locally depleted, while when the value of $\nabla^2\rho(\mathbf{r})$ is less than zero, the density of the electrons at the BCP is locally concentrated. In addition, $\nabla^2\rho(\mathbf{r})$ can be used to identify the nature of the bond where covalent bonds have charge concentration ($\nabla^2\rho(\mathbf{r}) < 0$) but ionic bonds have charge depletion ($\nabla^2\rho(\mathbf{r}) > 0$).⁶⁸

Another way to determine the nature of the bond interaction is to investigate the potential energy density, $V(\mathbf{r})$ and the gradient kinetic energy density, $G(\mathbf{r})$ at the BCP. The $V(\mathbf{r})$ value is always negative, while $G(\mathbf{r})$ is everywhere positive. The sum of $V(\mathbf{r})$ and $G(\mathbf{r})$ provide another quantity for determining the nature of the bond that is the total energy density, $H(\mathbf{r})$, proposed by Cramer and Kraka.⁷⁰ The sign of $H(\mathbf{r})$, which is controlled by the balance between $V(\mathbf{r})$ and $G(\mathbf{r})$, is used to classify the nature of the bond. The dominant $V(\mathbf{r})$ causes $H(\mathbf{r})$ to be more negative, representing more electron density accumulation at the BCP which indicates a shared interaction between atoms. On the other hand, $H(\mathbf{r})$ has a positive sign when the $G(\mathbf{r})$ value is greater than $V(\mathbf{r})$, representing the depletion of electron density which indicates a closed-shell interaction.

2.9.3 π -character in the single bond

As mentioned above, the curvatures (their summation) can be used to characterise the nature of a bond. They can also be used to describe the π -character. The ratio of two curvatures λ_1 and λ_2 are used to determine how pronounced the elliptical shape is and leads to the so-called ellipticity parameter, ε :

$$\varepsilon = \frac{\lambda_1}{\lambda_2} - 1 \quad (2.54)$$

where $|\lambda_1| \geq |\lambda_2|$ and the ε are in the ranges between zero and infinity. Thus, when ε is equal to zero i.e. $|\lambda_1| = |\lambda_2|$, and the ellipticity is zero, it represents a single or triple bond.⁶⁸ In the case of a single bond, the π -character increases with increasing ε value.⁶⁸

2.10 Natural bond orbital (NBO) analysis

In this work, the NBO program was used to analyse the bond between donor atom and Pd-centre where the NBO program performs “the analysis of a many-electron molecular wavefunction in terms of localized electron-pair bonding units”.⁷¹ The NBO analysis, first developed by Weinhold and co-workers, can be used to investigate hybridisation and covalency effects.⁷² The concept idea for this analysis is to transform a wavefunction to a localised form to try to get the Lewis structure picture and it is constructed from the natural atomic orbital (NAO) which is transformed from a density matrix.⁷¹

The starting point of NAO construction is that the density matrix is written in terms of blocks of “basis functions”:⁴¹

$$\mathbf{D} = \begin{pmatrix} \mathbf{D}^{AA} & \mathbf{D}^{AB} & \mathbf{D}^{AC} & \vdots \\ \mathbf{D}^{BA} & \mathbf{D}^{BB} & \mathbf{D}^{BC} & \vdots \\ \mathbf{D}^{CA} & \mathbf{D}^{CB} & \mathbf{D}^{CC} & \vdots \\ \dots & \dots & \dots & \ddots \end{pmatrix} \quad (2.55)$$

The NAO for each atom will be defined as a diagonalised density matrix i.e. the NAO for atom A in the molecule is \mathbf{D}^{AA} , for atom B in the molecule is \mathbf{D}^{BB} *etc.* The off-diagonal elements in the block matrix can be used to identify bonds between atoms. The procedure for finding the NBO is as follows:⁴¹

1. In the density matrix, NAOs that have occupancy numbers very close to 2 (greater than 1.999) are identified as core orbitals and are removed from the density matrix.
2. NAOs that have occupancy numbers greater than 1.90 are identified as lone pair orbitals and their contribution are also removed.
3. The off-diagonal matrix elements are considered and NBOs are identified when they have occupancy numbers greater than 1.90.
4. If the sum of the occupancy number from the above procedure are less than the number of electron in the system, an alternative search is required. An alternative means is to search for rare three-centre two-electron bonds for

example some boron compounds. The NBO acceptance criteria can be lowered gradually until an adequately large fraction of the electron has been assigned to bonds. Contribution from diatomic bonds are removed from the density matrix, followed by diagonalisation of all 3×3 sub-blocks.

In this thesis, the donor-acceptor interaction was used to investigate the interaction of dative bonds where it can be extracted from the donor-acceptor stabilisation energy $E(2)$ from each donor NBO (i) and acceptor NBO (j). The equation used by the program for its determination is:

$$E(2) = \Delta E_{ij} = q_i \frac{F(i, j)^2}{\varepsilon_i - \varepsilon_j} \quad (2.56)$$

where q_i is the donor orbital occupancy; ε_i and ε_j are diagonal elements (orbital energies) and $F(i, j)$ is the off-diagonal NBO Fock matrix element.⁷¹ The NBO program implemented in the Gaussian09 package is used in this work.

Chapter 3

Determining a Method for Pincer Palladacycle Calculations

This chapter presents density functional theory (DFT) calculations on symmetrical pincer palladacycles, PdYCY, to test the method and basis set for the determination of their geometric and electronic structures.

3.1 Introduction

The structure and bonding of palladacycles can be investigated using DFT, however an appropriate choice of functional, basis set, and relativistic effective core potential (ECP) for Pd, is essential for obtaining accurate structures, and hence thermodynamic and kinetic data.⁷³ Moreover, the DFT and *ab initio* methods have been widely used to study and predict electronic structure, spectroscopy and reaction mechanism in both organic and inorganic chemistry.^{74,75}

There has been an increasing level of interest in the study of transition metals using DFT calculations to accurately predict of chemistry phenomena at a cheap computational cost compared to electron-corrected *ab initio* methods. Such DFT methods are applied to probe the properties of the reactions involving transition metals. For example, DFT has been used to study bond lengths and vibrational frequencies,⁷⁶ and to determine binding energies for cationic hydrides.⁷⁷ DFT has many functionals to predict physical and chemical properties.⁷⁵ As a review through the literature, we have found that several works focused on validation studies

using DFT in studying the geometries of transition metal complexes compared to experimental data, including a 2007 study by Waller and co-workers.⁷⁸ They employed DFT to study the geometries of second row transition metal complexes, where the ability of 15 different functionals used in the determination of the geometries of 19 metal complexes were evaluated. The structures with hybrid functionals, compared to experimental data, have standard deviations smaller than pure generalised gradient approximation (GGA) functionals indicating that the hybrid functionals are better than GGA functionals in predicting the structures of second-row transition metal complexes. The smallest errors were obtained for the hybrid functionals, i.e. B3P86 \approx B3PW91 \approx PBE-hybrid < TPSSh \approx B3LYP < BP86 < BLYP < LSDA \approx VSXC.

Sieffert and Bühl⁷⁹ investigated the bond distances around the metal centre of the complexes Ru(CO)Cl(PPh₃)₂(CH=CHPh) and Ru(CO)Cl(PPh₃)₃(CH=CHPh) using BP86, B3LYP, B3LYP-D and B97D. They claimed that the metal-ligand bonds of structures optimised using BP86 (standard GGA functional) are in good agreement with the experimental data. They also found that B97D (dispersion functional) agreed well with the experiment except for the Ru-Cl bond with a slight deviation of 0.07 Å, while the B3LYP functional had the largest deviation from the experimental Ru-P distance (by 0.089-0.239 Å). Similarly, Rydberg and Olsen⁸⁰ concluded, in their study, that the B3LYP functional gave the largest average bond deviation for metal-ligand bonds (Fe-N) when the performance of seven DFT functionals (BP86, PBE, PBE0, TPSS, TPSSh, B3LYP and B97D) in the study of Fe complexes was investigated. These functionals were good for studying geometries except for the B3LYP functional that had a problem with over-estimation of Fe-ligand distances. They also found, in terms of computational cost, that BP86, PBE and TPSS functionals could save the cost of computational time significantly. They suggested that TPSS is one of the best functionals for studying transition metal systems.⁸⁰

Marom *et al.*⁸¹ claimed that the dispersion corrected functionals were important in determining the geometry. They found that M06 and PBE+vdW (van der Waals (vdW) interaction is a term of dispersion correction) for considering metal-phthalocyanine dimers (metal=Ni and Mg) gave accurate geometries. This result was contradictory to the ones given in Rydberg's⁸⁰ work which claimed to achieve accurate metal-ligand distances without the inclusion of a dispersion correction.

In 2012, Minenkov *et al.*⁸² investigated the eight most commonly used DFT functionals B3LYP, BP86, PBE, TPSS, B97D, ω B97XD, M06 and M06L in the study of organometallic and transition metal complexes with the effective core potential (ECP) of the Stuttgart-Dresden (SDD) basis set for all non-hydrogen elements. The ECPs replaced the inner electrons such as two-electron ECP for C, N, O and F and ten-electron for P and Cl. Hydrogen atoms were determined by a Dunning double- ζ basis set. The B3LYP, BP86, PBE and TPSS are standard functionals without dispersion, whereas the B97D, ω B97XD, M06 and M06L have dispersion effects included. Eighteen ruthenium organometallic complexes were studied for validating these methods using the crystal structures as a starting point for DFT geometry optimisation calculation. Furthermore, in the same study, ten other organometallic complexes (Ti, Fe, Co, Ni, Zr, Mo, Rh, Pd, W and Ir transition metal complexes) were also tested by comparing the DFT optimised and crystal structures. The root mean square (RMS) deviations were used to evaluate the quality of the eight DFT methods in the study of the geometries. The results showed that the methods without dispersion correction (B3LYP, BP86, PBE and TPSS), over-estimated all interatomic distances. On the other hand, the functionals which incorporate dispersion (B97D, ω B97XD, M06 and M06L) gave a significantly lower absolute error for the ruthenium complexes. ω B97XD was found to be the best method to study geometry and minimises the over-estimated bond lengths of the ligand and metal-ligand bonds. In addition, the calculations with dispersion functionals showed that the geometries of the ten transition metal (Ti, Fe, Co, Ni, Zr, Mo, Rh, Pd, W and Ir) complexes were also accurately reproduced. Minenkov *et al.* pointed out that this method may be used to study classes of relatively large transition metal complexes.

Moreover, not only the method is important for the study of inorganic molecules but the basis set and the ECP also strongly influence the accuracy in the study of heavy metal compounds. A Stuttgart/Dresden (SDD)⁵⁷ basis set or Los Alamos National Laboratory double ζ (LanL2DZ)^{58,59} with an effective core potential (ECP) is a popular basis set to study metals in complexes.

Zhao *et al.*⁸³ reported the performance of the basis set ECPs (LanL2MB, LanL2DZ and SDD) for determining transition metal complex structures. RHF and B3LYP were used with the three basis sets to study the MX_2 , where M is Zn, Cd, Hg and X

is F, Cl, Br, and compared to the experiment. They found that B3LYP/SDD level was the best functional and basis set for reproducing the experiment.

The palladium and platinum complexes (*cis*-M(Met)X₂ and *cis*-M(His)X₂ where M = Pd and Pt; X = F, Cl, Br and I; Met = methionine; His = histidine) were studied by Yang *et al.* (Figure 3.1).⁸⁴ Two relativistic ECP LanL2DZ and SDD were used to treat the Pd and the Pt complexes. Their results proved that the SDD basis set is closer to experimental data. The best method and basis set for these complexes is B3LYP/SDD.

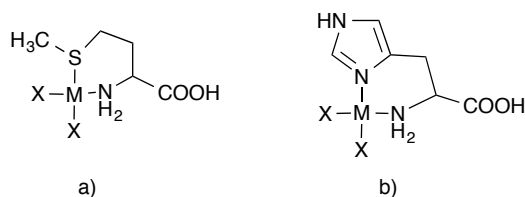


Figure 3.1. Structure of a) *cis*-M(Met)X₂ and b) *cis*-M(His)X₂ where M is Pd and Pt, and X is F, Cl, Br and I.⁸⁴

Li *et al.*⁸⁵ studied the performance of method and basis set using an ONIOM calculation for ten palladium complexes in 2005. They evaluated the seven DFT functionals i.e. B3LYP, PBEP86, B3P86, B3PW91, BPBE, PW91PW91 and six ECP basis sets i.e. CEP-121G, CRENBL, LanL2DZ, LanL2DZ+p, SDD and sbkjcvdz. These were used for determining in the core layer of the ONIOM method. The HF method with LandL2MB basis set was fixed in the whole layer for all of the molecules. Their results showed that the six ECP basis sets provided the similar performance. However, the LanL2DZ+p basis set was slightly better than the other methods. Overall, the ONIOM(B3P86/LanL2DZ+p//HF/LanL2MB) was the best method for geometry with the smallest average error for bond lengths, bond angles and dihedral angles.

3.2 Aim of this work

The effects of the computational method and the basis set for light atoms such as C, H, N, O, Cl etc. and the relativistic effective core potential (ECP) for Pd are important in calculating accurate geometries of transition-metal complexes. Therefore, the aim of this chapter is to determine an optimum DFT methodology and basis set for the study of pincer palladacycles that combines accuracy and computational speed. This will be achieved by evaluating the performance of a range of functionals in their ability to reproduce the structural features of two experimentally characterised symmetrical pincer palladacycles. This work has been published in "Dalton Transactions".⁸⁶

3.3 Computational details

All calculations were performed using the Gaussian09 package.⁸⁷ The geometries and electronic structures of complexes **1** [PdCl{2,6-(NMe₂CH₂)₂(C₆H₃)}] and **2** [PdCl{2,6-(SMeCH₂)₂(C₆H₃)}] in Figure 3.2 were calculated using eight density functionals. The set of density functionals investigated were three generalized gradient approximation (GGA) functionals: BP86,⁴⁷ PBE^{45,46} and B97D,⁸⁸ a hybrid-GGA functional (HGGA): B3LYP,^{47,89} two meta-GGA functionals (MGGA): TPSS⁵⁰ and M06L,⁵¹ and two hybrid meta-GGA functionals (HMGGA): ω B97XD⁵³ and M06.⁵² The B97D, M06L, M06 and ω B97XD functionals include the dispersion correction, while the PBE, BP86, TPSS and B3LYP functionals do not contain the dispersion correction. The basis sets tested are 6-31G(d) and 6-31+G(d,p) for all atoms except Pd in which an effective core potential (ECP), Los Alamos National Laboratory double ζ (LanL2DZ)^{58,59} or Stuttgart/Dresden ECP (SDD),⁵⁷ was employed to replace the core electrons. These will be referred to as follows: BS1 = 6-31G(d)[LanL2DZ], BS2 = 6-31G(d)[SDD], BS3 = 6-31+G(d,p)[LanL2DZ] and BS4 = 6-31+G(d,p)[SDD], where [SDD] and [LanL2DZ] means that ECPs SDD or LanL2DZ were used on Pd, respectively. The neutral complexes were studied in this case. The spin singlet complexes were considered in all calculations and the local minimum structures were confirmed by frequency calculation. All optimization calculations were compared with X-ray crystallography to check for their accuracy. The Cambridge Structural Database entries for complex **1**⁹⁰ is 720256 and for complex

2⁹¹ is 725124.

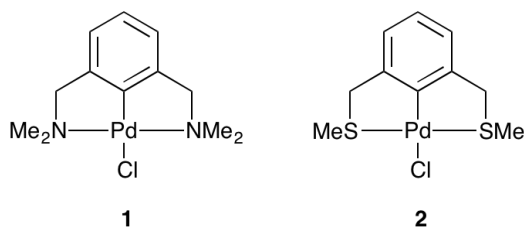


Figure 3.2. Symmetrical pincer palladacycle complexes **1**⁹⁰ and **2**⁹¹ investigated in this study.

3.4 Results and discussion

Complexes **1** and **2** were optimised starting from X-ray crystal structure coordinates and compared to their X-ray crystal structures.

3.4.1 The RMS error in Cartesian coordinates, and the error of interatomic and bond distances, in symmetrical pincer palladacycles

In the fully optimised geometry, complex **1** (Figure 3.3a) is a distorted square-planar complex and the NMe₂ groups of the aryldiamine unit on opposite sides of the aryl plane are in excellent agreement with the X-ray crystal structure.⁹⁰ In addition, because hydrogen is a light atom, it is hard to determine its position in the X-ray structure. Therefore, it is not considered in the RMS error in Cartesian coordinates, interatomic and bond distances analyses.

The Quatfit program⁹² determines the error between the calculated and experimental X-ray structures by analysing the difference between the Cartesian coordinates of each atom pair in the complex. The reference molecule is fixed, while the analysed molecule is translated and rotated to align to the centre of the reference molecule for fitting with each pair of atoms. Particularly important atom pairs can be given a greater weight. In this work, the crystal structure was fixed and the calculated structure was analysed using the Quatfit program.

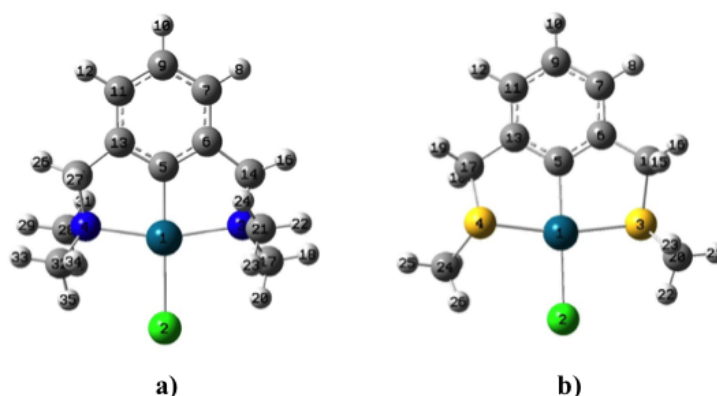


Figure 3.3. a) Optimised geometry of complex **1** and b) optimised geometry of complex **2** (grey = carbon, white = hydrogen, dark blue = nitrogen, light green = chlorine, dark green = palladium and yellow = sulphur).

The RMS error in Cartesian coordinates using the Quatfit program was performed on all pairs of atoms with equal weight except for the hydrogen atoms which were not considered. We analysed complexes **1** and **2** separately. The result for the complex **1** are illustrated in Figure 3.4. The GGA B97D, MGGA M06L and HMGGGA ω B97XD show larger RMS errors while the other five functionals give smaller RMS errors and prove to be effective for complex **1**. When comparing the effect of the diffuse and polarisation functions in the basis set on the optimisation, when basis sets were changed from 6-31G(d) to 6-31+G(d,p), a small change in RMS error was found (comparing between BS1 and BS3 or between BS2 and BS4). In addition, studying the effect of ECP on the Pd heavy atom, the SDD basis (BS2 and BS4) for Pd shows a smaller RMS error than LanL2DZ (BS1 and BS3) indicating that SDD is superior to LanL2DZ for Pd in all calculations. This result agrees well with the result of Yang *et al.*⁸⁴ where SDD and LanL2DZ were used for Pd and the bond length deviation was compared.

Considering complex **2** (Figure 3.3b), it is also distorted from a perfect square planar geometry. The orientation of the methyl groups, which are connected to sulfur, is *trans* and equatorial. The comparison of eight functionals for complex **2** is shown in Figure 3.5 and shows that all functionals have a similar error. Furthermore, the calculations reveal that SDD is again a better choice for Pd compared to LanL2DZ.

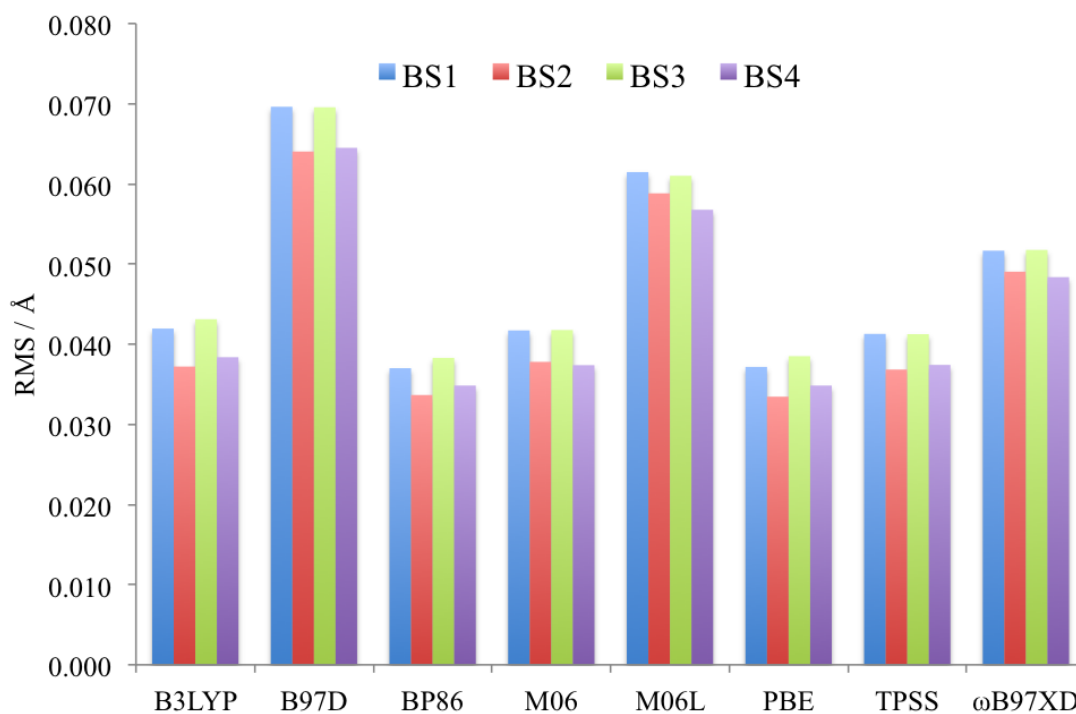


Figure 3.4. RMS error for complex 1. Optimised structure compared to its X-ray crystal structure using the Quatfit program.

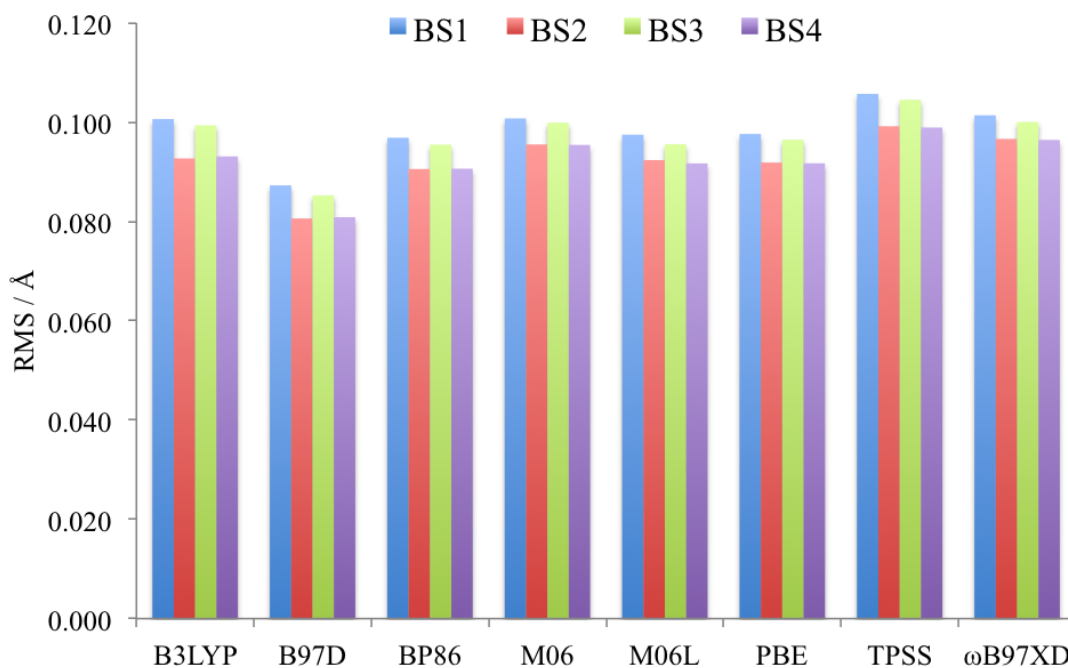


Figure 3.5. RMS error for complex 2. Optimised structure compared to its X-ray crystal structure using the Quatfit program.

We have analysed the average RMS errors between the optimised complex and X-ray crystal structure for complexes **1** and **2** together using the Quatfit program. The complexes **1** and **2** have different numbers of atoms. For unbiased analysis, we have used equation 3.1 to calculate the average RMS of complexes **1** and **2**;

$$\text{RMS}_{\text{average}} = \sqrt{\frac{((\text{RMS}_1)^2 \times n_1) + ((\text{RMS}_2)^2 \times n_2)}{n_1 + n_2}} \quad (3.1)$$

where n is the number of atoms excluding hydrogen; n_1 for complex **1** and n_2 for complex **2**. RMS_1 and RMS_2 are RMS errors for complex **1** and **2**, respectively. The average RMS error by Quatfit shows that the GGAs PBE and BP86 have slightly smaller errors than other functionals. However, the difference between the best and worst functionals is less than 0.020 Å.

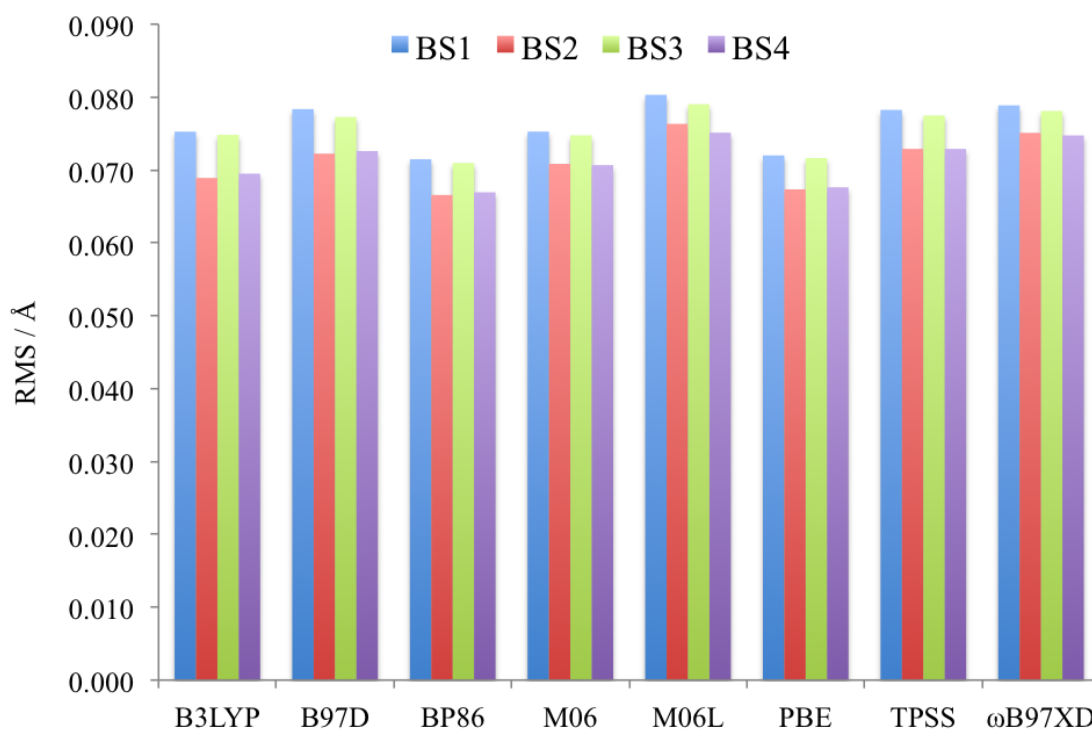


Figure 3.6. Average RMS errors for complex **1** and **2** optimised structures compared to their X-ray crystal structures using the Quatfit program.

To clarify and gain an insight into the systematic over or underestimation, the bonded and interatomic distances are determined. We have analysed the mean signed errors (MSE) and the mean unsigned errors (MUE) for each structure. The MSE is the average of the deviation between calculation and experiment (equation 3.2), whereas the MUE is the absolute deviation (equation 3.3).

$$\text{MSE} = \frac{1}{N} \sum_{i,j=1}^N (R_{ij}(\text{DFT}) - R_{ij}(\text{Experiment})) \quad (3.2)$$

$$\text{MUE} = \frac{1}{N} \sum_{i,j=1}^N |R_{ij}(\text{DFT}) - R_{ij}(\text{Experiment})| \quad (3.3)$$

where R_{ij} is the atom-atom distance and N is the number of atoms (excluding hydrogen atoms). Therefore, a total of 240 interatomic distances of complex **1** and 182 interatomic distances of complex **2** were determined and compared with their corresponding X-ray crystal structures. Moreover, we have considered 18 bonded and 16 bonded distances for complexes **1** and **2**, respectively.

Figure 3.7 shows MSE and MUE for interatomic distances in complex **1**. It reveals three excellent performers; M06, M06L and ω B97XD functionals which include dispersion correction, accurately determine the geometry of the complex **1** and have small MSE ($<0.023 \text{ \AA}$) and MUE ($<0.037 \text{ \AA}$). Whereas, B3LYP, BP86, PBE and TPSS, where dispersion was not included, over-estimated distance in agreement with Minekov *et al.*⁸² A comparison between MSE and MUE for each of the functionals suggests that the smaller error of MSE than MUE is due to the fact that some of the over-estimated distances cancel out some under-estimated distances.

The 18 bonded distance for complex **1** is analysed to investigate the bond distances between atoms (Figure 3.8). The results for the MSE shows that the functionals containing the dispersion correction (M06, M06L and ω B97XD with the exception of B97D) have small errors ($<0.009 \text{ \AA}$). The functionals without dispersion over-estimated the bond distance in a similar manner to interatomic distances. This result agrees with Waller *et al.* where they claimed that the standard DFT functionals over-estimated bond distances.⁷⁸

We have investigated changing the basis set from 6-31(d) to 6-31+G(d,p), and LanL2DZ to SDD. In the Figure 3.7 and Figure 3.8, the MSE and MUE of 6-31G(d) and 6-31+G(d,p) are very similar. However when considering the ECP for Pd the MUE and MSE of interatomic and bond distance show a greater difference. It is found that the SDD (BS2 and BS4) is better than LanL2DZ (BS1 and BS3) in all DFT calculations.

The 182 interatomic distances are analysed for complex **2** and compared with the *rac*-form X-ray crystal structure.⁹¹ The interatomic distances in Figure 3.9 show that functionals including the dispersion M06, M06L and ω B97XD, with the exception of B97D functionals, have the smallest MSE and MUE, as in the case of complex **1**. The MSE and MUE of 16 bonded distances of complex **2** are shown in Figure 3.10. The MSE and MUE for bonded distances also show the functionals that include dispersion correction have smaller errors. The SDD is a better ECP basis set compared to LanL2DZ for complex **2** optimisation.

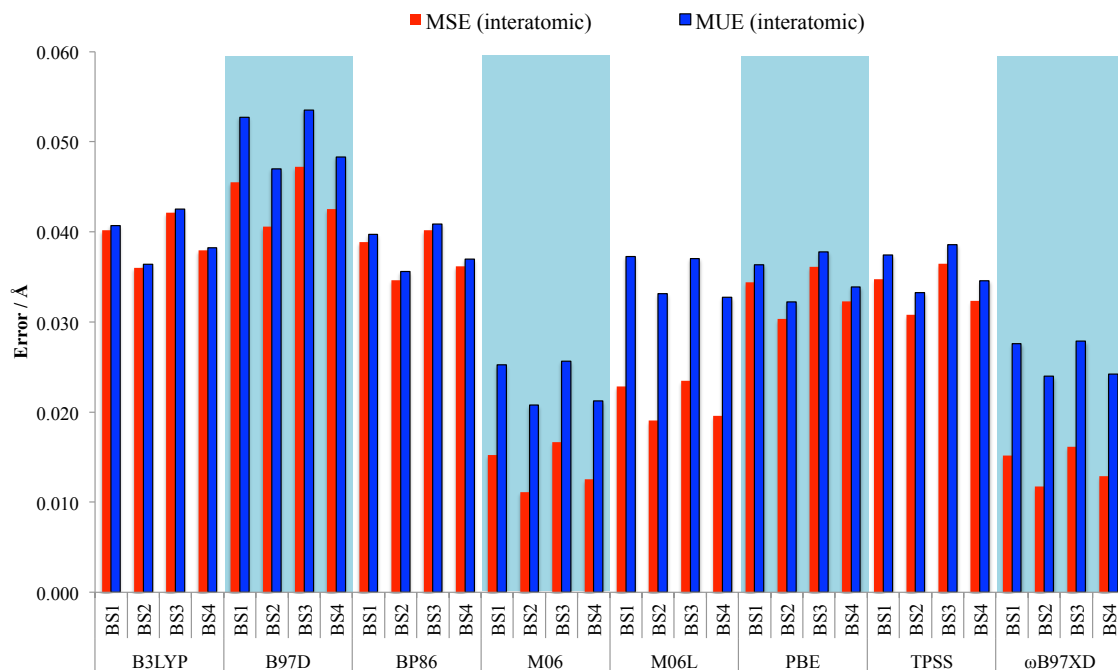


Figure 3.7. Interatomic distance MSE and MUE for complex **1** (excluding hydrogen) compared to the X-ray crystal structure varying the method and basis set.

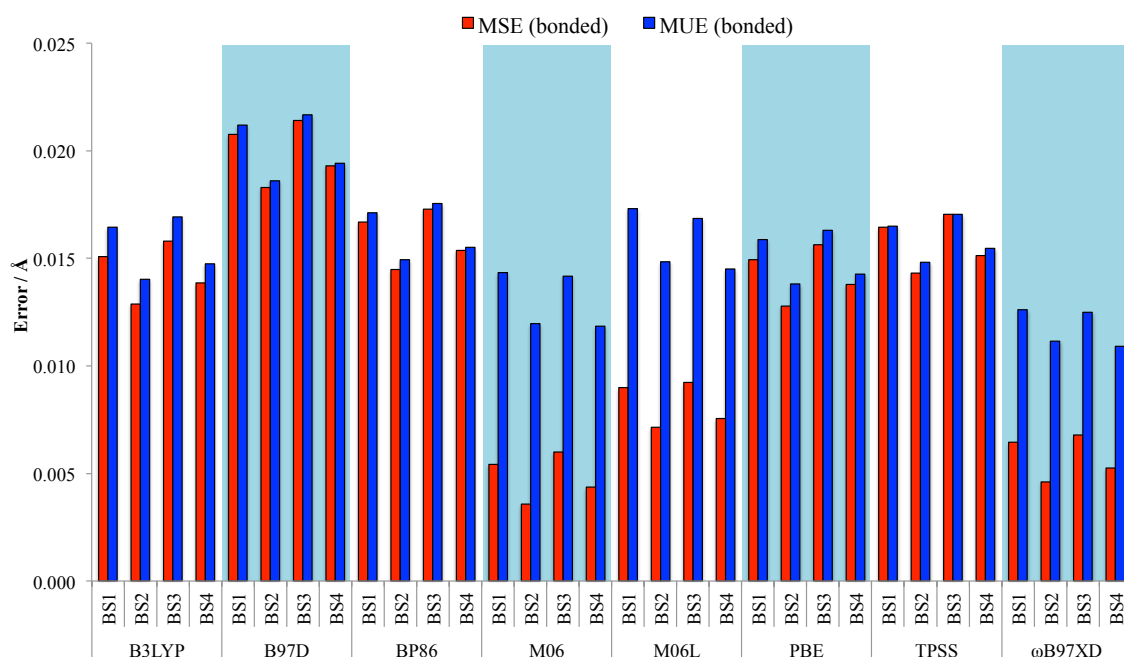


Figure 3.8. Bonded distance MSE and MUE for complex 1 (excluding hydrogen) compared to the X-ray crystal structure varying the method and basis set.

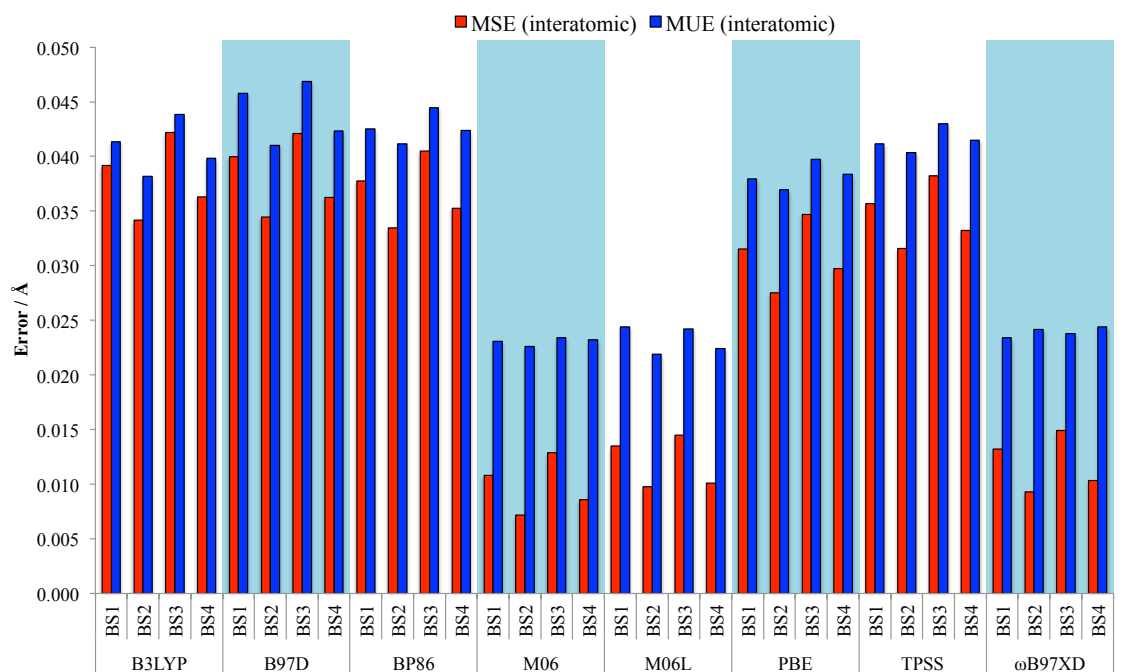


Figure 3.9. Interatomic distance MSE and MUE for complex 2 (excluding hydrogen) compared to the X-ray crystal structure varying the method and basis set.

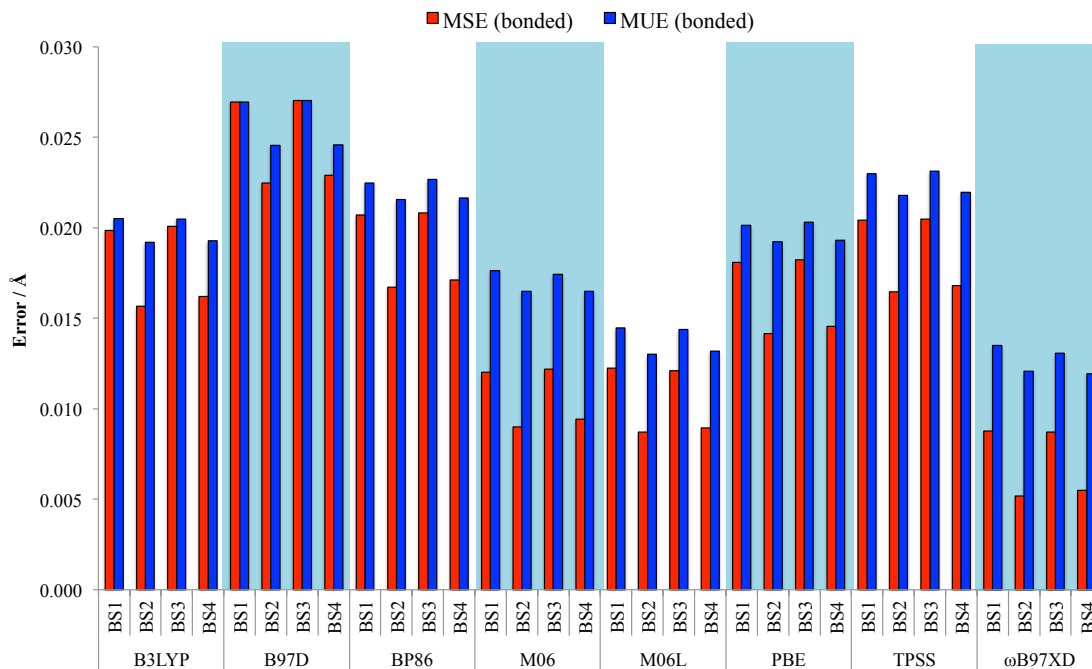


Figure 3.10. Bond distance MSE and MUE for complex **2** (excluding hydrogen) compared to the X-ray crystal structure varying the method and basis set.

It is important to study the average MUE and MSE to determine the efficiency of functionals for investigating pincer palladacycles. Due to different numbers of atoms in complexes **1** and **2**, we have used equations 3.4 and 3.5 for the calculation of average MSE and MUE.

$$\text{MSE}_{(average)} = \frac{(\text{MSE}_1 \times n_1) + (\text{MSE}_2 \times n_2)}{n_1 + n_2} \quad (3.4)$$

$$\text{MUE}_{(average)} = \frac{(\text{MUE}_1 \times n_1) + (\text{MUE}_2 \times n_2)}{n_1 + n_2} \quad (3.5)$$

where n is the number of interatomic or bonded distances; n_1 for complex **1** and n_2 for complex **2**, respectively. The MSE_1 and MUE_1 are for complex **1**, and the MSE_2 and MUE_2 are for complex **2**.

It is clear that the SDD ECP for complexes **1** and **2** from the Cartesian coordinates approach using the Quatfit program, and MSE and MUE, show good agreement with their X-ray crystal structures. Moreover, the difference between RMS error, MSE and MUE errors of the 6-31(d) and 6-31+G(d,p) is small. Our results suggest that the small basis set with SDD is adequate to study geometry optimisation. However,

the diffuse and polarisation functions are desirable to study geometry because this provides flexibility for the calculation of the structure. Adding diffuse function to the basis set, however, does not significantly increase the computational time. Therefore, in what follows, only BS4 for studying the average MSE and MUE were analysed. A total of 422 interatomic distances (240 interatomic distances of complex **1** and 182 interatomic distances of complex **2**) with BS4 and eight different methods are analysed. Figure 3.11 reveals that the functionals that have dispersion interaction result in a lower MSE and MUE. The three good functionals provide MUE and MSE in the range of 0.010 - 0.012 Å and 0.023 - 0.025 Å, respectively. The MSE is lower than MUE because the over-estimated values cancel out the under-estimated ones.

In Figure 3.11, the 34 bond distances, which are 18 bond distances of complex **1** and 16 of **2**), were studied. The result reveals a similar trend to that found in the analysis of average MSE and MUE of interatomic distance, when dispersion is accounted for in the functional (except B97D) a more accurate geometry is obtained. The three best functionals have average MSE and MUE in the range of 0.005 - 0.009 Å and 0.012 - 0.015 Å, respectively.

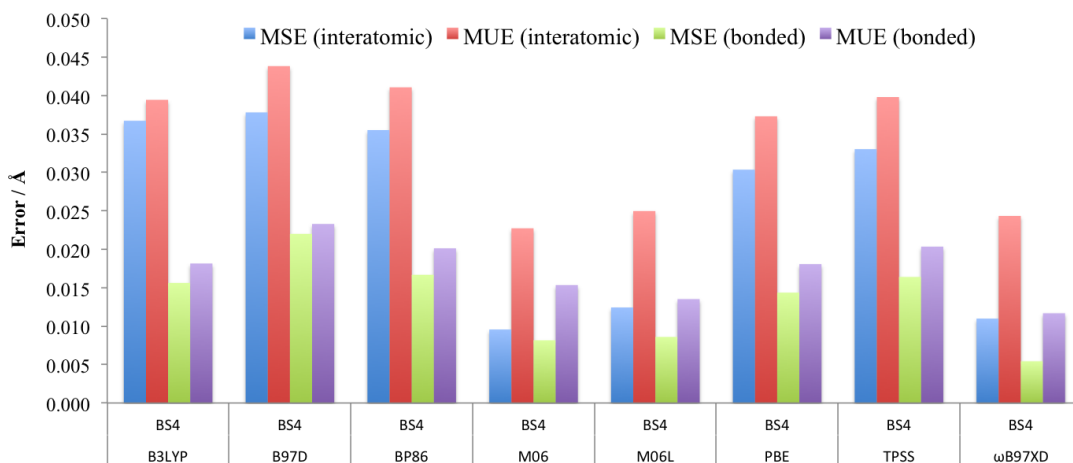


Figure 3.11. Average bonded and interatomic distance MSE and MUE for PdNCN and PdSCS compared to their X-ray crystal structures.

3.4.2 The RMS Cartesian coordinates, and the error of interatomic and bond distances of Pd-L

The catalytic activity of a transition metal complex is directly controlled by metal-ligand bonds since many reactions involve bond cleavage or formation of a metal-ligand bond,⁹³ therefore, we have investigated the accuracy of the bonds around the Pd centre (i.e. the Pd-L bond where L = N, S, C, Cl). From the results in the **RMS error in Cartesian coordinates, and the error of interatomic and bond distances in the symmetrical pincer palladacycles** section, only BS4 is used for the validation of the Pd-L bond study using the RMS, MSE and MUE. The average performance of the eight functionals is shown in Figure 3.12. Firstly, the RMS error from Cartesian coordinate approach by the Quatfit program is used to judge the accuracy of the method. Our analysis shows that non-hybrid functionals with no dispersion included, PBE, BP86 and TPSS give smaller RMS errors when, predicting the Pd-L bonds, with RMS errors in the range 0.036 - 0.037 Å. Additionally, the dispersion-included MHGGA ω B97XD also provides good accuracy in predicting the Pd-L bonds. The popular B3LYP functional and dispersion-included B97D, M06 and M06L show the lowest accuracy. The over- and under-estimation of bond length of Pd-L bonds are observed using MSE and MUE (Figure 3.12). In the MSE result, the PBE, TPSS, BP86 and ω B97XD show good performance with a range of 0.014 - 0.015 Å. Based on MUE, the PBE, TPSS, BP86 and ω B97XD also give excellent performance in Pd-L bond prediction. Overall, the most accurate method for determining Pd-L bond distance having obtained the lowest RMS error and the lowest MSE and MUE is PBE (RMS/MSE/MUE = 0.036 Å/0.014 Å/0.023 Å) in agreement with Minenkov *et al.*⁸² and Jiménez-Hoyos *et al.*⁹⁴ where they claimed that the PBE gave the best performance for Pd-L bond prediction.

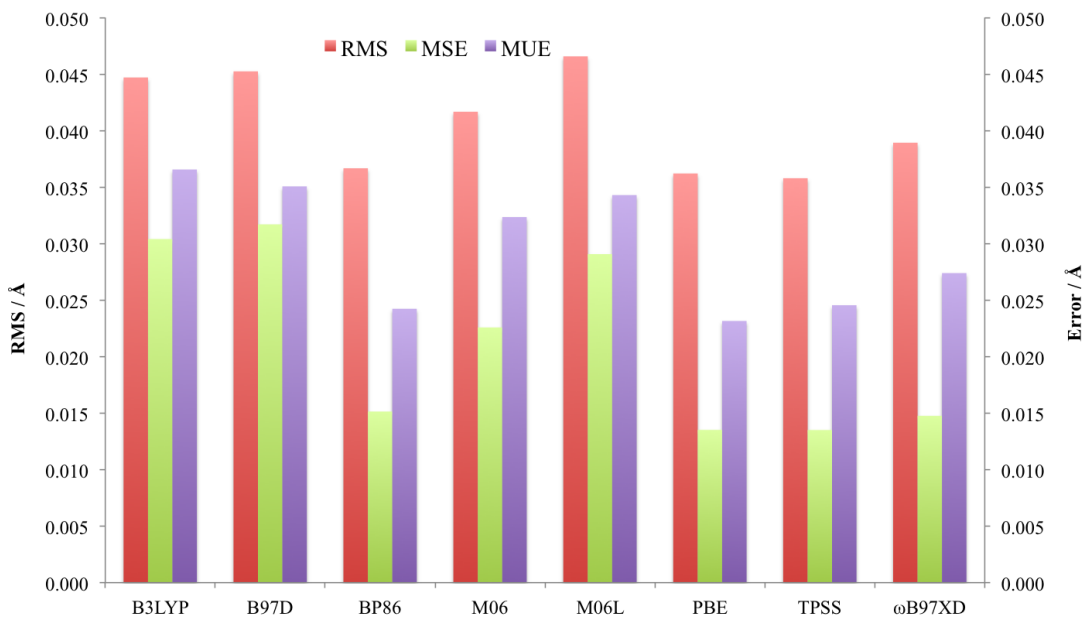
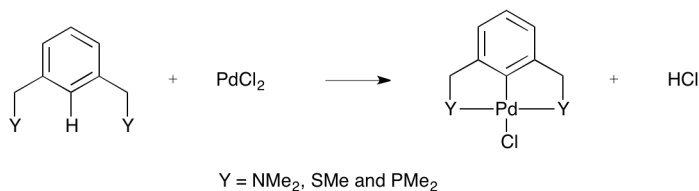


Figure 3.12. Average RMS error using the Quatfit program, bond and interatomic distance MSE and MUE for Pd-L bonds of complexes **1** and **2** compared to their X-ray crystal structures.

On considering the data from all average MUE, MSE of interatomic and bonded distances, it was concluded the ω B97XD gives the best performance, having the smallest error (Figure 3.11). In addition to the accuracy of method, the computational cost is also important to consider for large molecules. Given the high performance of PBE for key Pd-L bonds, the PBE functional is preferred for studying pincer palladacycles due to lower computational cost compared to ω B97XD. However, the ω B97XD is an equally acceptable choice. To confirm this statement, we have studied the Gibbs free energy of palladacycle formation between the pincer ligands and PdCl₂ (Scheme 3.1) using PBE and ω B97XD functionals with 6-31+G(d,p)[SDD] basis set for optimisation of the geometry and frequency analysis. To evaluate the accurate energy, we have used ω B97XD/6-311++G(2df,2p)[SDD] to determine the single point energy. The Gibbs free energy of formation shows that the PBE and ω B97XD optimised geometries provide very similar energy (less than 2 kJ mol⁻¹) (Table 3.1). Furthermore, the PBE functional has been used previously to study the ligand free Pd reaction.^{95,96}



Scheme 3.1. Formation reaction of pincer palladacycles.

Table 3.1. Gibbs free energy, ΔG^0 , of complexes **1**, **2** and PdPCP ([ClPd2,6-(Me₂PCH₂)₂C₆H₃]) for the formation reaction using ω B97XD/6-311++G(2df,2p) for both PBE/6-31+G(d,p) and ω B97XD/6-31+G(d,p)-optimised geometries.

Complex	$\Delta G^0/\text{kJ mol}^{-1}$	
	PBE	ω B97XD
1	-207.3	-206.6
2	-213.2	-214.9
PdPCP	-318.7	-320.4

3.5 Conclusion

Eight density functionals and four basis sets have been used to calculate the structures of the pincer complexes **1** [PdCl{2,6-(NMe₂CH₂)₂(C₆H₃)}] and **2** [PdCl{2,6-(SMeCH₂)₂(C₆H₃)}] and validate the performance of the computational methodologies compared to their experimental crystal structures. From average MSE and MUE analysis, we found that functionals that include dispersion provide slightly better performance than non-dispersion corrected functionals. Moreover, the SDD ECP (used for the Pd atom) gives greater accuracy than the LanL2DZ ECP. The critical bonds around Pd (Pd-L bonds), which are important in the complex, were analysed. The RMS error, MSE and MUE showed that the GGAs PBE and BP86, and the meta-GGA TPSS gave the lowest errors (RMS < 0.037 Å, MSE < 0.015 Å and MUE < 0.025 Å) indicating that they were in good agreement with X-ray crystal structure. However, we found that the structural data obtained at all levels of theory agreed well with the crystal structure data having the average RMS error, MSE (interatomic), MSE (bonded), MUE (interatomic) MUE (bonded) less than 0.080 Å, 0.038 Å, 0.022 Å, 0.044 Å and 0.023 Å, respectively. Overall, in order to save computational costs while maintaining good accuracy for Pd-L bonds, the PBE/6-31+G(d,p)[SDD] was shown to be a good choice for geometry optimisation.

Chapter 4

Pincer Palladacycles Studied Using CASSCF Method

In this chapter, complete active space self-consistent field (CASSCF) calculations are performed on pincer palladacycles to determine their geometric and electronic structures. This provides a reliable indication of the reference character (single-reference or multireference) required to study the electronic structures of pincer palladacycles.

4.1 Introduction

4.1.1 Electronic structure using CASSCF method

CASSCF is a quantum chemistry method based on the concept of configuration interaction (CI), first introduced by Björn Roos in 1972.⁹⁷ Like DFT, the CASSCF method has been used to study the electronic structures and chemical properties of molecular systems. The fundamental limitation of the DFT method is that it uses a single-reference to determine electronic structures of molecules. Sometimes, DFT cannot describe the electronic structure of the metal complex structure sufficiently. For example, Yamamoto and Kashiwagi⁹⁸ used CASSCF to determine the electronic structure of an oxyheme model complex (Figure 4.1). It was shown that the major weight configuration for the ground state was only 0.683 (coefficient = 0.826), which implied that this structure had a multireference character.

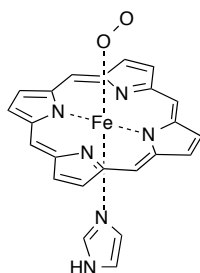


Figure 4.1. Model of oxyheme studied by Yamamoto and Kashiwagi *via* CASSCF.⁹⁸

Jensen⁹⁹ reported the ground state structure of cob(I)alamin, first studied by CASSCF then followed by complete active space second-order perturbation theory (CASPT2) (Figure 4.2). The results showed that cob(I)alamin had multireference character, with 67% weight in the major configuration state. Kumar *et al.*¹⁰⁰ also studied the electronic properties cob(I)alamin in 2011. They studied the role of the axial base in cob(I)alamin using CASSCF, followed by quasi-degenerate perturbation theory with multiconfiguration self-consistent field reference function (MC-XQDPT2).¹⁰¹ Their results revealed that this complex also had multireference character.

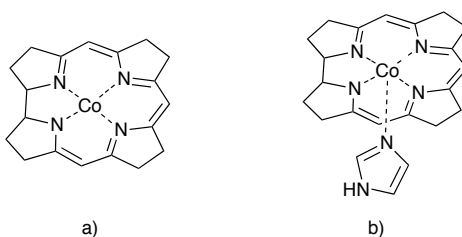


Figure 4.2. Structure of a) the cob(I)alamin⁹⁹ and b) the interaction of base with cob(I)alamin.¹⁰⁰

In 2009 Takatani *et al.*¹⁰² reported the electronic structure of d^6 metal-salen complexes using CASSCF (Figure 4.3). They found that the singlet state of Fe(II)-salen, as well as the singlet and the quintet states of Ru(II)-salen exhibited multireference character, while the triplet and quintet states of Fe(II)-salen, and the triplet state of Ru(II)-salen had single-reference character.

CASSCF calculations require as input the active orbitals, inactive orbitals, the number of electrons and total spin. The probability of an electronic configuration within the active orbitals is determined. The electrons in inactive orbitals remain fully occupied. Specifying the number of active orbitals and the number of electrons herein is a challenging issue for the user. Roos's rules can provide a guide to selecting

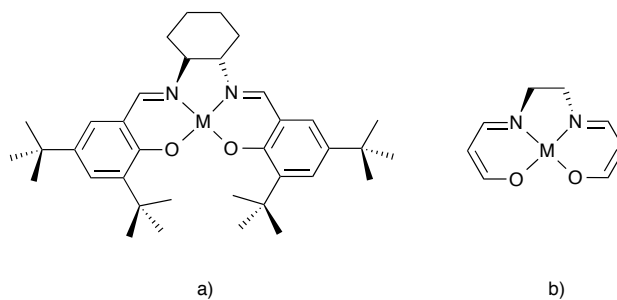


Figure 4.3. Metal-salen catalysts; a) full salen ligand and b) model for simulation.¹⁰²

the active space for transition compounds. Björn's rules suggest that for second and third row transition metal compounds, the extra d-shell and all orbitals of d-character are not required to be put in the active space. For high oxidation states, more active orbitals are required to be included due to large charge transfers.¹⁰³ For instance, the protonation of square-planar palladium(II) complex reaction ($[\text{Pd}(\text{H})_2(\text{Cl})(\text{NH}_3)]^- + \text{H}^+ \rightarrow [\text{Pd}(\text{H})_3(\text{Cl})(\text{NH}_3)]$) was studied by Milet and Dedieu.¹⁰⁴ They calculated the palladium(II) complexes, determining the proton affinity using two different sizes of active space; i) 4 electrons in 4 active orbitals (CAS(4,4)) and ii) 10 electrons in 10 active orbitals (CAS(10,10)). CASSCF method followed by CASPT2 calculation was performed. The active orbitals for CAS(4,4) involved the orbitals along the z-axis: the Pd-H bond at the axial position was described by these orbitals, while the CAS(10,10) calculation could observe all metal-ligand bonds at both axial and equatorial positions. Their results showed that the deviation of the proton affinity results between CASSCF and CASPT2 using 10 electrons in 10 active orbitals was 26.3 kJ mol^{-1} . By comparing CASSCF with HF theory, most of the correlation effects are shown to be of the non-dynamical nature with an energy difference of $108.7 \text{ kJ mol}^{-1}$. The CASSCF calculation (non-dynamic correlation effect) was sufficient for calculating the protonation of the square-planar palladium(II) complex reaction. Additionally, the difference in the proton affinities between CAS(4,4) and CAS(10,10) was 33.5 kJ mol^{-1} , which the proton affinity for CAS(4,4) was $1197.9 \text{ kJ mol}^{-1}$ and for CAS(10,10) was $1231.4 \text{ kJ mol}^{-1}$. This energy (33.5 kJ mol^{-1}) was recovered from the metal-ligand bond at the equatorial positions. This demonstrates the importance of selecting an active space that is sufficient to model the system accurately.

In 2000, the electronic spectra of $M(2\text{-thienylpyridine})_2$, where M is Pd or Pt, were reported using the CASSCF/CASPT2 method (Figure 4.4).¹⁰⁵ Sixteen electrons in twelve active orbitals were chosen involving bonding and antibonding interactions between 2-thienylpyridine (thpy) and M , the low-lying excited state orbitals (four for the d orbitals) and the HOMO-LUMO thpy π orbitals. They¹⁰⁵ included the thpy π orbitals in order to determine the nature of the π - π^* ligand-centred excited state. The method successfully explained the electronic spectra. Matsushita *et al.*¹⁰⁶ studied the emission mechanism of $M(2\text{-thienylpyridine})_2$. Seven orbitals including d and π orbitals were chosen for calculation. These orbitals were selected to provide a description of both metal-to-ligand charge transfer (MLCT) and ligand-centred (LC) transitions. Their results showed good agreement with experimental data.

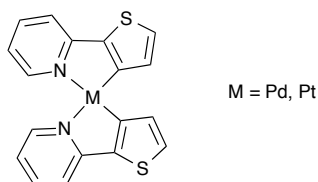


Figure 4.4. Structure of $M(2\text{-thienylpyridine})_2$.^{105,106}

Another example of a calculation on a metal complex using CASSCF was reported by Freitag and co-workers.¹⁰⁷ They investigated how the NO ligand coordinated to Ru in their complex and its effect on the central Ru oxidation state (NO is known to be a non-innocent ligand). The NO ligand coordination mode to Ru in *trans*-[RuCl₄(NO)(1 *H*-indazole)] was investigated to explain its electronic structure (Figure 4.5). All Ru d orbitals and those of the ligands interacting with them were selected as active orbitals. Sixteen electrons in thirteen active orbitals were chosen for the CASSCF calculation, where active orbitals involve the five Ru 4d, two pairs of NO π and π^* , the π and π^* of the indazole, one p for σ bond between Cl and Ru on the Cl atom and the NO σ . This calculation showed that the formal Ru oxidation state is 2.5 since the electronic configuration of Ru consisted of nearly equal d⁵(Ru(III)) and d⁶(Ru(II)) contributions. The electronic structure of this complex was Ru(III)-NO⁰, rather than Ru(II)-NO⁺, due to the NO electron configuration displaying a predominantly neutral character.

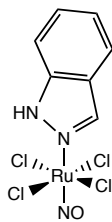


Figure 4.5. *trans*-[RuCl₄(NO)(1*H*-indazole)] structure studied by Freitag and co-workers.¹⁰⁷

4.2 Aims of this work

The main goal of this chapter is to determine the method requirements (single-reference or multireference character) for studying pincer palladacycles. We have probed the electronic structure of symmetrical and unsymmetrical pincer palladacycles using CASSCF method, to determine the weight of the dominant configurations and hence the reference character of the ground state.

4.3 Computational details

All calculations were carried out using the Gaussian09 program.⁸⁷ Both symmetrical and unsymmetrical pincer palladacycles (PdYCY and PdYCY') in Figure 4.6 were studied. The pincer palladacycle optimisation geometries were obtained using PBE^{45,46}/6-31+G(d,p)[SDD⁵⁷] (SDD ECP for Pd and 6-31+G(d,p) for the other atoms), which were then used as starting structures for a geometry optimisation using CASSCF.^{108–112} Canonical orbitals at the pincer palladacycle optimisation geometries were generated using the restricted Hartree-Fock (RHF) method with the contracted Gaussian function STO-3G basis set for all atoms and SDD effective core potential (ECP) for Pd (HF/STO-3G[SDD]). The canonical orbitals at HF/STO-3G[SDD] were used to select the active space for the CASSCF calculations. The CASSCF with *n* electrons in *m* active orbitals, referred to as CAS(*n*,*m*), was then studied. Electron occupations, using diagonal elements of the density matrix, were examined to check the active orbitals. If the occupancy value is equal to two it represents a doubly occupied state, and if the value is equal to zero, it represents an empty orbital. Therefore, in either case, there is no electron promotion in the active space indicating that the electrons are not distributed.¹⁰³ Some calculations were found

difficult to converge, therefore the maximum number of iterations was extended to increase and/or a quadratically convergent SCF procedure was used. The keyword for increasing the number of iterations is SCF(maxcycle=N) where N is the number of SCF cycles. For the quadratically convergent SCF procedures, the keyword is use=L506 or SCF=qc. Optimised PdNCN and PdSCS geometries were compared to their experimental X-ray crystal structure data.^{90,91}

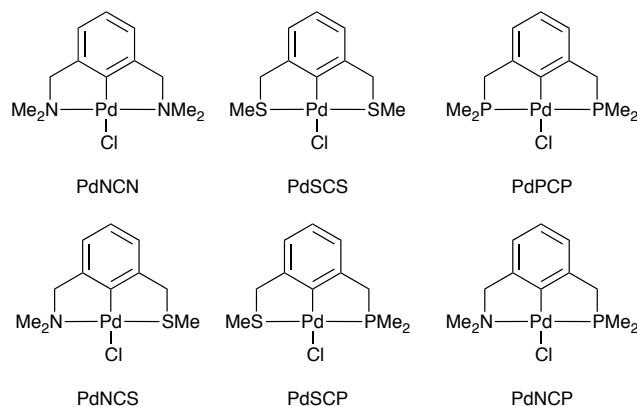


Figure 4.6. Symmetrical and unsymmetrical pincer palladacycles used in this study.

4.4 Results and discussion

4.4.1 Symmetrical pincer palladacycles

The canonical orbitals from HF used for CASSCF are shown in Figure A.1, Figure A.2 and Figure A.3 in Appendix A for pincer palladacycles PdNCN, PdSCS and PdPCP, respectively. Orbitals with a significant d character were chosen for the active space of the CASSCF calculation. For allowing electronic promotion from the ground state to excited states and getting a realistic description, we have added π^* valence virtual orbitals in the active orbitals.

PdNCN: The chosen occupied orbitals 58a, 59a, 60a, 61a, 62a, 63a and 65a and unoccupied orbitals 75a, 76a, 77a and 78a are studied. The CAS(14,11), CAS(12,10), CAS(10,9), CAS(8,8) and CAS(6,6) were evaluated.

Table 4.1 gives information involving the ground-state electronic structure where the numbering labels of the orbitals have no relation to orbital energies. All CAS(n,m) geometry optimisations at the ground state have the configuration interaction (CI) coefficient (configuration contribution) more than 0.90 (81%). The CI coefficient of

the CAS(14,11), CAS(12,10), CAS(10,9), CAS(8,8) and CAS(6,6) contain 0.96, 0.97, -0.97, 0.97 and 0.97, respectively. This result shows that PdNCN has the electronic ground state well separated from the excited state with a contribution of more than 94% indicating that the overall wavefunction of PdNCN has a single-reference character. The occupation number is used to analyse the size of CAS(n,m). It should not be near 2.00 (double occupation) and 0.00 (unoccupied).¹⁰³ CAS(14,11) has nearly 2.00 in the orbitals 60a and 59a, CAS(12,10) has 59a and 60a, and CAS(10,9) has 60a (Table 4.1). This result suggests a reduction of the active space is acceptable. When decreasing the CASSCF active space to CAS(8,8) and CAS(6,6), the maximum occupation number was found to be 1.988 which is far enough away from 2.00 to be acceptable.

According to the occupation number analysis, the CAS(8,8) and CAS(6,6) have been chosen as they do not have an occupation number near 2.00. Table 4.2 reveals details of the configuration interaction (CI) coefficient and its weight (square of CI coefficient) of optimised PdYCY. The configuration pattern at the largest weight are the closed-shell singlet configuration 22220000 for CAS(8,8) and 222000 for CAS(6,6). The second dominant configuration has been analysed. It has a weight of just 0.03 and has a closed-shell configuration, where for CAS(8,8) it is 02222000 and for CAS(6,6) it is 0222000 (Table 4.2). The weight configuration suggests a single-reference character is sufficient for determining the PdNCN ground state structure.

Table 4.1. Occupation number of CAS(n,m) in symmetrical pincer palladacycles (PdYCY), where n is number of electrons and m is number of active orbitals. The configuration interaction (CI) coefficient and weight (w.) of the dominant configuration is also provided. The numbering of orbitals is not based on orbital energy level.

PdYCY	Orbital	Occupation number				
		CAS(14,11)	CAS(12,10)	CAS(10,9)	CAS(8,8)	CAS(6,6)
PdNCN	11a	0.018	0.018	0.017	0.017	0.016
	10a	0.010	0.011	0.010	0.017	
	9a	0.040	0.015	0.015	0.015	0.015
	8a	0.080	0.075	0.073	0.073	0.073
	7a	1.982	1.981	1.982	1.982	1.983
	6a	1.988	1.988	1.988	1.988	
	5a	1.989	1.984	1.984	1.984	1.984
	4a	1.927	1.931	1.931	1.931	1.929
	3a	2.000	2.000	2.000		
	2a	1.995	1.997			
	1a	1.972				
	CI/w.	0.96/0.92	0.97/0.94	-0.97/0.94	0.97/0.94	0.97/0.94
PdSCS	11a	0.016	0.017	0.017	0.016	0.014
	10a	0.013	0.013	0.013	0.012	
	9a	0.015	0.015	0.015	0.014	0.014
	8a	0.070	0.073	0.074	0.069	0.071
	7a	1.998				
	6a	1.986	1.986	1.986	1.987	
	5a	1.995	1.995	1.995		
	4a	1.938	1.935	1.934	1.934	1.931
	3a	2.000	1.999			
	2a	1.985	1.984	1.984	1.985	1.985
	1a	1.983	1.983	1.983	1.983	1.984
	CI/w.	-0.97/0.94	0.97/0.94	-0.97/0.94	0.97/0.94	0.98/0.96
PdPCP	11a	0.017	0.016	0.016	0.016	0.015
	10a	0.018	0.016	0.016	0.016	0.016
	9a	0.065	0.056	0.056	0.056	0.061
	8a	0.016	0.015	0.015	0.015	
	7a	1.982	1.982	1.982	1.982	1.983
	6a	1.983	1.983	1.983	1.983	1.984
	5a	1.943	1.947	1.947	1.947	1.941
	4a	2.000	2.000	2.000		
	3a	1.984	1.984	1.984	1.984	
	2a	2.000	2.000			
	1a	1.993				
	CI/w.	0.97/0.94	0.97/0.94	0.97/0.94	0.97/0.94	0.98/0.96

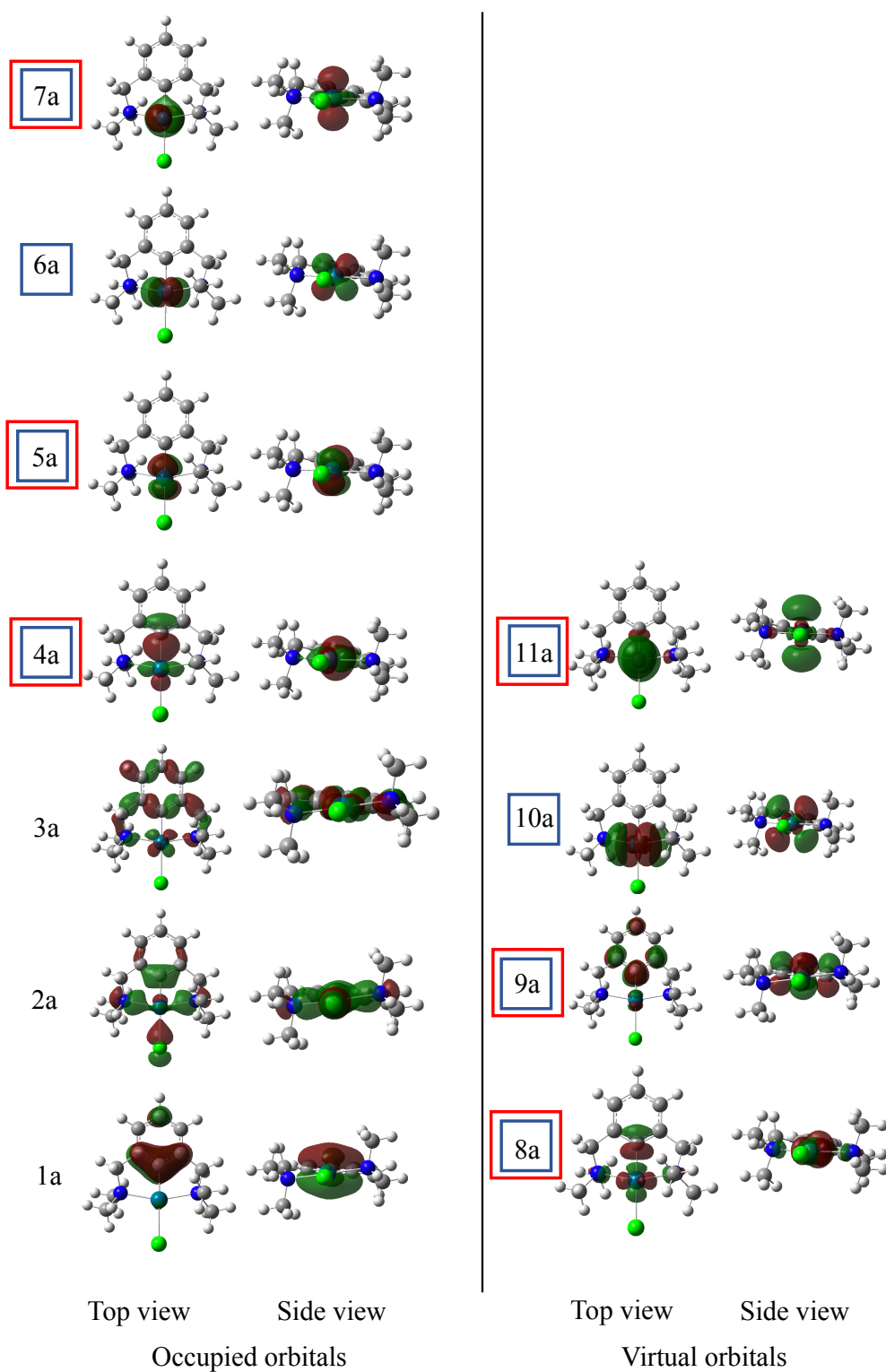


Figure 4.7. Active space orbitals of PdNCN resulting from CASSCF optimisation calculation and an orbital numbering scheme which is not based on orbital energy. The orbitals in blue and red squares are the active orbitals for CAS(8,8) and CAS(6,6), respectively. The isovalue for representative orbitals is 0.05 (grey = carbon, white = hydrogen, dark green = palladium, light green = chlorine and dark blue = nitrogen).

Table 4.2. Configuration state function (CSF), configuration interaction (CI) coefficient and its weight of optimised-PdYCY ground state using CASSCF(6,6) and CASSCF(8,8) with 6-31+G(d,p)[SDD]. All configurations with weight > 0.01 are listed.

PdYCY	CAS(n,m)	CSF	CI coefficient	Weight
PdNCN	CAS(8,8)	22220000	0.97	0.94
		02222000	-0.16	0.03
	CAS(6,6)	222000	0.97	0.94
		022200	-0.17	0.03
PdSCS	CAS(8,8)	22220000	0.97	0.94
		02222000	-0.16	0.03
	CAS(6,6)	222000	0.98	0.96
		022200	-0.17	0.03
PdPCP	CAS(8,8)	22220000	0.97	0.94
		20220200	-0.13	0.02
	CAS(6,6)	222000	0.98	0.98
		022020	-0.15	0.02

PdSCS: The chosen orbitals are 58a, 59a, 60a, 61a, 62a, 63a, 65a for occupied orbitals and 75a, 76a, 77a and 78a for unoccupied orbitals (Figure A.2 in Appendix A). We have studied CAS(14,11), CAS(12,10), CAS(10,9), CAS(8,8) and CAS(6,6) the same size as for the PdNCN study. All leading configuration state functions (CSFs) have the weights greater than 0.94, indicating that a single-configuration wavefunction is used for determining the ground state structure of PdSCS (Table 4.1). CAS(14,11), CAS(12,10) and CAS(10,9) have the doubly occupied state: orbitals 60a and 62a for CAS(14,11), orbitals 60a and 62a for CAS(12,10), and orbital 62a for CAS(10,9).

We have analysed the quality for CAS(8,8) and CAS(6,6). In Table 4.2, there are two types of the configuration for CAS(8,8) and CAS(6,6), where each configuration has a weight greater than 0.01. The largest weight shows the closed-shell singlet configuration in both CAS(8,8) and CAS(6,6). The configuration for the second most dominant CI coefficient with small weight 0.03 is 02222000 and 0222000 for CAS(8,8) and CAS(6,6), respectively.

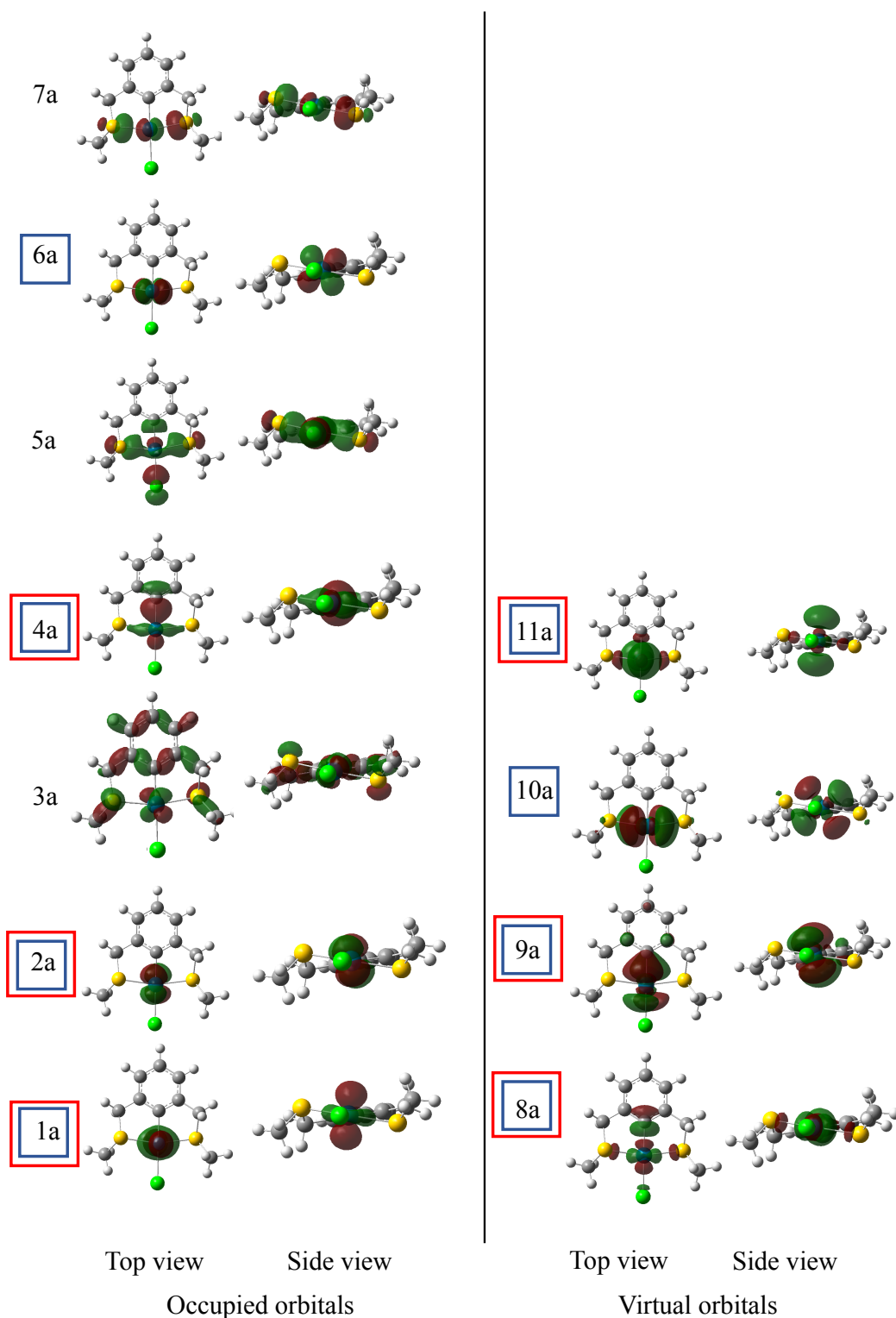


Figure 4.8. Active space orbitals of PdSCS resulting from CASSCF optimisation calculation and an orbital numbering scheme which is not based on orbital energy. The orbitals in blue and red squares are the active orbitals for CAS(8,8) and CAS(6,6), respectively. The isovalue for representative orbitals is 0.05 (grey = carbon, white = hydrogen, dark green = palladium, light green = chlorine and yellow = sulphur).

PdPCP: The chosen orbitals for occupation are 66a, 67a, 68a, 69a, 70a, 71a and 73a, and those for unoccupation are 83a, 84a, 85a and 86a (Figure A.3). In Figure 4.6, it is also shown that the wavefunction for the PdPCP ground state is dominated by a single configuration as all the leading configurations for CAS(n,m) have a percent weight over 94%. CAS(14,11), CAS(12,10) and CAS(10,9) have the doubly occupied state: orbitals 66a, 67a and 69a for CAS(14,11), orbitals 67a and 69a for CAS(12,10), and orbital 69a for CAS(10,9).

To evaluate the electron distribution of CAS(8,8) and CAS(6,6), the electron configuration with the occupation number is determined. The calculation shows that the largest weight is for the singlet ground state configuration: 22220000 and 222000 for CAS(8,8) and CAS(6,6), respectively. The second configuration, with small weight of 0.02 for CAS(8,8) and CAS(6,6) are 20220200 and 022020, respectively (Figure 4.9).

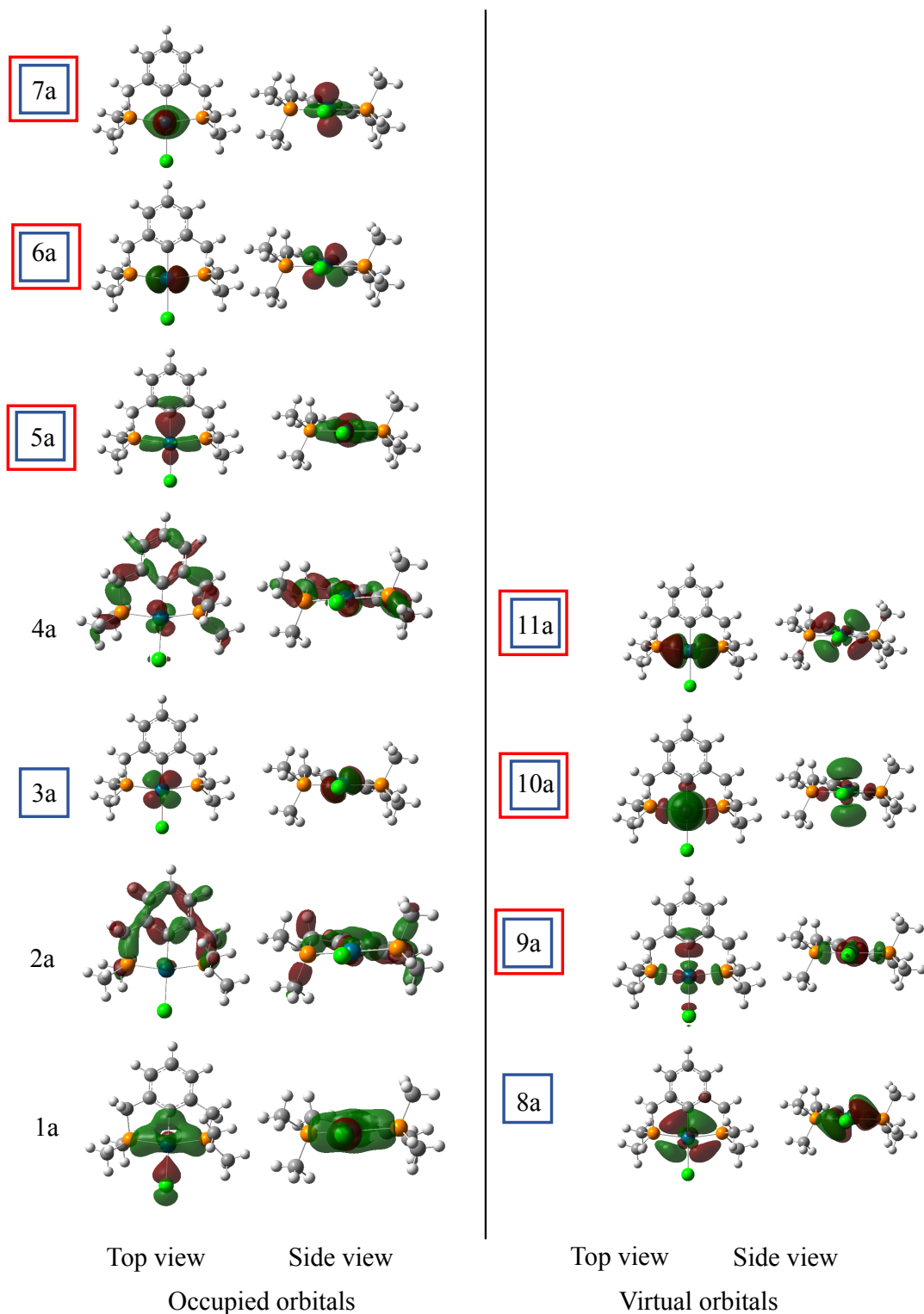


Figure 4.9. Active space orbitals of PdPCP resulting from CASSCF optimisation calculation and an orbital numbering scheme which is not based on orbital energy. The orbitals in blue and red squares are the active orbitals for CAS(8,8) and CAS(6,6), respectively. The isovalue for representative orbitals is 0.05 (grey = carbon, white = hydrogen, dark green = palladium, light green = chlorine and orange = phosphorus).

4.4.2 Electronic structures of symmetrical pincer palladacycles

In order to perform the occupation number analysis, CAS(8,8) and CAS(6,6) are good choices for symmetrical pincer palladacycles. Interestingly, both PdNCN orbital 59a and PdPCP orbital 66a involve the interaction between Pd and donor atoms (see Figure A.1 for PdNCN and Figure A.3 for PdPCP). These orbitals are doubly occupied, indicating no promotion of electrons from these. It is shown that some bonding orbitals of Pd-Y bonds are not important for including as active orbitals that determine the PdYCY ground state structures. However, Pd-L bonding, where L = Y, C and Cl, orbitals is important as these bonds involve two-electron excitation from $[d_{x^2-y^2} + \sigma]$ to $[d_{x^2-y^2} - \sigma]^*$, which are the bonding and antibonding orbitals of Pd-L bonds, and these bonds occur simultaneously. When we analyse the second dominant configuration of PdYCY, the configuration for both CAS(8,8) and CAS(6,6) involve a two-electron excitation from $[d_{x^2-y^2} + \sigma]$ to $[d_{x^2-y^2} - \sigma]^*$, which are the bonding and antibonding orbitals of Pd-L bonds, respectively (see Figure 4.7 for PdNCN, Figure 4.8 for PdSCS and Figure 4.9 for PdPCP), and hence why we include Pd-L bonding in active orbitals. To clarify the picture of the chemical bond information around the Pd centre, the isovalue contour plots of $[d_{x^2-y^2} + \sigma]$ and $[d_{x^2-y^2} - \sigma]^*$ are set to 0.02 (Figure 4.10). Figure 4.10 shows more electron delocalisation between Pd and C rather than other bonds. It indicates the strong interaction of the Pd-C bond compared to Pd-Cl and Pd-Y bonds. However, the choice of active space should in general be minimised because of computational costs.⁹⁹ Therefore, the CAS(6,6) has been chosen as the best choice for studying PdYCY.

4.4.3 CASSCF efficiency for optimisation of the pincer structure

To determine the accuracy of the predicted CASSCF geometry, testing was done on the optimised structure using CAS(6,6) with 6-31+G(d,p)[SDD] basis set. The mean signed error (MSE) and mean unsigned error (MUE) are used to evaluate the accuracy of CASSCF optimisation, and their geometries by comparison to X-ray data.^{90,91} Considering MSE (interatomic) and MUE (interatomic) values, CAS(6,6) optimised

geometries are in good agreement with X-ray structures, with MSE (interatomic) $< 0.048 \text{ \AA}$ and MUE (interatomic) $< 0.055 \text{ \AA}$ (Table 4.3). To gain insight into the accuracy of the calculated chemical bonds, the MSE and MUE of bond distances are measured, and it is shown that they have a small error. However, MSE and MUE show that the DFT geometry (PBE exchange-correlation function) has slightly smaller errors than CAS(6,6) optimised geometries.

Table 4.3. Bond and interatomic distance MSE and MUE (excluding hydrogens) using PBE and CAS(6,6) with a 6-31+G(d,p)[SDD] basis set, compared to X-ray crystal structure.

PdYCY	Analysis	Error / \AA	
		PBE	CAS(6,6)
PdNCN	MSE (interatomic)	0.032	0.046
	MUE (interatomic)	0.014	0.055
	MSE (bonded)	0.014	0.014
	MUE (bonded)	0.014	0.026
PdSCS	MSE (interatomic)	0.030	0.048
	MUE (interatomic)	0.038	0.052
	MSE (bonded)	0.015	0.019
	MUE (bonded)	0.019	0.024

4.4.4 Unsymmetrical pincer palladacycles

The chosen canonical orbitals from HF for PdNCS, PdSCP and PdNCP are shown in Appendix, Figure A.4, Figure A.5 and Figure A.6, respectively. Orbitals with a significant d character and virtual p-orbitals are considered important to include in the active space when studying unsymmetrical pincer palladacycles (PdYCY'). We have studied CAS(14,11), CAS(12,10), CAS(10,9), CAS(8,8) and CAS(6,6).

PdNCS: The results of the CASSCF calculation for PdNCS are shown in Table 4.4. The CASSCF optimisations are converged except for CAS(12,10) (Table 4.4). The results suggest that the single-reference wavefunction is acceptable for PdNCS structure optimisation (weight greater than 0.94). For CAS(14,11) and CAS(10,9), orbitals with double occupancy are found. Double occupation has not been found, when decreasing the number of the electrons and the active spaces to CAS(8,8) and CAS(6,6) (Table 4.4). Table 4.5 shows the configuration interaction coefficient and its weight of CAS(8,8) and CAS(6,6). The large weight configuration in this case also shows a closed-shell singlet electron configuration 22220000 and 222000 for CAS(8,8)

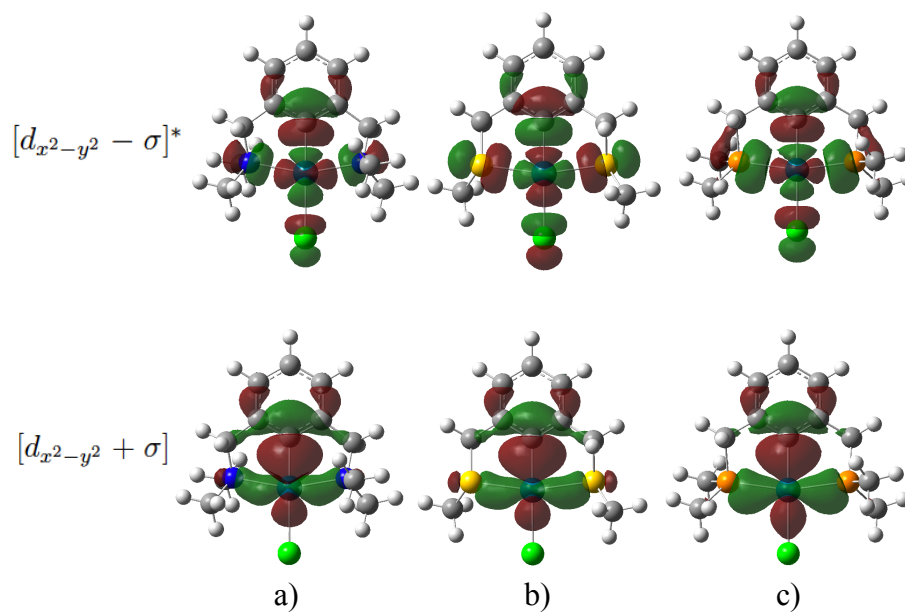


Figure 4.10. Molecular orbitals involved in the excited state configuration of symmetrical pincer palladacycles: a) PdNCN, b) PdSCS and c) PdPCP. Contour plots for isovalue 0.02 leading to clearer plot between Pd-L bond interactions (grey = carbon, white = hydrogen, dark green = palladium, light green = chlorine, dark blue = nitrogen, yellow = sulphur and orange = phosphorus).

and CAS(6,6), respectively. The configuration which has a weight over 0.01 still has a small value (weight < 0.03). The configuration for this weight is 20222000 and 022002 for CAS(8,8) and CAS(6,6), respectively. The active orbitals which are involved in the CASSCF optimisation for CAS(8,8) and CAS(6,6) are shown in Figure 4.11.

Table 4.4. Occupation number of CAS(n,m) in unsymmetrical pincer palladacycles (PdYCY'), where n is number of electrons and m is number of active orbitals. The configuration interaction (CI) coefficient and weight (w.) of the dominant configuration state is also provided. The numbering of orbitals is not based on orbital energy level.

PdYCY'	Orbital	Occupation number					
		CAS(14,11)	CAS(12,10)	CAS(10,9)	CAS(8,8)	CAS(6,6)	
PdNCS	13a	0.017	n/a	0.018	0.016	0.015	
	12a			0.012	0.011		
	11a	0.012					
	10a	0.069		0.074	0.070	0.072	
	9a	0.015		0.015	0.014	0.015	
	8a	1.983		1.982	1.982	1.984	
	7a			1.986	1.987		
	6a	1.988					
	5a	1.938		1.933	1.933	1.931	
	4a	1.984		1.984	1.984	1.985	
	3a	1.995		1.995			
	2a	1.999					
	1a	1.999					
		CI/w.	-0.97/0.94		-0.97/0.94	0.97/0.94	0.98/0.96
PdSCP	11a	0.018	0.019	0.018	0.016	0.015	
	10a	0.017	0.017	0.016	0.014		
	9a	0.065	0.068	0.068	0.060	0.064	
	8a	0.019	0.019	0.019	0.016	0.014	
	7a	1.983	1.982	1.982	1.983	1.984	
	6a	1.998					
	5a	1.982	1.982	1.982	1.983	1.984	
	4a	1.945	1.943	1.942	1.944	1.939	
	3a	1.985	1.984	1.985	1.985		
	2a	1.999	1.997				
	1a	1.989	1.989	1.989			
		CI/w.	0.97/0.94	0.97/0.94	-0.97/0.94	0.97/0.94	0.98/0.96
	PdNCP	13a	0.020	0.019	0.019	0.017	0.016
		12a		0.017	0.016	0.014	
11a		0.021	0.020	0.020	0.016	0.015	
10a		0.077	0.069	0.069	0.062	0.065	
9a		0.042					
8a		1.981	1.981	1.981	1.982	1.983	
7a			1.984	1.985			
6a		1.981	1.981	1.981	1.983	1.984	
5a		1.935	1.942	1.941	1.942	1.938	
4a		1.991			1.985		
3a		1.987	1.988	1.988			
2a		1.969					
1a		1.998	1.998				
		CI/w.	0.96/0.92	-0.97/0.94	0.97/0.94	0.97/0.94	0.98/0.96

n/a = not available because optimisation of this CAS is not converge.

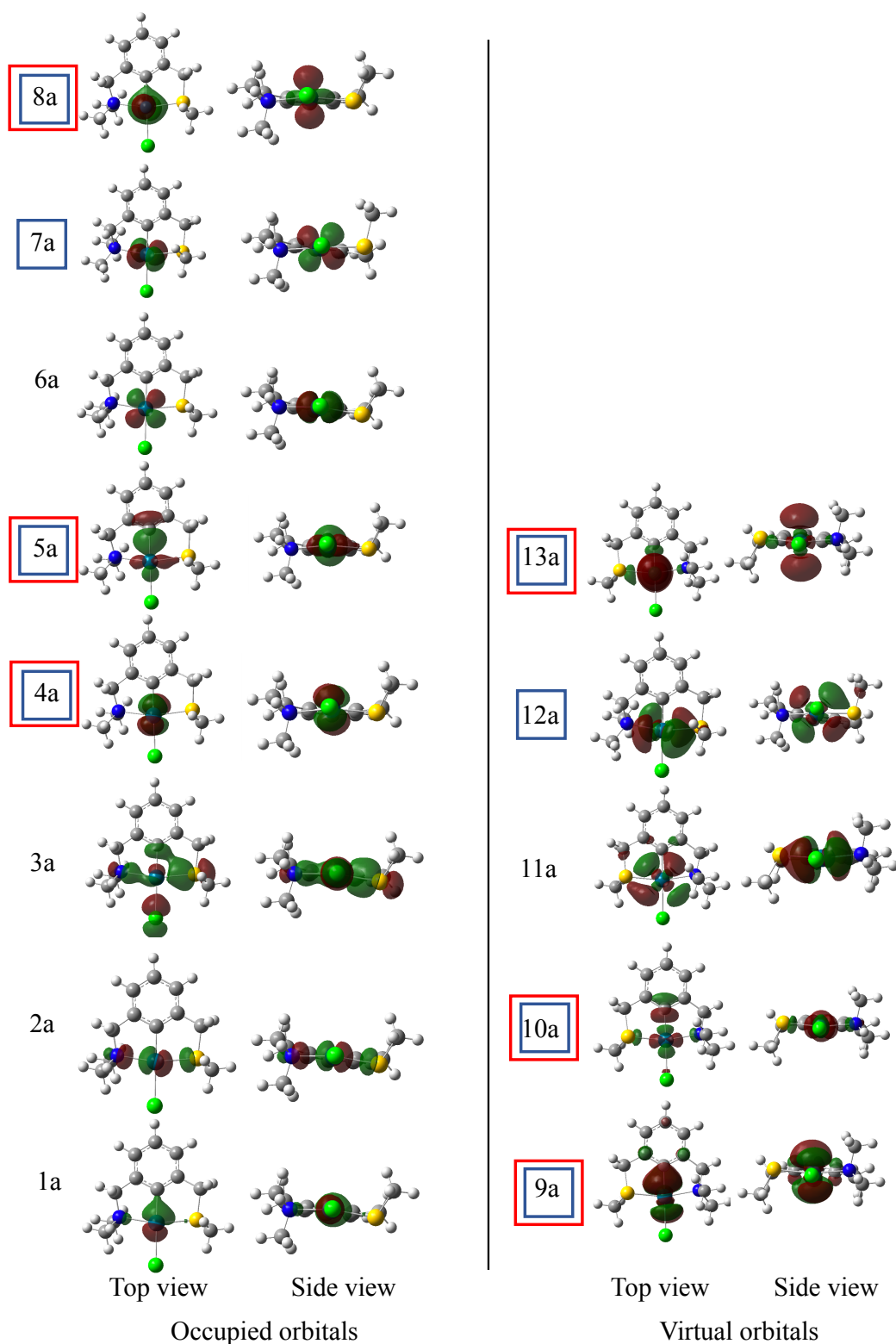


Figure 4.11. Active space orbitals of PdNCS resulting from CASSCF optimisation calculation and an orbital numbering scheme which is not based on orbital energy. The orbitals in blue and red squares are the active orbitals for CAS(8,8) and CAS(6,6), respectively. The isovalue for representative orbitals is 0.05 (grey = carbon, white = hydrogen, dark green = palladium, light green = chlorine, dark blue = nitrogen and yellow = sulphur).

Table 4.5. Configuration state function (CSF), configuration interaction (CI) coefficient and its weight of optimised-PdYCY' ground state using CASSCF(6,6) and CASSCF(8,8) with 6-31+G(d,p)[SDD]. All configurations with weight > 0.01 are listed.

PdYCY'	CAS(n,m)	CSF	CI coefficient	Weight
PdNCS	CAS(8,8)	22220000	0.97	0.94
		20222000	-0.16	0.03
	CAS(6,6)	222000	0.98	0.96
		022002	-0.17	0.03
PdSCP	CAS(8,8)	22220000	0.97	0.94
		02220200	-0.14	0.02
	CAS(6,6)	222000	0.98	0.96
		022020	-0.16	0.03
PdNCP	CAS(8,8)	22220000	0.97	0.94
		20220200	-0.13	0.02
	CAS(6,6)	222000	0.98	0.98
		022020	-0.16	0.03

Unsymmetrical SCP pincer palladacycle (PdSCP): For PdSCP, the chosen orbitals are 63a, 64a, 65a, 66a, 67a, 68a and 69a for occupied molecular orbitals, and 79a, 80a, 81a, and 82a for unoccupied molecular orbitals. The wavefunction is dominated by a single configuration having a weight greater than 0.94 in all CASs. Only CAS(14,11) and CAS(12,10) have a doubly occupied orbital (64a) but the system does not have a doubly occupied state when optimised using CAS(10,9), CAS(8,8) and CAS(6,6) (Table 4.4).

For CAS(10,9), the largest weight, 0.94, corresponds to the ground state configuration 222220000. Due to the limitation of Gaussian output files, we cannot show the excited-state configuration of CAS(10,9). Here, we have focused on CAS(8,8) and CAS(6,6). Figure 4.12 shows the active space orbitals and their occupation numbers for PdSCP. Table 4.5 shows that the largest weight ground state configurations of both CAS(8,8) and CAS(6,6) are greater than 0.94 and the second most important configuration contributes less than 0.03. This corresponds to the configuration 02220200 for CAS(8,8) and 022020 for CAS(6,6) (Figure 4.12).

Unsymmetrical NCP pincer palladacycle (PdNCP): The chosen occupied orbitals are 61a, 62a, 64a, 65a, 66a, 67a and 69a and the unoccupied orbitals are 79a, 80a, 81a and 82a. The weight results from all CAS indicate a single-reference character with contribution 0.92 of the weight. It is also shown that CAS(14,11) and

CAS(12,10) are doubly occupied (Table 4.4).

For CAS(10,9), CAS(8,8) and CAS(6,6), the calculations reveal that the overall wavefunction for PdNCP has single-reference character with a large weighting (over 0.96). On considering all configurations of weight greater than 0.01, the dominant configuration involves the closed-shell singlet configuration, while the second configuration has a much smaller weight (<0.03). This is also a closed-shell singlet configuration. These are 20220200 and 022020 for CAS(8,8) and CAS(6,6), respectively (Table 4.4). The active space orbitals for these CASSCFs are shown in Figure 4.13.

4.4.5 Electronic structures of unsymmetrical pincer palladacycles

The overall wavefunction of unsymmetrical pincer palladacycles shows significant single-reference character, as was found in the case of symmetrical pincer palladacycles. The orbitals from CAS calculations were used to describe the bonding in the unsymmetrical pincer palladacycles. Figure 4.14 shows that Pd interacts with both donor atoms simultaneously, i.e. electron density is delocalised over the Y-Pd-Y' bonds. However, by increasing the isovalue of the electron density plot (Figure 4.12 and Figure 4.13), it is clear that the Pd-P interaction is stronger than the Pd-S bond (in PdSCP; Figure 4.12) and Pd-N bond (in PdNCP; Figure 4.13). Moreover, the electron promotion occurs from the bonding Y-Pd-Y' orbitals (with occupation $\sim 1.94e$) to the antibonding Y-Pd-Y' orbital (with occupation $\sim 0.06e$), see Figure 4.11, Figure 4.12 and Figure 4.13 for PdNCS, PdSCP and PdNCP, respectively. It appears to be this specific orbital that is involved in the two-electron excitation, i.e. $[d_{x^2-y^2} + \sigma]$ to $[d_{x^2-y^2} - \sigma]^*$, in both symmetrical and unsymmetrical pincer palladacycles.

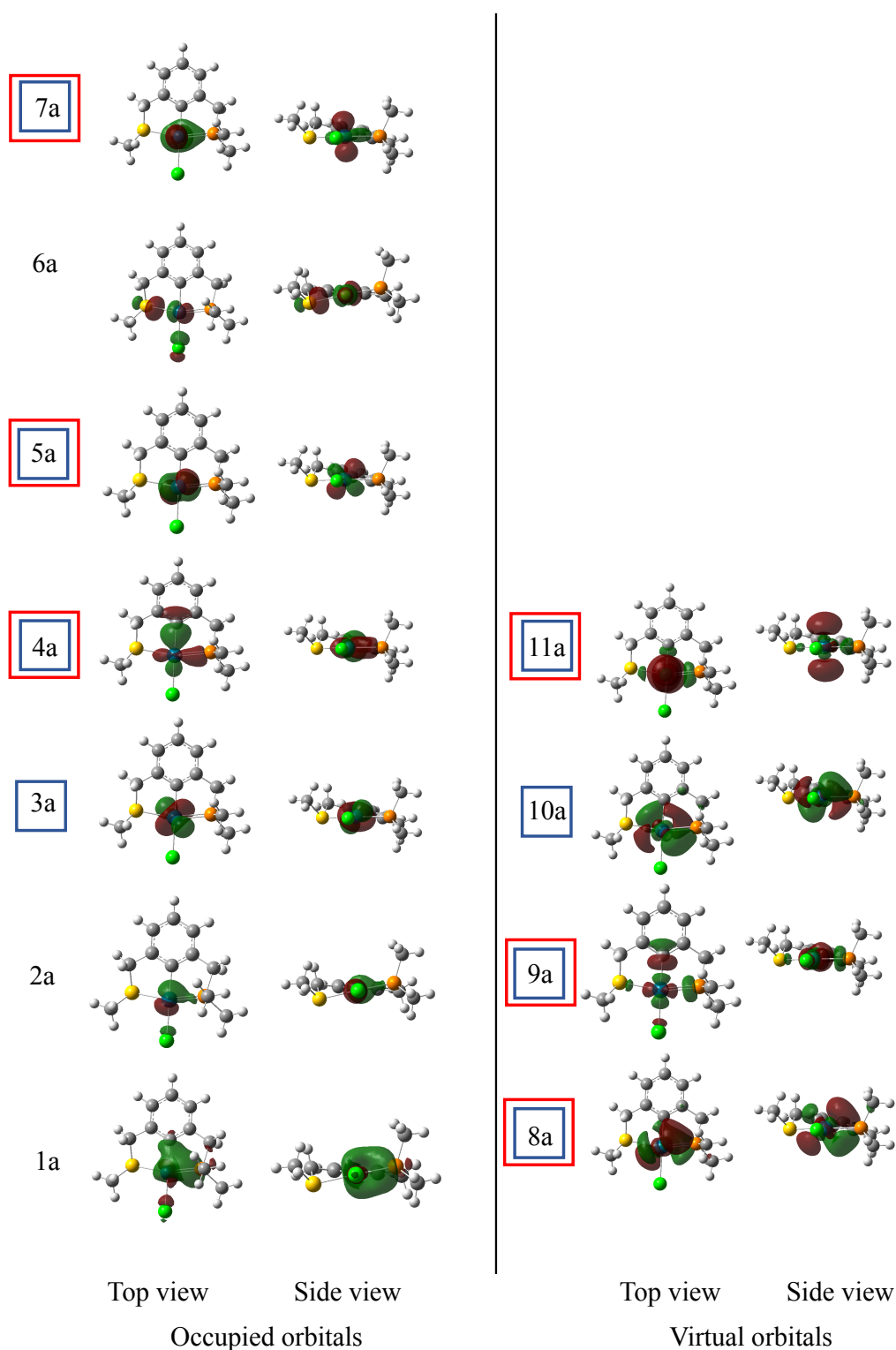


Figure 4.12. Active space orbitals of PdSCP resulting from CASSCF optimisation calculation and an orbital numbering scheme which is not based on orbital energy. The orbitals in blue and red squares are the active orbitals for CAS(8,8) and CAS(6,6), respectively. The isovalue for representative orbitals is 0.05 (grey = carbon, white = hydrogen, dark green = palladium, light green = chlorine, yellow = sulphur and orange = phosphorus).

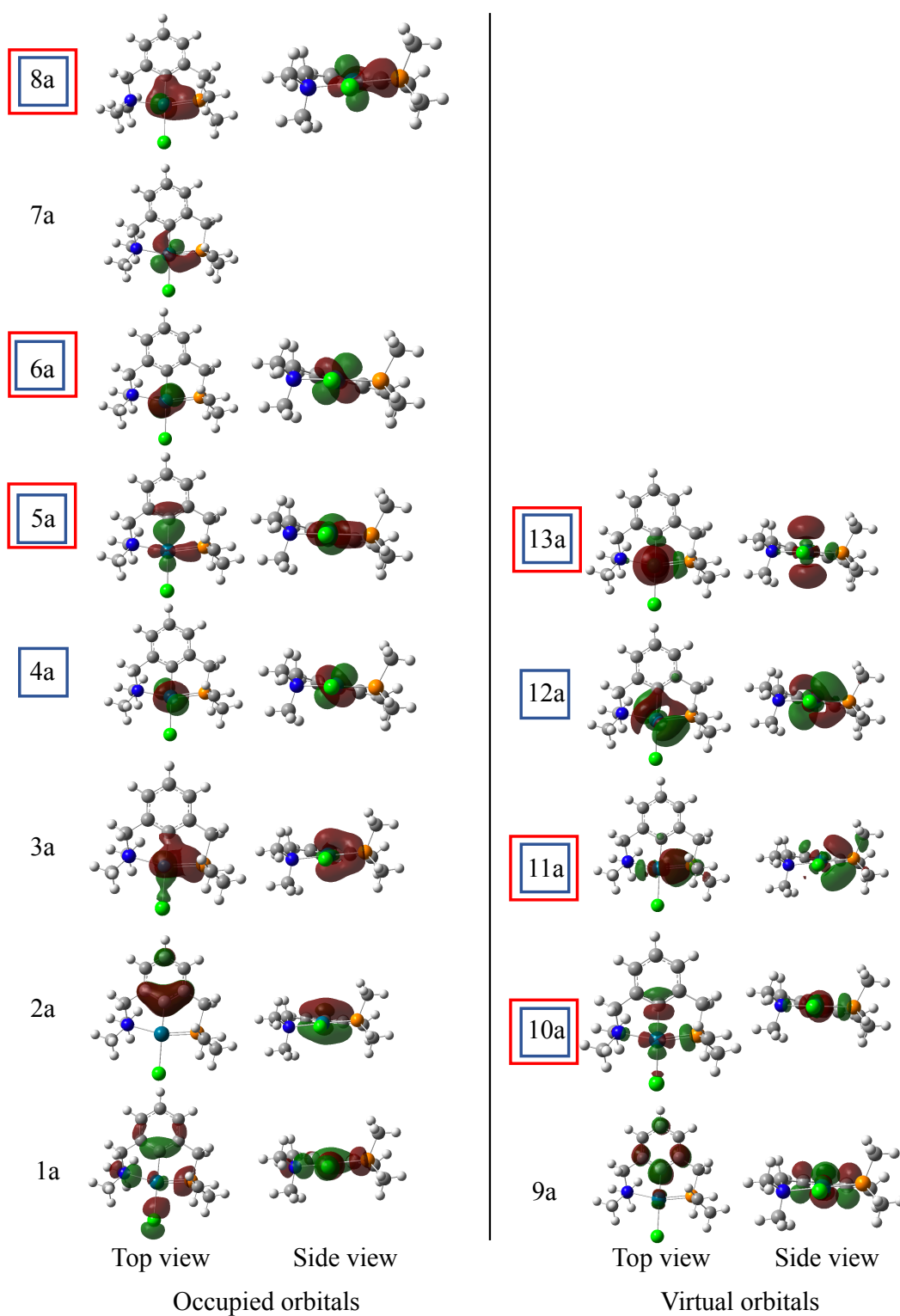


Figure 4.13. Active space orbitals of PdNCP resulting from CASSCF optimisation calculation and an orbital numbering scheme which is not based on orbital energy. The orbitals in blue and red squares are the active orbitals for CAS(8,8) and CAS(6,6), respectively. The isovalue for representative orbitals is 0.05 (grey = carbon, white = hydrogen, dark green = palladium, light green = chlorine, dark blue = nitrogen and orange = phosphorus).

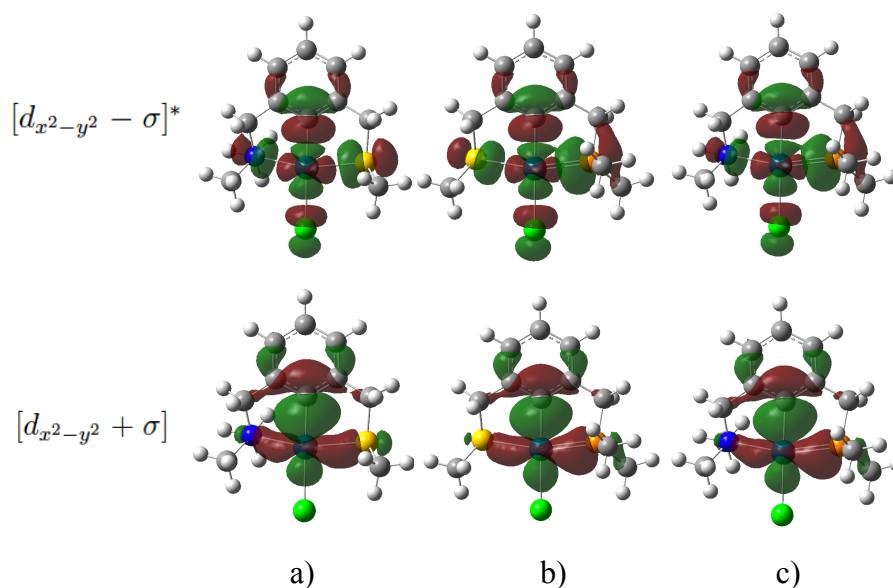


Figure 4.14. Molecular orbitals involved in the excited state configuration of unsymmetrical pincer palladacycles: a) PdNCS, b) PdSCP and c) PdNCP. Contour plots for isovalue 0.02 leading to clearer plot between Pd-L bond interactions (grey = carbon, white = hydrogen, dark green = palladium, light green = chlorine, dark blue = nitrogen, yellow = sulphur and orange = phosphorus).

4.5 Conclusion

The geometry and electronic structures of pincer palladacycles have been analysed using the CASSCF/6-31+G(d,p)[SDD] method. It was found that the CAS(6,6) optimised structure was in good agreement with X-ray crystal data.^{90,91} Moreover, our calculation showed that the ground state structure of the pincer palladacycles had a significant single-reference character and a closed-shell singlet configuration for large and small active spaces. The weight of the dominant configuration was greater than 0.92 in all cases. It was found that CAS(8,8) and CAS(6,6) are adequate for investigating the ground state of the pincer palladacycles. Given the significant single-reference character for all pincer palladacycle structures both symmetric and unsymmetric, our calculations suggest that density functional theory is a good and appropriate method for studying pincer palladacycles.

Chapter 5

Formation Reaction of Pincer Palladacycles

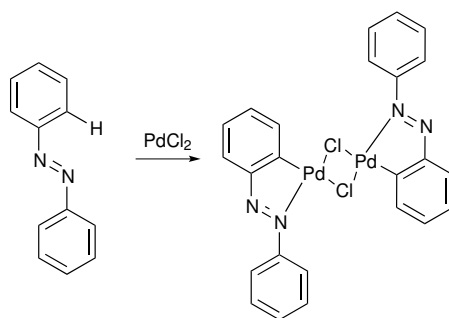
In this chapter, the formation pathways for symmetrical and unsymmetrical pincer palladacycle have been investigated using density functional theory (DFT). The thermodynamic and kinetic properties and energy barriers of the formation reactions are also described. In addition, the stability of the pincer palladacycles are studied and presented.

5.1 Introduction

Palladacycles are organometallic compounds and are popular and attractive choices as the catalyst or pre-catalyst in organic reactions. A way to synthesise palladacycles is through C-H bond activation with palladium. C-H bond activation is a simple method for palladacycle formation because the ligand does not need to be modified, leading to fewer synthesis steps.¹¹³ For example, the first successful palladacycle synthesis *via* C-H bond activation was reported through the reaction of azobenzene and PdCl₂ by Cope *et al.* (Scheme 5.1).¹

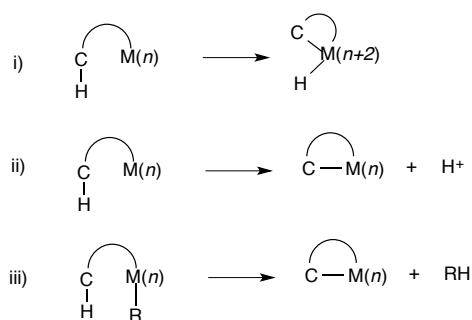
5.1.1 C-H bond activation

C-H bond activation is a fundamental method for forming palladacycles after Cope *et al.* reported.¹ Palladacycle chemistry has become of increasing interest.¹¹⁴ For example, Takahashi and Tsuji¹¹⁵ first studied substituted azobenzene reacting with



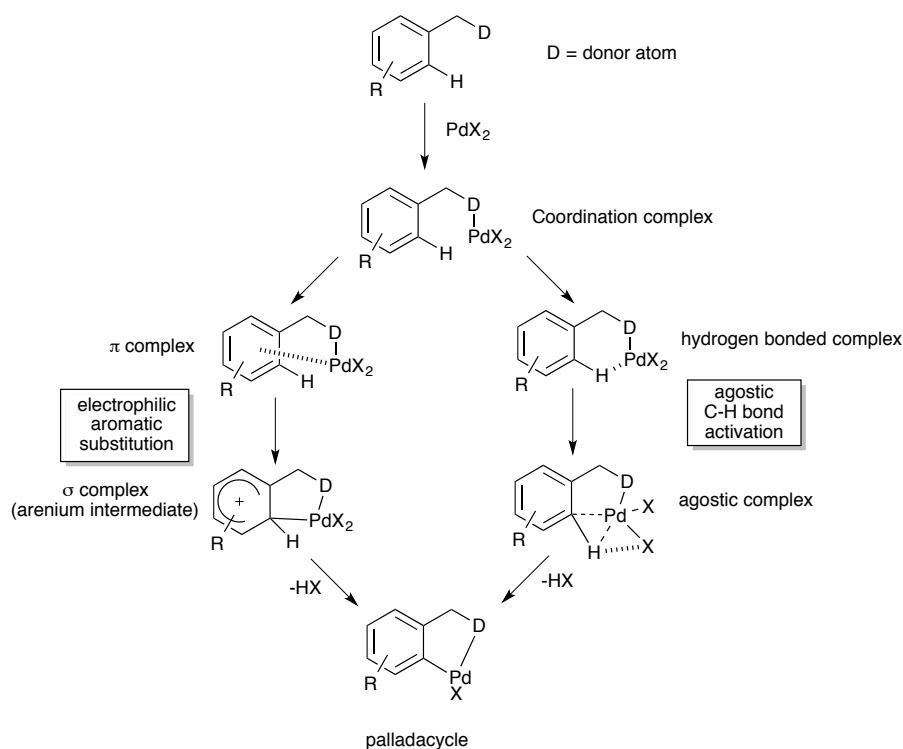
Scheme 5.1. Formation reaction of palladacycle by Cope *et al.*¹

PdCl_2 to form palladacycles *via* C-H bond activation. They investigated the effect of substituents on the benzene ring in reactions with PdCl_2 to form palladacycles. Ryabov¹¹⁴ wrote a useful review providing details of the C-H bond activation in transition-metal complexes including C-H bond activation of palladacycle formation reactions. There are three simple C-H bond activation mechanisms; i) oxidative addition, ii) electrophilic substitution and iii) multicentred reaction (Scheme 5.2).¹¹⁴ For oxidative addition, the C-H bond activation occurs *via* donation of two electrons from metal centre to σ^* orbital of the C-H bond. The oxidation state of the metal centre of the product increases whereas the reactant is reduced. For electrophilic substitution mechanism, the central metal does not change its oxidation state. The hydrogen cleaves from the complex. It is a free proton in solution or bound to base. For the last type, the alkyl group forms with hydrogen, then RH is eliminated from the complex.



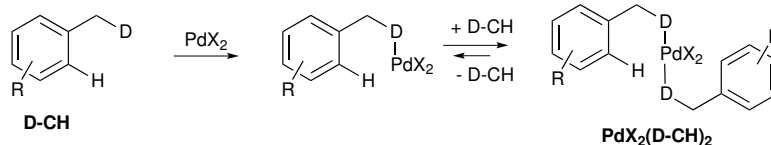
Scheme 5.2. C-H bond activation types; i) oxidative addition, ii) electrophilic substitution and iii) multicentred reaction.¹¹⁴

For palladacycle formation *via* C-H bond activation, two possible mechanisms have been proposed (Scheme 5.3).⁶ These pathways are controlled by the substituent on the arene. The initial step of this reaction is donor atom coordination to the palladium centre followed by either electrophilic aromatic substitution or an agostic C-H bond activation. In electrophilic aromatic substitution, the π complex is formed followed by a σ complex intermediate giving the palladacycle product. In the agostic pathway, a hydrogen bond complex (see Scheme 5.3) has been proposed followed by an agostic complex then producing a palladacycle.⁶



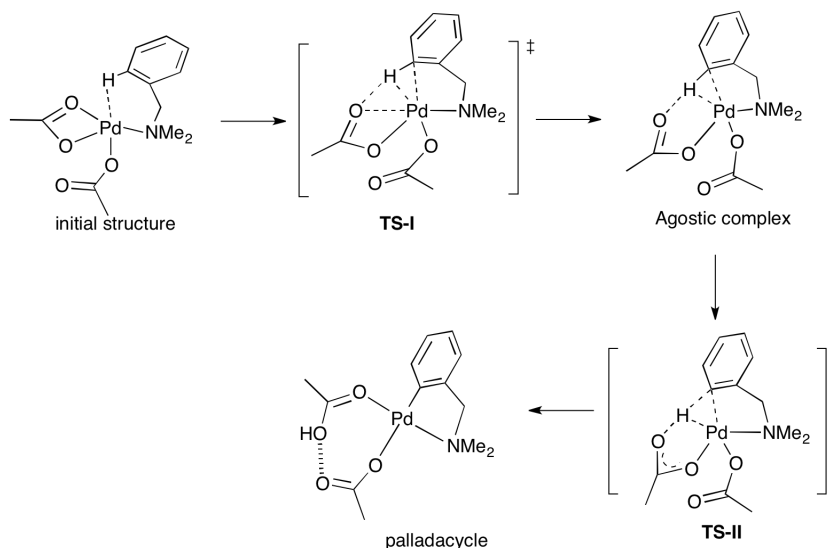
Scheme 5.3. Two proposed reaction mechanism pathways: electrophilic aromatic substitution (left hand side) and agostic C-H bond activation (right hand side).⁶

There is another process competing with the reaction in Scheme 5.3, namely a bridge formation to make a 14e species, $\text{PdX}_2(\text{D}-\text{CH})_2$ (Scheme 5.4). The strength of Pd-D, where D is donor atom, controls the direction of pathway. If the Pd-D bond is strong, the 14e species is formed more easily.⁶ In contrast, if the Pd-D bond is too weak, the D of the ligand arm cannot coordinate to PdX_2 . The nature of the Pd-D bond has great importance in controlling whether a palladacycle or 14e species is formed.



Scheme 5.4. Formation of palladium coordination complex as 14e species, $\text{PdX}_2(\text{D-CH})_2$.⁶

In 2005, a density functional theory (using BP86 method, and SDD ECP for Pd and 6-31G(d,p) for C, H, N and O atoms) study of the formation of a palladacycle between palladium acetate, $\text{Pd}(\text{OAc})_2$, and dimethylbenzylamine was reported.¹¹⁶ This calculation found that the process occurred *via* an agostic C-H bond activation intermediate. There were two transition states; one arm of a κ^2 -acetate was replaced by the agostic interaction (**TS-I**), and proton was transferred *via* six-membered ring (**TS-II**), shown in Scheme 5.5.

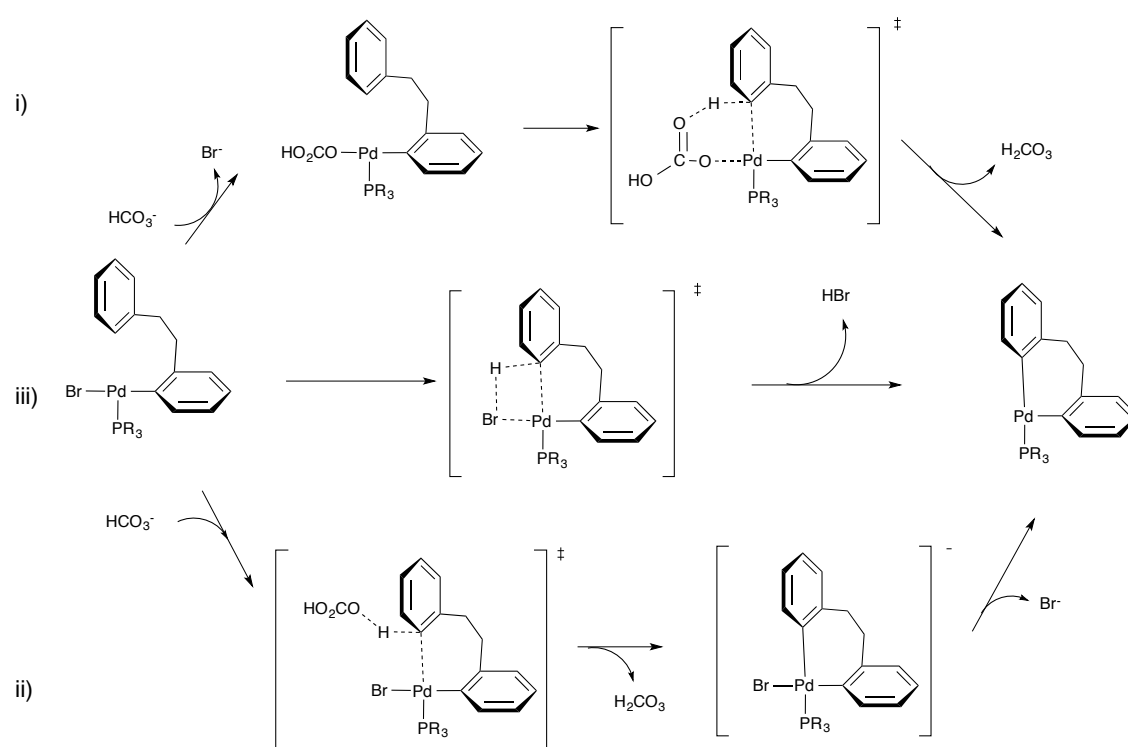


Scheme 5.5. Pincer palladacycle reaction profile calculated by Davies *et al.*¹¹⁶

Moreover, in a theoretical study, Pascual *et al.*¹¹⁷ and García-Cuadrado *et al.*¹¹⁸ (Scheme 5.6) studied the palladacycle formation reaction. Pascual *et al.* used the B3LYP method with LanL2DZ for Pd and Br which basis set for Br was expanded to add polarisation and diffuse function. For the other atoms, they used 6-31+G(d) basis set. Whereas, García-Cuadrado *et al.* used the ONIOM(B3LYP:UFF) method with LanL2DZ for Pd and Br, which in the case of Br d polarisation was included. 6-31+G(d) basis set was used for others. Their work found no evidence of an agostic intermediate. They found that there were three variations of mechanistic pathways;

i) assisted intramolecular, ii) assisted intermolecular and iii) unassisted pathways. In the case of the assisted pathways, an external base could coordinate with either the metal (assisted intramolecular) or the hydrogen (assisted intermolecular), whereas the unassisted pathway was that the metal-carbon bond was involved in a concerted reaction without the hydrogen transferred to the base.

For controlling the reaction mechanism pathway, there are three main influences in palladacycle formation. These are i) the donor group on the side arm, ii) Pd precursor and iii) the C-H bond strength which depends on substitution on the aromatic carbon.⁶

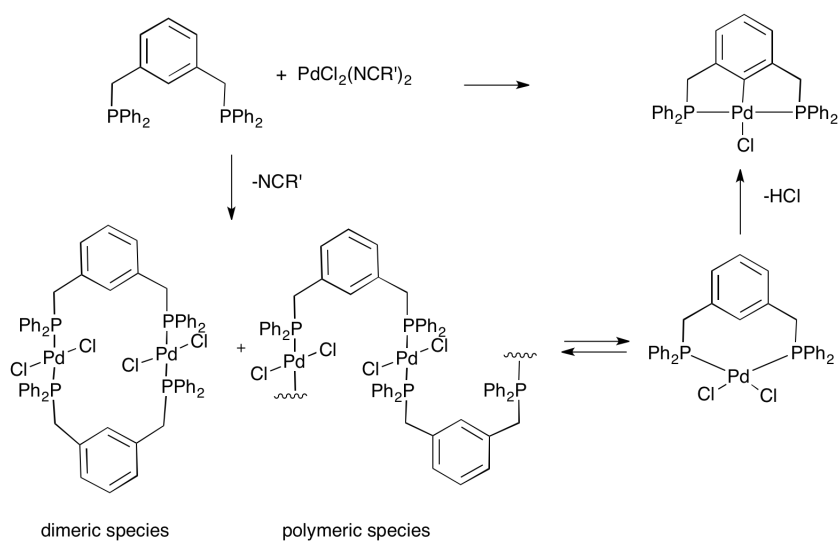


Scheme 5.6. Possible formation reaction; i) assisted intramolecular, ii) assisted intermolecular and iii) unassisted mechanism.^{117,118}

5.1.2 C-H bond activation on pincer palladacycles

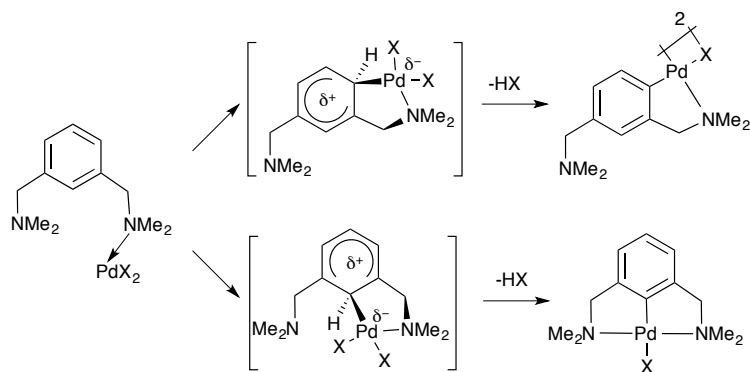
A pincer ligand (YCY) is a specific type of ligand. It consists of tridentate ligand that can coordinate to a Pd centre *via* two donor and an anionic carbon atoms giving a pincer palladacycle.⁹ A pincer palladacycle is also synthesised through C-H bond activation. There are two possible reaction mechanism processes. The C-H bond activation occurs *via* a dimeric/polymeric compound to form the pincer palladacycle

or the C-H bond activation occurs directly to form the pincer palladacycle. In the C-H bond activation *via* dimeric or polymeric compound, for example, the pincer palladacycle is formed by reaction between $\text{PdCl}_2(\text{NCR}')_2$ (where R' is Ph) and a PCP pincer ligand. The reaction mechanism is proposed in Scheme 5.7. The strong interaction between Pd and P atoms leads to polymeric or dimeric species (Scheme 5.7). Then, the polymeric or dimeric species is rearranged to form a four coordinate Pd intermediate. In the last step, C-H bond activation occurs to give a pincer palladacycle.⁶



Scheme 5.7. Formation reaction mechanism of a pincer palladacycle.⁶

Another reaction mechanism pathway of C-H bond activation to form pincer palladacycle was proposed by Steenwinkel *et al.*¹¹⁹ Only one donor atom of the pincer ligand coordinates to Pd in PdCl_2 (Scheme 5.8). In the next step, the arenium ion interacts with the PdCl_2 . Then, there are two possible products; only one arm coordinated to Pd or two arms coordinated to Pd.



Scheme 5.8. Proposed reaction mechanism for C-H bond activation.¹¹⁹

5.1.3 Palladium chloride chemistry

There are several useful Pd(II) precursors for pincer palladacycle formation, for example Pd(OAc)₂, PdCl₂, PdCl₂(NCR)₂, [Pd(NCR)₄]²⁺. Pd(OAc)₂ was found to be polymeric or trimeric and PdCl₂ also formed a polymeric structure, all of which are not simple from a calculation standpoint. In the literature, it is shown that the PdCl₂ molecule is one of the good choices to be used for studying the reaction mechanism pathways using DFT because it is a simplest structure. For instance, a DFT study investigated the reaction mechanism of cyclopalladation between azobenzene and *trans*-PdCl₂(dmf)₂ (dmf = N,N-dimethylformamide).¹²⁰

When PdCl₂ geometry is considered, it was found that there are two possible geometries of PdCl₂; bent singlet and linear triplet structures.¹²¹ Previously, the singlet state monomeric PdCl₂ was used to study bond activation for checking performance of DFT.¹²² To study the pincer palladacycle formation reaction, therefore the singlet state monomeric palladium chloride (PdCl₂) is used in the present work as a simple precursor to determine the C-H bond activation.

5.1.4 *Trans* influence

A pincer palladacycle has a square planar palladium centre. In the ground state, the bond strength between metal and ligand is affected by the bond *trans* to itself in the complex. This term is known as *trans* influence that was first defined by Pidcock¹²³ as “the tendency of a ligand to weaken the bond *trans* to itself”. This is the key effect in explaining the structure in the ground state or thermodynamic state. Therefore, sometimes, it is called the thermodynamic *trans* effect. The *trans* effect refers to

the kinetic rate of ligand substitution in square planar or octahedral complexes. In this case, it is sometimes called the kinetic *trans* effect.¹²⁴ The view of the *trans* influence can be explained in terms of the metal orbital overlap with the ligand orbital (Figure 5.1). If the ligand L has strong overlap with M, the strength of the M-X interaction is weaker than the M-L bond as ligand L withdraws the electron density from the M-X bond leading to decreasing electron density of M-X bond. The *trans* influence has often been brought into study in the organometallic field. It is used to explain stability of compounds in square planar complexes. The *trans* effect is important for explaining reaction pathways. There are many experimental studies on the *trans* influence that generally use spectroscopy or X-ray crystallography to study the *trans* influence.¹²⁵⁻¹²⁸ The DFT study of structure optimisation and molecular orbital analysis has been also employed for the study of *trans* influence in organometallic complexes and to explain the *trans* influence in complexes.¹²⁹⁻¹³³ Considering the pincer palladacycle structure, the geometry of this is a square planar. Therefore, the *trans* influence will affect the strength of interaction between Pd and donor atom.

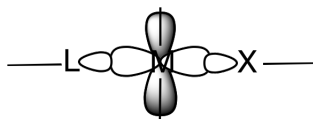


Figure 5.1. *Trans* influence involves sigma orbitals. The strength of the interaction and bond distance between Pd-X depends on the effect of the ligand L which is situated *trans* to X donor atom.

5.2 Aims of this work

The aims of this chapter are to determine the reaction mechanism of the formation of symmetrical and unsymmetrical pincer palladacycles (PdYCY and PdYCY', respectively) and to determine the role of the donor atom (Y, Y' = N, S, or P), on the stability and reactivity of the pincer palladacycles. The nature of the bonding and the strength of the bonds around the Pd centre (Pd-L, L = Y, Y', Cl, C) in the pincer complexes are also determined.

5.3 Computational details

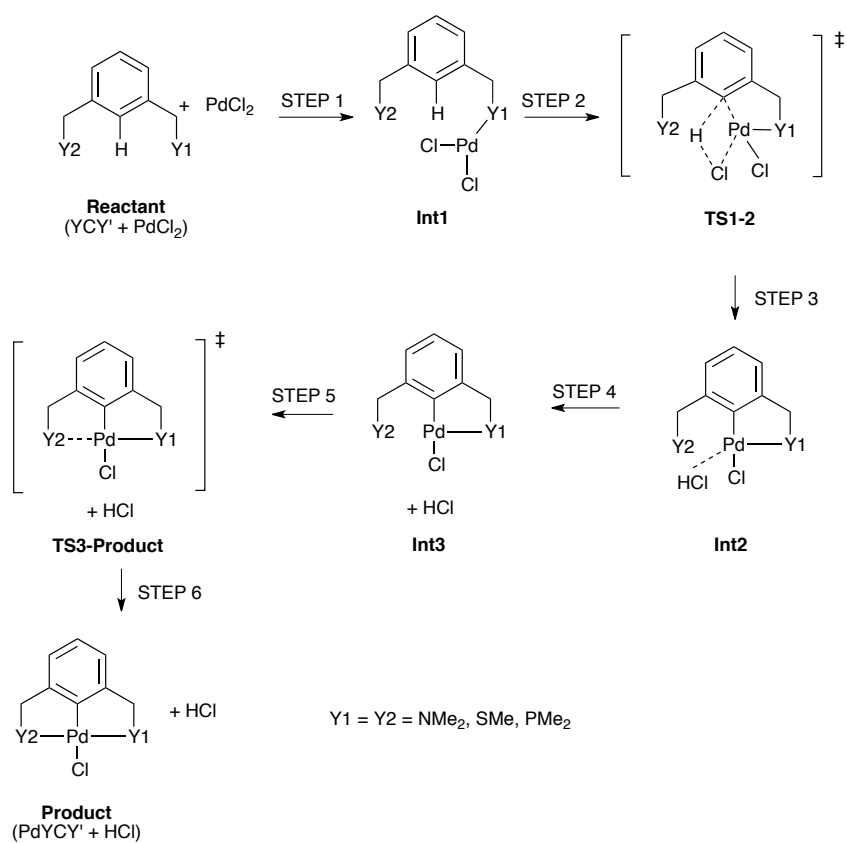
All calculations were performed with the Gaussian09 package.⁸⁷ Geometry optimizations were carried out at the PBE^{45,46}/6-31+G(d,p)[SDD] level of theory. The 6-31+G(d,p) basis set was used for all atoms except Pd for which a Stuttgart/Dresden effective core potential⁵⁷ (SDD ECP) was used. For the ECP, the ECP28MWB⁵⁷ (28 electron in the core) data was used as a multi electron fit using the quasi-relativistic formalism. A single point energy calculation using the ω B97XD⁵³/6-311++G(2df,2p)[SDD] methodology was performed. This functional includes non-covalent interactions that are important to obtain accurate energetics.^{79,134-136} The spin singlet state of the neutral ligands, intermediates, complexes, PdCl₂ and HCl was calculated in all cases. The frequencies were used to confirm stationary points by the presence of one imaginary mode for transition states (TS) and absence of imaginary modes for minimum structures.

A topological analysis of quantum theory of Atoms in Molecules (QTAIM)⁶⁶⁻⁶⁸ was used to carry out investigations into the strength and nature of the bonds around the Pd centre. The ω B97XD/6-311+G(2df,2p)[DGDZVP] methodology was used instead of ω B97XD/6-311+G(2df,2p)[SDD]. The all-electron DGDZVP basis set was used to treat Pd atom because the bond path cannot be found using an ECP.^{68,137} The electron density, $\rho(\mathbf{r})$, the Laplacian of the electron density, $\nabla^2\rho(\mathbf{r})$, and total energy density, $H(\mathbf{r})$, at the bond critical point (BCP) are evaluated using the Multiwfn program.¹³⁸ The $\rho(\mathbf{r})$ at the BCP can be used to measure the strength of the bond. The $\nabla^2\rho(\mathbf{r})$ provides information on the charge accumulation or the charge depletion. The negative value of $\nabla^2\rho(\mathbf{r})$ shows that the charge is accumulated at BCP indicating a shared covalent interaction, whereas the positive value $\nabla^2\rho(\mathbf{r})$ shows that the charge is depleted at BCP indicating a closed-shell interaction (ionic interaction). The $H(\mathbf{r})$ is sum of potential electron energy density, $V(\mathbf{r})$, and kinetic electron energy density, $G(\mathbf{r})$. The sign of $H(\mathbf{r})$ parameter indicates the covalent interaction when $H(\mathbf{r})$ is negative value, while the $H(\mathbf{r})$ parameter indicates ionic interaction if $H(\mathbf{r})$ is positive value.

5.4 Results and discussion

The results for the formation reaction pathway of symmetrical (YCY) and unsymmetrical (YCY') pincer ligands with PdCl₂ calculated using density functional theory (DFT) in the gas phase are presented. Their mechanisms are proposed based on the unassisted mechanism of Pascual *et al.*¹¹⁷ and García-Cuadrado *et al.*¹¹⁸ (Scheme 5.6). The reaction mechanism and Gibbs free energy barriers are studied. In the first step, the donor atom of one of the arms coordinates to Pd atom of PdCl₂. In the first transition state, a Pd-C bond is formed in a concerted process and a C-H bond is activated. Then, the second donor atom arm coordinates to the Pd centre giving the pincer palladacycles, PdYCY' (Y'=Y or Y'≠Y) (Scheme 5.9). All Gibbs free energies presented for the PdYCY and PdYCY' formation pathways are relative to YCY'(Y'=Y or Y'≠Y) + PdCl₂ (i.e. the **Reactant**) in kJ mol⁻¹.

Various ligand conformers were investigated to ascertain whether they have an effect on the formation reaction energy profile. Firstly, the *cis*- and *trans*-ligand conformers are studied (Figure 5.2). We define the position of the N donor atoms in the ligand to be either *cis* in the same direction or *trans* in opposite direction relative to the plane of the benzene ring. The starting conformer is maintained throughout the reaction. The energy profile for PdNCN formation reaction starting from *cis*- and *trans*-form are compared in Figure 5.3. The differences in their energies are insignificant (less than 5.5 kJ mol⁻¹). This result indicates that the ligand conformer has no effect on the reaction energy mechanism profile. Therefore, for studying the effect of donor atom with no biased results, the same conformer of NCN, SCS and PCP ligands are studied. We have used only *trans* conformer ligands.



Scheme 5.9. An unassisted formation reaction pathway for PdYCY. YCY = Pincer ligand, Int = Intermediate, TS = Transition state and PdYCY = Symmetrical pincer palladacycle

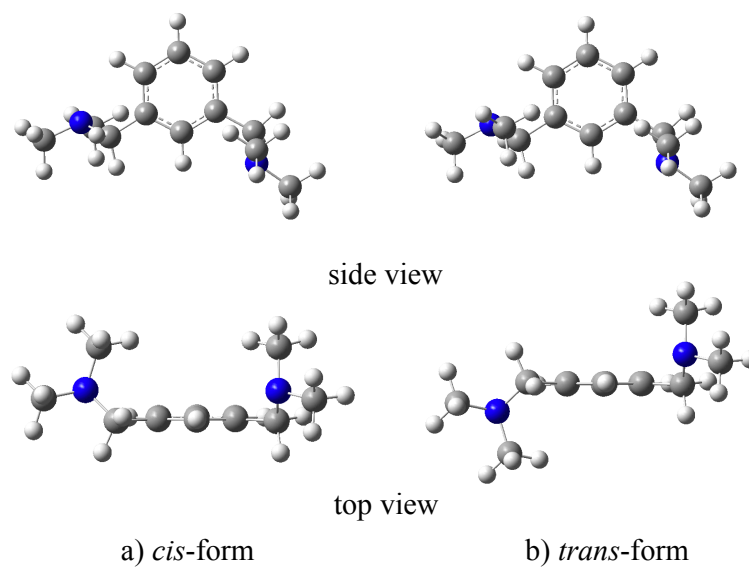


Figure 5.2. NCN ligand conformer; a) *cis*-form and b) *trans*-form.

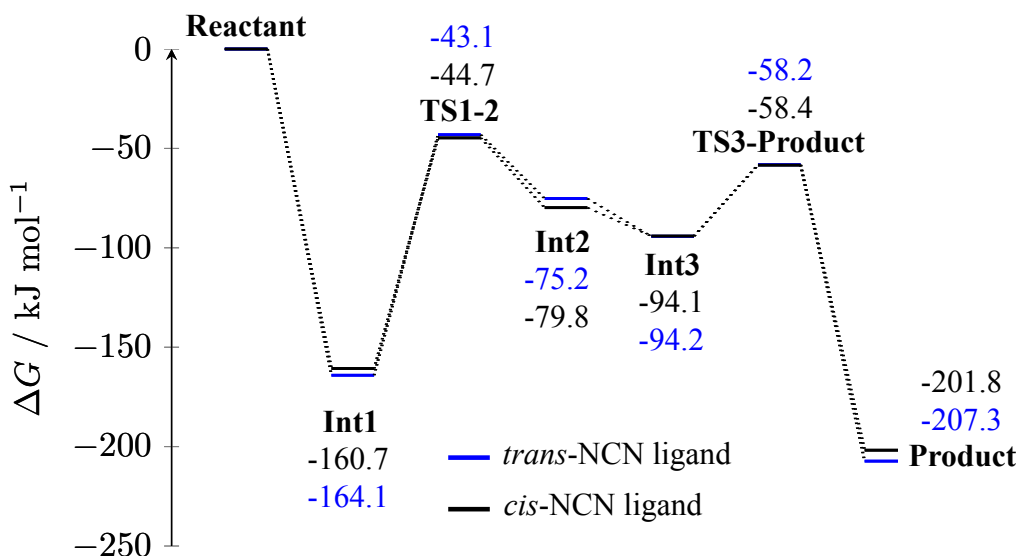


Figure 5.3. Gibbs free energy profile of *trans*-NCN and *cis*-NCN pincer ligands in the gas phase.

5.4.1 Formation reaction of symmetrical pincer palladacycles

The pathway involving the symmetrical pincer palladacycle formation reaction is shown in Scheme 5.9. The first step of the reaction mechanism is that one of the donor atoms (Y1) of the ligand coordinates to PdCl₂ to form **Int1**. Next, a metal-carbon bond is formed in a concerted fashion and a carbon-hydrogen bond is broken to form **Int2** *via* **TS1-2**. HCl is eliminated from the complex leaving **Int3**. Finally, the symmetrical pincer complex is formed *via* **TS3-Product** which involved an inversion configuration for NCN and PCP or a rotation for SCS of the uncoordinated pincer arm to form the Pd-Y2 bond.

The Gibbs free energy profile for the formation reaction pathways of symmetrical NCN, SCS and PCP pincer palladacycles (PdNCN, PdSCS and PdPCP, respectively), with *trans* conformers of the YCY ligands, are presented in Figure 5.4. The stationary points along the reaction pathway are labelled as **Reactant**, **Int1**, **TS1** and **Product** (the **Reactant**, **Int**, **TS** and **Product** stand for YCY + PdCl₂, intermediate, transition state and PdYCY + HCl, respectively). In the discussion to follow, N, S and P are appended to the named of each part along their reactions, e.g. **Int1N** for Intermediate 1 of the NCN pathway. The key bond distances in each step are shown in Table 5.1. The optimised geometry of each stationary point along the pathways for PdNCN, PdSCS and PdPCP is shown in Figure 5.5, Figure 5.6 and Figure 5.7,

respectively.

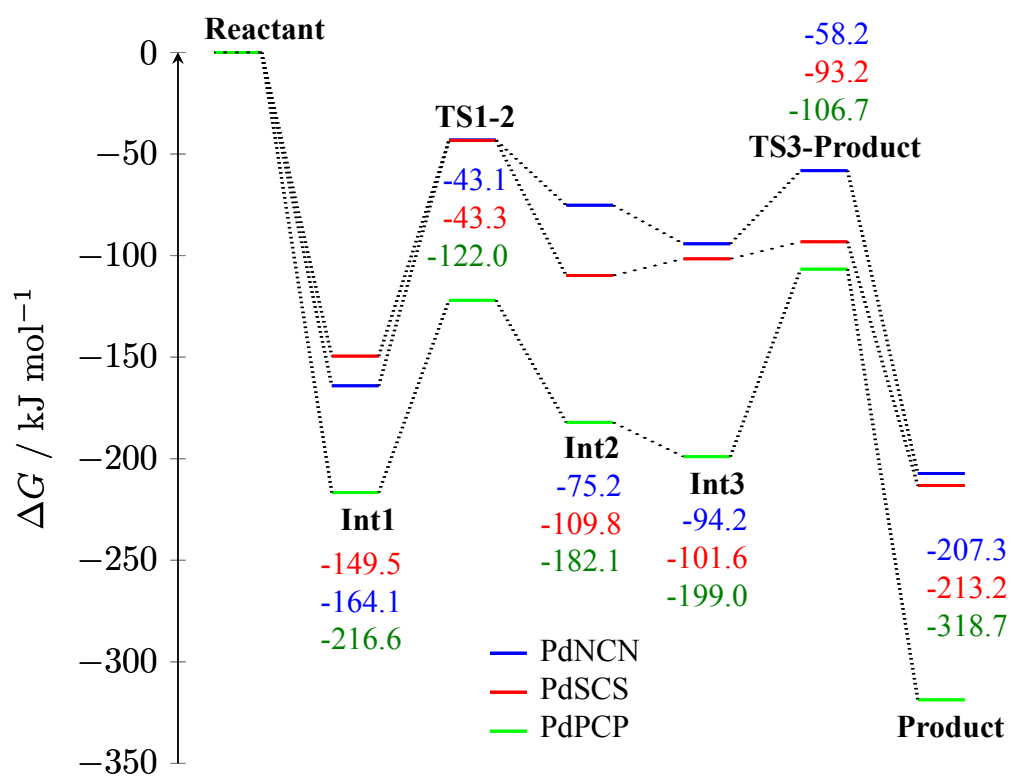


Figure 5.4. Gibbs free energy profile for the formation reaction pathway of symmetrical NCN, SCS and PCP pincer palladacycles (PdNCN, PdSCS and PdPCP, respectively).

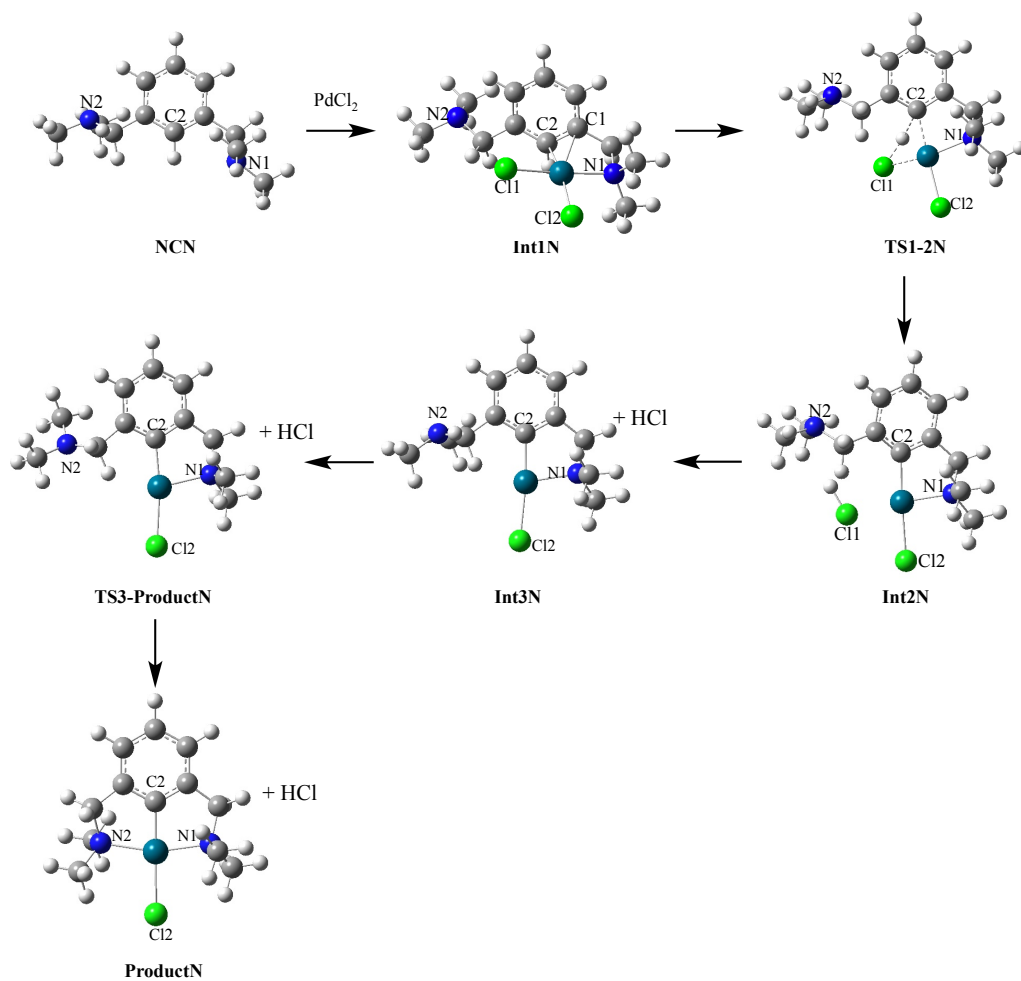


Figure 5.5. Optimised geometry of each stationary point along the PdNCN formation reaction pathway (grey = C, white = H, green = Cl, green/blue = Pd and blue = N).

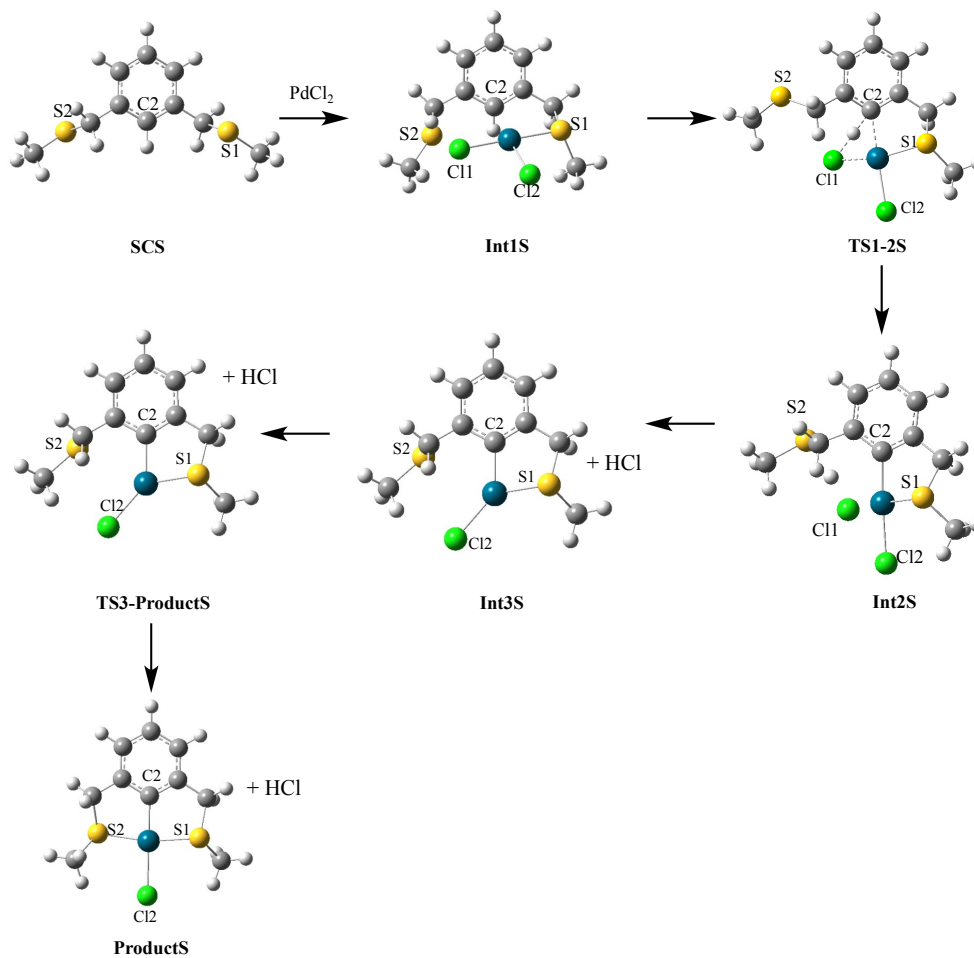


Figure 5.6. Optimised geometry of each stationary point along the PdSCS formation reaction pathway (grey = C, white = H, green = Cl, green/blue = Pd and yellow = S).

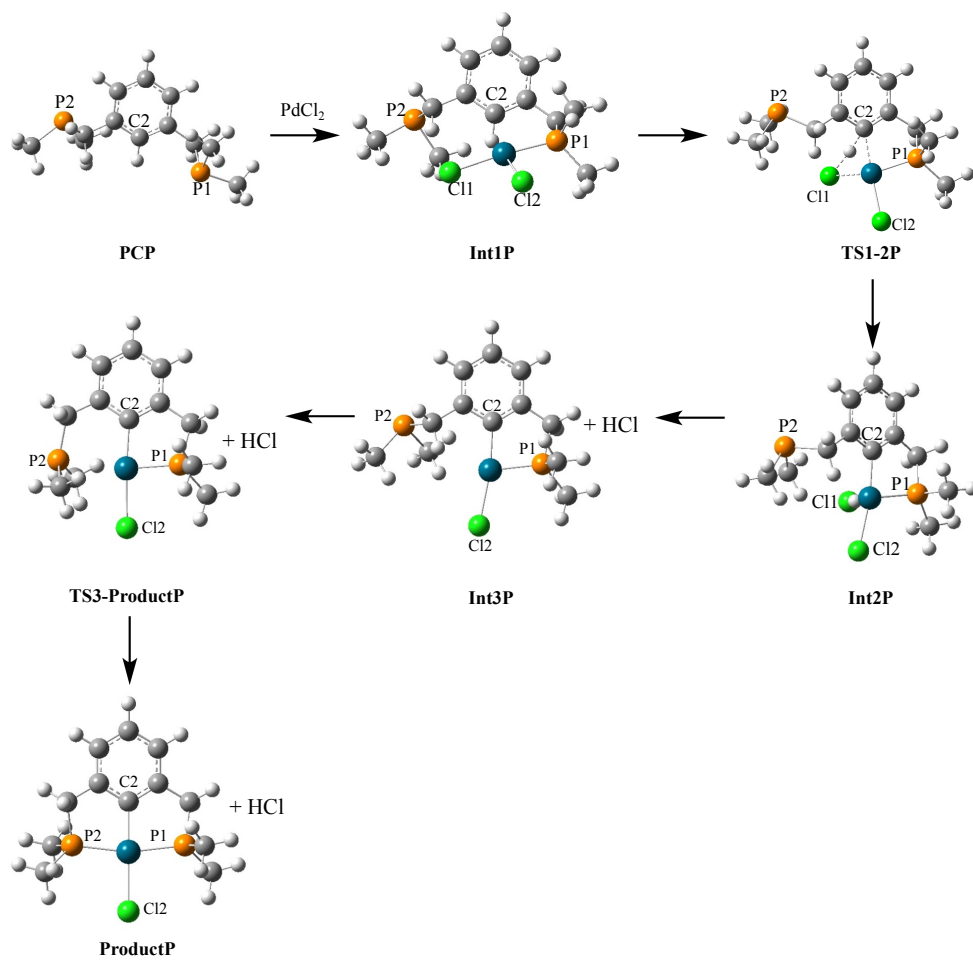


Figure 5.7. Optimised geometry of each stationary point along the PdPCP formation reaction pathway (grey = C, white = H, green = Cl, green/blue = Pd and orange = P).

In the first step (STEP 1, Scheme 5.9), one donor atom coordinates to PdCl₂ directly. The Gibbs free energy for donor atom binding to PdCl₂ (YCY + PdCl₂ → YCY--PdCl₂ (**Int1**)) is negative indicating this step is spontaneous. The formation of **Int1** is exergonic by -149.5, -164.1 and -216.6 kJ mol⁻¹ for SCS, NCN and PCP ligands, respectively (Figure 5.4). The significant change in the Gibbs free energy of this step suggests the possibility of additional steps, such as solvent coordination to PdCl₂ prior to it coordinating to the ligand. However, the simplest way to model this step is by the direct ligand coordination to PdCl₂. In an earlier report of phosphine binding to Pd, they found a strong interaction between Pd and phosphine due to a view of π back-donation.⁹⁵ This interaction occurs from d _{π} -d _{π} overlap involving occupied palladium d orbital into an empty d orbital on phosphorus. The traditional Pd-P overlapping orbital diagram is shown in (Figure 5.8).¹³⁹ However, Orpen and Connelly¹³⁹ modified the traditional Pd-P diagram and reported that the back-donation occurred from mixing of P-R phosphine σ^* and d orbital overlapping to provide π -acceptor hybrid orbital. In our results, the phosphorus arm binds strongly to PdCl₂, for the same reason Pd is stabilised by the lone-pair on the P and π back-donation leading to the most stability. We have found that the **Int1** for N coordination to Pd is more favourable than S. This is attributed to the π donor and π^* -acceptor in the double bond on benzene stabilising PdCl₂ leading to a strong interaction between PdCl₂ and ligand. Figure 5.9 reveals the molecular orbital **Int1**. The d-orbital on Pd in **Int1N** have more electron density than d-orbital on Pd in **Int1S**, showing that **Int1N** has a stronger overlap with benzene than in **Int1S**, and the bond distance between the Pd and C2 in **Int1N** is shorter than in **Int1S** (Table 5.1).

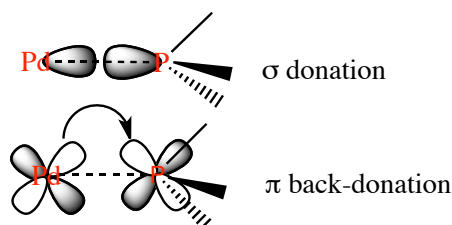


Figure 5.8. Traditional orbital of metal-P interaction. Upper figure is σ donation and π back-donation.¹³⁹

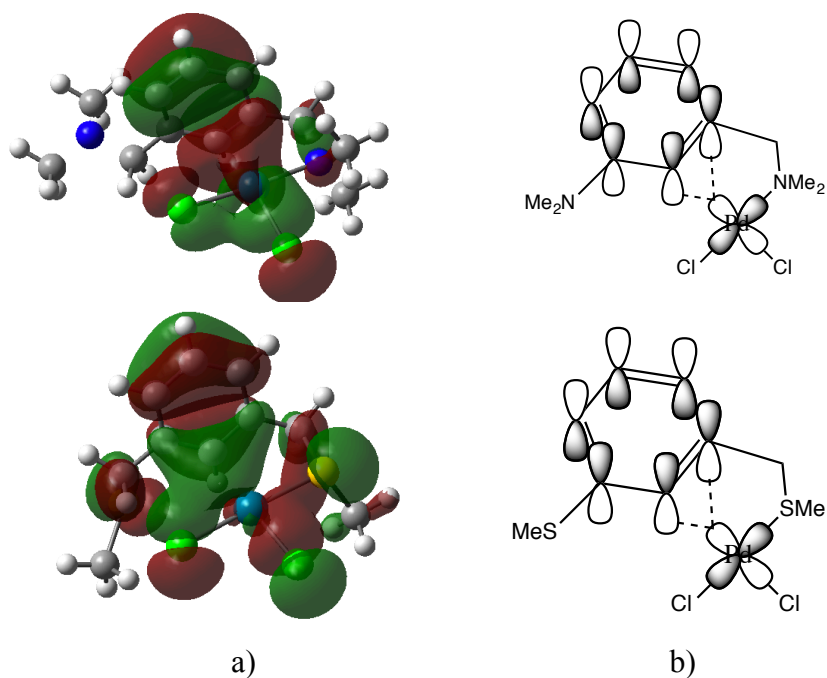


Figure 5.9. Molecular orbital showing the Pd overlap with the benzene ring; a) **Int1N** and b) **Int1S**.

In the next step (STEP 2, Scheme 5.9), the C-H bond of the benzene ring is activated and Pd inserts *via* this concerted mechanism of **TS1-2**. The calculations of **TS1-2** show that the Gibbs free energy barriers are 121.0, 106.2 and 94.6 kJ mol⁻¹ for PdNCN, PdSCS and PdPCP processes, respectively (Table 5.2) indicating that C-H bond breaking *via* PCP process is easier than SCS and NCN pathways. Considering the selected bond distance at **TS1-2**, Pd forms a bond with the C2 on the benzene ring and Cl1 forms a bond with H (Figure 5.5 - Figure 5.7). Intramolecular distances for both Pd-C2 and H-Cl1 decrease compared to **Int1**. At the same time, the bond length of both C2-H and Pd-Cl1 increase. These data indicate that the Pd-C2 bond and H-Cl1 are forming (Table 5.1).

In **Int2**, the complexes are stabilised by HCl. The Pd can coordinate with either the H or the Cl of the HCl molecule. A BCP between Pd and ClH (for N and S), and Pd and HCl are shown in Figure 5.10. The Gibbs free energy of **Int2P** is the lowest because the lone-pair donor and π -acceptor in phosphine plays a role in stabilising Pd, while **Int2N** and **Int2S** have only lone-pair donors. Moreover, **Int2S** has a lower Gibbs free energy than **Int2N** because, in **Int2S**, the HCl binds to S2 and

Pd with the stronger interactions, $\rho(\mathbf{r})_{\text{Cl-Pd}} = 0.060$ a.u. and $\rho(\mathbf{r})_{\text{H-S}_2} = 0.087$ a.u. (Figure 5.10b), while in **Int2N** HCl binds to palladium complex with the weaker interactions, $\rho(\mathbf{r})_{\text{Cl-Pd}} = 0.057$ a.u., $\rho(\mathbf{r})_{\text{Cl-H}} = 0.011$ a.u. and $\rho(\mathbf{r})_{\text{H-H}} = 0.018$ a.u. (Figure 5.10a). Moreover, in **Int2S**, HCl stabilises the structure but, in addition the softer S prefers binding to soft Pd rather than N binding to Pd.

In STEP 4 (Scheme 5.9), the HCl is removed from the complex. The Gibbs free energies for **Int2** to **Int3** are -19.0, 8.2, -16.9 kJ mol⁻¹ for NCN, SCS and PCP, respectively (Figure 5.4). The Gibbs free energy is negative in NCN and PCP processes leading to a favourable spontaneous process, while the Gibbs free energy in the SCS process is slightly positive. We have determined the enthalpy change of this step. These are endothermic processes of 27.6, 56.7, 21.8 kJ mol⁻¹, respectively. The effect is to eliminate the interaction between complex and HCl.

STEPS 5 and 6 (Scheme 5.9) are the formation of the bond between the second donor atom of Y2 and Pd. To form this bond, **TS3-Product** shows that N and P coordination to Pd involve N and P inversion of configuration, respectively, whereas S coordination to Pd involves a rotation of the ligand arm. The P inversion leads to production of PdPCP with a Gibbs free energy barrier 92.3 kJ mol⁻¹, i.e. a higher Gibbs free energy barrier than N inversion (36.0 kJ mol⁻¹). We have found that the activation of N inversion of N(CH₃)₃ calculated by Kölmel *et al.*¹⁴⁰ has a significantly smaller energy barrier than P inversion in P(CH₃)₃. The energy barriers for N(CH₃)₃ and P(CH₃)₃ are 38.4 kJ mol⁻¹ and 185.6 kJ mol⁻¹, respectively. Moreover, Montgomery¹⁴¹ mentioned that the energy barrier for amine is in the range round 20 to 40 kJ mol⁻¹, whereas phosphine inversion normally requires in excess of 125 kJ mol⁻¹. His statement showed that phosphorus inversion had a significantly higher energy barrier than nitrogen inversion. Again, our calculation for phosphorus inversion has a significantly higher Gibbs free energy than for nitrogen inversion in agreement with Montgomery's statement and Kölmel *et al.*'s work. The **TS3-Product** for S has very small barrier (8.4 kJ mol⁻¹) compared to **TS3-ProductN** and **TS3-ProductP** because the second Y2 arm for S rotates to bond with Pd (no inversion configuration).

The ΔG for the formation reaction of PdYCY (Figure 5.11) are -207.3, -213.2 and -318.7 kJ mol⁻¹ for PdNCN, PdSCS and PdPCP, respectively. The results show

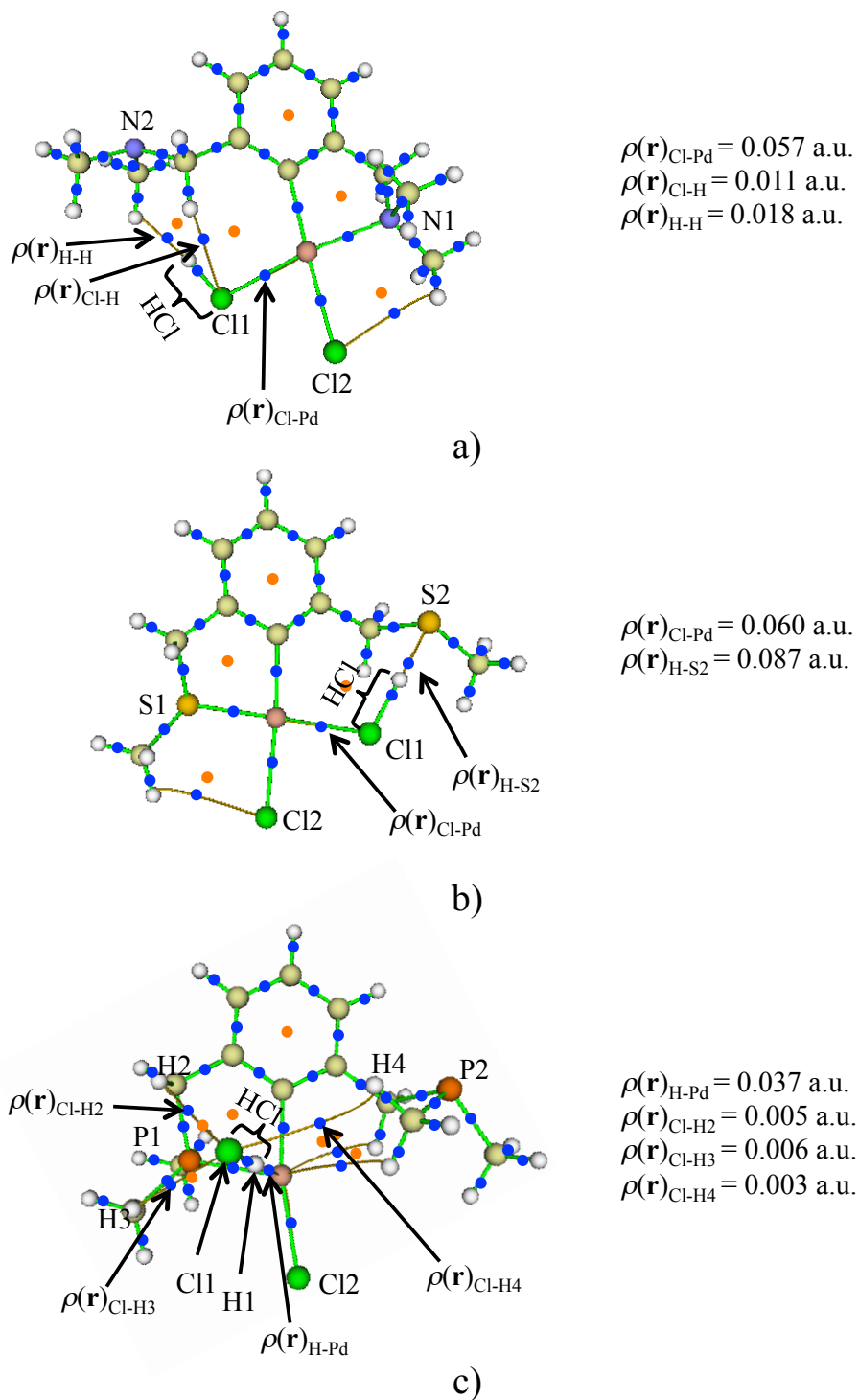


Figure 5.10. Molecular graphs of **Int2**; a) **Int2N**, b) **Int2S** and c) **Int2P**. The BCPs are shown as small blue dots and RCPs are shown as orange dots. In **Int2N** and **Int2S**, the HCl position is on the plane of palladium complex leading to have a few interactions between HCl and palladium complex. While, in **Int2P**, the HCl position is perpendicular to Pd complex leading to more interactions between H ($-\text{CH}_3/-\text{CH}_2-$) and Cl (HCl).

clearly that the ΔG values are negative for all reactions indicating the formation reaction of the symmetrical pincer palladacycles in the gas phase *via* this mechanism is spontaneous. The formation of P-donor pincer palladacycles is the most favourable. For NCN and SCS ligands, the reaction energy is much smaller (difference < 5.9 kJ mol⁻¹). The reaction trends of the symmetrical pincer palladacycles under thermodynamic control are PdPCP $>$ PdSCS \approx PdNCN. The ΔG^\ddagger along the symmetrical pathways of all cases show that the C-H bond activation has the highest barrier indicating that the C-H bond activation is the rate-determining step (Table 5.2).

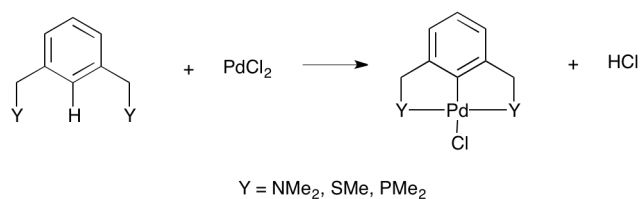


Figure 5.11. Model formation reaction of palladacycles from PdCl₂.

Table 5.1. Key structure data along pathway of PdYCY formation.

YCY	Bond type	Bond distance/Å					
		Int1	TS1-2	Int2	Int3	TS3-Product	Product
NCN	Pd-C2	2.384	2.070	2.027	1.952	1.954	1.930
	Pd-Cl1	2.307	2.490	2.456	∞	∞	∞
	Pd-Cl2	2.308	2.353	2.413	2.375	2.370	2.424
	Pd-N1	2.140	2.116	2.101	2.108	2.108	2.140
	Pd-N2	5.474	4.926	4.778	4.034	4.085	2.141
	Pd-H	2.675	1.799	3.124	∞	∞	∞
	C2-H	1.098	1.768	3.408	∞	∞	∞
	H-Cl1	3.772	1.508	1.316	1.293 ^a	1.293 ^a	1.293 ^a
SCS	Pd-C2	2.455	2.101	2.044	2.002	1.993	1.993
	Pd-Cl1	2.307	2.495	2.394	∞	∞	∞
	Pd-Cl2	2.312	2.341	2.448	2.288	2.318	2.402
	Pd-S1	2.323	2.292	2.279	2.298	2.253	2.313
	Pd-S2	4.614	4.944	4.361	4.464	3.779	2.313
	Pd-H	2.492	1.880	3.160	∞	∞	∞
	C2-H	1.102	1.618	3.254	∞	∞	∞
	H-Cl1	3.565	1.518	1.467	1.293 ^a	1.293 ^a	1.293 ^a
PCP	Pd-C2	2.500	2.113	2.018	2.010	2.010	2.032
	Pd-Cl1	2.346	2.654	3.459	∞	∞	∞
	Pd-Cl2	2.308	2.332	2.334	2.346	2.418	2.402
	Pd-P1	2.251	2.211	2.200	2.186	2.215	2.287
	Pd-P2	5.230	5.167	4.288	4.180	2.798	2.287
	Pd-H	2.051	1.882	2.108	∞	∞	∞
	C2-H	1.127	1.530	2.902	∞	∞	∞
	H-Cl1	3.082	1.574	1.357	1.293 ^a	1.293 ^a	1.293 ^a

^aThe bond distance for HCl calculation.

The calculation data of bond length for HCl using PBE with high basis set (cc-pCVTZ) from the NIST website is 1.289 Å (<http://cccbdb.nist.gov/geom2.asp>).

Table 5.2. Gibbs free energy barrier, ΔG^\ddagger for symmetrical pincer palladacycles in kJ mol^{-1} .

Compound	ΔG^\ddagger (TS1-2)	ΔG^\ddagger (TS3-Product)
PdNCN	121.0	36.0
PdSCS	106.2	8.4
PdPCP	94.6	92.3

5.4.2 Formation reaction of unsymmetrical pincer palladacycles

Unsymmetrical NCS pincer palladacycle (PdNCS) formation reaction: there are two possible mechanisms for PdNCS formation; N coordination to Pd first or S coordination to Pd first (Figure 5.12). The stationary points along the reaction pathways are labelled with the suffix, **NCS** when N is first coordinated to Pd (**Path A**), and **SCN** when S is first coordinated to Pd (**Path B**). For example, intermediate 1 along **Path A** is labelled **Int1NCS**. The key bond distance in each step is shown in Table 5.3.

Figure 5.13 and Figure 5.14 show the geometries along the two pathways, **Path A** and **Path B**, respectively. In the first step, the NCS pincer ligand bonds with PdCl₂. The Gibbs free energy for NCS + PdCl₂ → **Int1** is -160.2 kJ mol⁻¹ for **Int1NCS** (blue pathway in Figure 5.15) and -147.4 kJ mol⁻¹ for **Int1SCN** (red pathway in Figure 5.15). Therefore, both **Path A** and **Path B** are spontaneous favourable processes in this step.

The next step is formation of the C-H bond activation transition state. The calculation of **TS1-2NCS** shows that the Gibbs free energy barrier is 117.0 kJ mol⁻¹ and **TS1-2SCN** is 100.2 kJ mol⁻¹. This result indicates that the Pd of the unsymmetrical pincer favours **Path A** more than **Path B** because **Int1NCS** is more stable than **Int1SCN**. The key structural data (Table 5.3) show the Pd-C2 bond distance at **TS1-2** of both **Path A** and **Path B** are shorter compared to **Int1**, while in both cases the C2-H distance is longer than the C2-H distance in **Int1**. It indicates that the Pd-C2 bond is forming and the C2-H bond is breaking to generate HCl (Table 5.3).

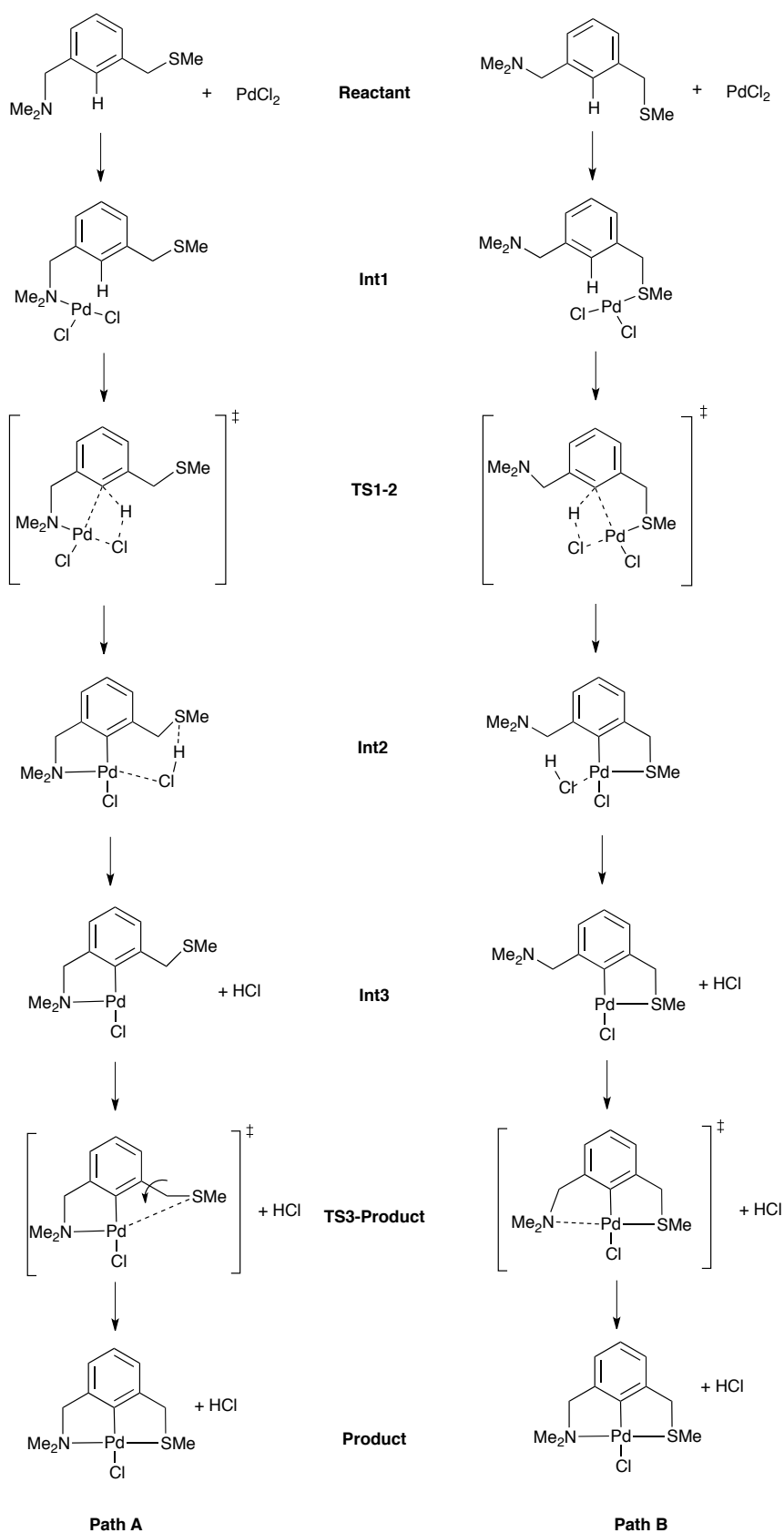


Figure 5.12. An unassisted formation reaction pathway for unsymmetrical NCS pincer palladacycle (PdNCS); **Path A** is N coordination to Pd first and **Path B** is S coordination to Pd first (**Reactant** = pincer ligand (YCY') + PdCl_2 , **Int** = Intermediate, **TS** = Transition State and **Product** = palladacycle (PdYCY') + HCl).

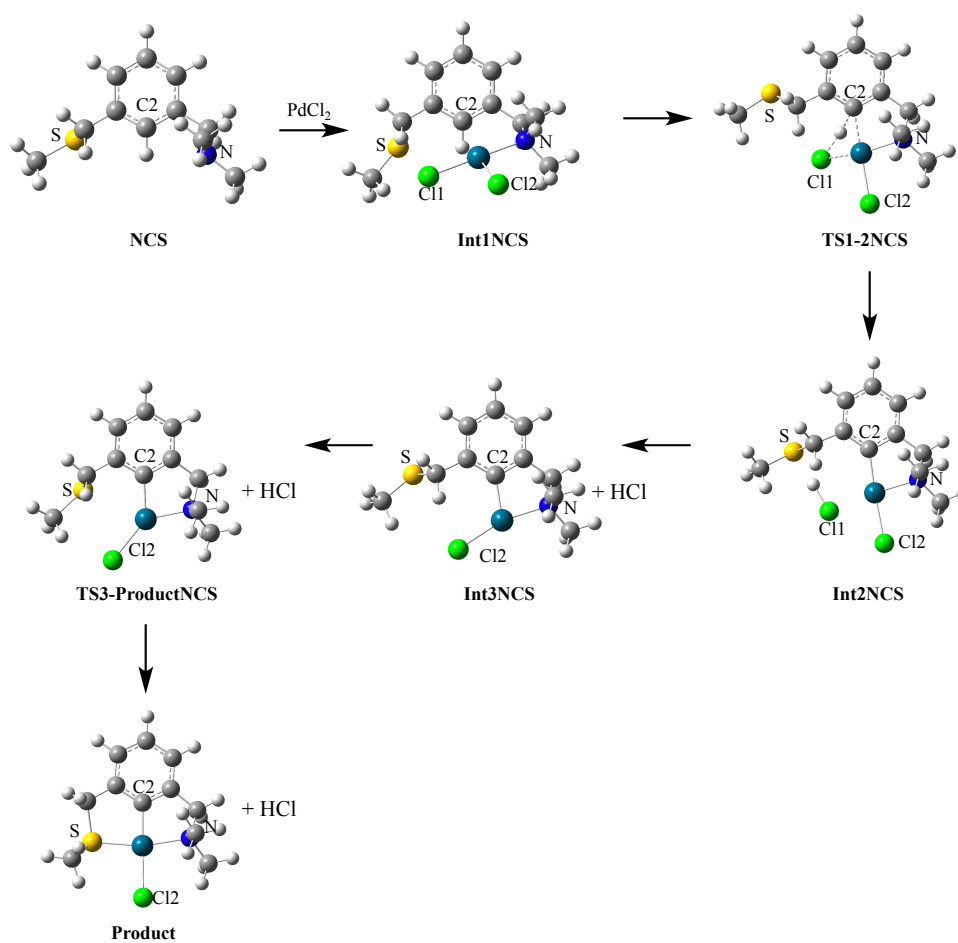


Figure 5.13. Optimised geometry of each stationary point along the PdNCS formation reaction pathway which N coordinates to Pd first (**Path A**) (grey = C, white = H, green = Cl, green/blue = Pd, blue = N and yellow = S).

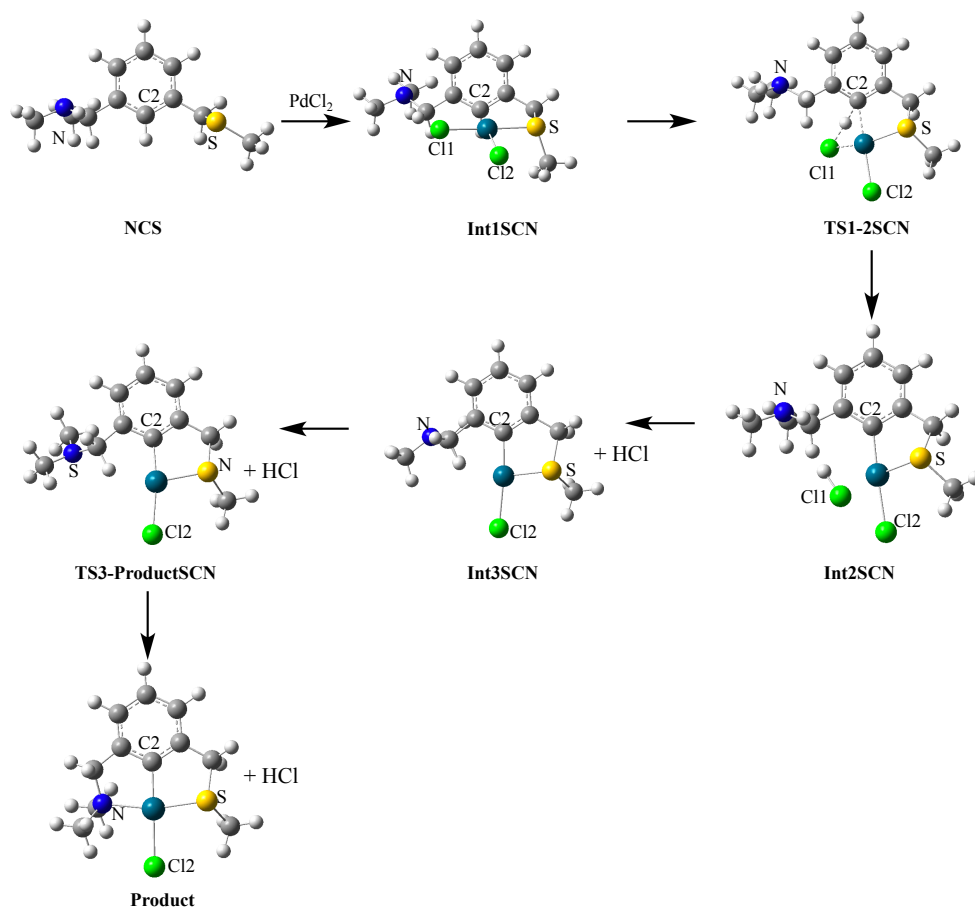


Figure 5.14. Optimised geometry of each stationary point along the PdNCS formation reaction pathway which S coordinates to Pd first (**Path B**) (grey = C, white = H, green = Cl, green/blue = Pd, blue = N and yellow = S).

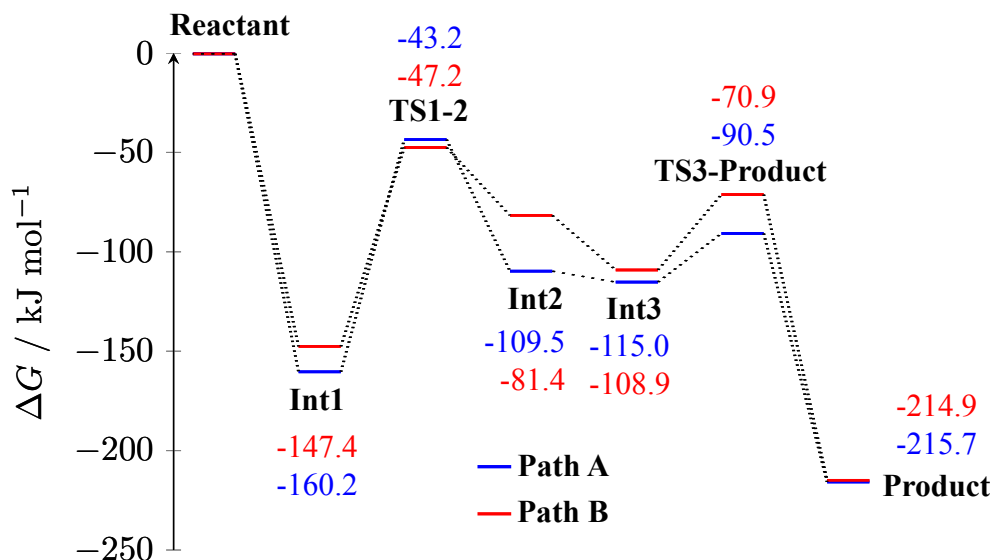


Figure 5.15. The formation reaction mechanism profile of PdNCS. **Path A** corresponding to the blue pathway represents the N coordination first to the Pd atom while **Path B** corresponding to the red pathway represents the S coordination first to the Pd atom.

Int2NCS and **Int2SCN** are both stabilised by HCl. The **Int2NCS** shows strong interaction between HCl and palladium complex ($\rho(\mathbf{r})_{\text{Pd-Cl}} = 0.089$ a.u. and $\rho(\mathbf{r})_{\text{H-S}} = 0.067$ a.u., Figure 5.16a), while for **Int2SCN** the HCl interaction is weaker ($\rho(\mathbf{r})_{\text{H-H}} = 0.014$ a.u., $\rho(\mathbf{r})_{\text{Pd-Cl}} = 0.051$ a.u. and $\rho(\mathbf{r})_{\text{Cl-H}} = 0.010$ a.u., Figure 5.16b). This is why the **Int2NCS** is more stable than **Int2SCN** (Figure 5.15 and Figure 5.16).

The HCl is removed from the complex. The Gibbs free energy for these processes are -5.5 and -27.5 kJ mol⁻¹ for **Path A** and **Path B**, respectively. Therefore, both **Int2NCS** \rightarrow **Int3NCS** and **Int2SCN** \rightarrow **Int3SCN** are spontaneous processes. The enthalpies of HCl elimination from the complex of **Int2NCS** \rightarrow **Int3NCS** and **Int2SCN** \rightarrow **Int3SCN** are 40.3 and 13.8 kJ mol⁻¹, respectively. This evidence indicates the HCl binding with the complex in the **Int2NCS** is stronger than in the **Int2SCN**.

The **TS3-Product** is the formation of a bond between the second donor atom and Pd, and reveals that the inversion configuration of nitrogen *via* **Path B** (**TS2SCN** is 38.0 kJ mol⁻¹) has a higher Gibbs free energy than the rotation of the sulfur arm *via* **Path A** (**TS2NCS** is 24.5 kJ mol⁻¹).

Upon comparison between the **TS1-2** and **TS3-Product** for both **Path A** and

Path B, we find that in both cases the **TS1-2** has a higher Gibbs free energy barrier than **TS3-Product**, indicating that the C-H bond activation is the rate-determining step of PdNCS formation. In the rate-determining step, S coordination to Pd first is slightly lower in Gibbs free energy than N coordination first. Moreover, the PdNCS formation reaction is a spontaneous process (ΔG for **Path A** is $-215.7 \text{ kJ mol}^{-1}$ and ΔG for **Path B** is $-214.9 \text{ kJ mol}^{-1}$).

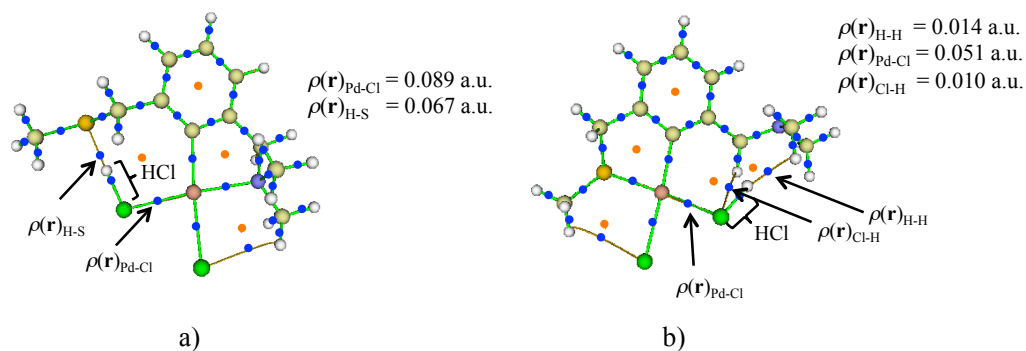


Figure 5.16. Molecular graph of **Int2** for a) **Path A** and b) **Path B**. The BCPs are shown as small blue dots and RCPs are shown as orange dots.

Table 5.3. Key structure data along pathway of PdNCS formation.

Pathway	Bond type	Bond distance/Å					
		Int1	TS1-2	Int2	Int3	TS3-Product	Product
NCS (Path A)	Pd-C2	2.402	2.081	2.030	1.985	1.968	1.963
	Pd-Cl1	2.300	2.442	2.409	∞	∞	∞
	Pd-Cl2	2.302	2.350	2.404	2.277	2.338	2.412
	Pd-N	2.147	2.115	2.110	2.117	2.108	2.156
	Pd-S	4.712	4.943	4.340	4.512	3.442	2.285
	Pd-H	2.078	1.778	3.112	∞	∞	∞
	C2-H	1.124	1.753	3.216	∞	∞	∞
	H-Cl1	3.055	1.535	1.474	1.293 ^a	1.293 ^a	1.293 ^a
SCN (Path B)	Pd-C2	2.447	2.092	2.039	1.973	1.975	1.963
	Pd-Cl1	2.304	2.542	2.512	∞	∞	∞
	Pd-Cl2	2.311	2.342	2.399	2.364	2.358	2.412
	Pd-N	5.315	4.844	4.730	3.939	3.950	2.156
	Pd-S	2.327	2.289	2.269	2.256	2.254	2.285
	Pd-H	2.567	1.899	3.171	∞	∞	∞
	C2-H	1.100	1.613	3.401	∞	∞	∞
	H-Cl1	3.717	1.508	1.311	1.293 ^a	1.293 ^a	1.293 ^a

^aThe bond distance for HCl calculation.

The calculation data of bond length for HCl using PBE with high basis set (cc-pCVTZ) from the NIST website is 1.289 Å (<http://cccbdb.nist.gov/geom2.asp>).

Unsymmetrical SCP pincer palladacycle (PdSCP) formation reaction: This formation reaction has two pathways; either S coordination to Pd first, **Path C**, or P coordination first, **Path D**, (Figure 5.17). Figure 5.18 shows the Gibbs free energy profile for the SCP ligand. The geometric structures of the stationary points along the formation reaction pathway of PdSCP **Path C** and **Path D** are shown in Figure 5.19 and Figure 5.20, respectively.

When PdCl₂ binds to the SCP ligand, the formation of **Int1** is exergonic by -145.5 and -210.3 kJ mol⁻¹ for S coordination first (red pathway, **Path C**) and P coordination first (green pathway, **Path D**), respectively (Figure 5.18).

Int1PCS (green pathway, **Path D**) have a lower Gibbs free energy than **Int1SCP** (red pathway, **Path C**) owing to the π back-donation. From **Int1PCS** \rightarrow **Product** at each stationary point along the pathway, the **Path D** formation has a greater stability than the **Path C** (Figure 5.18).

For both pathways in the next step, the C-H bond activation (**TS1-2**), the Pd-C2 distance at **TS1-2** shortens compared to **Int1**, indicating that the Pd-C bond is formed and the H-Cl1 distance also shortens leading to the formation of the HCl molecule (Table 5.4). On comparing the Gibbs free energy barrier, the P coordination first (**Path D**) has a lower Gibbs free energy barrier than S coordination first (**Path C**). This result is consistent with the findings in earlier symmetrical pincer formation reactions that in the C-H activation transition state PdPCP formation has a lower Gibbs free barrier than PdSCS formation.

Int2 \rightarrow **Int3** involves the removal of HCl. Both **Path C** and **Path D** are spontaneous reactions, where the Gibbs free energy of reaction for this process is -30.8 and -11.3 kJ mol⁻¹ for **Path C** and **Path D**, respectively. When HCl is removed from the complex in **Path C**, an agostic interaction is found in **Int3SCP**. The distance between Pd and H-CH₂-P arm is 1.959 Å, and Pd-H-C angle is 103.2°, and are in the range of an agostic interaction. For an agostic interaction, the distance between metal and hydrogen in the range 1.8 - 2.3 Å and the metal-hydrogen-carbon angle in the range 90 -140°. ¹⁴²

In the **TS3-4** transition state, the C-P rotation is found only for **Path C** with a Gibbs free energy barrier of 51.9 kJ mol⁻¹. In **PathD**, the product is formed directly.

TS3/4-Product involves the other arm coordinating to Pd. For the **TS3-**

product *via* **Int3** (**Path D**), the S arm rotates to coordinate with Pd, while for **TS4-product** *via* **Int4** (**Path C**) the Pd coordinates P through P inversion configuration. The Gibbs free energy barrier for the **TS3-product** *via* S rotation is 9.4 kJ mol^{-1} , which is significantly lower than for the **TS4-product** *via* P inversion configuration (69.4 kJ mol^{-1}).

In overall reaction, the PdSCP formation is the spontaneous process in both pathways ($\Delta G = -275.6 \text{ kJ mol}^{-1}$ for **Path C** and $\Delta G = -269.8 \text{ kJ mol}^{-1}$ for **Path D**). The reaction pathway shows that the C-H bond activation is still the rate-determining step.

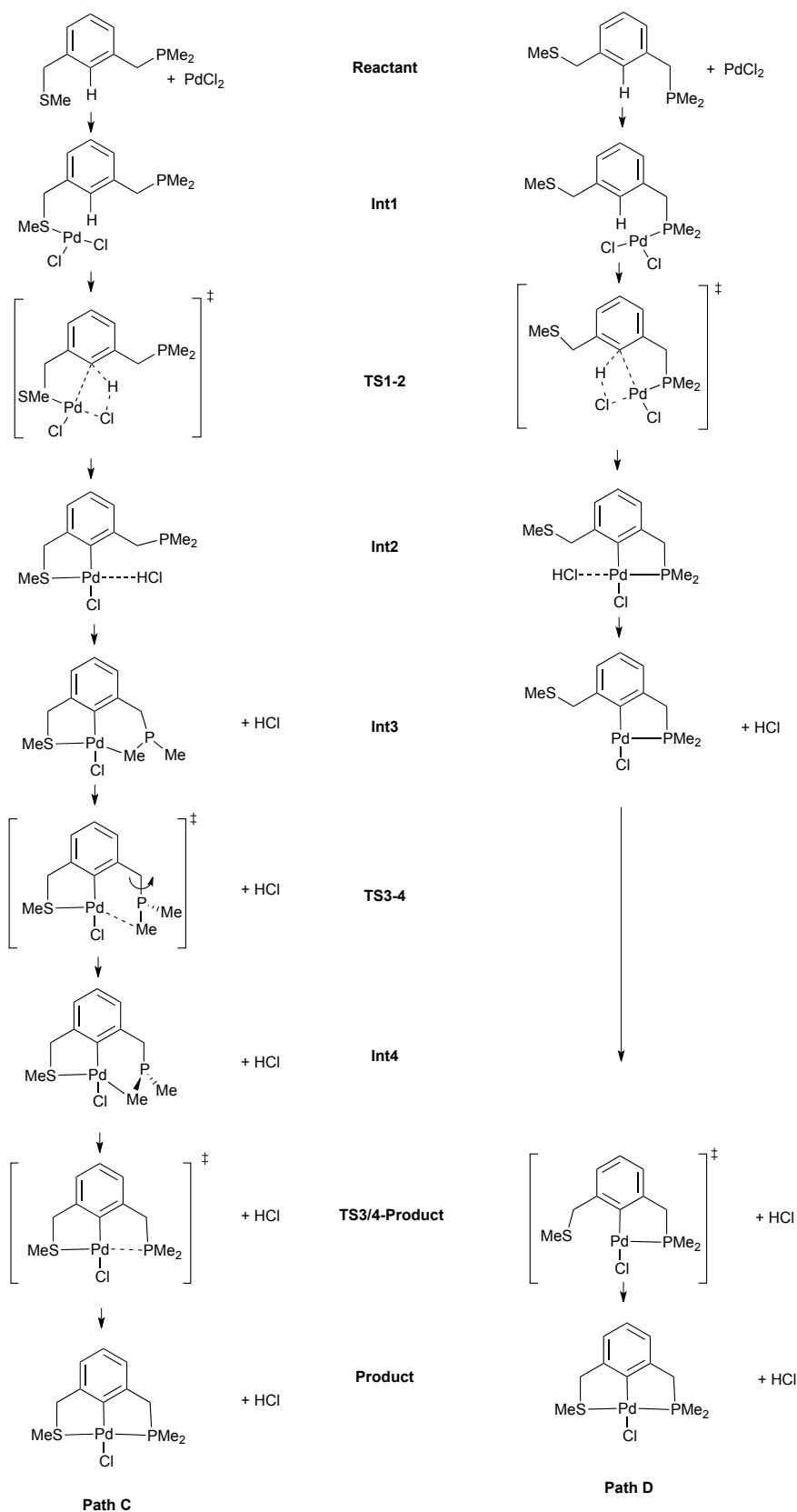


Figure 5.17. An unassisted formation reaction pathway for unsymmetrical SCP pincer palladacycle (PdSCP); **Path C** is S coordination to Pd first and **Path D** is P coordination to Pd first (**Reactant** = pincer ligand (YCY') + PdCl₂, **Int** = Intermediate, **TS** = Transition State and **Product** = palladacycle (PdYCY') + HCl. The Me---Pd represents the agostic Pd---H---CH₂ interaction.

Table 5.4. Key structure data along pathway of PdSCP formation.

Pathway	Bond type	Bond distance/Å									
		Int1	TS1-2	Int2	Int3	TS3-4	Int4	TS3/4-Product	Product		
SCP (Path C)	Pd-C2	2.479	2.089	2.031	2.032	2.055	2.028	1.996	2.010		
	Pd-Cl1	2.308	2.560	2.507	∞	∞	∞	∞	∞		
	Pd-Cl2	2.303	2.344	2.395	2.391	2.394	2.384	2.423	2.402		
	Pd-S	2.329	2.288	2.271	2.269	2.277	2.274	2.274	2.364		
	Pd-P	5.302	5.191	5.133	3.800	3.768	3.787	2.791	2.240		
	Pd-H	2.075	1.910	3.055	∞	∞	∞	∞	∞		
	C2-H	1.123	1.651	3.113	∞	∞	∞	∞	∞		
	H-Cl1	3.010	1.490	1.304	1.293 ^a						
PCS (Path D)	Pd-C2	2.496	2.116	2.020	2.036	n/a	n/a	2.015	2.011		
	Pd-Cl1	2.345	2.641	3.454	∞	n/a	n/a	∞	∞		
	Pd-Cl2	2.309	2.331	2.328	2.379	n/a	n/a	2.344	2.402		
	Pd-S	5.175	5.144	4.357	3.786	n/a	n/a	3.984	2.364		
	Pd-P	2.254	2.213	2.198	2.201	n/a	n/a	2.182	2.240		
	Pd-H	2.025	1.873	2.102	∞	n/a	n/a	∞	∞		
	C2-H	1.129	1.531	2.861	∞	n/a	n/a	∞	∞		
	H-Cl1	3.062	1.577	1.356	1.293 ^a	n/a	n/a	1.293 ^a	1.293 ^a		

^aThe bond distance for HCl calculation.

The calculation data of bond length for HCl using PBE with high basis set (cc-pCVTZ) from the NIST website is 1.289 Å (<http://cccbdb.nist.gov/geom2.asp>).
n/a = not available.

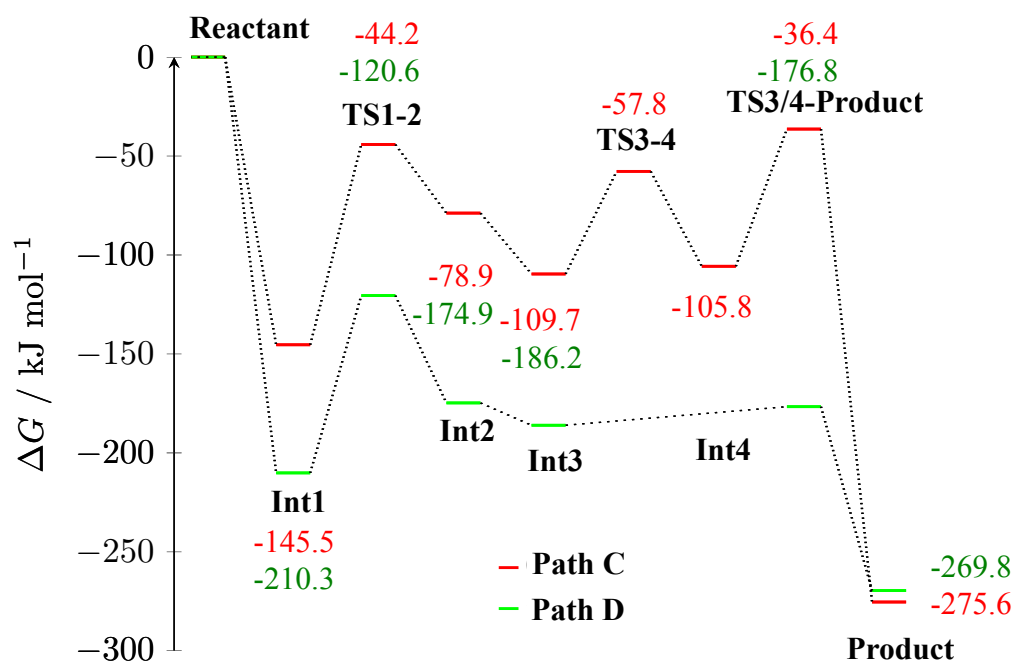


Figure 5.18. The formation reaction mechanism profile of PdSCP. **Path C** corresponding to the red pathway represents the S coordination first to the Pd atom, while **Path D** corresponding to the green pathway represents the P coordination first to the Pd atom.

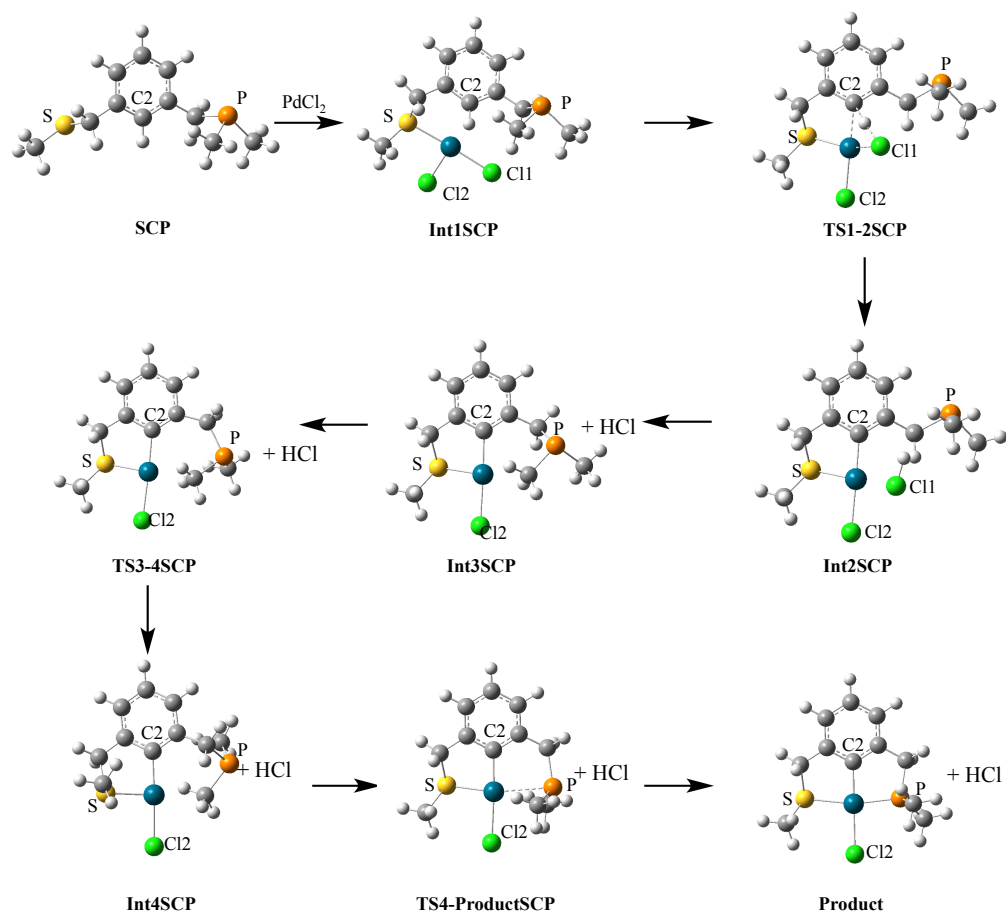


Figure 5.19. Optimised geometry of each stationary point along the PdSCP formation reaction pathway which S coordinates to Pd first (**Path C**) (grey = C, white = H, green = Cl, green/blue = Pd, yellow = S and orange = P).

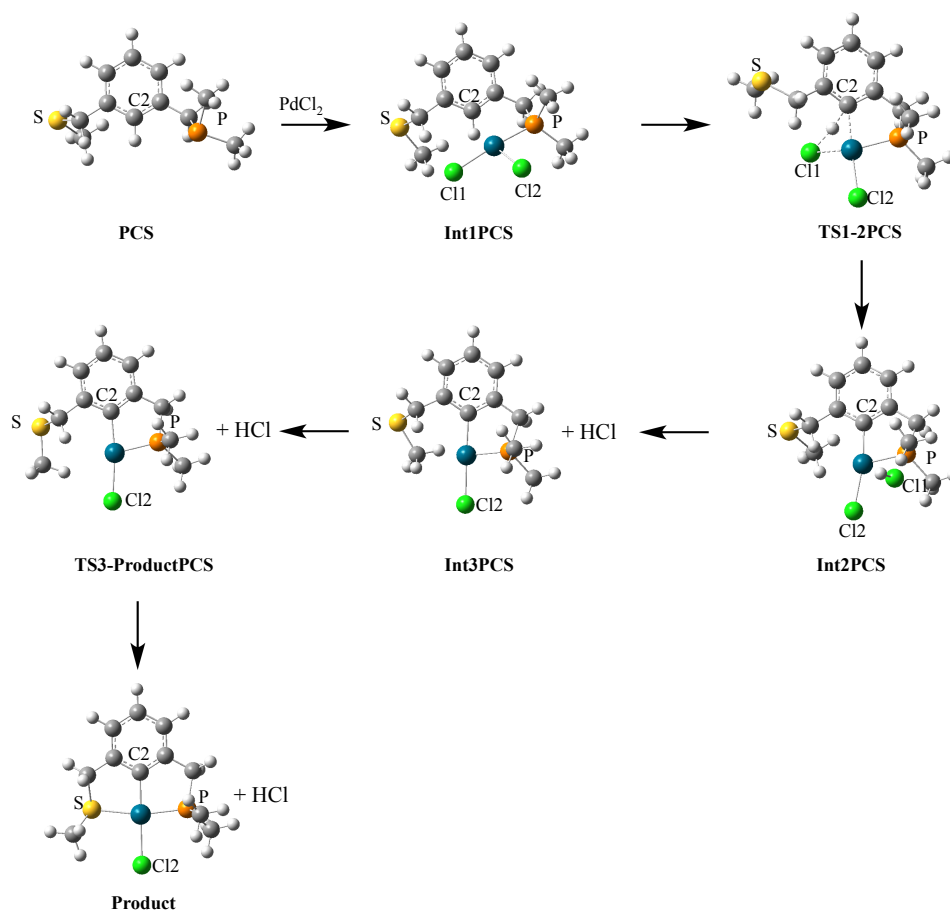


Figure 5.20. Optimised geometry of each stationary point along the PdSCP formation reaction pathway which P coordinates to Pd first (**Path D**) (grey = C, white = H, green = Cl, green/blue = Pd, yellow = S and orange = P).

Unsymmetrical NCP pincer palladacycle (PdNCP) formation reaction: In Figure 5.21, two PdNCP formation reaction mechanism pathways are N coordination to Pd first, as in **Path E**, and P coordination to Pd first as in **Part F**. Figure 5.22 and Figure 5.23 present the geometry of the reaction mechanism for N coordination to Pd first and P coordination to Pd first, respectively.

In the key C-H bond activation step, transition state (**TS1-2**), Pd-C2 and H-Cl1 distances decrease, while Pd-Cl1 and C2-H distances increase compared to **Int1** indicating Pd-Cl1 and HCl are formed in this step (Table 5.5). Considering the transition barrier in this step, the Gibbs free energy barrier for **Path F** (green pathway) is lower than **Path E** (blue pathway) (ΔG^\ddagger for **Path F** and **Path E** are 90.8 and 120.1 kJ mol⁻¹, respectively). This indicates that P coordination to Pd first is more favourable than N coordination first.

Int2 then undergoes dissociation to form HCl and the palladium complex (**Int3**). The Gibbs free energies for this process are -46.2 and -17.3 kJ mol⁻¹ for **Path E** and **Path F**, respectively. This shows that **Int2** → **Int3** (both **Path E** and **Path F**) represent the spontaneous process.

TS3-4 for **Path E** and **TS3-5** for **Path F** concern a C-C bond rotation, with both the barriers very similar (25.2 kJ mol⁻¹ for **Path E** and 26.6 kJ mol⁻¹ for **Path F**). From this point, **Path E** and **Path F** have different numbers of steps to form **PdNCP**. In **Path E**, an agostic interaction is found in **Int4** (the Pd-H distance and Pd-H-C angle are 1.880 Å and 102.7°, respectively). A rotation of the C-P bond occurs in **TS4-5** with Gibbs free energy barrier 38.9 kJ mol⁻¹. The agostic interaction is preserved in **Int5** with P now in position to coordinate with Pd. Whereas, in the **Path F** after **TS3-5** transition state, **Int5** is produced directly. An agostic interaction between Pd and H of MeN arm of **Int5** for **Path F** is found (the Pd-H distance is 1.878 Å and Pd-H-C angle is 116.2°).

In the last step, the second arm donor atom coordinates to the Pd centre to form **PdNCP**. On comparing the Gibbs free energy barrier of **TS5-Product** between **Path E** and **Path F**, **Path F** which involves N inversion ($\Delta G^\ddagger = 26.2$ kJ mol⁻¹) is more favourable than **Path E** which involves P inversion ($\Delta G^\ddagger = 67.8$ kJ mol⁻¹).

In the overall reaction pathways, C-H bond activation has the highest Gibbs free energy barrier in both cases (**Path E** and **Path F**) for **PdNCP** formation, indicating that this step is rate-determining.

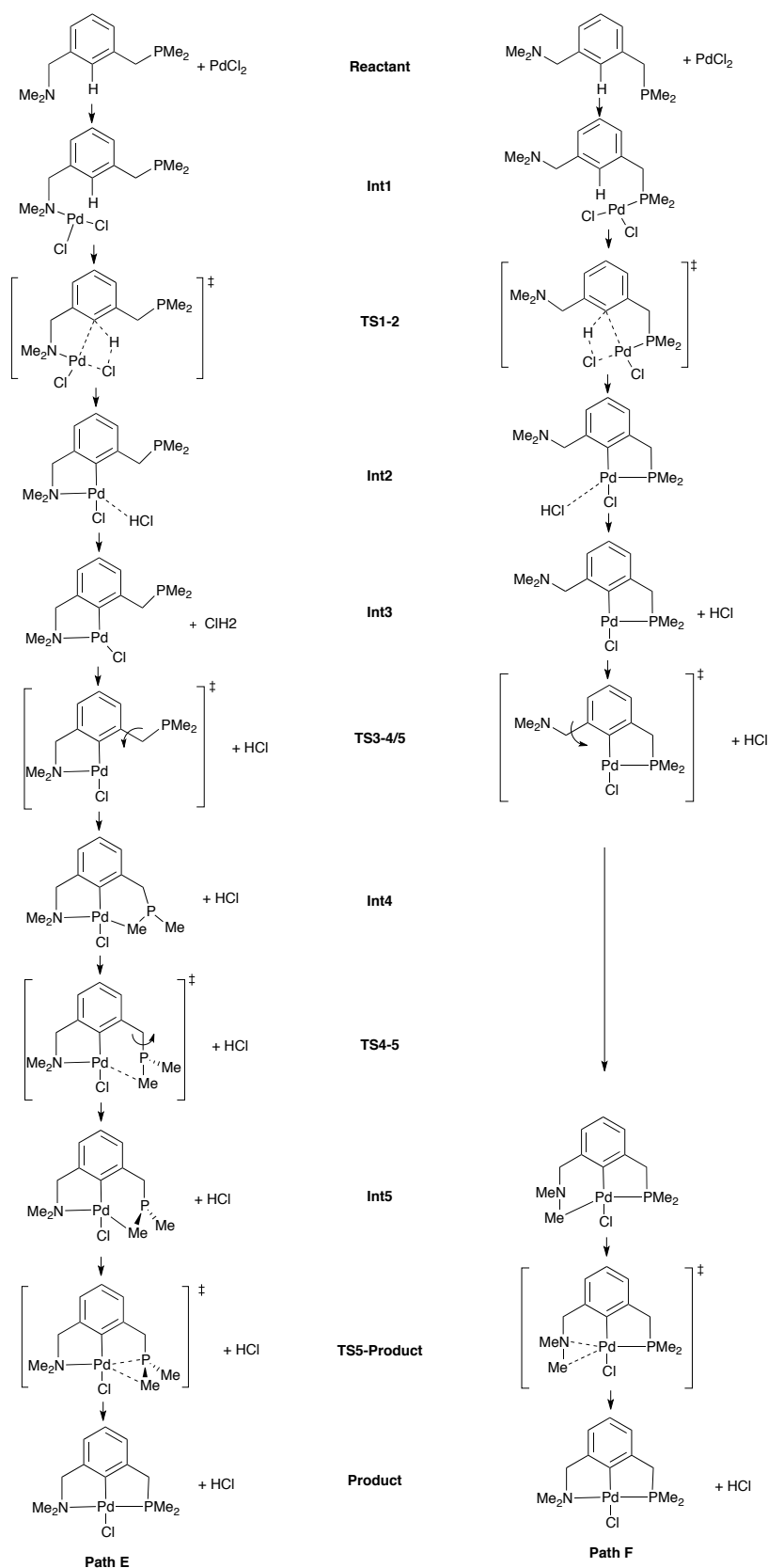


Figure 5.21. An unassisted formation reaction pathway for unsymmetrical NCP pincer palladacycle (PdNCP); **Path E** is N coordination to Pd first and **Path F** is P coordination to Pd first (**Reactant** = pincer ligand (YCY') + PdCl₂, **Int** = Intermediate, **TS** = Transition State and **Product** = palladacycle (PdYCY') + HCl. The Me---Pd represents the agostic Pd---H-CH₂ interaction.

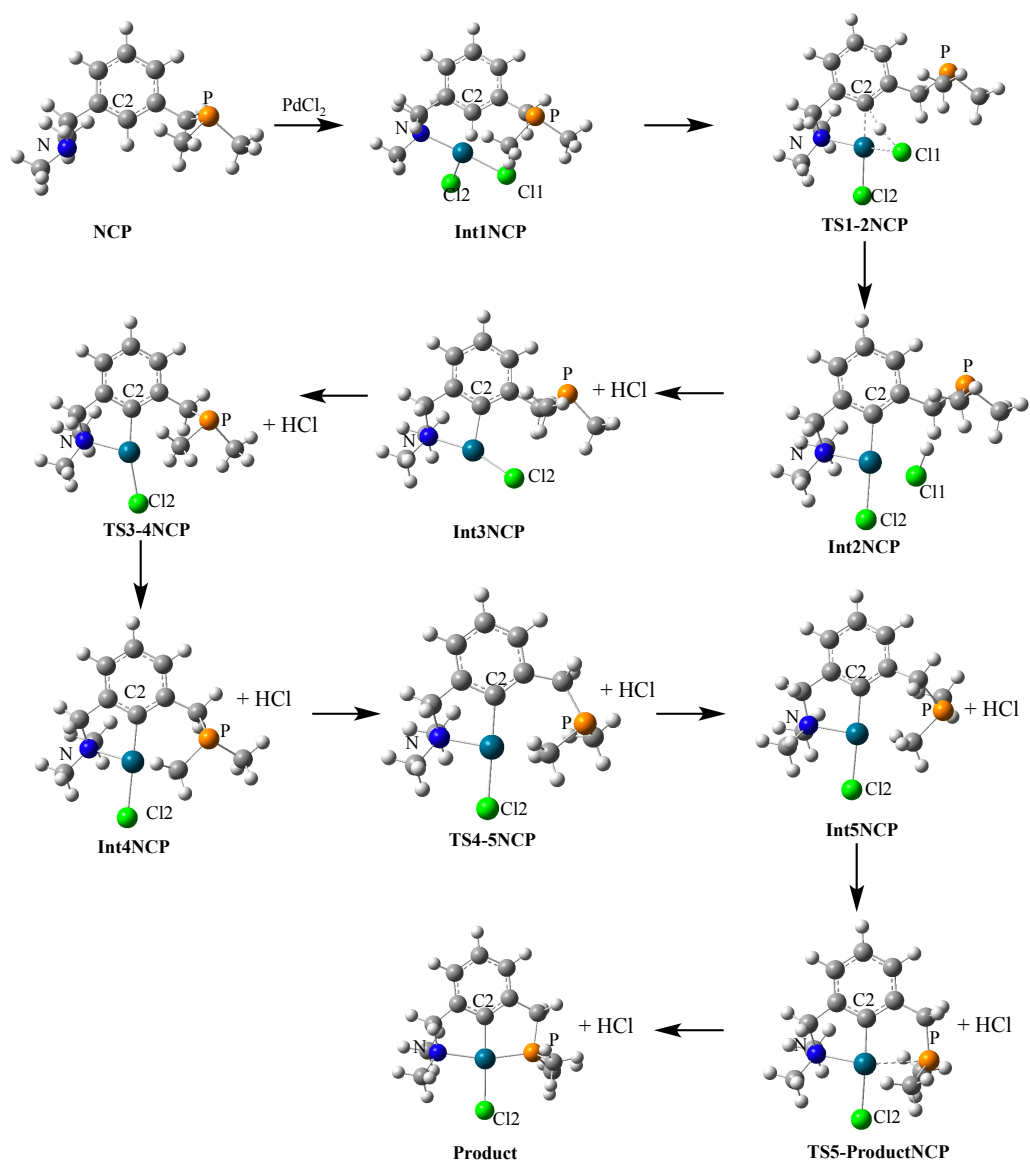


Figure 5.22. Optimised geometry of each stationary point along the PdNCP formation reaction pathway which N coordinates to Pd first (**Path E**) (grey = C, white = H, green = Cl, green/blue = Pd, blue = N and orange = P).

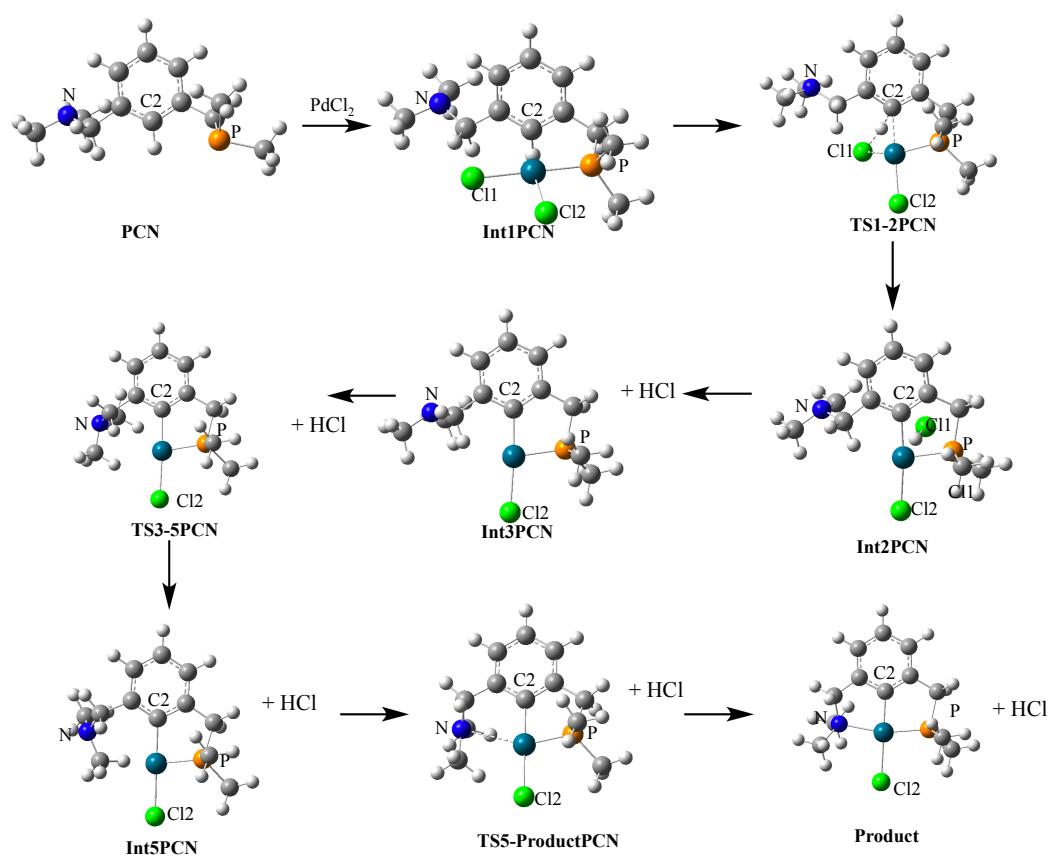


Figure 5.23. Optimised geometry of each stationary point along the PdNCP formation reaction pathway which S coordinates to Pd first (**Path F**) (grey = C, white = H, green = Cl, green/blue = Pd, blue = N and orange = P).

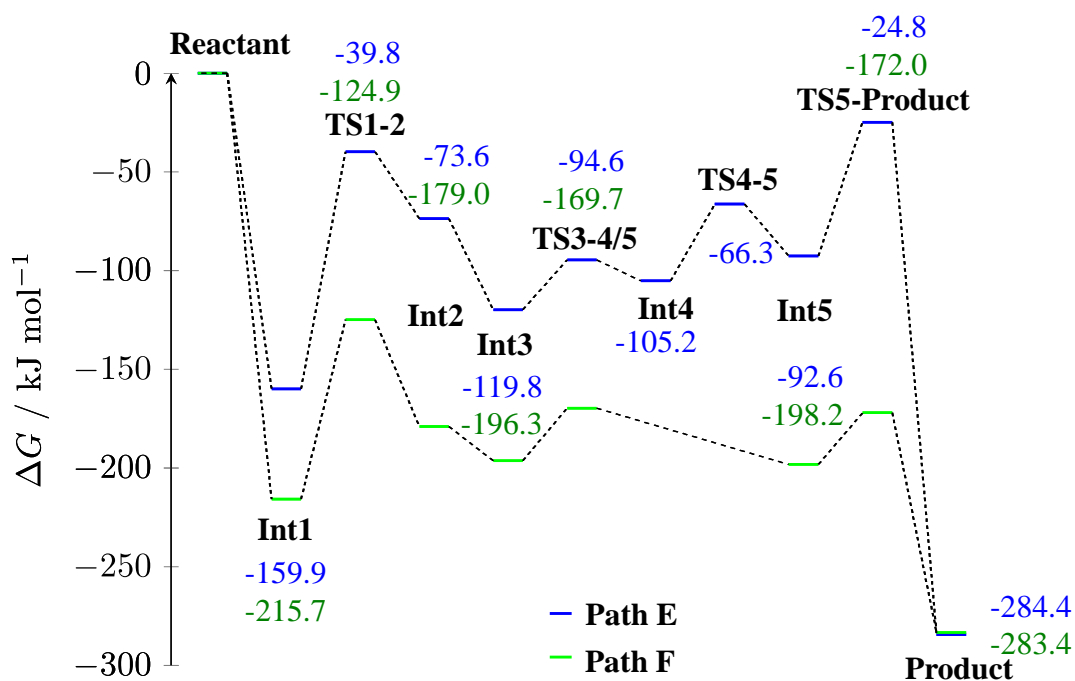


Figure 5.24. The formation reaction mechanism profile of PdNCP. **Path E** corresponding to the blue pathway represents the N coordination first to the Pd atom, while **Path F** corresponding to the green pathway represents the P coordination first to the Pd atom.

Table 5.5. Key structure data along pathway of PdNCP formation.

Pathway	Bond type	Bond distance/Å										
		Int1	TS1-2	Int2	Int3	TS3-4/5	Int4	TS4-5	Int5	TS5-Product	Product	
NCP (Path E)	Pd-C2	2.407	2.072	2.025	1.990	1.973	2.008	2.027	2.012	1.972	1.982	
	Pd-Cl1	2.302	2.481	2.447	∞	∞	∞	∞	∞	∞	∞	
	Pd-Cl2	2.300	2.355	2.415	2.283	2.362	2.401	2.403	2.408	2.438	2.405	
	Pd-N	2.147	2.116	2.098	2.114	2.091	2.110	2.113	2.117	2.136	2.203	
	Pd-P	5.262	5.271	5.167	4.881	4.187	3.770	3.763	3.784	2.726	2.222	
	Pd-H	1.993	1.772	3.072	∞	∞	∞	∞	∞	∞	∞	
	C2-H	1.130	1.826	3.317	∞	∞	∞	∞	∞	∞	∞	
	H-Cl1	2.937	1.518	1.309	1.293 ^a							
	PCN (Path F)	Pd-C2	2.491	2.117	2.007	1.999	2.021	n/a	n/a	2.036	2.022	1.982
		Pd-Cl1	2.338	2.634	3.438	∞	∞	n/a	n/a	∞	∞	∞
Pd-Cl2		2.317	2.333	2.347	2.358	2.358	n/a	n/a	2.383	2.377	2.405	
Pd-N		5.282	4.812	4.095	4.073	3.608	n/a	n/a	3.437	3.138	2.203	
Pd-P		2.254	2.213	2.208	2.190	2.193	n/a	n/a	2.215	2.182	2.222	
Pd-H		2.504	1.874	2.078	∞	∞	n/a	n/a	∞	∞	∞	
C2-H		1.103	1.509	2.729	∞	∞	n/a	n/a	∞	∞	∞	
H-Cl1		3.675	1.587	1.362	1.293 ^a	1.293 ^a	n/a	n/a	1.293 ^a	1.293 ^a	1.293 ^a	

^aThe bond distance for HCl calculation.

The calculation data of bond length for HCl using PBE with high basis set (cc-pCVTZ) from the NIST website is 1.289 Å (<http://ccbdb.nist.gov/geom2.asp>).
n/a = not available.

5.4.3 Kinetic study

The Gibbs free energy barriers at the rate-determining step for C-H bond activation are used to determine the rate constant. In term of kinetic reaction, we calculated the reaction rate by following Eyring equation;¹⁴³

$$k(T) = \frac{k_B T}{h c^0} e^{-\Delta G^\ddagger / RT} \quad (5.1)$$

where $k(T)$ is the reaction rate constant at temperature T , k_B is Boltzmann constant ($k_B = 1.381 \times 10^{-23} \text{ J K}^{-1}$), T is temperature ($T = 298.15 \text{ K}$), h is Planck's constant ($h = 6.626 \times 10^{-34} \text{ J s}$), c^0 is concentration ($c^0 = 1$) and ΔG^\ddagger is Gibbs free energy of activation and R is the gas constant ($R = 8.314 \text{ J mol}^{-1} \text{ K}^{-1}$).

As shown in Table 5.6, the rate constants are calculated using ΔG^\ddagger at **TS1-2** (C-H bond activation barrier) as the rate-determining step. For PdYCY formation, the PdPCP formation rate constant is about 2 and 5 orders of magnitude faster than that for the PdSCS and PdNCN formation reaction, respectively. For PdYCY', P coordination to Pd first for the SCP and NCP ligands is fastest due to the important role played by P stabilising the charge on Pd resulting in a lower Gibbs free energy barrier. In combination of PdYCY and PdYCY' formation, the P coordination to Pd first is the fastest due to the lowest Gibbs free energy barrier being the rate-determining step in all cases (the difference between PdPCP, **Path D** fo PdSCP and **Path F** of PdNCP formations is very small, $< 4.9 \text{ kJ mol}^{-1}$).

Table 5.6. Gibbs free energy barrier, ΔG^\ddagger , and rate constant of reaction, k , at the rate-determining step C-H bond activation.

YCY(Y')	$\Delta G^\ddagger / \text{kJ mol}^{-1}$	k / s^{-1}
NCN	121.0	3.9×10^{-9}
SCS	106.2	1.5×10^{-6}
PCP	94.6	1.7×10^{-4}
NCS (Path A)	117.0	2.0×10^{-8}
NCS (Path B)	100.2	1.7×10^{-5}
SCP (Path C)	101.3	1.1×10^{-5}
SCP (Path D)	89.7	1.2×10^{-3}
NCP (Path E)	120.1	5.6×10^{-9}
NCP (Path F)	90.8	7.7×10^{-4}

5.4.4 The energetic span model for pincer palladacycle formation

It has been discussed in the literature that the concept of a rate-determining step is badly defined, and a more accurate description is the rate-determining state. This is defined as “the transition state and intermediate which exert the strongest effect on the overall rate with a differential change on their Gibbs energies”.¹⁴⁴ To determine the rate-determining state for the pincer palladacycle formation reaction the energetic span model has been used.¹⁴⁴ δE is the energetic span of the reaction and serves as the apparent activation energy of the full reaction.¹⁴⁴ δE is defined in terms of the highest transition state (TS_{\max}) and the lowest intermediate (I_{\min}). When TS_{\max} occurs after I_{\min} in the Gibbs free energy profile, $\delta E = TS_{\max} - I_{\min}$. When TS_{\max} occurs before I_{\min} in the Gibbs free energy profile, $\delta E = TS_{\max} - I_{\min} + \Delta G_r$. A comparison of δE for the reactions considered in this chapter are provided in Table 5.7. For PdYCY formation, the δE for the SCS and PCP symmetrical ligand reactions are similar (less than 4.0 kJ mol⁻¹). In the case of PdYCY', it shows that P coordination to Pd first (**Path D** and **Path F**) is more reactive (smaller δE) than when N or S coordinates to Pd first (**Path C** and **Path E**). In addition, PdNCS formation reactions for N or S coordination (**Path A** and **Path B**) have a large δE value compared to when P coordinates to Pd first. The result of PdYCY formation indicates that the reactivity of SCS and PCP ligands are similar but based on both symmetrical and unsymmetrical pincer palladacycle formations, the δE reveals that P coordination to Pd first is the most reactive in agreement with when a rate-determining step is used for studying reactivity.

Table 5.7. Energetic spans (δE) of PdYCY(Y') formation.

YCY(Y')	Figure	$I_{\min}/\text{kJ mol}^{-1}$	$TS_{\max}/\text{kJ mol}^{-1}$	$\delta E/\text{kJ mol}^{-1}$
NCN	5.4	-164.1	-43.1	121.0
SCS		-149.5	-43.3	106.2
PCP		-216.6	-106.7	109.9
NCS (Path A)	5.15	-160.2	-43.2	117.0
NCS (Path B)		-147.4	-47.2	100.2
SCP (Path C)	5.18	-145.5	-36.4	109.1
SCP (Path D)		-210.3	-174.9	35.4
NCP (Path E)	5.24	-159.9	-24.8	135.1
NCP (Path F)		-215.7	-124.9	90.8

5.4.5 Nature of bonding in pincer palladacycles

The quantum theory of Atoms in Molecules (QTAIM) and natural bond orbital (NBO) analysis are tools used to characterise the strength and the nature of the Pd-L bond, where L = Y (N, S, P), C, Cl. The bond critical point (BCP) is the point to be a minimum of the shared electron density along the bond path between interacting atoms. The BCPs (blue points) around the Pd centre are observed for all complexes in molecular graphs and contour maps as expected (Figure 5.25). We have found an unexpected BCP between the Cl atom and H atom of the YCH_3 arm for PdNCN and PdSCS, while we have not found it for PdPCP. The absence of a BCP between Cl and H atom in PdPCP is attributed to the longer Cl-H distance (3.33 Å) compared to those in PdNCN (2.76 Å) and PdSCS (2.95 Å).

The magnitude of the electron density (ρ) at the bond critical point (BCP) indicates the strength of the interaction between atoms. The values of $\rho(\mathbf{r})$ at BCP for each Pd-L interaction are shown in Table 5.8. The $\rho(\mathbf{r})$ around Pd-L bond indicates that the Pd-C bond is strongest, while Pd-Cl bond is the weakest in all three PdYCYs. Moreover, we have found the order value of $\rho(\mathbf{r})$ is Pd-P > Pd-S > Pd-N indicating that Pd-P bonds are stronger than the Pd-S bonds, which are stronger than the Pd-N bonds.

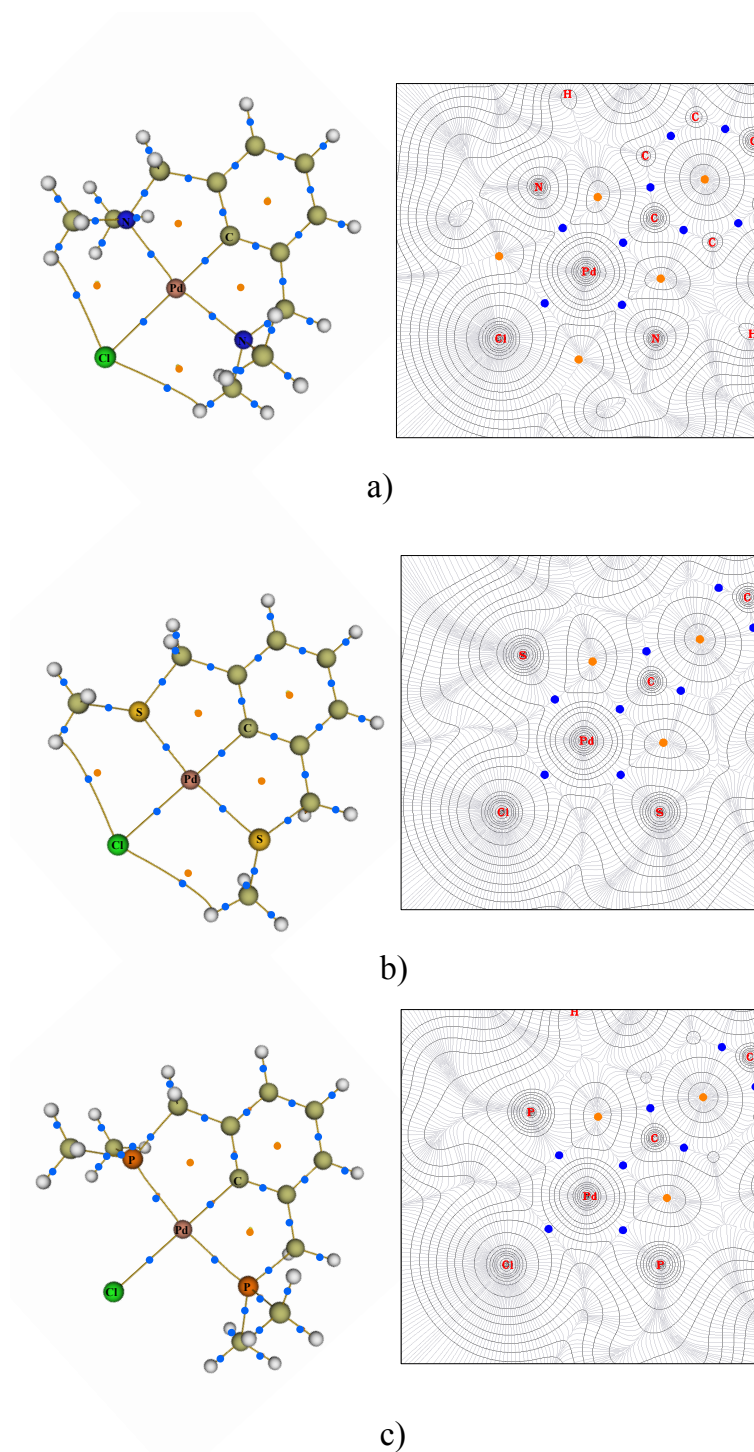


Figure 5.25. Left hand pictures are shown the molecular graphs and pictures of right hand are shown the contour map of electron density. The bond critical points (BCPs) are shown in blue dots and ring critical points (RCPs) are shown in orange dots; a) PdNCN, b) PdSCS and c) PdPCP.

Table 5.8. Electron density, $\rho(\mathbf{r})$, calculated using QTAIM analysis, Pd-L interaction (L=Y, C and Cl) in PdYCY, Y=N, S or P

Structure	Pd-L	Optimised structure		Optimised structure with fixed Pd-Y bond ^a	
		Bond length/Å	$\rho(\mathbf{r})/\text{a.u.}$	Bond length/Å	$\rho(\mathbf{r})/\text{a.u.}$
PdNCN	Pd-N1	2.140	0.086	2.300	0.062
	Pd-N2	2.140	0.086	2.300	0.062
	Pd-C	1.930	0.156	1.939	0.154
	Pd-Cl	2.424	0.064	2.405	0.066
PdSCS	Pd-S1	2.313	0.091	2.300	0.094
	Pd-S2	2.313	0.091	2.300	0.094
	Pd-C	1.993	0.137	1.994	0.137
	Pd-Cl	2.402	0.068	2.403	0.068
PdPCP	Pd-P1	2.287	0.101	2.300	0.098
	Pd-P2	2.287	0.101	2.300	0.098
	Pd-C	2.032	0.126	2.031	0.126
	Pd-Cl	2.402	0.069	2.402	0.069

^aThe Pd-Ys are fixed as we have investigated the interaction between Pd-Y bond with absence of the bond length effects.

Table 5.9. Laplacian, $\nabla^2\rho(\mathbf{r})$, total energy density, $H(\mathbf{r})$, ellipticity, ε and delocalisation index, $\delta(\text{Pd-L})$. All values are in atomic units.

Structure	Bond type	$\nabla^2\rho(\mathbf{r})$	$H(\mathbf{r})$	ε	$\delta(\text{Pd-L})$
PdNCN	Pd-N1	0.383	-0.014	0.033	0.908
	Pd-N2	0.383	-0.014	0.033	0.908
	Pd-C	0.236	-0.070	0.081	1.126
	Pd-Cl	0.238	-0.011	0.198	1.219
PdSCS	Pd-S1	0.257	-0.025	0.040	1.157
	Pd-S2	0.257	-0.025	0.040	1.157
	Pd-C	0.223	-0.055	0.061	1.051
	Pd-Cl	0.237	-0.013	0.114	1.234
PdPCP	Pd-P1	0.183	-0.036	0.022	1.124
	Pd-P2	0.183	-0.036	0.022	1.124
	Pd-C	0.224	-0.047	0.050	1.029
	Pd-Cl	0.232	-0.013	0.085	1.258

In terms of Pd-Y bond length, the results show that the Pd-S bond (2.312 Å) is rather long compared to the Pd-P bond (2.287 Å), which is longer than Pd-N (2.140 Å) (Table 5.8). The calculated bond lengths correlate with the ionic radii of the donor atom, i.e. $\text{P}^{3-} = 2.12 \text{ \AA}$, $\text{S}^{2-} = 1.84 \text{ \AA}$ and $\text{N}^{3-} = 1.71 \text{ \AA}$.¹⁴⁵

To evaluate the strength of interaction in the absence of bond length effects the Pd-Y bond was fixed at 2.300 Å and Pd-Y bond strength has been evaluated. We have found that the $\rho(\mathbf{r})$ values at BCP showing the strength of the Pd-Y bonds are Pd-P > Pd-S > Pd-N (Table 5.8). This trend is similar to the optimised structures. This confirms that the interaction between Pd and P is the strongest, while Pd and N is the weakest. The Pd-P bonds is stronger than the Pd-S bonds in view of π back-donation.

To confirm the strong back-donation interaction, the second order perturbation of natural bond orbital (NBO) is used to study back-donation. A ligand interacts with metal using a σ -donor, while it also can accept electron density from Pd in the form of a π -acceptor. Therefore, the back donation from the free electron pair, denoted as n-to- π -acceptor, are analysed to explain back-donation in Pd-Y bonds. The calculation shows the $E(2)$ of back donation of PdNCN to be 6.4 kJ mol⁻¹, in PdSCS it is 32.2 kJ mol⁻¹ and in PdPCP it is 46.4 kJ mol⁻¹. This result shows that the Pd has the strongest back donation to the phosphine.

In addition, to gain insight into the nature of Pd-L bond, $\rho(\mathbf{r})$ at BCP can be used. When this has greater value than 0.20 a.u. the interaction is considered as covalent and when $\rho(\mathbf{r})$ is less than 0.10 a.u. it is considered as the closed-shell (e.g. ionic, van der Waals, hydrogen bond, etc.).⁶⁸ Moreover, using the combination of the Laplacian of electron density ($\nabla^2\rho(\mathbf{r})$), total energy density ($H(\mathbf{r})$) and delocalisation index $\delta(\text{Pd-L})$, the nature of the bonding of Pd-L can be determined. The combination of $H(\mathbf{r})$ and $\nabla^2\rho(\mathbf{r})$ are good indices to describe the nature of bond.^{137,146} Both $\nabla^2\rho(\mathbf{r})$ and $H(\mathbf{r})$ are negative at the BCP indicating a purely covalent bond. If $\nabla^2\rho(\mathbf{r})$ is positive whereas $H(\mathbf{r})$ is negative, described as transit closed shell bonding with some covalent interaction.^{147,148} The transit closed shell interactions are typically in many dative bonds.^{137,149–152} For pure closed-shell interactions, both $\nabla^2\rho(\mathbf{r})$ and $H(\mathbf{r})$ are positive. The $\delta(\text{Pd-L})$ is used to determined the degree of covalency.^{149,153}

The sign of $\nabla^2\rho(\mathbf{r})$ of the Pd-L bonds are positive in the range from 0.083 to 0.101 a.u., while $H(\mathbf{r})$ are negative, in the range from -0.013 to -0.036 a.u. (Table 5.9). Therefore, Pd-L bonds are transit closed shell interactions.^{147,148} The extent of the electron sharing around Pd, $\delta(\text{Pd-L})$, gives an independent measure of the degree of covalency. The $\delta(\text{Pd-L})$ is in the range 0.9-1.3 a.u., indicating that the Pd-L bonds have significant covalent character.

The Pd-N bonds have most ionic character, as they have the largest $\nabla^2\rho(\mathbf{r})$ and $H(\mathbf{r})$ value, and the smallest $\delta(\text{Pd-L})$ values. Moreover, the Pd-S bonds are more ionic in character than the Pd-P bonds.

The degree of σ and π character in the Pd-L bonds can be studied by the bond ellipticity (ε). The value of ε reflects the shape of electron density distortion, when distorted away from the bond axis.¹⁵⁴ A low ε value indicates dominant σ character. Table 5.9 reveals that the Pd-Cl bond of Pd-L bonds exhibit a greater π contribution, whereas Pd-Y bonds give a lower π character.

Next, we discuss the strength and the nature of bonding in PdYCY' (PdNCS, PdSCN and PdNCP), where Y is *trans* to Y' and the geometry around Pd is square planar. Therefore, the strength of Pd-Y bond depends on the donor atom *trans* to itself. The *trans* influence is the tool for explaining the strength of the Pd-Y and Pd-Y' bonds.

There are no experimental data with which to study the *trans* influence of PdYCY'.

We have tried to understand how the donor atoms on the side arms affect the strength of interaction between donor atoms and the Pd centre on PdYCY'. In the literature, it has been shown that the $\rho(\mathbf{r})$ at BCP of Pd-Cl bond, where Cl is *trans* with respect to the donor atom, is a good way to measure the *trans* influence in PdCl₃X complexes.^{155–157} Therefore, firstly, we have studied the structure **I**, **II** and **III** in Figure 5.26 to measure Pd-Cl interactions relating to the *trans* influence directly from the donor atom. We have then studied the *trans* influence on the PdYCY'.

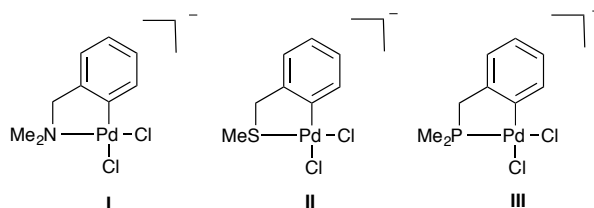


Figure 5.26. Model palladacycles **I** - **III** studied to investigate *trans* influence.

***Trans* influence in **I** - **III**:** The compounds shown in Figure 5.26 were studied to evaluate the *trans* influence before studying the *trans* influence on unsymmetrical pincer palladacycles (**4** - **6**). These structures contain the same ligand, Cl, *trans* to different donor atoms (NMe₂, SMe₂ and PMe₂). The Cl *trans* to the donor atom is fixed in order to monitor the strength of *trans* influence. $\rho(\mathbf{r})$ at the BCP of the Pd-Cl bond that is situated *trans* to the donor atom is determined using topological analysis of QTAIM. When a $\rho(\mathbf{r})$ value at BCP of the Pd-Cl bond has a high value, it indicates that the donor atom situated *trans* to Cl has a weak *trans* influence. By contrast, the low $\rho(\mathbf{r})$ value at BCP of Pd-Cl bond indicates a strong *trans* influence of the donor atom *trans* to Cl. In practice, the Pd-Cl bond distance is also affected by the strength of the *trans* influence. Therefore, we have also studied the *trans* influence using the Pd-Cl bond distance. On considering Cl situated *trans* to donor atom, when the donor atom has a strong *trans* influence, Pd-Cl bond distance increases. In contrast, if the Pd-Cl bond is situated *trans* to a group exerting weak influence, Pd-Cl bond distance decreases. Table 5.10 shows the Pd-Cl bond length and $\rho(\mathbf{r})$ value. The $\rho(\mathbf{r})$ value at BCP of the Pd-Cl bond in **III** is smallest, while the $\rho(\mathbf{r})$ value of **II** is intermediate and **I** is largest. It indicates the *trans* influence trends PMe₂ > SMe > NMe₂. To support the $\rho(\mathbf{r})$ data, we have considered the Pd-Cl bond length. It is found that the Pd-Cl bond situated *trans* to NMe₂ is shorter than that situated *trans* to SMe. Furthermore, the Pd-Cl bond situated *trans* to PMe₂ is

significantly longer than that *trans* to NMe₂ and SMe. It again demonstrates that PMe₂ has the strongest *trans* influence, SMe is intermediate and NMe₂ is the weakest. Based on this analysis the ordering of *trans* influence series is PMe₂ > SMe > NMe₂. This is in good agreement with Kapoor and Nakkar's study.¹⁵⁸ They studied square planar Pt complexes using DFT. Their results showed the order of *trans* influence to be P > S > N for these complexes. Moreover, Sajith and Suresh¹⁵⁶ studied the correlation between $\rho(\mathbf{r})$ and *trans* influence on square planar Pd complexes and found a good linear relation between $\rho(\mathbf{r})$ and the strength of the *trans* influence. The order of *trans* influence strength was PMe₃ > SMe₂ > NH₃.¹⁵⁶

Table 5.10. The electron density, $\rho(\mathbf{r})$, from the topological analysis parameters of QTAIM and Pd-Cl bond length *trans* to donor atom (NCH₃ in **I**, SMe in **II** and PMe₂ in **III**).

Compound	$\rho(\mathbf{r})$ at BCP of Pd-Cl bond/a.u.	Pd-Cl bond length/Å
I	0.080	2.334
II	0.077	2.352
III	0.070	2.395

***Trans* influence in PdYCY':** The $\rho(\mathbf{r})$ value at BCP of Pd-L bonds using a topological analysis of QTAIM, was used to investigate the strength of the *trans* influence in the PdYCY' shown in Figure 5.27. This result showed clearly that there are four Pd-L interactions. The $\rho(\mathbf{r})$ value between Pd and donor atoms (N, S and P) were evaluated. For the species PdPCY', where Y' is N or S, the $\rho(\mathbf{r})$ value at BCP of the Pd-P bond increases compared to PdPCP, for which $\rho(\mathbf{r})$ of the Pd-P bond in PdPCN is 0.114 a.u.; $\rho(\mathbf{r})$ of the Pd-P bond in PdPCS is 0.110; $\rho(\mathbf{r})$ of the Pd-P bond in PdPCP is 0.101 a.u. (Table 5.8 for PdPCP and Table 5.11 for PdPCY'). The difference is attributed to the strengths of *trans* influence of N and S donors being weaker than that of the P donor, leading to a stronger Pd-P interaction. This is confirmed by the $\rho(\mathbf{r})$ at BCP of Pd-N in PdNCP where it is 0.075 a.u. and the $\rho(\mathbf{r})$ at BCP of Pd-S in PdSCP where it is 0.082 a.u. as shown in Table 5.11. This is confirmed by the $\rho(\mathbf{r})$ value at BCP of Pd-N bond in PdNCP (0.075 a.u.) and the $\rho(\mathbf{r})$ value at BCP of Pd-S bonds in PdSCP (0.082 a.u.) shown in Table 5.11. On the other hand, the N donor ligand has a weak influence on the P donor ligand *trans* to it, which manifests as an decreased $\rho(\mathbf{r})$ of compare to $\rho(\mathbf{r})$ at BCP of Pd-N bond in PdNCN (0.086 a.u.). Furthermore, $\rho(\mathbf{r})$ of Pd-S in PdSCP decreases compared to

$\rho(\mathbf{r})$ of Pd-S in PdSCS (0.091 a.u.). We have also studied bond lengths in order to evaluate the effect of the *trans* influence. Table 5.12 provides bond distances around the Pd centre. The effect of *trans* influence is explained in term of bond length between donor atoms (N, S and P) on PdYCY'. We have found that the Pd-N bond in PdNCP (2.203 Å) increases compared to the Pd-N bond in PdNCN (2.140 Å), while Pd-P bond in PdNCP bond decreases (2.222 Å) compared to Pd-P bond in PdPCP (2.287 Å). These show that the N donor has *trans* influence weaker than the P donor. Similarly in case of PdNCS the stronger *trans* influence of S leads to an increased Pd-N bond distance.

Investigating the nature of bond for PdYCY' using the combination of $\nabla^2\rho(\mathbf{r})$ and $H(\mathbf{r})$ parameters, the Pd-L bonds are transit closed shell interactions (Table 5.11). Moreover, the ε value of all Pd-L bonds indicates domination of the σ character rather than π character. The $\delta(\text{Pd-L})$ of PdYCY' reveal significant covalent character and fall in the range 0.9-1.3 a.u. (Table 5.11).

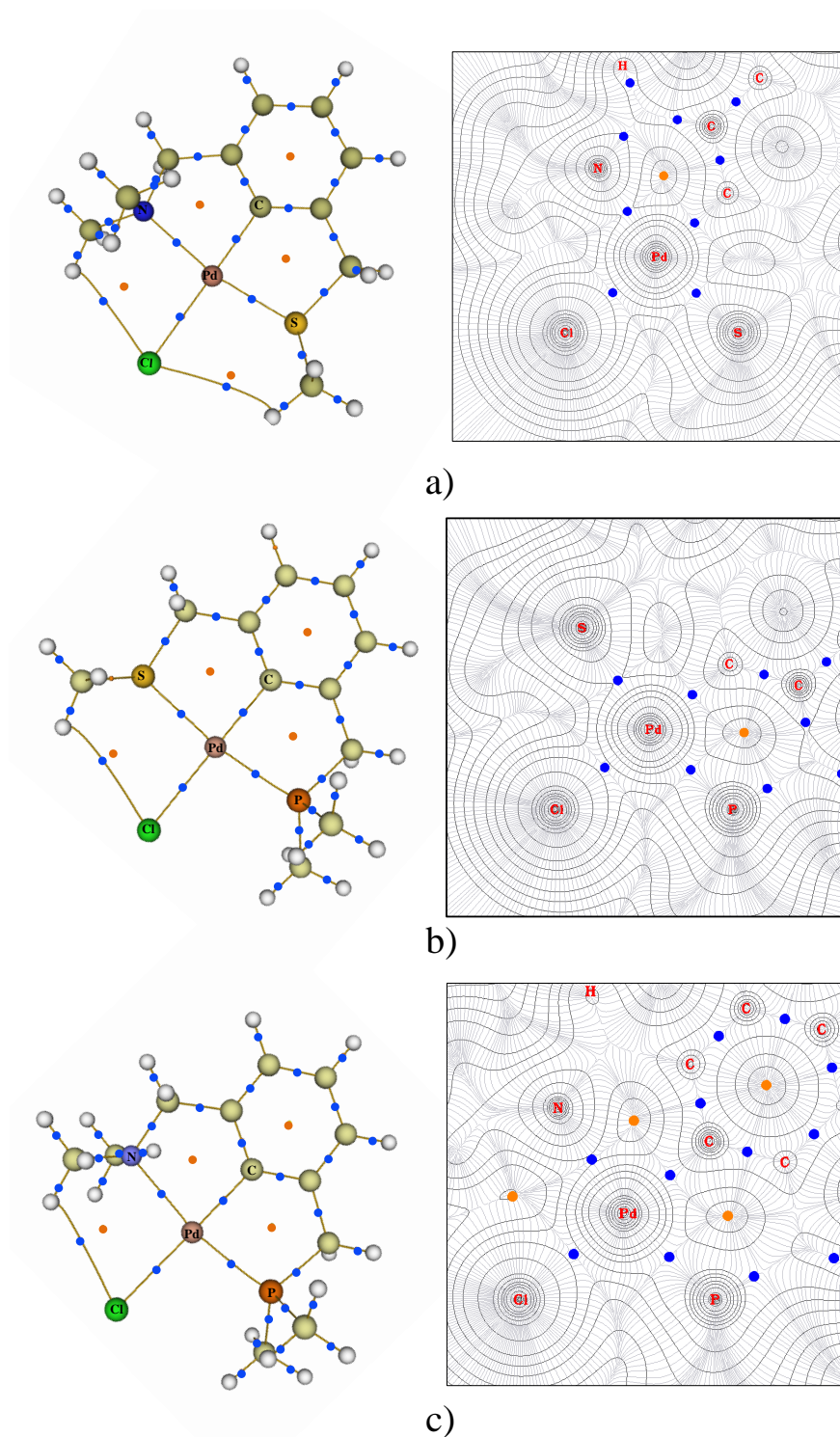


Figure 5.27. Pictures of left hand are shown the molecular graphs and pictures of right hand are shown the contour map of electron density. The BCPs are shown in blue dots and RCPs are shown in orange dots; a) PdNCS, b) PdSCP and c) PdNCP.

Table 5.11. The topological analysis parameters from QTAIM: electron density $\rho(\mathbf{r})$, Laplacian of the electron density $\nabla^2\rho(\mathbf{r})$, total energy density $H(\mathbf{r})$, ellipticity ε , and delocalisation index $\delta(\text{Pd-L})$ at the bond critical point of Pd-Y(Y') in PdNCS, PdSCP and PdNCP. All values are in atomic units.

Compound	Bond type	$\rho(\mathbf{r})$	$\nabla^2\rho(\mathbf{r})$	$H(\mathbf{r})$	ε	$\delta(\text{Pd-L})$
PdNCS	Pd-N	0.083	0.369	-0.013	0.046	0.883
	Pd-S	0.097	0.271	-0.028	0.039	1.217
	Pd-C	0.146	0.229	-0.061	0.072	1.085
	Pd-Cl	0.066	0.237	-0.012	0.150	1.228
PdSCP	Pd-S	0.082	0.241	-0.021	0.064	1.073
	Pd-P	0.110	0.170	-0.043	0.012	1.194
	Pd-C	0.132	0.228	-0.051	0.055	1.041
	Pd-Cl	0.069	0.235	-0.013	0.098	1.246
PdNCP	Pd-N	0.075	0.333	-0.010	0.064	0.828
	Pd-P	0.114	0.169	-0.046	0.006	1.243
	Pd-C	0.139	0.235	-0.056	0.065	1.068
	Pd-Cl	0.068	0.239	-0.012	0.117	1.249

Table 5.12. The bond distance in compound of symmetrical and unsymmetrical pincer palladiacycles.

Compound, PdYCY'/PdYCY	Pd-Y/Å	Pd-Y/Y'/Å	Pd-C/Å	Pd-Cl/Å
PdNcN	2.140 (Y=N)	2.140 (Y=N)	1.930	2.424
PdSCS	2.313 (Y=S)	2.313 (Y=S)	1.993	2.402
PdPCP	2.287 (Y=P)	2.287 (Y=P)	2.032	2.402
PdNCS	2.156 (Y=N)	2.285 (Y'=S)	1.963	2.412
PdSCP	2.364 (Y=S)	2.240 (Y'=P)	2.011	2.402
PdNCP	2.203 (Y=N)	2.222 (Y'=P)	1.982	2.405

5.5 Conclusion

The formation reactions of symmetrical and unsymmetrical pincer palladacycles (PdYCY and PdYCY', respectively) and the role of the donor atom (N, S and P) in the stability and reactivity of the PdYCY and PdYCY' have been investigated. It was found that, for all pincer formation reactions, the Gibbs free energy barriers for the C-H bond activation are highest. It indicates that the C-H bond activation is the rate-determining step of the formation reaction.

For symmetrical pincer palladacycles, the PdPCP is both thermodynamically and kinetically stable, while the PdNCN is the least stable. The stability of the pincer complex is supported by the topological analysis of quantum theory of Atoms in Molecules (QTAIM). The results reveal that the Pd-P bond is the strongest, whereas the Pd-N bond is the weakest. It was also found that the Pd-P bond has more covalent character than the Pd-S bond or the Pd-N bond. The Pd-N bond was the most ionic in character. The nature of all Pd-Y bonds is classed as a transit closed shell interaction.^{147,148} Work conducted on the symmetrical pincer palladacycle formation reaction has been published in "Dalton Transactions".⁸⁶

For the reactivity of unsymmetrical pincer palladacycles, the PdPCY' formation (Y' = S and N) is the most kinetically favourable, while PdNCP formation is the most thermodynamically favourable. The strength of the bond interaction between Pd and donor atoms of PdYCY' depends upon the *trans* influence. The PdPCN shows the strongest Pd-P interaction and the weakest Pd-N interaction, due to the *trans* influence. The calculations of the nature of the bond between Pd and Y are the transit closed shell interaction. Work conducted on the *trans* influence has been published in the peer reviewed journal "Inorganics".¹⁵⁹

For both PdYCY and PdYCY' formation reactions, the calculations clearly show that the P coordination to Pd first is the most reactive (lower C-H activation barrier and formation most exergonic). This greater stability is attributed to the lone-pair donor and π -acceptor ability of the phosphine making the strong interaction of Pd-P bond and stabilising the transition state structure.

Chapter 6

Formation of the Active Catalyst Pd(0) from Symmetrical and Unsymmetrical Pincer Palladacycles

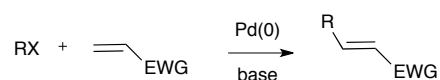
This chapter provides the details of the formation of Pd(0) from a pincer palladacycle pre-catalyst. The Pd(0) formation reaction mechanism proceeds via two key steps, transmetallation and reductive elimination, which are investigated using density functional theory (DFT) calculations. The catalytic reactivity of both symmetrical and unsymmetrical pincer palladacycles in the gas phase with and without base and with and without solvation corrections are studied using DFT.

6.1 Introduction

In Chapter 5, the pincer palladacycle formation reaction mechanism and the nature of the bonding around the palladium centre were presented. In this chapter, we will study pincer palladacycles acting as pre-catalysts. First of all, we will introduce the proposed mechanism pathways and then the calculated stationary points along these reaction mechanism pathways will be presented. This chapter will conclude with a comparison to experimental catalytic activity.

6.1.1 Palladium complex (pre)-catalysts

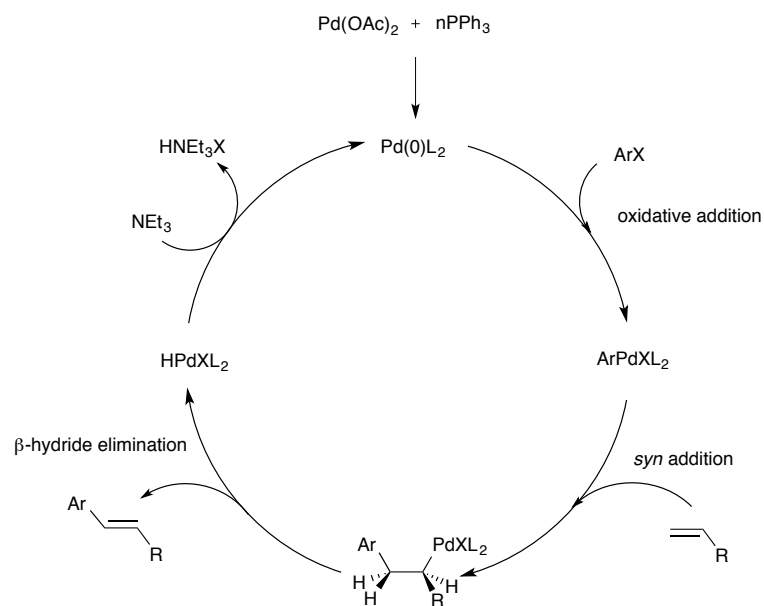
In 1968, an alkyl or aryl halide was reacted with an alkene using palladium salt and is now referred to as the Heck reaction.¹⁶⁰ A conventional Heck reaction occurs from a reaction between an aryl iodide or bromide reacting with a terminal alkene in the presence of the catalyst Pd(0) to facilitate C-C bond formation (Scheme 6.1).¹⁶¹



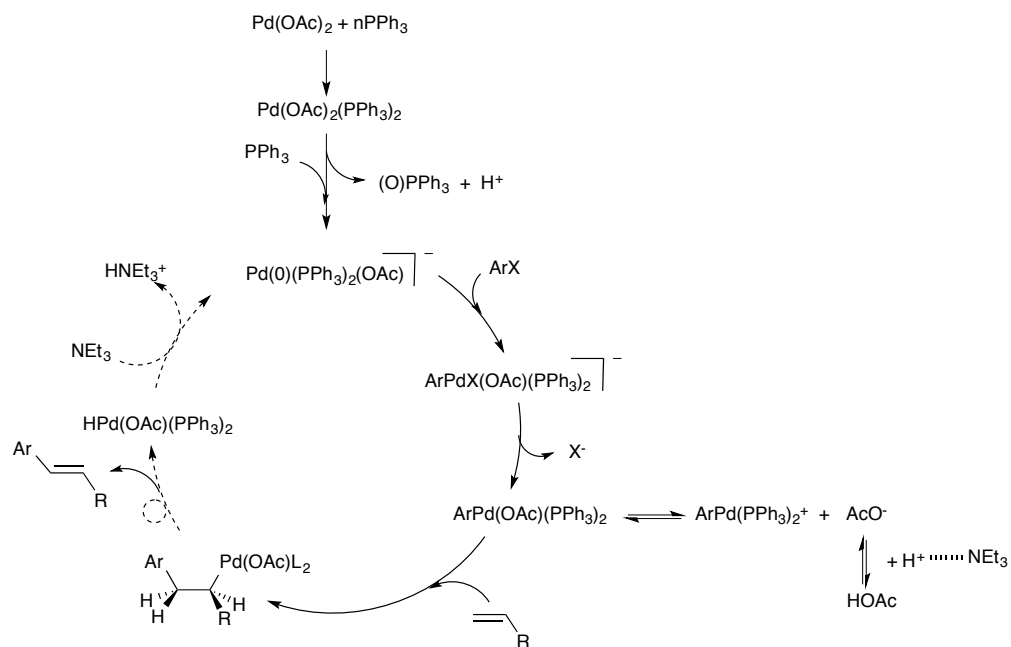
Scheme 6.1. A traditional Heck coupling reaction, where R is aryl or vinyl and EWG is electron withdrawing group.¹⁶¹

Scheme 6.2 shows the typical Heck catalytic cycle reaction which involves a Pd(0)-complex and Pd(II)-complex.¹⁶² The reaction begins with the Pd(0)-complex catalyst generated from the Pd(II)-complex pre-catalyst. Then an aryl halide (ArX) reacts with the Pd(0)-complex in an oxidative addition step to produce a Pd(II)-complex intermediate. Next, the Pd(II)-complex intermediate binds to the alkene (*syn* addition) to yield an alkyl intermediate, creating the Pd-C and C-C bonds. Finally, the product and the HPdXL₂ are produced in the β-hydride elimination step.

Amatore and Jutand¹⁶³ proposed a new mechanism for the Heck reaction to clarify the classical Heck catalytic reaction. Scheme 6.3 depicts the new Heck reaction where the new pathway is shown as the solid arrow, while the classical pathway is shown as a dashed line arrow. The new Heck reaction begins from Pd(OAc)₂ reacting with nPPh₃ rapidly to form Pd(OAc)₂(PPh₃)₂, which can be observed by ¹³P-NMR and electrochemical techniques.^{164,165} Slow formation of a Pd(0)-complex then occurs *via* intramolecular reduction of Pd(OAc)₂(PPh₃)₂ to form a [Pd⁰(PPh₃)₂(OAc)]⁻ active species (tricoordinated anionic palladium(0)). The latter reacts with an aryl halide in the oxidative addition step to produce [ArPdX(OAc)(PPh₃)₂]⁻ (pentacoordinated complex). After oxidative addition, ArPd(OAc)(PPh₃)₂ is formed, releasing a halide ion. ArPd(OAc)(PPh₃)₂ reacts with styrene, which is a *syn*-addition reaction, and this reaction competes with the equilibrium process (ArPd(OAc)(PPh₃)₂ ⇌ ArPd(PPh₃)₂⁺ + AcO⁻). The final step is a β-hydride elimination, which is the same step as in the classical mechanism.



Scheme 6.2. General process for the Heck catalytic cycle reaction.¹⁶²

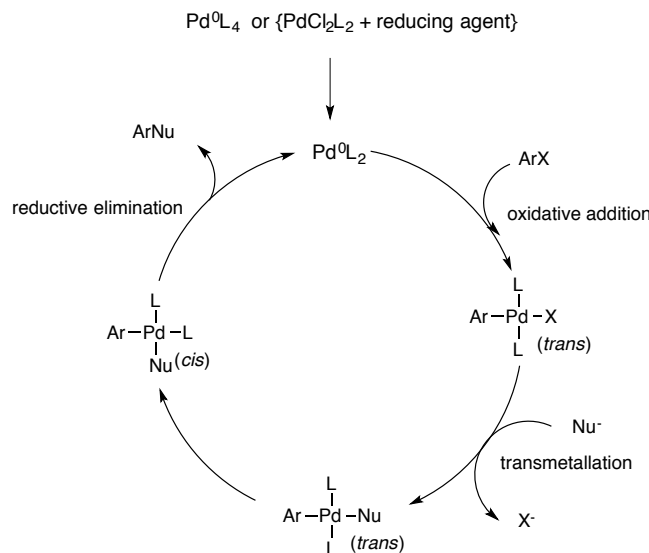


Scheme 6.3. The Heck catalytic cycle reaction proposed by Amatore and Jutand.¹⁶³

The active Pd(0)-complex is also used in the cross-coupling reaction, which is the reaction between an aryl halide and a nucleophile (Scheme 6.4).¹⁶³ The classic process of catalytic cycle is shown in Scheme 6.5. Pd⁰L₄, or PdCl₂L₂ + reducing agent, is a source of the Pd⁰L₂ active species. The first step in the catalytic cycle for the classical cross-coupling reaction is an oxidative addition. In this step the Pd⁰L₂ reacts with aryl halide to produce a *trans*-ArPdXL₂. The second step is a transmetalation, a nucleophilic attack on the *trans*-ArPdXL₂, followed by the isomerisation step. The final step is the formation of the product by reductive elimination.



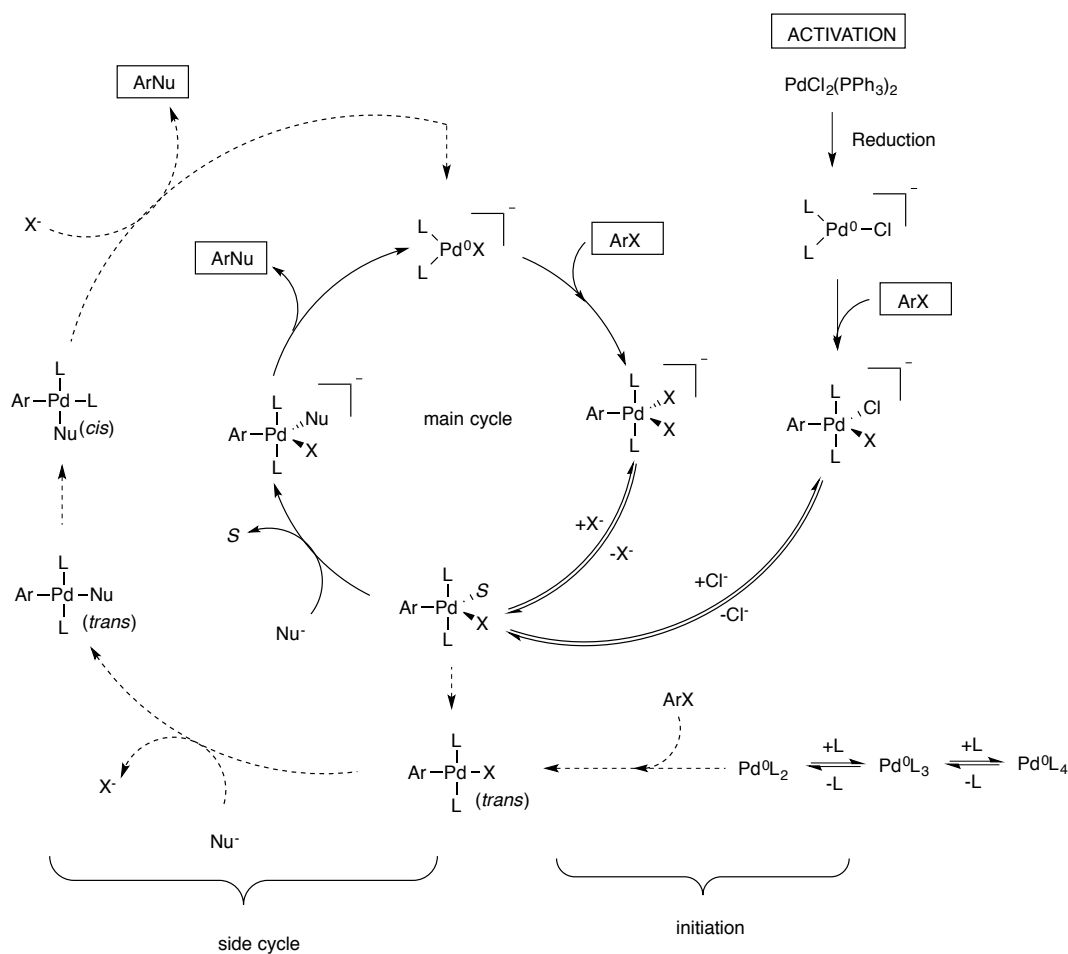
Scheme 6.4. A traditional cross-coupling reaction, where Ar is an aryl group and Nu⁻ is a nucleophile.¹⁶³



Scheme 6.5. General process for cross-coupling reactions.¹⁶³

A new cross-coupling reaction was proposed and the reaction cycle is shown in Scheme 6.6. Firstly, tricoordinated anionic Pd(0)-complex [L₂Pd⁰Cl]⁻ is produced *via* reduction of PdCl₂(PPh₃)₂. This anionic complex reacts quickly with ArX to form a pentacoordinated anionic Pd(0)-complex [L₂ArPdClX]⁻. Next, a chloride ion departs from the [L₂ArPdClX]⁻ and the solvent (*S*) coordinates with Pd instead to produce a neutral *trans*-pentacoordinated complex L₂ArPdSX. The L₂ArPdSX is attacked by the nucleophile to produce the anionic *trans*-pentacoordinated complex ([ArPdL₂NuX]⁻). Then the production of ArNu and [PdL₂X]⁻ occurs through oxidative addition. The evidence for supporting the new mechanism, which occurs

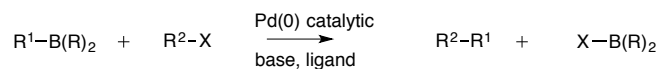
via pentacoordinated complexes are generated from reaction of 2-thiophenyl anion with anionic pentacoordinated complexes faster than reaction of 2-thiophenyl anion with *trans*-PhPdI(PPh₃)₂.¹⁶³ Moreover the reaction between the nucleophile and *trans*-PhPdI(PPh₃)₂ yields a slowly occurring cross-coupling product.¹⁶⁶ However, a side cycle can be found which is a possible competition reaction to the main cycle. If Pd⁰L₄ is introduced in the reaction, the process occurs *via* the side cycle first then it develops to the main cycle (see Scheme 6.6 at the bottom).



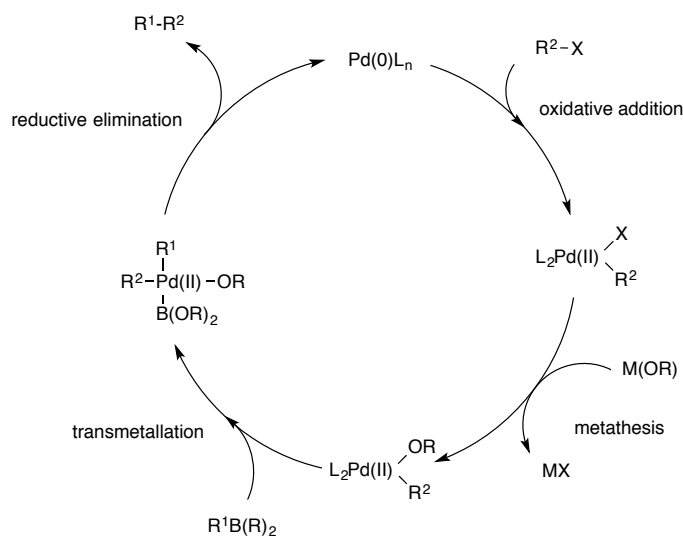
Scheme 6.6. New mechanism for the cross-coupling reactions proposed by Amatore and Jutand.¹⁶³

One of the popular reactions for formation of C-C bonds is the Suzuki-Miyaura reaction, which is a palladium catalyst cross-coupling reaction between organoboron compounds and an alkyl halide (Scheme 6.7).¹⁶⁷ Based on the proposed catalytic cycle from Suzuki, Scheme 6.8 is the reaction catalytic cycle of the Suzuki-Miyaura cross-coupling.¹⁶⁸ This reaction starts from Pd(0)-complex catalysts. The Pd(0)-complex is introduced and reacts with alkyl halide R²-X to generate the Pd(II)-complex *via*

oxidative addition, followed by the exchange of an anion between Pd and the metal (metathesis). Next, the organoboron compound reacts with $L_2Pd(OR)R^2$ via the transmetallation step, then in the final step the reductive elimination occurs to yield the production of C-C bond and Pd(0)-complex catalyst.

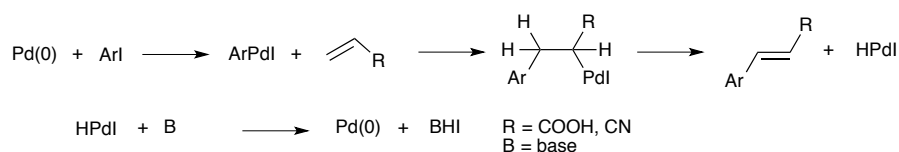


Scheme 6.7. Suzuki-Miyaura cross-coupling reaction.¹⁶⁷



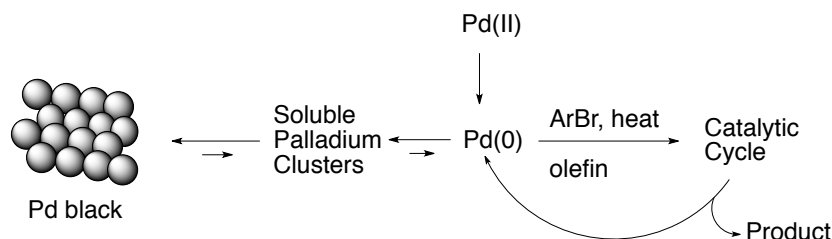
Scheme 6.8. General catalytic cycle of Suzuki-Miyaura cross-coupling reaction based on Suzuki proposal.¹⁶⁸

In 1989, Bumagin and co-workers¹⁶⁹ studied the arylation of acrylic acid and acrylonitrile using aryl halides with Pd(OAc)₂ in water. The proposed reaction mechanism consists of Pd(OAc)₂ acting as a pre-catalyst to generate a Pd(0)-active catalyst, which accelerates the reaction (Scheme 6.9). The Pd(0)-active catalyst reacts with aryl iodides, ArI to produce ArPdI. The ArPdI reacts with CH₂=CHR to yield an intermediate then the intermediate transforms to produce the product and HPdI. In the final step, the active Pd(0)-active catalyst is generated again by a reaction between HPdI and base.



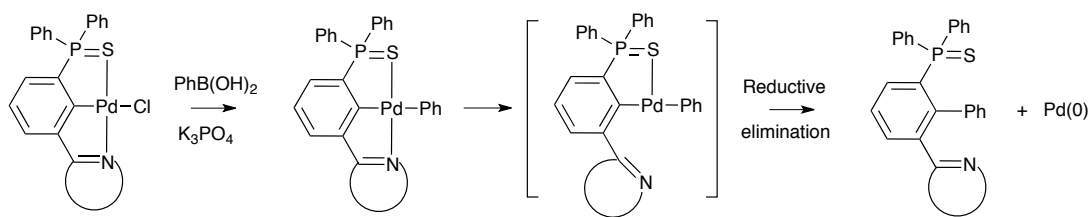
Scheme 6.9. Reaction of aryl halide with acrylic acid using a palladium catalyst.¹⁶⁹

de Vries *et al.*¹⁷⁰ reported the idea of ligand-free palladium acting as the active catalyst in the Heck reaction. They showed that the $\text{Pd}(\text{OAc})_2$, Pd(II), was a source for the Pd(0) active catalyst, and proposed the reaction process for its formation. They revealed that there were two competing processes. The active catalyst entered into a catalytic cycle or aggregated to form an inactive catalyst species, which is known as palladium black (Scheme 6.10).



Scheme 6.10. Proposed formation mechanism of ligand free palladium in the Heck reaction.¹⁷⁰

The Pd(0) catalyst can also be generated from pincer palladacycles. For example, pincer palladacycles were used as pre-catalyst in the Suzuki-Miyaura cross-coupling reactions. The unsymmetrical NCS pincer complex with phenylboronic acid and K_3PO_4 as a base in dimethylformamide (DMF) were studied to observe the reaction for formation of Pd(0) and investigate its catalytic activity. The proposed reaction pathway for this is shown in Scheme 6.11.¹⁷¹



Scheme 6.11. The reaction process for generating the Pd(0) catalyst.¹⁷¹

There is evidence indicating that Pd(0) formation can be achieved using PCP pincer palladacycles. For example, Pd(0) particle formation from PCP pincer palladacycles in the reaction of phenyl halides with styrene was confirmed by kinetic studies, a Hg drop test (the method for testing Pd(0) particles), NMR study and a quantitative poisoning test.¹⁷² Moreover, Nilsson and Wendt¹⁷³ (2005) proposed the PCP pincer palladacycles serving as pre-catalyst in the Heck reaction by decomposing and forming a colloidal Pd(0) species. There is no direct evidence to support their

proposal as they just examined the colloidal Pd(0) by using the Hg drop test. Clear evidence supporting Pd(0) particle formation from pincer palladacycle is found in work conducted by Costa *et al.*¹⁷⁴ They evaluated the pincer palladacycles as pre-catalysts in the Heck reaction by using pincer palladacycles in the reaction of iodobenzene and methyl acrylate. From observing particles by transmission electron microscopy, they found Pd(0) nanoparticles. This led to the conclusion that pincer palladacycles are decomposed to generate Pd(0) in the form of a colloidal, cluster or nanoparticle. Furthermore, work by Bedford *et al.*¹⁷⁵ also showed that the Pd(0) species from CN palladacycles can be formed *via* a reductive elimination in the Suzuki-Miyaura reaction.

In general, the pincer palladacycle generates the Pd(0) catalyst *via* two elementary processes: transmetalation and reductive elimination. We have found the literature to study the transition structures of both steps. For instance, in the transmetalation step, the intermediate $[(\text{Phbz})\text{Pd}(\text{Ph})(\text{PPh}_3)]$ (Figure 6.1a) Phbz is N-phenylbenzaldimine was detected using electrospray ionisation mass spectroscopy (ESI-MS) from the reaction of $[\text{Pd}(\text{Phbz})(\text{R})(\text{PPh}_3)]$ pre-catalyst (Figure 6.1b) with $\text{PhB}(\text{OH})_2$. This is an indirect method to prove the transmetalation product (Figure 6.1a).¹⁷⁶ Kapdi *et al.*¹⁷⁷ studied the reaction of $[\text{Pd}(\text{Phbz})(\text{OAc})(\text{PPh}_3)]$ with 2,4,6-trifluorophenylboronic acid in THF. They found the transmetalation product $[\text{Pd}(\text{Phbz})(2,4,6-\text{F}_3\text{C}_6\text{H}_2)(\text{PPh}_3)]$, which was verified by X-ray crystallography. This is direct evidence to confirm the formation of the transmetalation intermediate before generating Pd(0). They proposed the transition state structure for the reaction between arylboronic acid and palladacyclic complex (Figure 6.2).

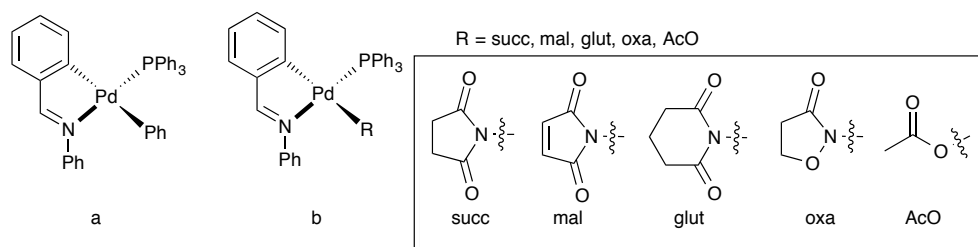


Figure 6.1. a) The transmetalation intermediate, $[(\text{Phbz})\text{Pd}(\text{Ph})(\text{PPh}_3)]$ and b) palladacycles (pre-catalyst), $[\text{Pd}(\text{Phbz})(\text{R})(\text{PPh}_3)]$.¹⁷⁶

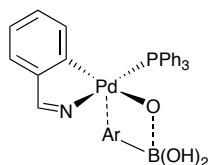
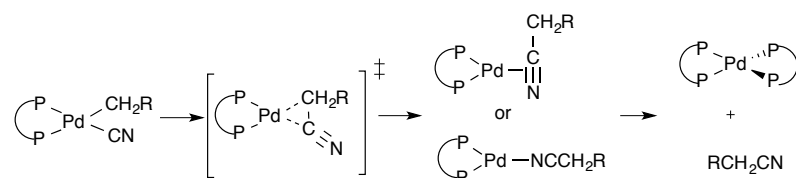


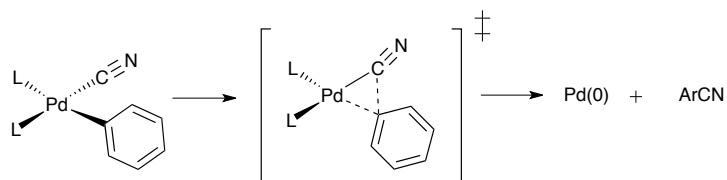
Figure 6.2. Transition state of transmetalation reaction between arylboronic acid and palladacyclic complex.¹⁷⁷

The reductive elimination step which is a transformation step in organometallic chemistry was investigated using palladium complexes, (diphosphine)Pd(R)(CN) (R = CH₂-TMS, CH₂CMe₂).¹⁷⁸ The results showed the kinetic rate depended on the environment of the phosphorus ligand, i.e., bite angles, chelate flexibility and steric hindrance. They suggested that the elimination product occurs *via* the transition state in Scheme 6.12.¹⁷⁸

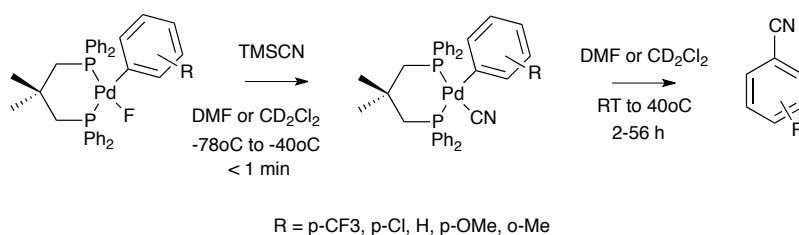


Scheme 6.12. Reductive elimination reaction pathway of palladium complex.¹⁷⁸

The reductive elimination from arylpalladium cyanide complexes were studied using both experiment and calculation.¹⁷⁹ The calculation was done using B3LYP with LANL2TZ for Pd and P and 6-311G(d,p) for all other atoms. They used PMe₃-ligated arylpalladium cyanide complexes for determining the effect of electron-donating and electron-withdrawing substituents on the aryl ligand *via* reductive elimination in Scheme 6.13. In the experimental part, they determined the kinetic rate through a reductive elimination reaction under the condition in Scheme 6.14 while in the calculation part they determined the energy barrier through the transition structure in Figure 6.3. The results from calculation revealed that the electron-rich arylpalladium cyanide complexes have a lower energy barrier than electron-poor complexes. This agrees with the experimental data that the electron-rich arylpalladium cyanide complex has a rate constant greater than electron-poor arylpalladium cyanide complex, indicating that the reaction rate of the electron-rich complex is faster than the electron-poor complex for rate of reductive elimination reaction.



Scheme 6.13. Reductive elimination of arylpalladium cyanide complexes to generate aryl nitrile and Pd(0).¹⁷⁹



Scheme 6.14. Reductive elimination step of arylpalladium cyanide complexes.¹⁷⁹

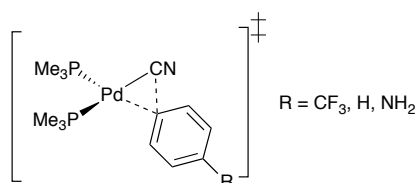


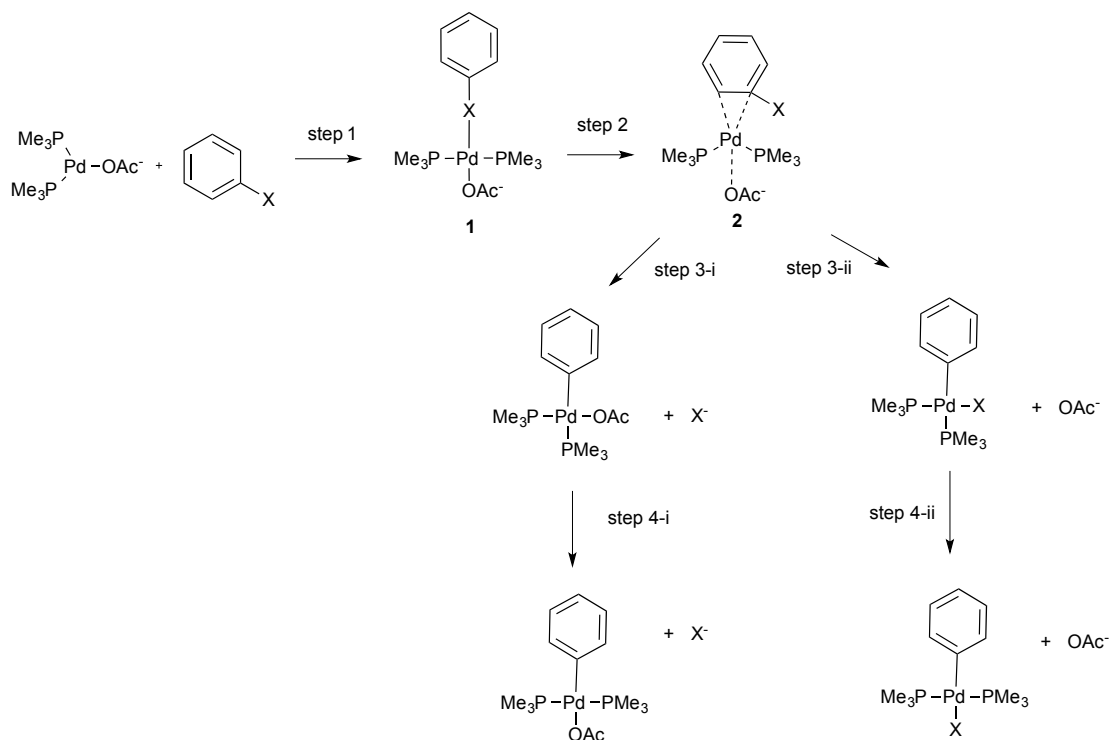
Figure 6.3. Transition state of reductive elimination studied by Klinkenberg and Hartwig.¹⁷⁹

Palladium catalysts have become commonly used in various organic reactions. It is very hard to observe the reaction mechanism processes by experimental measurements, therefore computational chemistry has a role to investigate the reaction mechanism processes. It can be used to calculate the geometric and energetic reaction profile involving the reactant, the intermediates, the transitions and products. In the next section, examples of reaction mechanism studies of palladium complex catalysts using computational chemistry are presented.

6.1.2 DFT study of Palladium catalysis

Over the last ten years, the reaction mechanism using the palladium catalyst has been covered extensively. Many researchers investigated to understand the catalytic processes using DFT.⁷⁴ In this section, literature examples will be shown of the mechanistic pathways when palladium catalysts were introduced in the organic reaction.

Goossen *et al.* reported a computational study investigating the reaction mechanism of the oxidative addition of aryl halides to Pd(0) complexes.¹⁸⁰ The BP86 functional with LANL2DZ for Pd, P and I, and Dunning/Huzinaga full double- ζ basis sets for C, H and O were used for investigating the transition states and intermediates. Single-point solvent-correction for THF using the CPCM model and UAKS radii was used to obtain the energy at the stationary points: SDD ECP was used to treat Pd, the SDB-cc-pVTZ for I, the aug-cc-pVTZ for O, P and C, and cc-pVDZ for H. Scheme 6.15 shows the reaction process and it was found that the tricoordinated anionic Pd(0)-complex that had a distorted-trigonal-planar structure around the Pd-centre, was a stable structure, and it could serve as a catalytically active species. Then, the halide of the aryl halide coordinates to the distorted-trigonal-planar palladium complex to form a square-planar palladium complex rapidly with no energy barrier (step 1). In the oxidative addition of square-planar palladium complex, they found a multistep process before forming the π -complex, which is an intermediate structure for carbon-halide bond cleavage (step 2). Next, the bond breaking of the carbon-halide is found in step 3, followed by the isomerisation process as the final step which is rate-determining.



Scheme 6.15. Oxidative addition of aryl halides to Pd(0) complexes study using DFT by Goossen and co-workers. The process involves coordination (step 1), oxidative addition (step 2), C-X bond cleavage (step 3) and isomerisation (step 4).¹⁸⁰

In 2006, a DFT computational investigation studied the full catalytic cycle of Suzuki-Miyaura cross-coupling between $\text{CH}_2=\text{CHBr}$ and $\text{CH}_2=\text{CHB}(\text{OH})_3^-$ using $\text{Pd}(\text{PH}_3)_2$ and PdPH_3 catalytic general models by Braga *et al.*¹⁸¹ All calculations were performed using the B3LYP functional. The Pd and Br heavy atoms were treated using an effective core potential LanL2DZ and H, B, C, O and P were calculated using 6-31G(d) basis set. In the reaction starting from $\text{Pd}(\text{PH}_3)_2$ catalyst, the main steps of the catalytic cycle consist of oxidative addition, first isomerisation, transmetalation, second isomerisation and reductive elimination. The oxidative addition concerns a formation of a four coordination sphere around the Pd-centre (*cis*- $\text{Pd}(\text{PH}_3)_2(\text{CH}_2=\text{CH})\text{Br}$) and a changing Pd oxidation state from 0 to +2. The *cis*- $\text{Pd}(\text{PH}_3)_2(\text{CH}_2=\text{CH})\text{Br}$ structure changes to *trans*- $\text{Pd}(\text{PH}_3)_2(\text{CH}_2=\text{CH})\text{Br}$ at the first isomerisation step. Then the halide from *trans*- $\text{Pd}(\text{PH}_3)_2(\text{CH}_2=\text{CH})\text{Br}$ is substituted by the organic group from the boronic acid species ($\text{CH}_2=\text{CHB}(\text{OH})_3^-$) to produce *trans*- $\text{Pd}(\text{PH}_3)_2(\text{CH}_2=\text{CH})_2$ via multiple steps. After this step, second isomerisation occurs to change *trans*- $\text{Pd}(\text{PH}_3)_2(\text{CH}_2=\text{CH})_2$ to *cis*- $\text{Pd}(\text{PH}_3)_2(\text{CH}_2=\text{CH})_2$. In the final step, a bond between the organic groups forms

to release $\text{CH}_2=\text{CH}-\text{CH}=\text{CH}_2$ and $\text{Pd}(\text{PH}_3)_2$ catalyst which is the reductive elimination step. For the monophosphine system, the PdPH_3 is coordinated with $\text{CH}_2=\text{CH}$ and Br^- to produce a T-shape complex and the oxidation state of Pd changes from 0 to +2. There are three possible isomers (Figure 6.4). Isomers **T1** and **T2** occur directly from oxidative addition. Isomer **T3** occurs *via* a Y-shape transition structure of isomer **T2**. Isomer **T2** goes directly to the transmetallation step, while isomer **T1** is changed to isomer **T2** before going to the transmetallation step *via* a Y-shape transition at the first isomerisation process. The transmetallation process starts from coordination between isomer **T2** and $\text{CH}_2=\text{CHB}(\text{OH})_3^-$. The organic group from the boronic acid species migrates to the Pd-centre while Br^- is removed from the complex to form $\text{Pd}(\text{PH}_3)(\text{CH}_2=\text{CH})_2$ and $\text{B}(\text{OH})_3$ *via* multiple steps. Finally, the reductive elimination occurs by C-C forming to produce $\text{CH}_2=\text{CH}-\text{CH}=\text{CH}_2$ and $\text{Pd}(\text{PH}_3)$ catalyst. In the theoretical investigation it is stated that the reaction mechanism is dependent on the experimental system considered.¹⁸¹

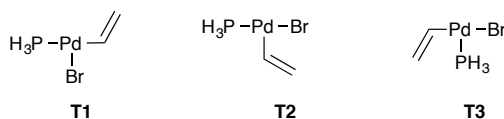


Figure 6.4. Three different T-shape isomers.¹⁸¹

The choice of ligand arm can affect the cross-coupling reaction. In 2008, Huang *et al.*¹⁸² studied the effect of the donor atoms (N and P) on the cross-coupling reaction. A study using B3LYP with a 6-31G(d) basis set for all atoms except LandL2DZ for Pd atom were treated for determining the reactions. Palladium complexes with three different categories of bidentate ligands diimines, diamines and diphosphines were used for determining the reaction mechanism of cross-coupling between phenyl chloride and phenylboronic acid in the presence of a base and base-free. The computational calculation showed that the main processes are oxidative addition, transmetallation and reductive elimination. The transmetallation step is a rate-determining step and the base is important for decreasing the energy barrier at this step. Comparing diimine, diamine and diphosphine ligands at the rate-determining step, they showed that palladium with a diphosphine ligand has the lowest energy barrier.

A palladium(II) pincer catalysed Heck coupling reaction *via* a Pd(II)/Pd(IV)

process was studied.¹⁸³ The reaction mechanism was studied using the B3PW91 functional with 6-31G(d) basis set for C, H, N, O, S atoms and LanL2DZ for Pd and I. They investigated the oxidative addition mechanism of hypervalent iodonium salts with pincer complexes and illustrated that the hypervalent iodonium salts are a good oxidising agent for palladium(II) pincer complexes with a low energy barrier compared to phenyl iodide (Figure 6.5).

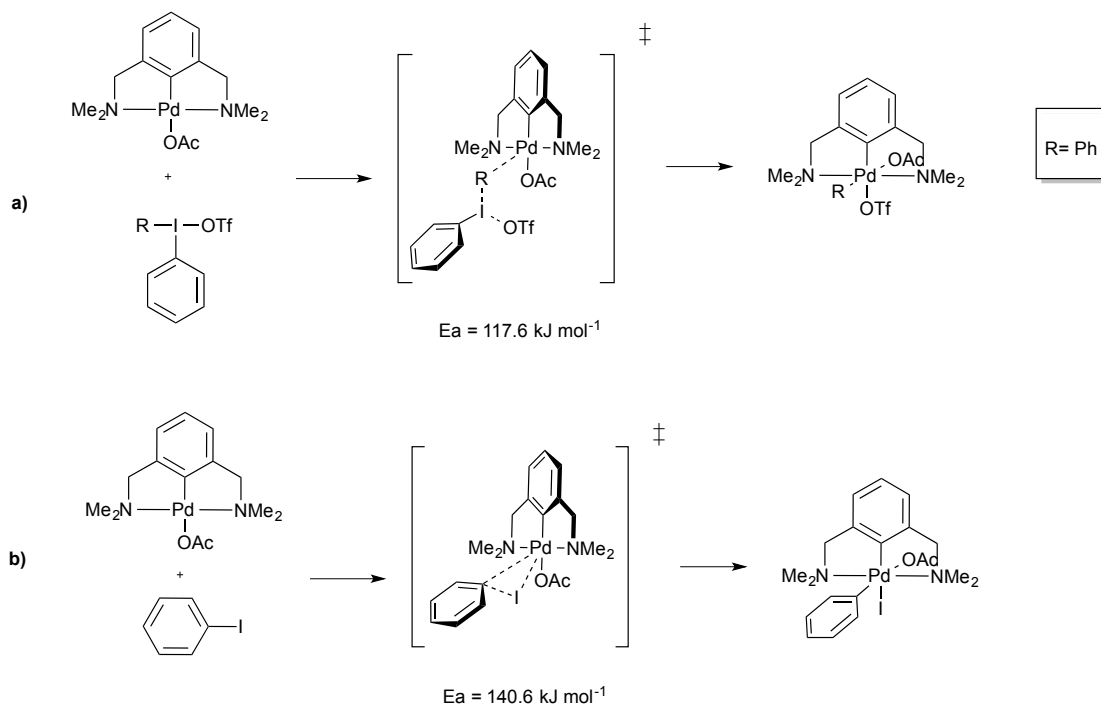


Figure 6.5. Reaction of oxidative addition of PdN(CN) pincer with a) hypervalent iodonium salts and b) phenyl iodides.¹⁸³

The excellent review by Tsipis⁷⁴ in 2014 showed that DFT methods are successful for applications to investigate the structure, bonding, and spectroscopy of complexes and from literature above DFT is a good method for studying the reaction mechanisms. To our knowledge, no one has reported the mechanism of Pd(0) active catalyst formation from pincer palladacycles as a pre-catalyst. Thus from this point of view it is interesting to elucidate Pd(0) formation from pincer palladacycles. Moreover, there are the two main types of pincer palladacycles: symmetrical and unsymmetrical. They are interesting for investigating the role of the donor atom in the Pd(0) formation pathways. Furthermore, some literature report unsymmetrical pincer palladacycles have higher catalytic activity than symmetrical pincer palladacycles.^{184–186} A member of the Spencer and Cox group, Dr G. W. Roffe, synthesised unsymmetrical pincer

palladacycles and tested their activity in the Suzuki-Miyaura coupling reaction and found that both symmetrical and unsymmetrical pincer palladacycles were good pre-catalysts.¹⁸⁷ The aim of this work is to rationalise the difference in the activity observed by studying the formation of the active Pd(0) catalyst from simple symmetrical and unsymmetrical pincer palladacycle pre-catalysts. These calculations will complement the calculations and experiment by Dr G. W. Roffe on his synthesised unsymmetrical pincer palladacycles.

6.2 Aims of this work

The aim of this chapter is to study the Pd(0) formation reaction mechanism of symmetrical pincer palladacycles, PdYCY which are PdNCN (**1**), PdSCS (**2**) and PdPCP (**3**) and unsymmetrical pincer palladacycles, PdYCY' which are PdNCS (**4**), PdSCP (**5**) and PdNCP (**6**) (Figure 6.6). These structural and energetic findings will be compared with experimental activity data to infer the role the donor atoms (Y, Y') play in the effective formation reaction of the active Pd(0) catalyst. This study starts from the investigation of Pd(0) formation of PdYCY and PdYCY' in the absence and presence of the base; then, the effects of non-polar and polar solvents are determined. This work has been published in "Journal of Organometallic Chemistry".¹⁸⁸

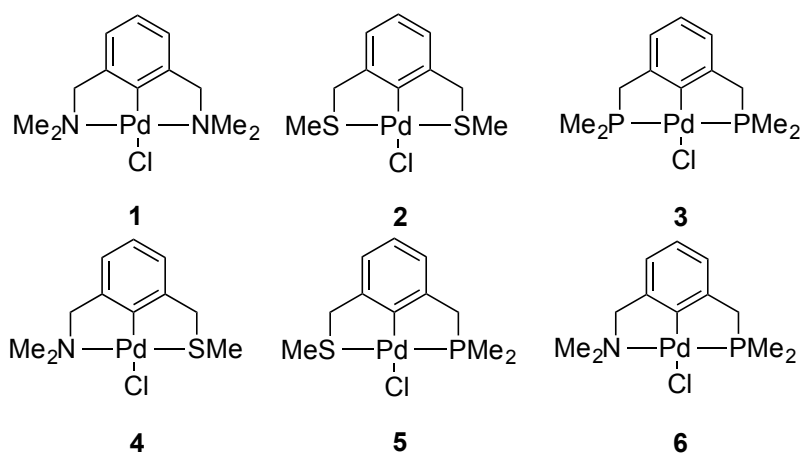


Figure 6.6. The symmetrical (**1-3**) and unsymmetrical (**4-6**) pincer palladacycles used in this study.

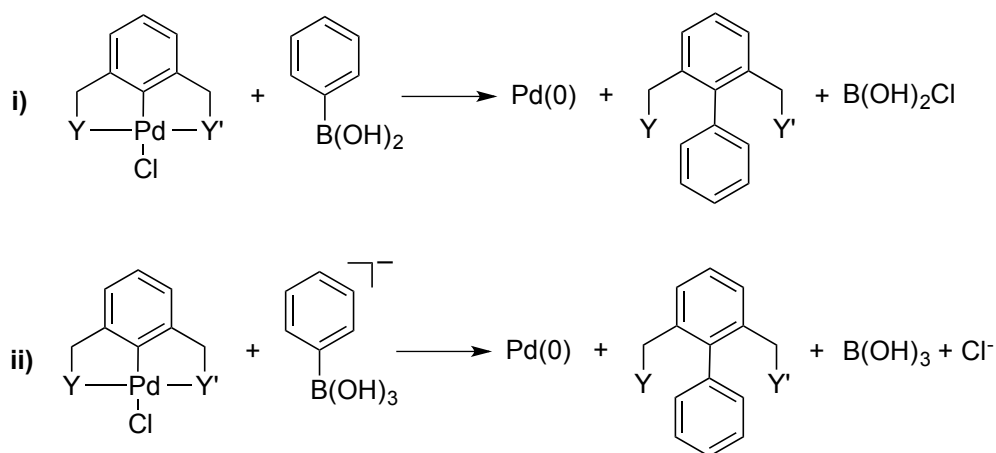
6.3 Computational details

All structures along the reaction pathways were optimised using the GGA PBE.^{45,46} The 6-31+G(d,p) basis set was used for C, H, Cl, O and B atoms while the SDD⁵⁷ effective core potentials (ECP) were used for describing Pd. In Chapters 3 and 4, it was shown that the PBE/6-31+G(d,p)[SDD] is a good method and basis set for studying the structure of pincer palladacycles. The vibrational frequencies were used for confirming the minimum structures which have no imaginary frequencies, while transition structures have one imaginary frequency. Eigenvector following was used in each case to ensure the transition state structure connected the desired minima. Single point energy calculations were performed at ω B97XD⁵³ which includes non-covalent interactions that are important to obtain accurate energetics.^{79,134–136} 6-311++G(2df,2p) was used for all atoms except Pd, for which SDD was used. Zhao and Truhlar¹³⁶ showed the ω B97XD functional is one of the best of the 30 functionals they tested. They showed that it had the smallest average mean unsigned error for calculating a range of reaction energies. All calculations in the present work were performed with the Gaussian 09 program.⁸⁷

Solvent effects were considered using continuum solvation models. The polarisable continuum model (PCM)⁶⁰ using Universal Force Field (UFF) atomic radii were employed to do single point energy calculation at the ω B97XD/6-311++G(2df,2p)[SDD] level of theory of all PBE/6-31+G(d,p)[SDD] optimised structures. The solvents considered were; the non-polar solvents toluene ($\epsilon = 2.374$) and tetrahydrofuran, THF ($\epsilon = 7.426$) and the polar solvent acetonitrile ($\epsilon = 35.688$), where ϵ is the dielectric constant.

6.4 Results and discussion

Scheme 6.16 presents the Pd(0) formation reaction from pincer palladacycles in the absence and the presence of a base. It has been experimentally proven by Serrano *et al.*¹⁷⁶ that the reaction can occur without base when mixing imine-palladacycles with PhB(OH)₂ in distilled THF at ambient temperature. Smith *et al.*¹⁸⁹ proposed that the reaction can occur with base, where the PhB(OH)₂ is bound by base to produce the arylboronate species (PhB(OH)₃⁻), the active species for the reaction. Therefore here the Pd(0) formation reaction mechanism from the pincer palladacycle is investigated in the absence of the base using arylboronic acid (PhB(OH)₂) and in the presence of the base using (PhB(OH)₃⁻). In this work, the Pd(0) formation reaction pathways from PdYCY, PdNCS, PdSCP and PdNCP in base-free condition are labelled as **A**, **B**, **C** and **D**, respectively, i.e. **Int1A** is an intermediate 1 for Pd(0) formation reaction from PdYCY (Table 6.1). In the presence of the base condition, PdYCY, PdNCS, PdSCP and PdNCP are labelled as **E**, **F**, **G** and **H**, respectively (Table 6.1).

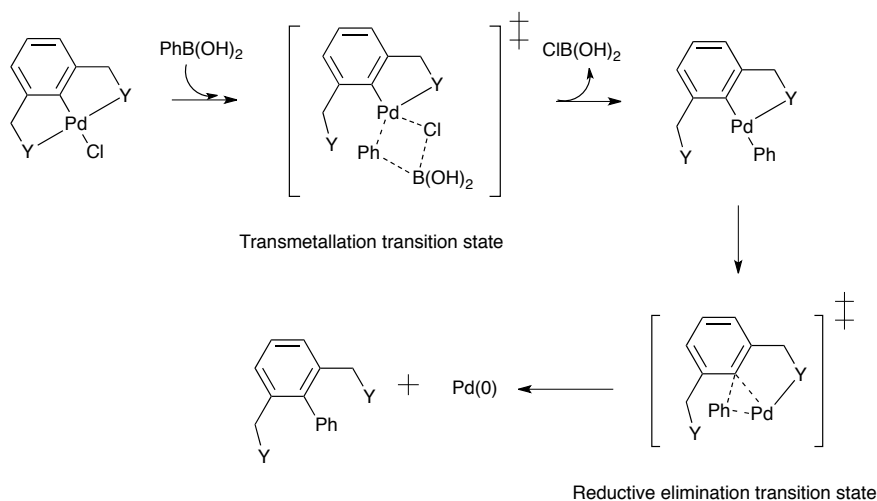


Scheme 6.16. Pd(0) formation for the pincer palladacycles **i)** without base and **ii)** with base.

Table 6.1. The label for Pd(0) formation reaction from each pincer type presented in this work, where Y = N, S or P.

Label	Pincer type	Condition
A	PdYCY	base-free
B	PdNCS	base-free
C	PdSCP	base-free
D	PdNCP	base-free
E	PdYCY	with base
F	PdNCS	with base
G	PdSCP	with base
H	PdNCP	with base

Based on Aleksanyan and co-workers' work,¹⁷¹ we proposed the general reaction mechanism of Pd(0) formation given in Scheme 6.17. There are two main processes in this reaction; a transmetallation (TM) step and a reductive elimination (RE) step.



Scheme 6.17. Proposed mechanism of generation of Pd(0) from pincer palladacycle by phenylboronic acid.

First of all, we have studied the geometry of phenylboronic acid, PhB(OH)₂ (Figure 6.7). There are three possible conformers of PhB(OH)₂. The calculation shows that the coordination sphere around boron of conformers i and ii is planar while conformer iii is distorted planar. The torsion angles (C-C-B-O) of conformer i, ii, and iii are 0.0, 0.0 and 30.1 degrees, respectively. In term of structural stability, conformer i is the most stable, whereas conformer iii is the least stable. The relative energies of conformer i, ii and iii compared with the conformer i are 0.0, 9.0 and 12.5 kJ mol⁻¹, respectively. Therefore, conformer i of PhB(OH)₂ shown in Figure 6.7 will be used to study the Pd(0) formation reaction mechanism.

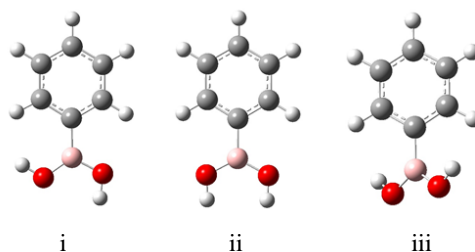


Figure 6.7. Geometrical optimisation of PhB(OH)_2 conformers i, ii and iii.

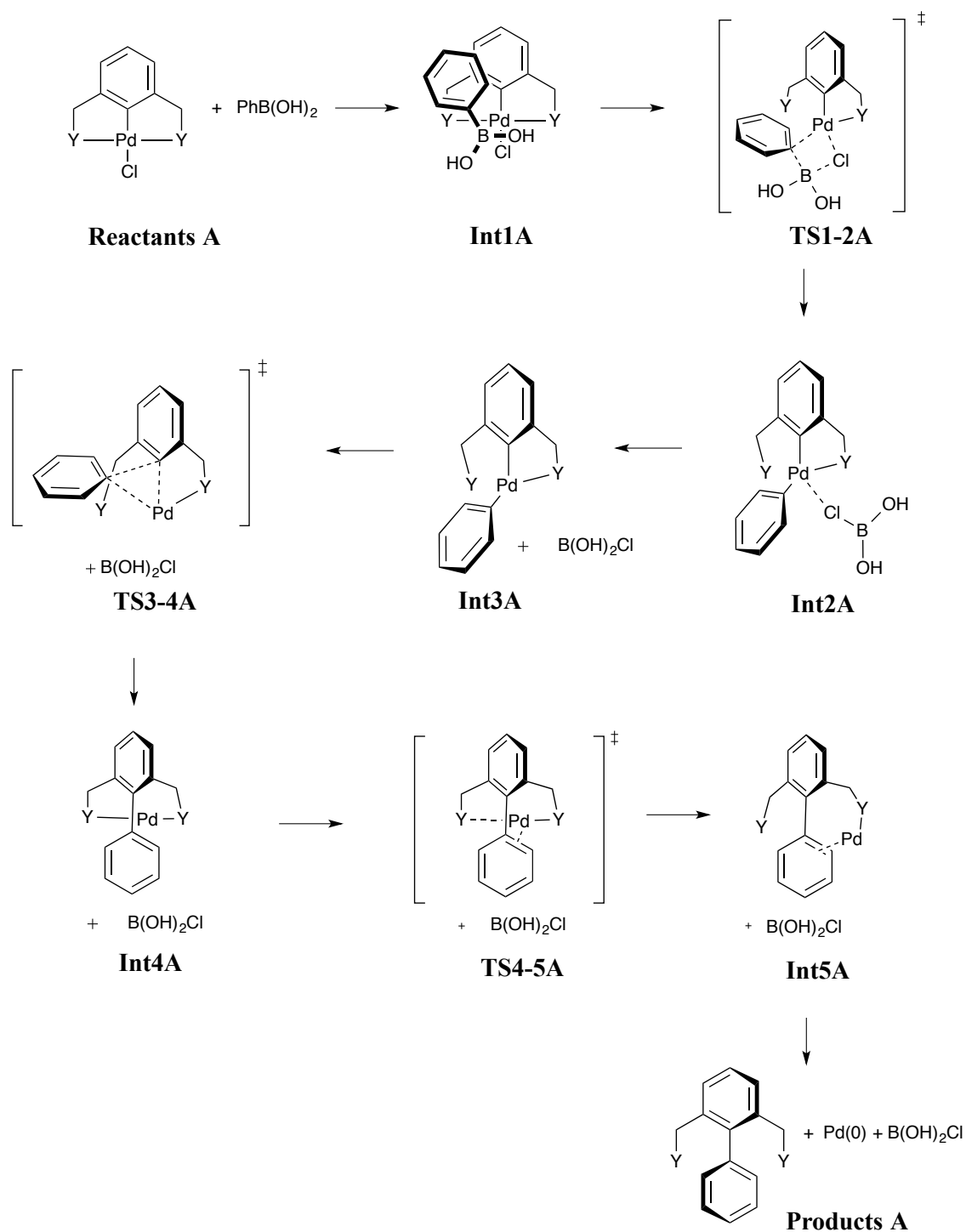
6.4.1 Base-free Pd(0) formation from symmetrical pincer palladacycles

We first consider the Pd(0) formation reaction mechanism of the symmetrical pincer palladacycles (PdYCY). The reaction mechanism of PdYCY is shown in Scheme 6.18. Figure 6.8 shows the Gibbs free energy profile of PdYCY where Y is N, S and P and the Gibbs free energy profile is relative to the energy of the separated reactants ($\text{PdYCY} + \text{PhB(OH)}_2$).

The reaction begins with the non-covalent interaction between the pincer palladacycle and the phenylboronic species (**Int1**). The Gibbs free energy in this step shows that **Int1** from PdPCP is more stable than **Int1** from PdNCN and PdSCS. **Int1** from PdPCP is the most stable due to the orientation of phenylboronic species relative to the pincer palladacycle.^{190,191}

In the TM transition state (**TS1-2**), the geometries of this transition state structure are shown in Figure 6.9. They represent the phenyl migration from the boronic species to the Pd-centre and involve the bond breaking of C-B and Pd-Cl and the bond forming of Pd-C and B-Cl *via* the concerted four-membered ring of Pd-C-B-Cl. The distance of Pd-C decreases while the distance of Pd-B increases in **TS1-2** compared with **Int1**. The Gibbs free energy barrier of the PdPCP reaction with 289.4 kJ mol^{-1} is the highest whilst the energy barriers of the PdNCN with 202.2 kJ mol^{-1} and PdSCS with 208.8 kJ mol^{-1} are similar. The results from Braga *et al.*,¹⁹² who studied the TM process from $[\text{PhPd}(\text{PH}_3)_2\text{Br}]$ with PhB(OH)_2 without base, where they used the B3LYP method and 6-31G(d) for all atoms except LANL2DZ for Pd and Br, found a high-energy barrier of the TM transition state (243.1 kJ mol^{-1}). The energy barrier of PdPCP in this work without thermal correction to Gibbs free

energy is $286.2 \text{ kJ mol}^{-1}$. This has a higher energy barrier than that of Braga *et al.* but has a similar magnitude. The overall TM reaction process using PdPCP in this work without thermal correction to Gibbs free energy is $172.4 \text{ kJ mol}^{-1}$ compared to $134.7 \text{ kJ mol}^{-1}$ found in the work of Braga *et al.* This shows that the reaction is endothermic similar to that reported by Braga *et al.* The Gibbs free energy barrier for TM with PdPCP is significantly larger than for PdNCN and PdSCS since the Pd-P bond is stabilised by the σ -donating and π -accepting character of the phosphine¹³⁹ leading to a strong interaction between Pd and phosphine compared to the Pd-S and Pd-N interactions.



Scheme 6.18. Catalytically active Pd(0) species formation reaction from symmetrical pincer palladacycles.

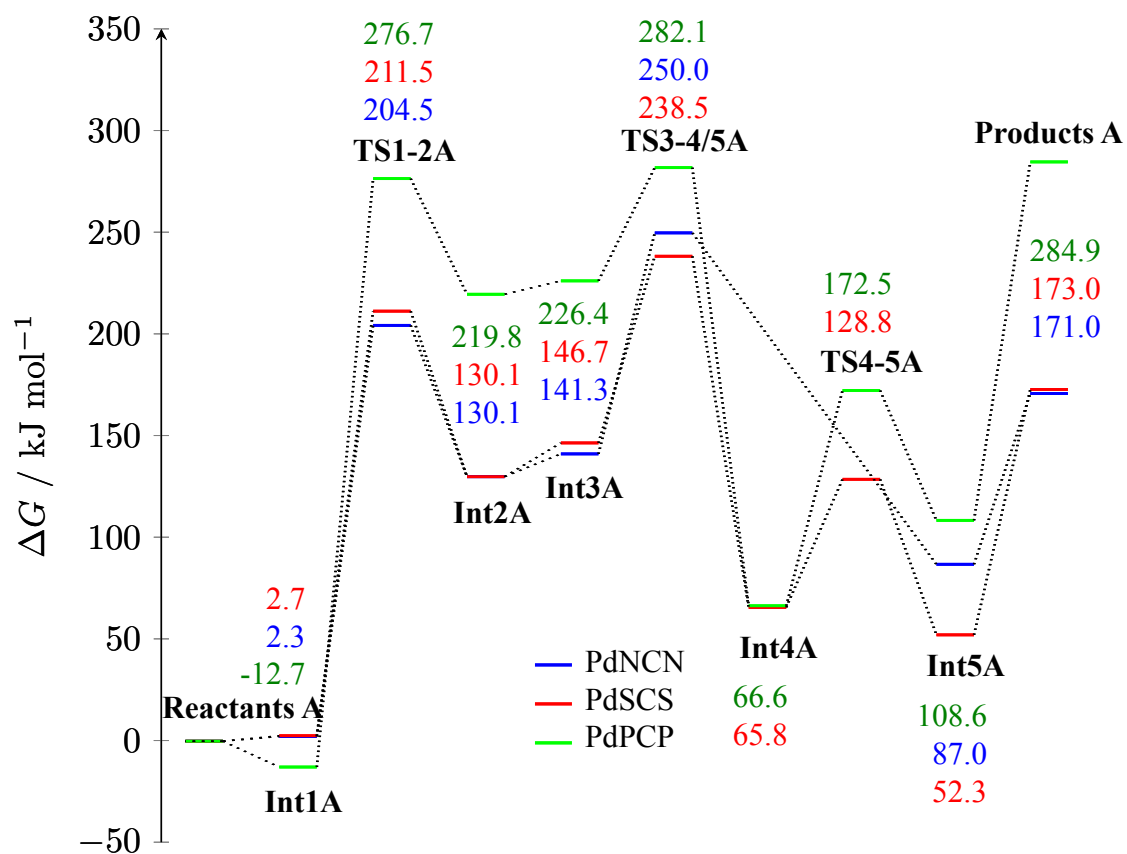


Figure 6.8. The Gibbs free energy profile of symmetrical pincer palladacycles to generate catalytically active Pd(0) species (base-free).

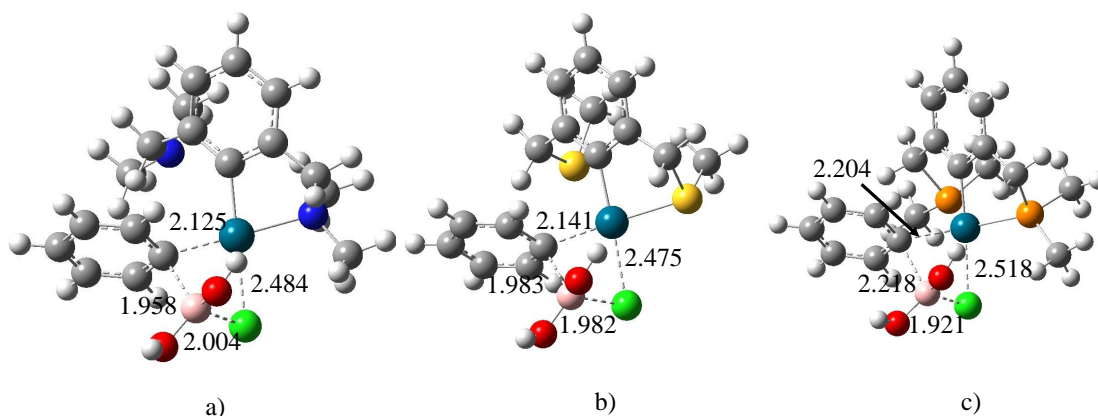


Figure 6.9. Geometry of the transition state structure for the transmetalation step **TS1-2** in the base-free for Pd(0) formation from a) PdNCN, b) PdSCS and c) PdPCP (grey = C, white = H, blue = N, red = O, pink = B, blue/green = Pd, light green = Cl, yellow = S and orange = P). Distances are in angstroms.

Then, $B(OH)_2Cl$ is removed from the complex; this involves the cleavage of the intermolecular interaction between **Int2** and $B(OH)_2Cl \rightarrow$ **Int3**. This process is endergonic. The structures of **Int3** in all cases have only one arm of the pincer ligand coordinated to the Pd-centre (Scheme 6.18).

The RE takes place leading to Pd(0) formation in **TS3-4/5** involving a three-centred dissociative transition state.^{137,193,194} In these calculations, we have found that RE involves the aryl group migrating to form a C-C bond and removing Pd from the complex (Scheme 6.18). The geometries of this transition are shown in Figure 6.10. In the case of PdNCN, the RE proceeds *via* a single transition step (**TS3-5**) due to the weaker interaction between Pd and N and the Gibbs free energy barrier of this step for PdNCN is $108.7 \text{ kJ mol}^{-1}$. **Int5** is the Pd coordination with N and with the aromatic ring before it is removed from the molecule. The aromatic ring interaction with Pd was found in the experimental data of palladium complexes, studied by Ossor *et al.*¹⁹⁵ In the cases of PdSCS and PdPCP, these proceed *via* two transition steps; RE (**TS3-4**) and a de-coordination (DC) transition step (**TS4-5**). The RE for PdSCS and PdPCP leads to the re-coordination of the side arm to form **Int4** due to the stronger interaction between Pd-S bond and Pd-P bond. The Gibbs free energy barrier from PdPCP is the lowest at 55.7 kJ mol^{-1} compared to RE of PdSCS which is 91.8 kJ mol^{-1} and PdNCN which is $108.7 \text{ kJ mol}^{-1}$. Then the

TS4-5 in the next step represents the ligand arm DC from Pd(0).

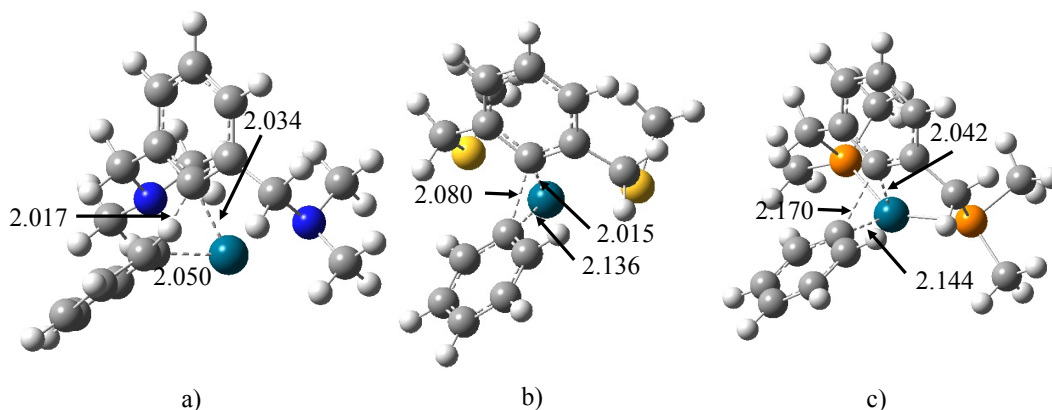


Figure 6.10. Geometry of the transition state structure for the reductive elimination step **TS3-4/5** in the base-free for Pd(0) formation from a) PdNCN, b) PdSCS and c) PdPCP (grey = C, white = H, blue = N, blue/green = Pd, yellow = S and orange = P). Distances are in angstroms.

The DC transition state (**TS4-5**) shows that the bond between Pd and donor atom is breaking, while the bond between Pd and C is forming. The Gibbs free energy barrier in this step from PdPCP is $105.9 \text{ kJ mol}^{-1}$ which is higher than from PdSCS which is 63.0 kJ mol^{-1} . The final product formation (**Int5** \rightarrow **Product**) requires 84.0 , 120.7 and $176.3 \text{ kJ mol}^{-1}$ for PdNCN, PdSCS and PdPCP, respectively. Overall, the Pd(0) active species formation reactions are endergonic processes with a total Gibbs free energy of 171.0 , 173.0 and $284.9 \text{ kJ mol}^{-1}$ for PdNCN, PdSCS and PdPCP, respectively. From these calculated results, it is shown that a lot of energy is required for generating the Pd(0) active species indicating that it is not realistic from an experimental perspective. However, there are many possible pathways to cleavage the Pd(0) species from the compound but in here we have used the simplest model which is the direct Pd(0) de-coordination from the compound to investigate the Pd(0) active species formation. In comparison of the two main steps, the results show that the transmetalation reaction has a larger energy barrier than the reductive elimination in all cases agreeing with palladium-catalysed Pd(0) formation calculation using a N- and P-chelating ligand with phenyl boronic acid.¹⁸²

6.4.2 Base-free Pd(0) formation from unsymmetrical pincer palladacycles

In this section, the Pd(0) formation reactions from unsymmetrical pincer palladacycles PdYCY' which are PdNCS, PdSCP and PdNCP were investigated to determine the role and effect of the donor ligand arms on the reaction mechanism pathway. The Gibbs free energy profile of Pd(0) formation from PdNCS, PdSCP and PdNCP are shown in Figure 6.11, Figure 6.12 and Figure 6.13, respectively where the relative Gibbs free energy of all reactions are compared with each PdYCY' + PhB(OH)₂. The full schemes of the reaction mechanism are provided in Scheme 6.19, Scheme 6.20 and Scheme 6.21 for PdNCS, PdSCP and PdNCP, respectively.

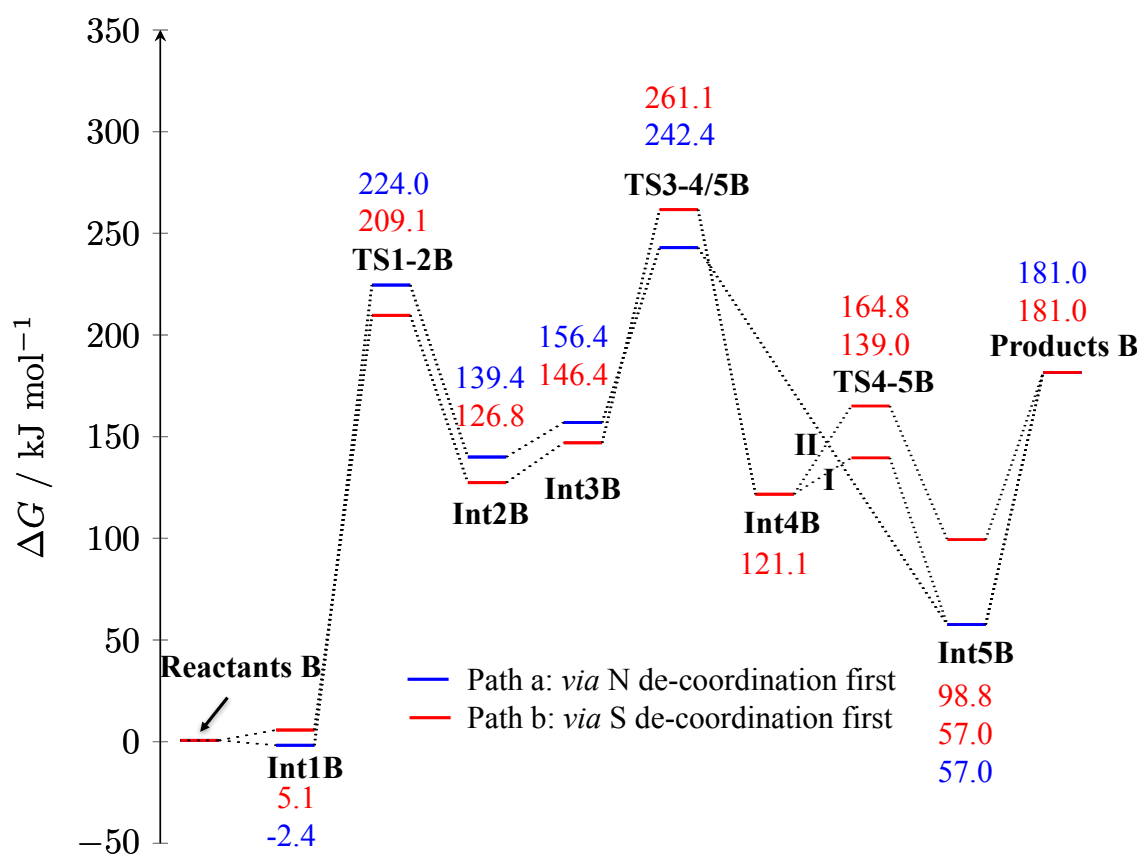


Figure 6.11. The Pd(0) formation reaction mechanism from PdNCS. The blue pathway shows the route of Pd(0) formation reaction *via* N de-coordination from Pd at **TS1-2** and the red pathway shows the route *via* S de-coordination from Pd. Route **I** represents the pathway *via* breaking the N-Pd bond and route **II** represents the pathway *via* breaking S-Pd bond (base-free).

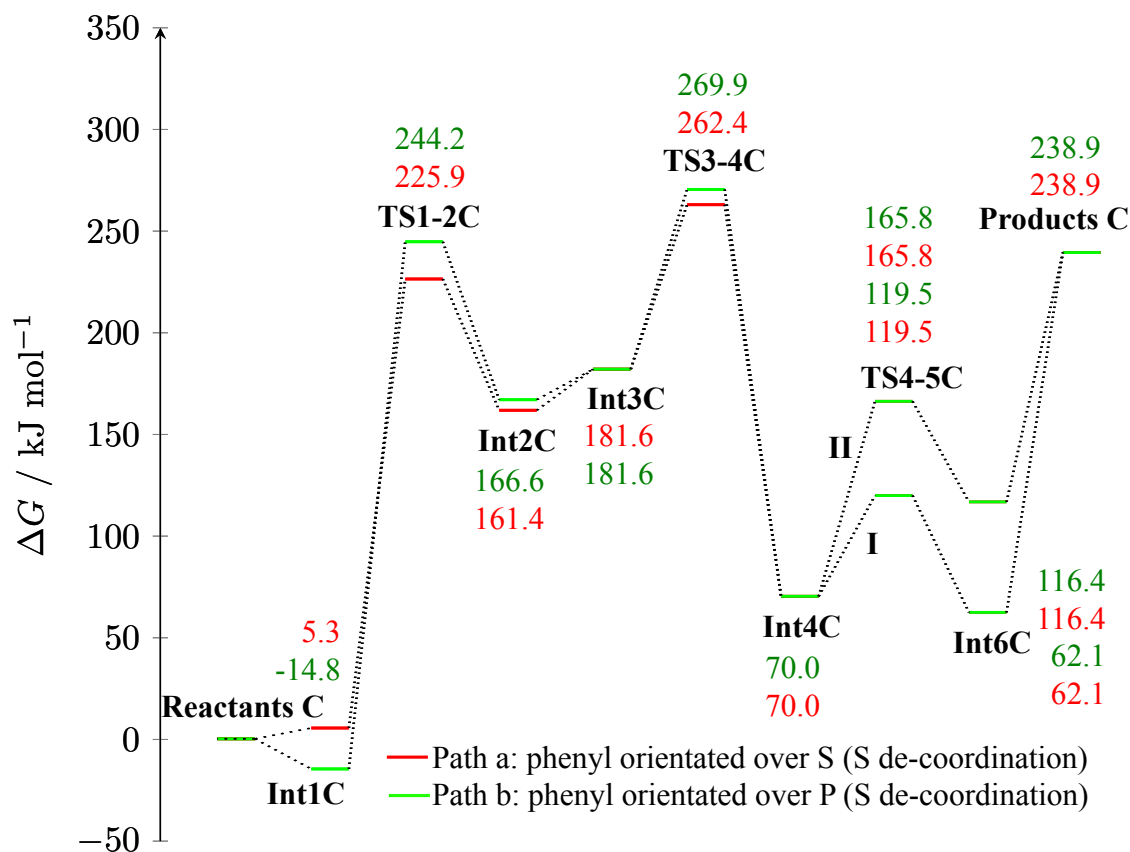


Figure 6.12. The Pd(0) formation reaction mechanism from PdSCP. The red pathway shows the route of Pd(0) formation reaction *via* phenyl orientated over S at **Int1** and the green pathway shows the route *via* phenyl orientated over P. Route **I** represents the pathway *via* breaking the S-Pd bond and route **II** represents the pathway *via* breaking the P-Pd bond (base-free).

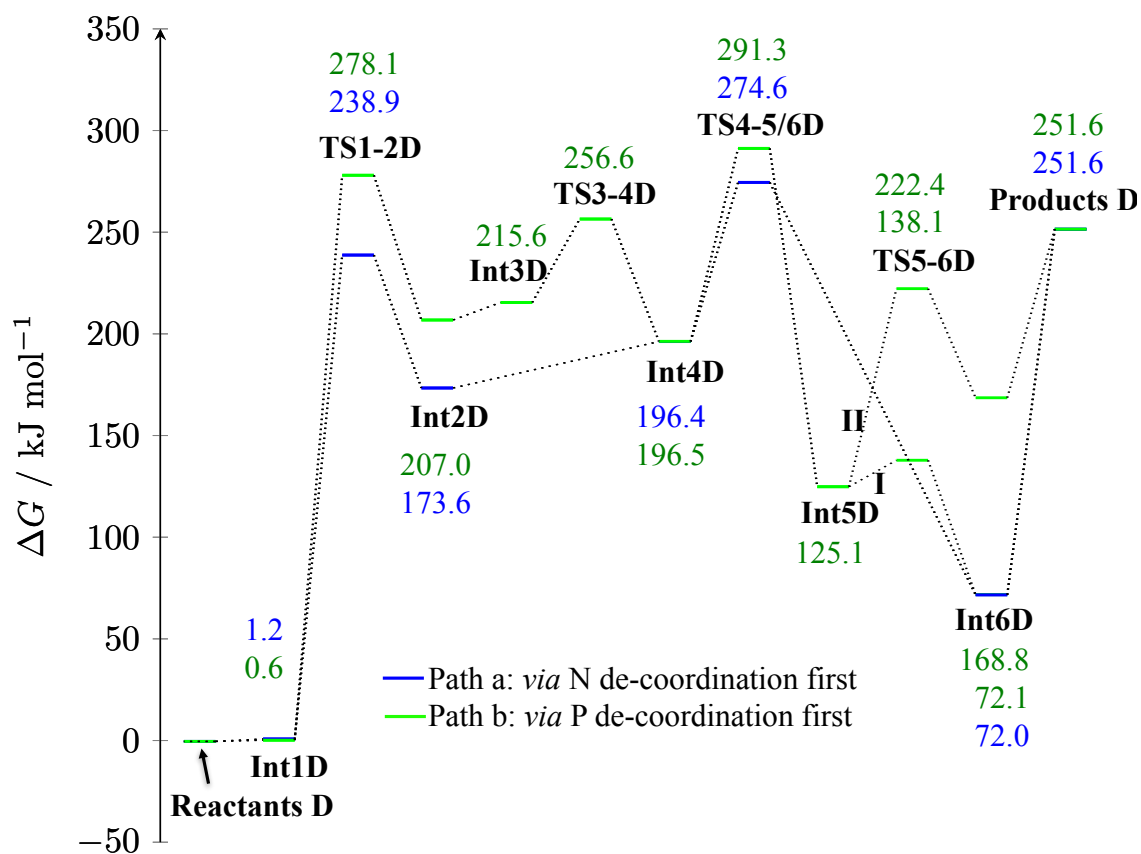
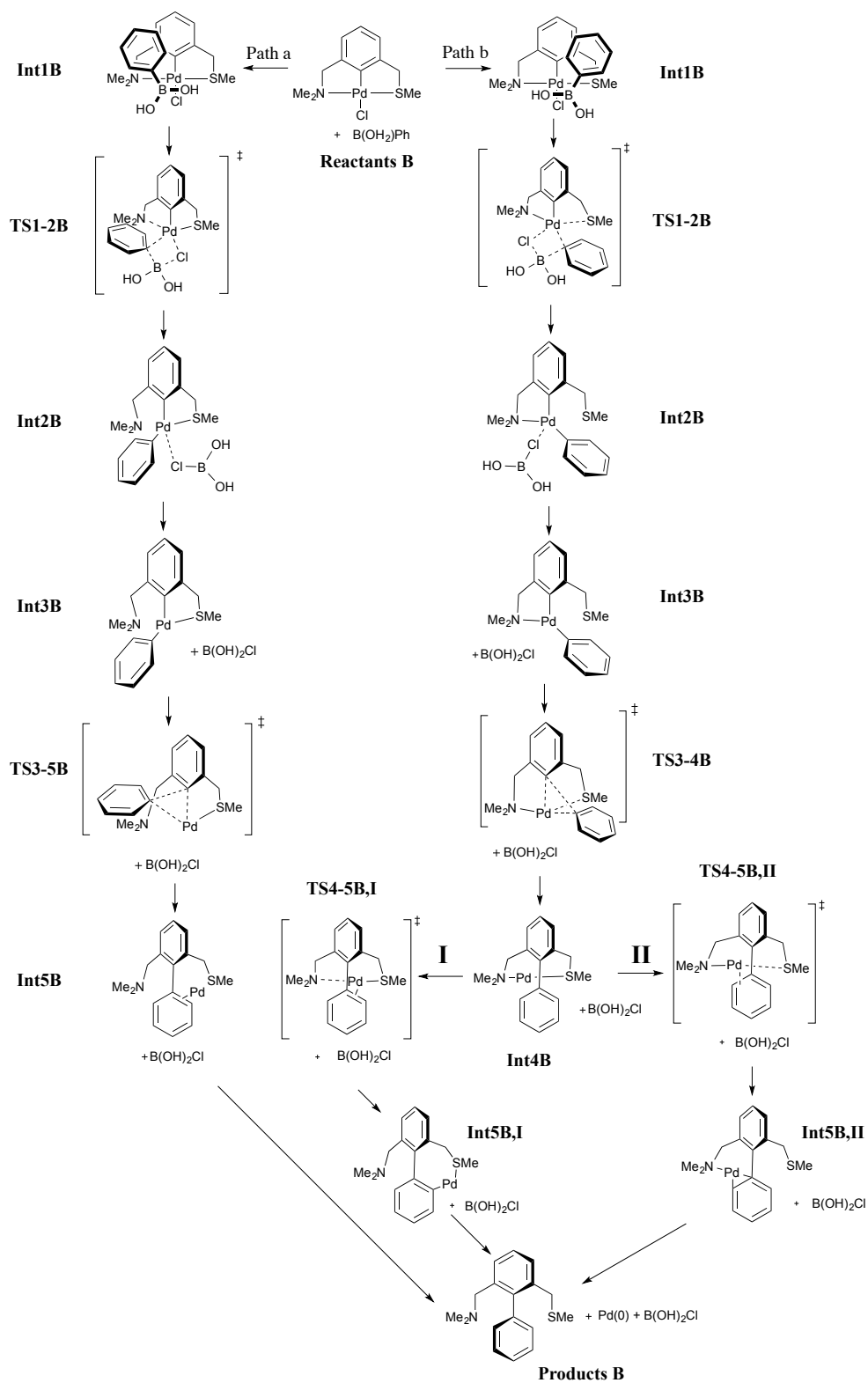
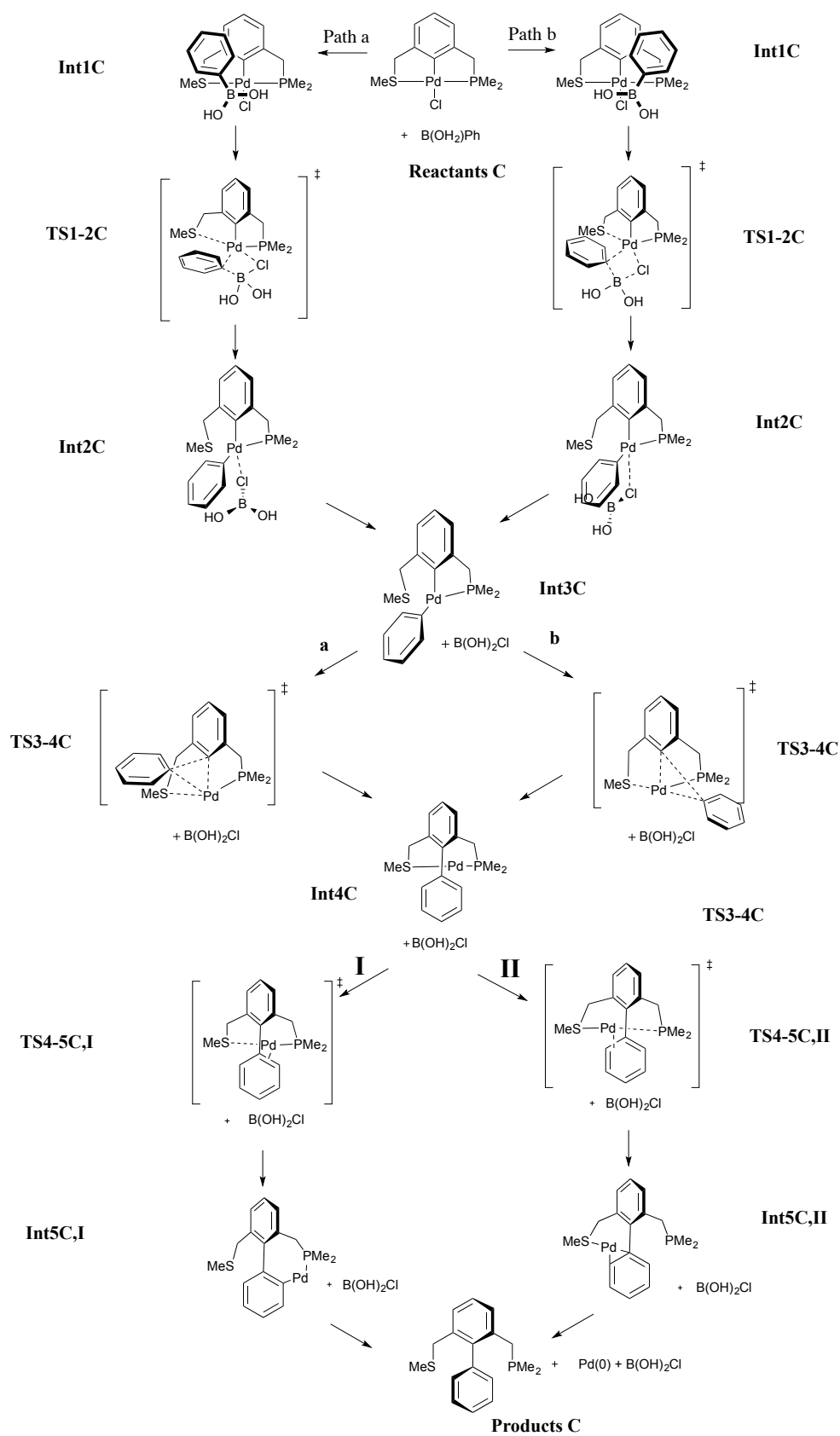


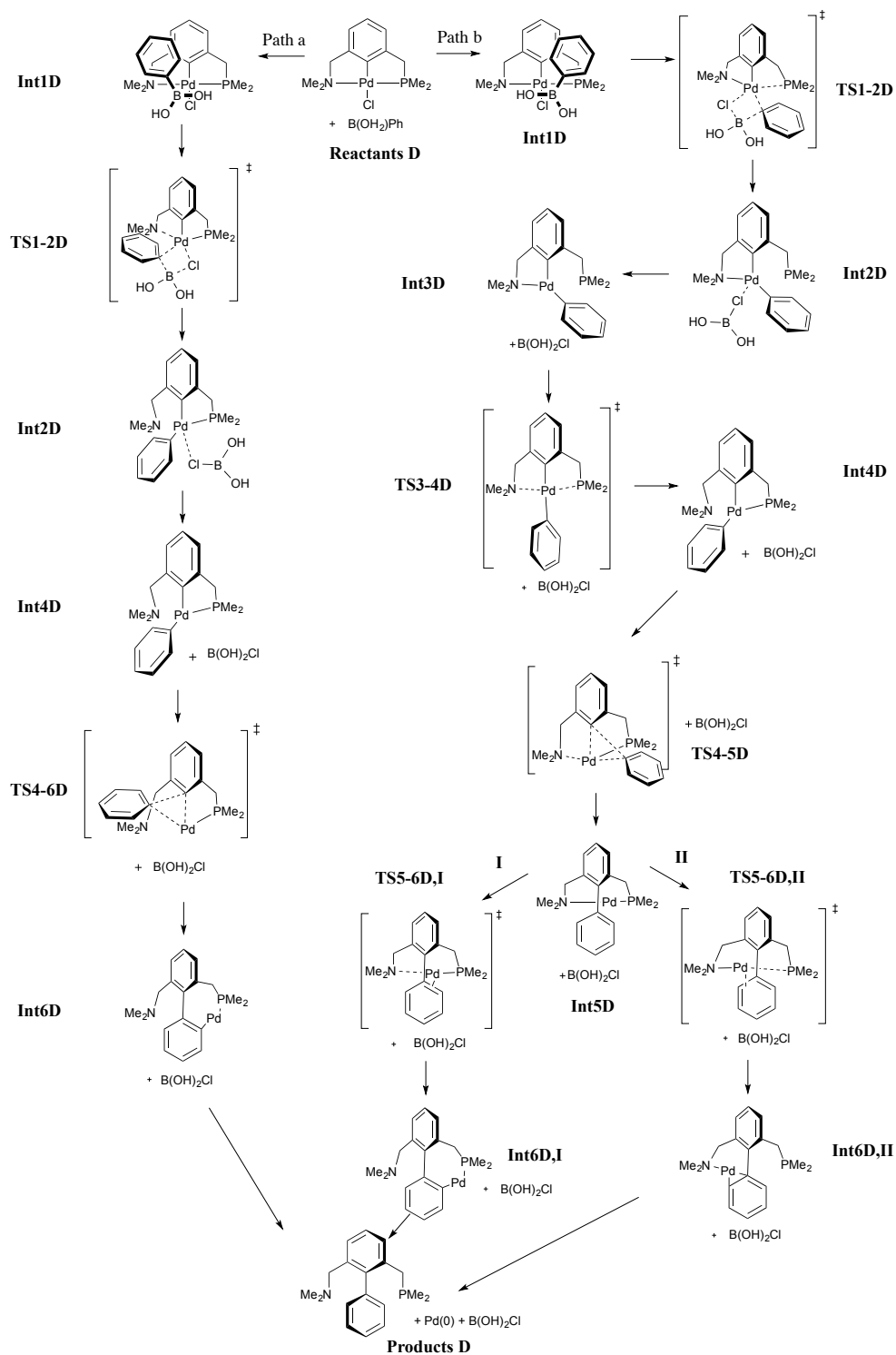
Figure 6.13. The Pd(0) formation reaction mechanism from PdNCP. The blue pathway shows the route to Pd(0) formation *via* N de-coordination from Pd at **TS1-2** and the green pathway shows the route *via* P de-coordination from Pd. Route **I** represents the pathway *via* breaking the N-Pd bond and the route **II** represents pathway *via* breaking the P-Pd bond (base-free).



Scheme 6.19. Catalytically active Pd(0) species formation reaction from unsymmetrical NCS pincer palladacycle (PdNCS).



Scheme 6.20. Catalytically active Pd(0) species formation reaction from unsymmetrical SCP pincer palladacycle (PdSCP).



Scheme 6.21. Catalytically active Pd(0) species formation reaction from unsymmetrical NCP pincer palladacycle (PdNCP).

In the first step of all unsymmetrical pincer palladacycles, **Int1B**, **Int1C** and **Int1D** are concerned with the interaction between PdYCY' and PhB(OH)₂. The unsymmetrical pincer palladacycles have two different ligand donor arms, leading to two possible pathways depending on either Y de-coordination first or Y' de-coordination first from Pd. The results of the computational calculation show that in **Int1B** for PdNCS of the N de-coordination from Pd first (blue pathway) and S de-coordination from Pd first (red pathway), the PhB(OH)₂ interaction with PdNCS produces **Int1B**. The Gibbs free energies of **Int1B** for both cases are quite similar, differing by 7.5 kJ mol⁻¹ (Figure 6.11). For the Pd(0) formation from PdNCP, it was also found that PdNCP corresponds to two different arm de-coordinations, i.e. N or P de-coordination first from Pd (Scheme 6.21) and **Int1D** for both cases has similar energy, only differing by 0.6 kJ mol⁻¹ (Figure 6.13). For PdNCS, only S de-coordination from the Pd-centre has been found but there are still two pathways which are path a and path b corresponding to the orientation of the phenyl group in the boronic species (Scheme 6.20). The Gibbs free energy difference between **Int1C** path a and **Int1C** path b is 20.1 kJ mol⁻¹. In the TM step, each reaction mechanism follows the same mechanism as the symmetrical pincer palladacycles. The geometries for PdYCY' of the TM structures are shown in Figure 6.14.

In the removal of the B(OH)₂Cl from **Int2**, the reaction is endergonic in all cases. Next, the Pd is eliminated in the RE step. However, for PdNCP path b an additional step occurs just prior to RE step. This involves a phenyl rotation (**Int3D** → **Int4D**).

In the RE process, for PdNCS, the Gibbs free energy barrier is 28.7 kJ mol⁻¹ lower when N de-coordinated first (**TS3-5B**) compared to when S de-coordinated first (**TS3-4B**) because **TS3-5B** is stabilised by strong S-Pd interaction compared to the N-Pd interaction in **TS3-4B**. Focusing on **TS3-4B** in the path of S de-coordination first, an additional re-coordination step is found after the RE step leading to both arms coordinating to Pd. In **TS4-5B** these results show that the transition energy barrier of N de-coordination (route **I** in Scheme 6.19) has a lower energy than S de-coordination (route **II**), which corresponds with the bond strength between Pd-N being weaker than Pd-S (as discussed in Chapter 5). The product **Int5B** *via* route **I** is significantly more stable than **Int5B** *via* route **II**. For PdSCP, the Gibbs free

energy barriers of both pathways differ by only 7.5 kJ mol^{-1} . The **TS3-4C** in both cases produce the same intermediate **Int4C** in which the Pd(0) coordinates with both the P and the S donor atoms simultaneously. Then, there are two routes for de-coordination from the donor atom which are S de-coordination from Pd in route **I** and P de-coordination in route **II** (Scheme 6.20). The energy barrier of the de-coordination step shows that route **II** has a higher energy barrier than route **I** as the interaction between P and Pd is stronger than that between S and Pd (Figure 6.12). For PdNCP, the transition from **Int4D** to **Int5D** *via* **TS4-5D** (green pathway), there is a re-coordination step, leading to both arms coordinating to Pd, whereas **TS4-6D** has not found this coordination, so only **Int6D** occurs. In the de-coordination step (**TS5-6D**), the calculation shows that N de-coordination from Pd has lower energy than P de-coordination from Pd. The bond strength of Pd-P is much greater than Pd-N so it is easier to cleave the bond between Pd-N (as discussed in Chapter 5). For **Int6D** the Pd coordination of both P and Ph is more stable than coordination with N and Ph in agreement with the results using symmetrical pincer palladacycles which showed that the Pd coordination with P is stronger than coordination with N.

The total Gibbs free energy of the Pd(0) active species formation reaction from unsymmetrical pincer palladacycles is greater than zero in all cases, indicating that the reaction is endergonic. Furthermore, in the reaction mechanism, when the pincer palladacycle has a S or P donor ligand arm, an additional DC step occurs after the RE step, similar to the situation for PdSCS and PdPCP.

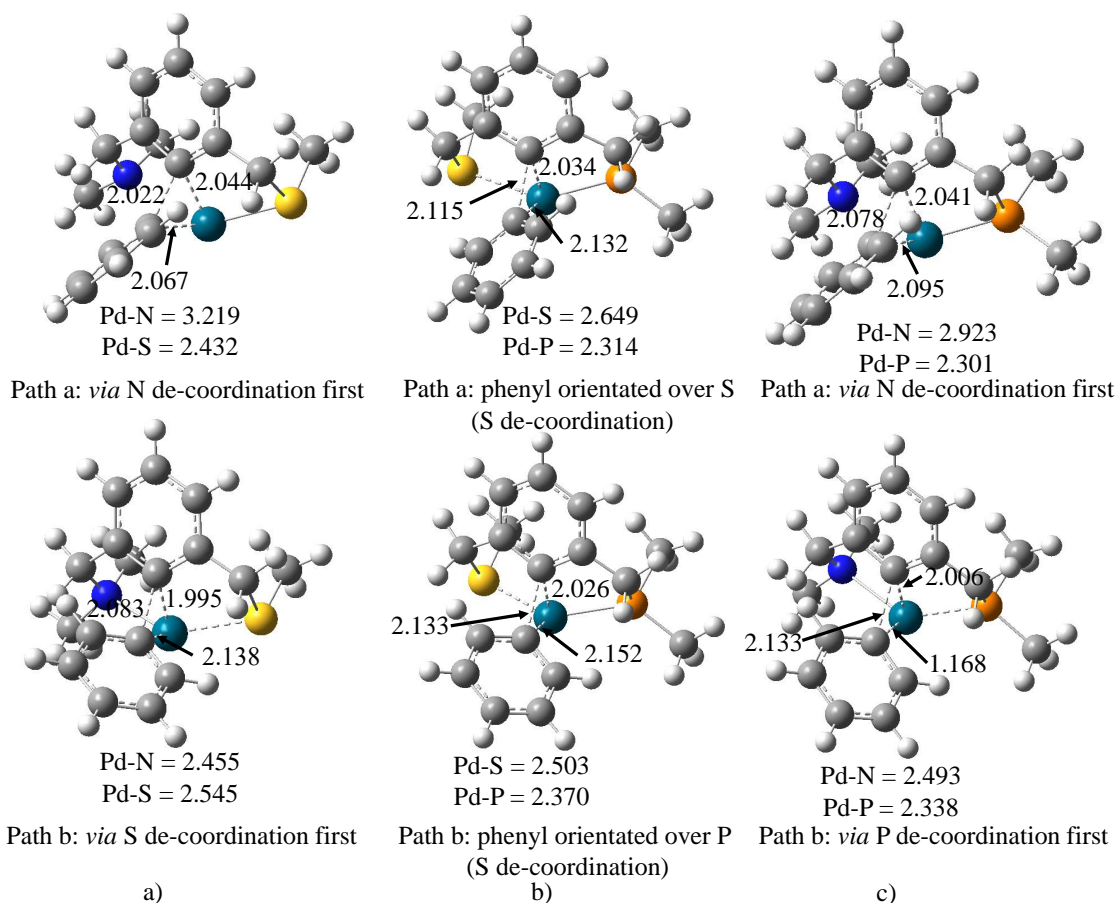


Figure 6.15. Geometry of the transition state structure for the reductive elimination step for Pd(0) formation from a) PdNCS, b) PdSCP and c) PdNCP (grey = C, white = H, red = O, pink = B, blue/green = Pd, light green = Cl, blue = N, yellow = S and orange = P). Distances are in angstroms.

6.4.3 Pd(0) formation reaction in the presence of a base

A base is normally required in the Suzuki-Miyaura cross-coupling reaction but the role of it has not been clarified.¹⁹⁶ For checking the effect of the base in the Pd(0) formation reaction, we have investigated the reaction following Scheme 6.16ii). The OH⁻ is chosen since it is the simplest, typical base. The reaction in the presence of the base starts from the organoboronic species binding to the base OH⁻ to form the organoboronate species PhB(OH)₃⁻. In the literature, PhB(OH)₃⁻ species was used for studying the presence of the base condition in the Suzuki-Miyaura cross-coupling reaction calculation.^{192,197,198} Therefore, based on Scheme 6.16ii), the Pd(0) formation reaction with base are studied using PhB(OH)₃⁻ as the reactant interacting with the pincer palladacycles.

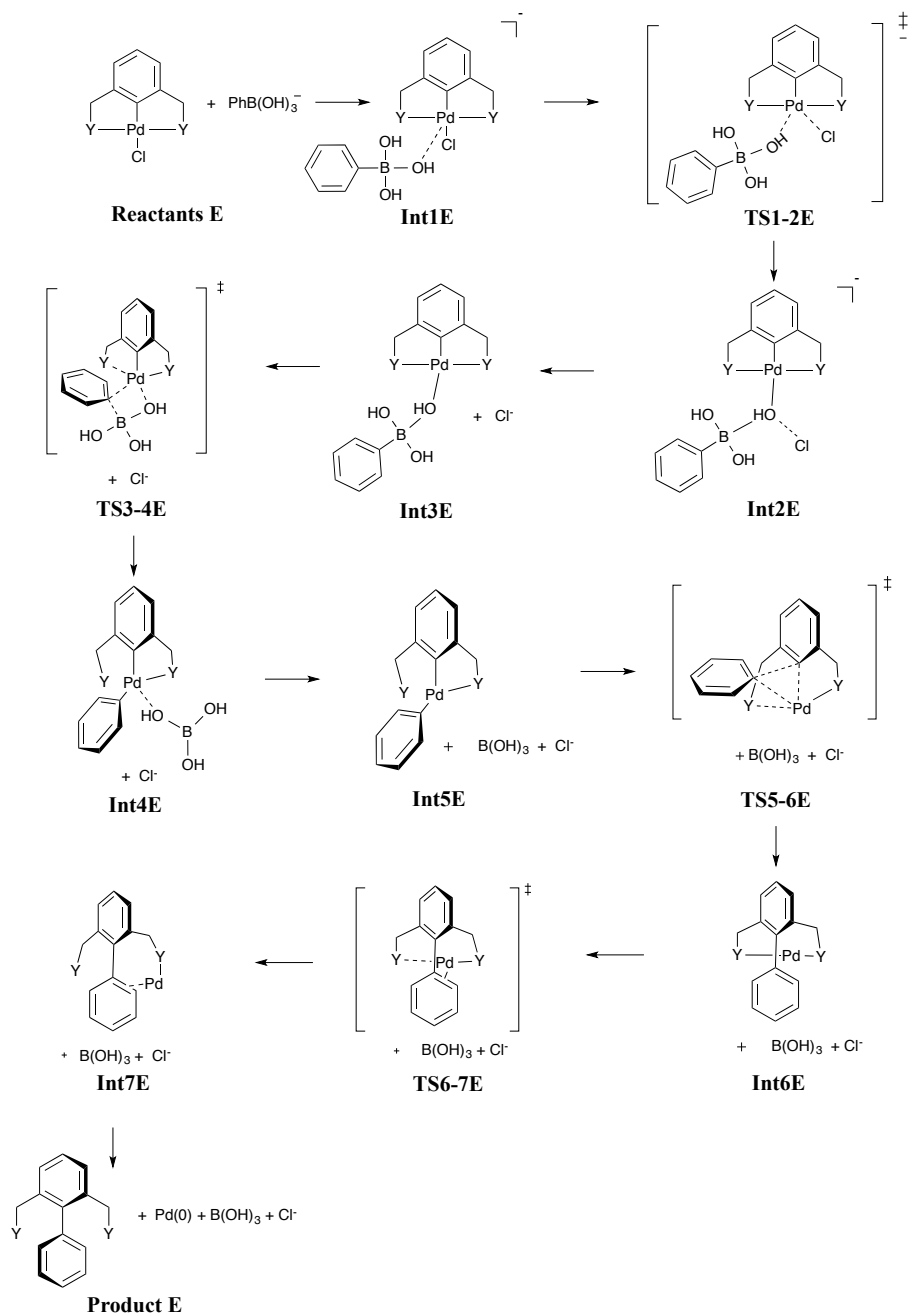
Firstly, the Pd(0) formation reaction generated from PdNCN, PdSCS and PdPCP are discussed. The general Pd(0) formation mechanisms for them are shown in Scheme 6.22. The initial step for this reaction starts with the intramolecular interaction between PdYCY and PhB(OH)_3^- to form **Int1E** which corresponds to the van der Waals complex of PdYCY and PhB(OH)_3^- . Evidence for a van der Waals complex is supported by Braga and co-workers,¹⁹⁷ who found a van der Waals complex between *trans*-Pd(CH=CH₂)(PH₃)₂Br and (CH=CH₂)B(OH)₃⁻. The Gibbs free energy profile of PdYCY in the presence of the base is presented in Figure 6.16, where the relative energies of the stationary points along the reaction pathway are compared with the separated reactants (PdYCY + PhB(OH)_3^-). Considering the Gibbs free energy formation of **Int1E**, the intramolecular interaction of PhB(OH)_3^- with PdNCN and PdPCP is an exergonic processes compared to **Reactants E** while it is an endergonic process for PdSCS.

The first transition state corresponds to a substitution nucleophilic bimolecular (S_N2) step which is the substitution of the Cl⁻ by the PhB(OH)_3^- in the coordination sphere of the Pd-centre. This process is shown in **TS1-2E** which is *via* a trigonal bipyramidal geometry to form **Int2E**. The intermediate **Int2E** involves the OH bridging between Pd and B, with Cl⁻ binding to the OH bridge. The **TS1-2E** for PdNCN, PdSCS and PdPCP has a low energy barrier of 31.6, 10.6 and 28.5 kJ mol⁻¹, respectively. Then, Cl⁻ is removed from the complex to produce **Int3E**, which is an endergonic process in all cases.

Next, the TM transition state occurs *via* **TS3-4E**. The transition state structure is similar to the instance with no base and takes place through a four-membered ring in which the phenyl migrates from B to the Pd centre. However, in the base-free pathway the four-membered ring involves Cl-B-C-Pd but here it involves O-B-C-Pd. The geometries of the TM step are presented in Figure 6.17. In consideration of the TM energy barrier, the PdPCP pathway has a large barrier of 162.0 kJ mol⁻¹ compared to that from PdNCN of 105.5 kJ mol⁻¹ and PdSCS of 93.5 kJ mol⁻¹ (Figure 6.16).

The RE step under base conditions is similar to that in the absence of the base, including the additional re-coordination of the ligand arm in **Int6E** for PdPCP and PdSCS. For PdNCN, the re-coordination of the ligand arm was not found, instead

Int7E is formed directly from the RE transition state as in the case of the base-free process. The geometry of the RE transition and de-coordination structures in the presence of the base is identical to that in the absence of the base. The energy barrier of RE is 108.6, 91.8 and 55.7 kJ mol⁻¹ for PdNCN, PdSCS and PdPCP, respectively. Moreover, we have found that these values are almost identical to the base-free values which are 108.7, 91.8 and 55.7 kJ mol⁻¹ for PdNCN, PdSCS and PdPCP, respectively.



Scheme 6.22. General mechanism of Pd(0) formation reaction from symmetrical pincer palladacycles with base.

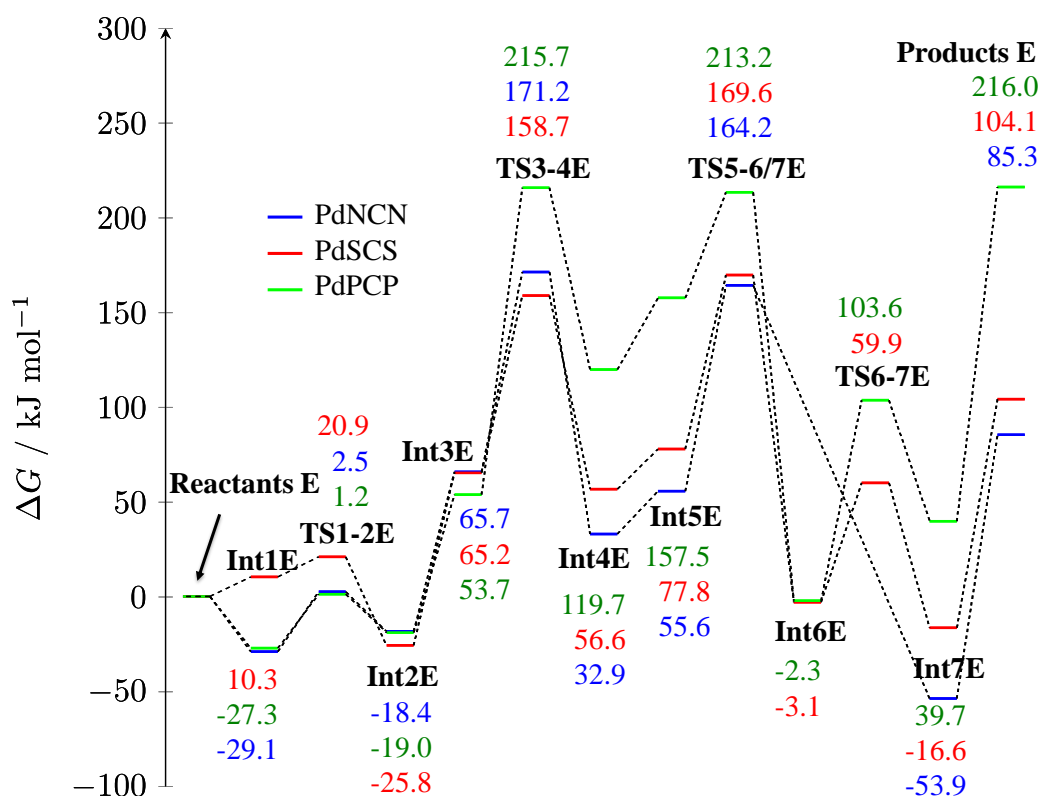


Figure 6.16. The Gibbs free energy profile of symmetrical pincer palladacycles to generate catalytically active Pd(0) species in the presence of the base.

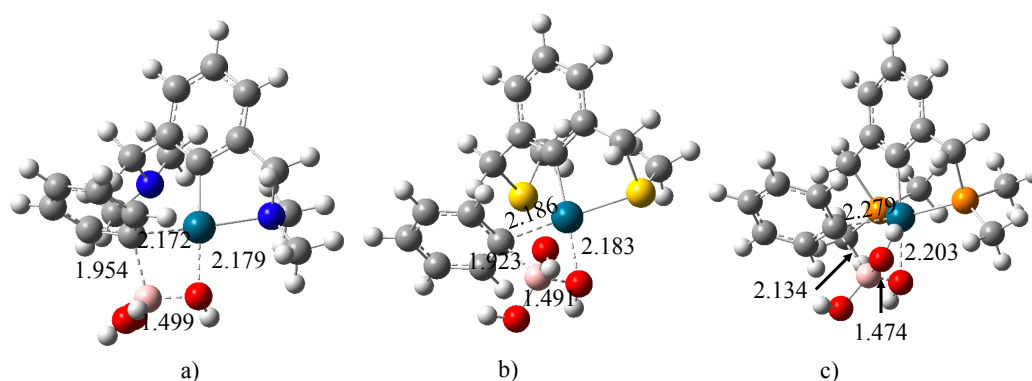


Figure 6.17. Geometry of the transition state structure for the transmetalation step **TS3-4** in the presence of the base for the Pd(0) formation from a) PdNCN, b) PdSCS and c) PdPCP (grey = C, white = H, red = O, pink = B, blue/green = Pd, blue = N, yellow = S and orange = P). Distances are in angstroms.

Within this section, the plausible mechanisms of Pd(0) formation from the unsymmetrical pincer palladacycles, PdNCS, PdSCP and PdNCP, have been investigated in the presence of the base. The full reaction paths are provided in Figure 6.18, Figure 6.19 and Figure 6.20 for PdNCS, PdSCP and PdNCP, respectively. In **Int1** for all cases, the pincer palladacycles bind to $\text{PhB}(\text{OH})_3^-$ to produce a van der Waals complex similar to **Int1** from the symmetrical pincer palladacycle process. The Cl^- is then replaced by $\text{PhB}(\text{OH})_3^-$ *via* a substitution reaction (**TS1-2**) with a low Gibbs free energy barrier of 13.5, 26.8 and 26.7 kJ mol^{-1} for PdNCS, PdSCP and PdNCP, respectively (Figure 6.21). It should be emphasised that the substitution step is the important initial step for the condition with base for both symmetrical and unsymmetrical pincer palladacycles. In the case of the unsymmetrical pincer palladacycle in the absence of the base, the results show that there are two possible pathways, depending on either Y or Y' de-coordination from the Pd-centre for PdNCS and PdNCP in the TM step or depending on the phenyl orientation for PdSCP in the **Int1**, whereas in the presence of the base, only one route has been found for each pincer palladacycle. At this transition step, Pd(0) formation from PdNCS and PdNCP involves N de-coordination from the Pd-centre leading to **Int4** and for PdSCP we have found S de-coordination to produce **Int4**. The Gibbs free energy barrier values of this transition state are 126.2, 122.0 and 130.1 kJ mol^{-1} for PdNCS, PdSCP and PdNCP, respectively (Figure 6.21). Based on the TM barrier, **Int4** from PdNCP is harder to produce than from PdNCS and PdSCP due to having the highest activation energy barrier. Another interesting observation from our calculation is that the activation energy in the presence of the base of all unsymmetric cases is significantly lower than in the absence of the base. The Gibbs free energy barriers with base for PdNCS, PdSCP and PdNCP are 126.2, 122.0 and 130.1 kJ mol^{-1} , respectively while barriers without base for PdNCS, PdSCP and PdNCP are 226.4 (path a: *via* N de-coordination first), 220.6 (path a: phenyl orientated over S) and 237.7 kJ mol^{-1} (path a: *via* N de-coordination first), respectively. The geometrical structures of this step are shown in Figure 6.22 which is the migration of phenyl group from boron to palladium.

The next step is the RE step (**TS5-6/7**). This step is similar to the base-free condition. **Int7s** are produced directly when the formation reaction occurs from

PdNCS (blue path) and PdNCP (green path), while the DC step (**TS6-7**) is found for PdSCP (red pathway). The geometries and the Gibbs free energy barrier at this transition state are identical to the base-free condition. The Gibbs free energy barriers of this step are 86.0, 80.8 and 78.2 kJ mol⁻¹ for PdNCS, PdSCP and PdNCP, respectively. In the case of the DC step for PdSCP, the energy barrier is 49.5 kJ mol⁻¹ for S de-coordination (route **I**) and 95.8 kJ mol⁻¹ for P de-coordination (route **II**). It is also found that the energy barrier of the DC for PdSCP in both the absence and presence of the base are identical.

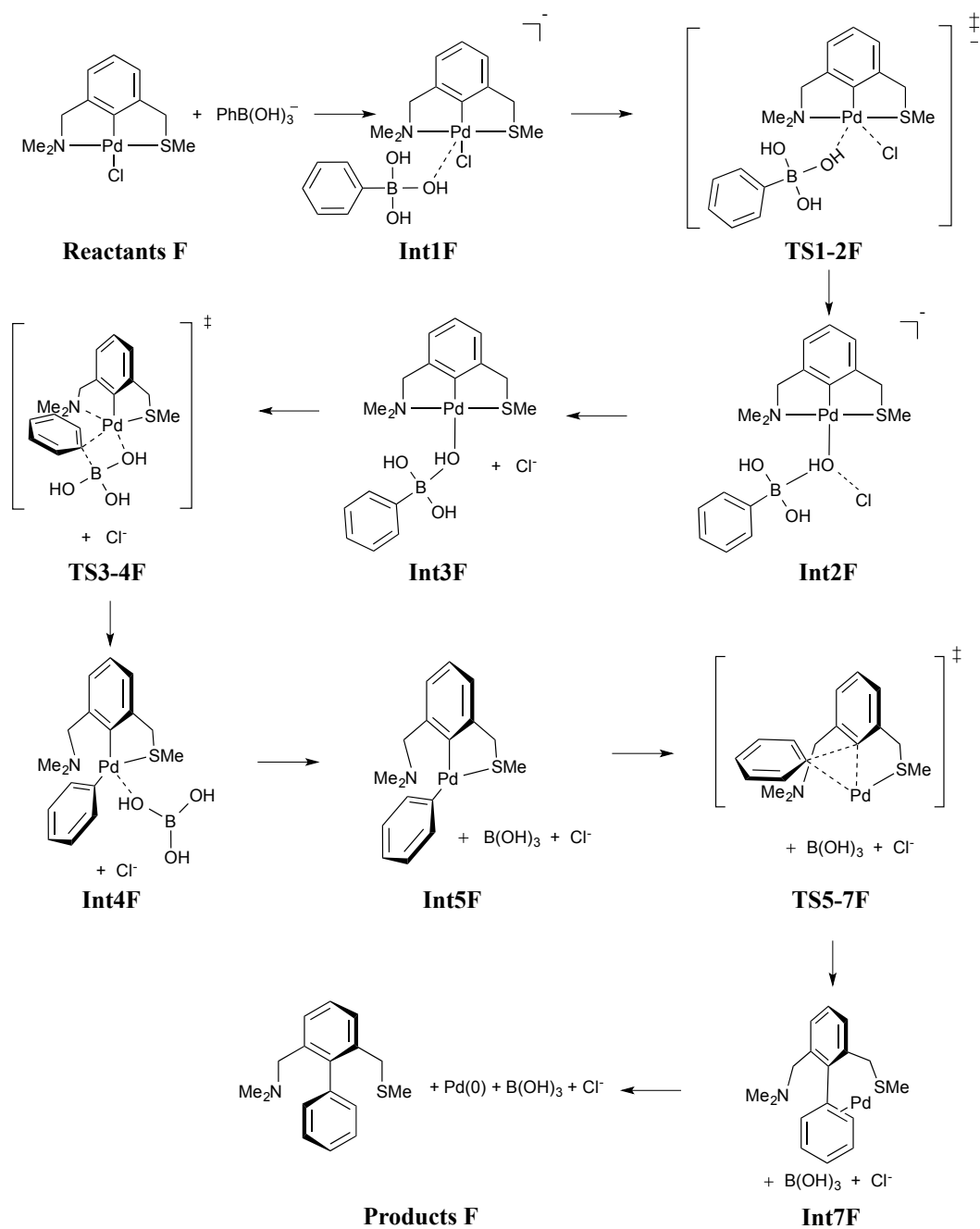


Figure 6.18. Pd(0) formation reaction from unsymmetrical NCS pincer palladacycle (PdNCS) in the presence of the base.

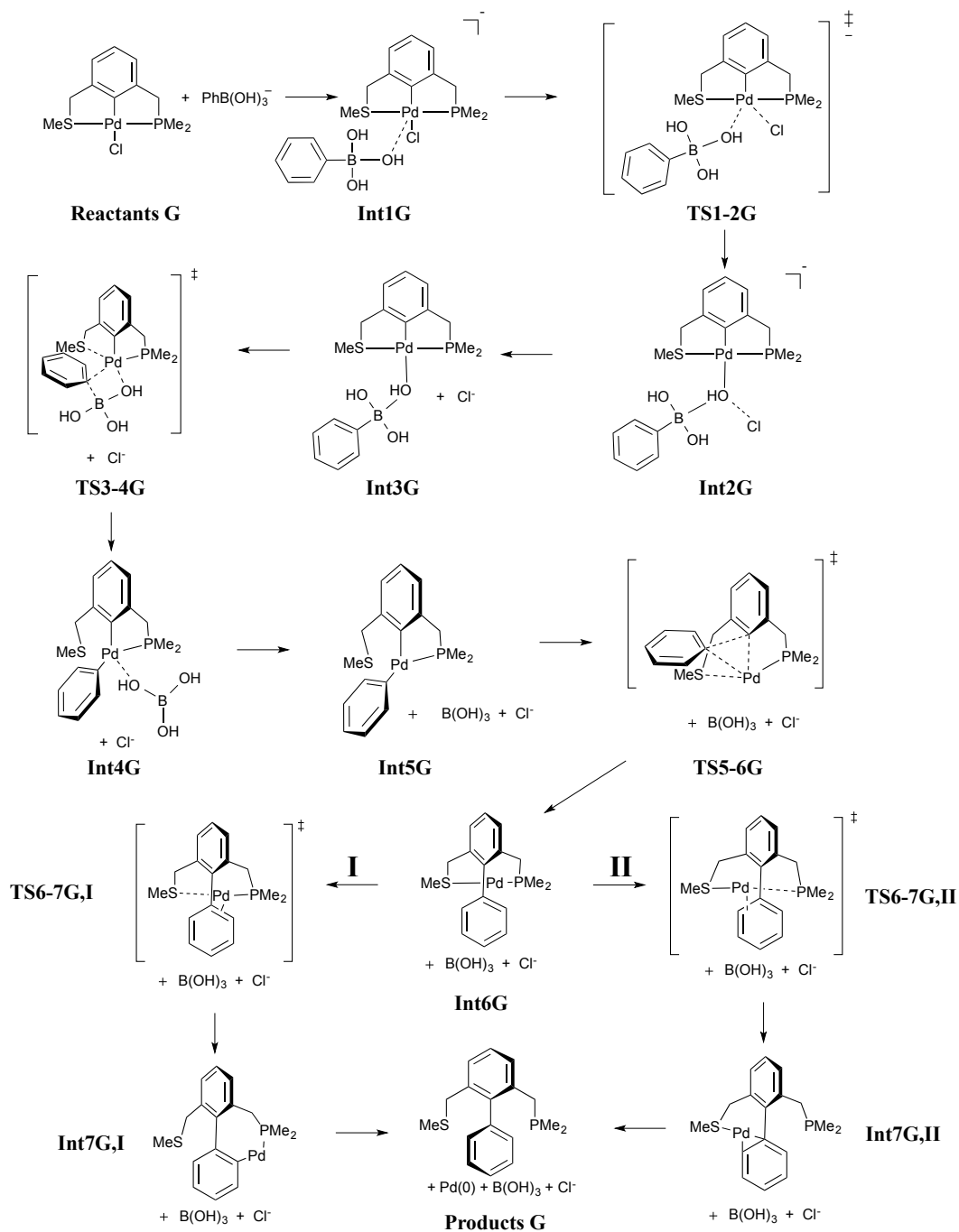


Figure 6.19. Pd(0) formation reaction from unsymmetrical SCP pincer palladacycle (PdSCP) in the presence of the base.

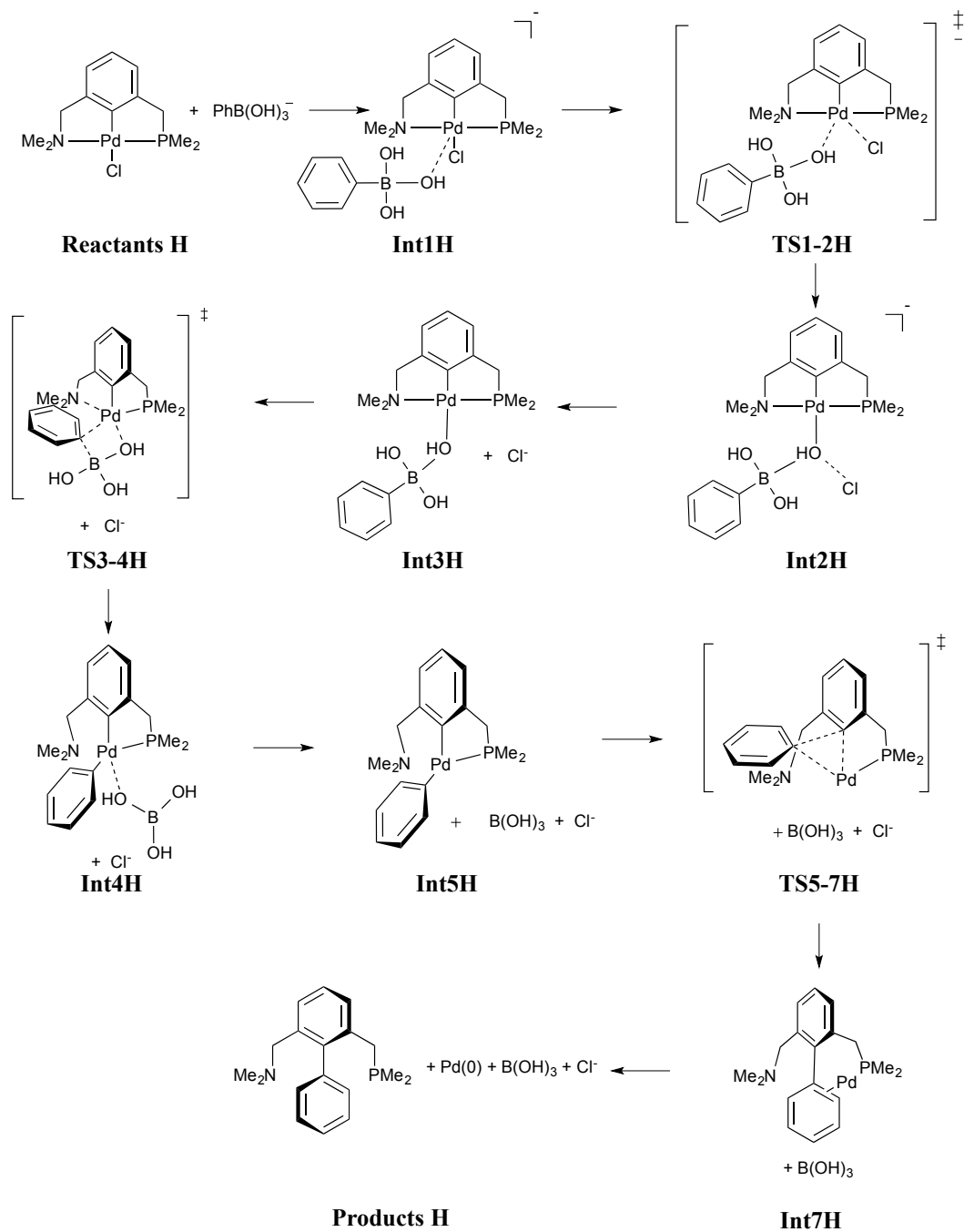


Figure 6.20. Pd(0) formation reaction from unsymmetrical NCP pincer palladacycle (PdNCP) in the presence of the base.

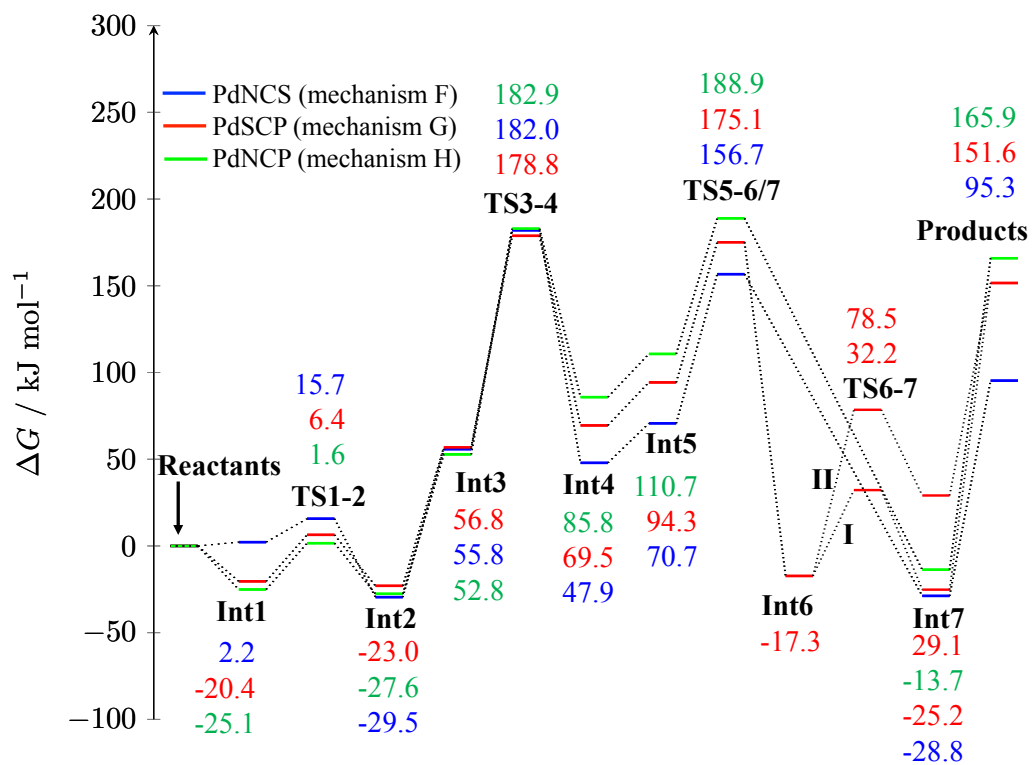


Figure 6.21. The Gibbs free energy profile of unsymmetrical pincer palladacycles to generate catalytically active Pd(0) species in the presence of the base.

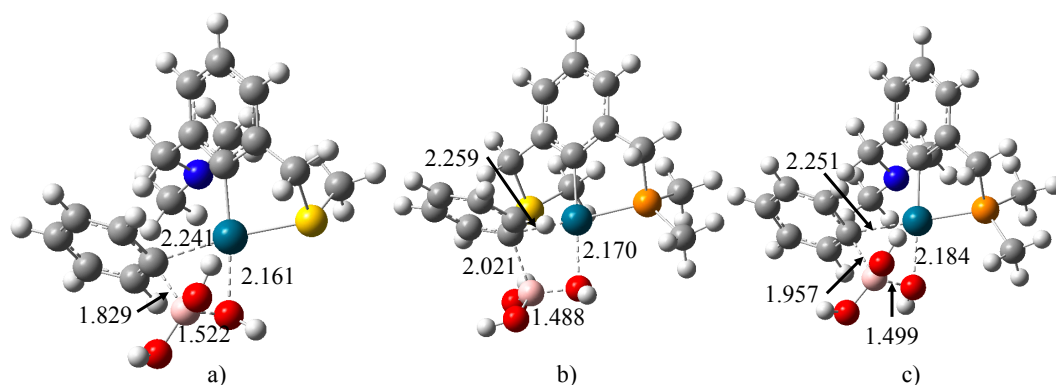


Figure 6.22. Geometry of the transition state structure for the transmetalation step **TS3-4** in the presence of the base for the Pd(0) formation from a) PdNCS, b) PdSCP and c) PdNCP (grey = C, white = H, red = O, pink = B, blue/green = Pd, blue = N, yellow = S and orange = P). Distances are in angstroms.

6.4.4 Analysis of reaction energy barriers of PdYCY and PdYCY' pathways to Pd(0) formation in the absence and presence of base

The results from the reaction pathway studies show that the mechanism is basically composed of two elementary steps, TM and RE. Based on the previous symmetrical and unsymmetrical pincer palladacycles data, the effect of the donor atoms of PdYCY' compared to PdYCY will be discussed.

Table 6.2 summarises the two elementary steps and the total Gibbs free energy without base. First of all, we have discussed the Gibbs free energy barrier of the elementary steps in the gas phase. In consideration of PdYCY, the Gibbs free energy barrier of TM step is higher than RE in all cases. This result indicates that the TM step is a rate-determining step for Pd(0) formation from PdYCY with no base. From this step, it is obvious that the energy barrier of Pd(0) from PdPCP is the highest, whilst the energy barriers of Pd(0) from PdNCN and PdSCS are lower and show little difference. Therefore, the active Pd(0) species from PdNCN and PdSCS will more readily occur when compared to the Pd(0) generation from PdPCP. In the case of PdYCY', the rate-determining steps are still the TM in all cases, as the TM step is higher than the RE. The results show that the TM energy barrier of PdNCP *via* P de-coordination has the highest, while PdNCS *via* S de-coordination has the lowest energy barrier. In addition, we have found that the Pd(0) formation from

PdYCP, where Y is S or N, has a lower energy barrier when P coordinates to Pd at the TM transition state as Pd is stabilised by the σ -donating and π -accepting character of the phosphine.¹³⁹

In the overall base-free reaction, the Gibbs free energies of both symmetrical and unsymmetrical pincer palladacycle reactions, in the gas phase are predicted to be endergonic, indicating non-spontaneous reactions.

Table 6.3 provides the results of the barrier of the two elementary steps and the total Gibbs free energy for the reaction with base. For active Pd(0) catalytic species formation, the presence of the base noticeably decreases the barrier of the TM step compared to the base-free condition. In the case of PdNCN and PdSCS, the energy barrier of TM is now similar to RE. It is not clear whether TM or RE is the rate-determining step. From the total Gibbs free energy with base compared to base-free, it is obvious that the role of the base affects the energy significantly leading to a decrease in the energy. In summary, the primary role of the base in the Pd(0) formation reaction is to reduce both the energy barrier of the TM step and the total Gibbs free energy, leading to easy release of the active catalyst Pd(0).

In the overall reaction, the TM or RE step is the rate-determining step depending on donor atoms and the total Gibbs free energy of the Pd(0) formation from both PdYCY and PdYCY' reactions indicate a non-spontaneous unfavourable process. This provides a foundation for understanding the unsymmetrical and symmetrical pincer complexes in solvent which will be used for predicting the catalytic activity.

Table 6.2. The Gibbs free energy barrier, ΔG^\ddagger for the main key steps TM and RE and the total Gibbs free energy of reaction, ΔG_r for pincer palladacycles in gas phase and solvent under base-free conditions. All energies are in kJ mol^{-1} .

Compound	Route	Step	Gas phase	Solvent		
				Toluene	THF	Acetonitrile
PdNCN		TM	202.2	207.8	211.6	213.2
		RE	108.7	114.6	121.0	125.1
		ΔG_r	171.0	185.0	196.3	201.5
PdSCS		TM	208.8	217.2	223.3	226.0
		RE	91.8	98.9	105.5	109.3
		ΔG_r	173.0	186.7	197.7	203.0
PdPCP		TM	289.4	297.6	303.6	306.7
		RE	55.7	62.4	67.8	70.5
		ΔG_r	284.9	299.0	309.9	315.0
PdNCS	path a: <i>via</i> N de-coordination first	TM	226.4	233.3	238.1	240.2
		RE	86.0	91.9	97.5	100.9
		ΔG_r	204.0	210.1	214.5	216.3
	path b: <i>via</i> S de-coordination first	RE	114.7	123.1	131.1	135.8
		ΔG_r	181.0	194.2	204.9	210.0
		TM	220.6	228.1	233.7	236.1
PdSCP	path a: phenyl orientated over S (S de-coordination)	RE	80.8	89.8	98.0	102.5
		TM	259.0	262.8	264.6	264.9
		ΔG_r	238.9	251.6	261.8	266.7
	path b: phenyl orientated over P (S de-coordination)	TM	237.7	244.9	250.3	252.6
		RE	78.2	85.4	92.1	95.9
		TM	277.5	282.8	286.4	287.8
PdNCP	path b: <i>via</i> P de-coordination first	RE	94.8	101.6	107.8	111.4
		ΔG_r	251.6	265.6	276.62	281.9
		TM	251.6	265.6	276.62	281.9

Table 6.3. The Gibbs free energy barrier, ΔG^\ddagger for the main key steps TM and RE and the total Gibbs free energy of reaction, ΔG_r for pincer palladacycles in gas phase and solvent in the presence of a base. All energies are in kJ mol^{-1} .

Compound	Step	Gas phase	Solvent		
			Toluene	THF	Acetonitrile
PdNCN	TM	105.5	107.9	107.5	106.0
	RE	108.6	114.7	120.9	125.1
	ΔG_r	85.3	43.6	31.4	29.4
PdSCS	TM	93.5	98.7	103.1	105.2
	RE	91.8	98.8	105.4	109.3
	ΔG_r	104.1	57.1	39.8	35.1
PdPCP	TM	162.0	163.1	163.6	163.7
	RE	55.7	62.3	67.8	70.6
	ΔG_r	216.0	169.4	151.9	147.2
PdNCS	TM	126.2	122.3	119.1	117.5
	RE	86.0	91.9	97.6	101.0
	ΔG_r	95.3	52.8	40.0	37.8
PdSCP	TM	122.0	119.0	115.9	114.1
	RE	80.8	89.9	78.9	102.5
	ΔG_r	151.6	110.9	99.0	97.2
PdNCP	TM	130.1	127.9	125.9	124.7
	RE	78.2	85.4	92.1	96.0
	ΔG_r	165.9	124.2	111.8	109.8

6.4.5 Solvation effects on the Pd(0) formation reaction

Three types of solvent, two non-polar solvents: toluene ($\varepsilon = 2.374$) and tetrahydrofuran ($\varepsilon = 7.426$) and the polar solvent acetonitrile ($\varepsilon = 35.688$), were used to investigate the solvent effect on the Pd(0) formation reaction from the PdYCY and PdYCY'.

The Gibbs free energy at each stationary point in the gas phase and solvent are in the appendices (Table B.1 to Table B.4 for base-free and Table B.5 to Table B.8 with base). It is shown that the Gibbs free energy increases along the pathway, with increasing solvent field. Table 6.2 and Table 6.3 show the effect of solvent on the key steps in the formation reaction.

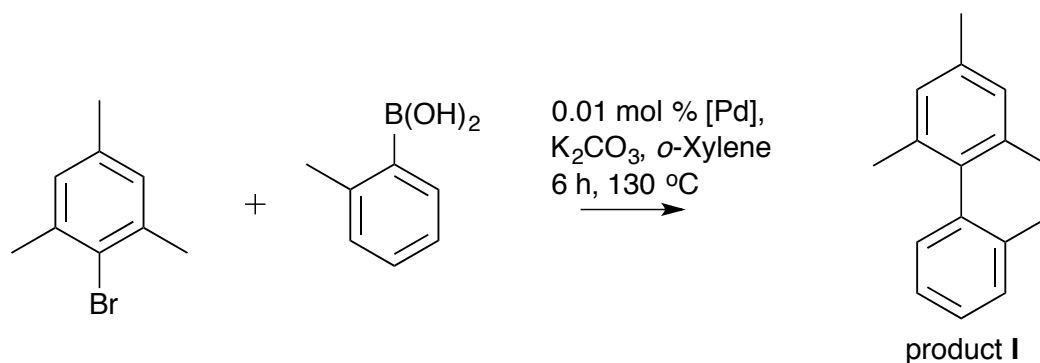
In considering the elementary steps under base-free conditions, the solvent effects increase the activation energy when increasing the dielectric constant and the trend in the reaction barrier follow a similar pattern as the gas phase (Table 6.2). Moreover, the solvent-correction also affects the total Gibbs free energy, making the reaction

less favourable (the total Gibbs free energy increases compared to gas phase).

Under the presence of the base, the energy barrier of the elementary steps are similar in magnitude when the dielectric constant increases, and have a similar trend to that in the gas phase (Table 6.3). However, the solvent effect on the total Gibbs free energy causes a dramatic decrease compared to that in the gas phase, due to the stabilisation of the free halide ion. It is clear that in the presence of the base the solvent effect is crucial for decreasing the total Gibbs free energy and hence making the reaction more favourable.

6.4.6 Rationalisation of the catalytic activity by the model Pd(0) formation reactions

In order to rationalise the catalytic activity using Pd(0) formation reactions, the experimental data of the catalytic activity in the Suzuki-Miyaura coupling reaction using pincer palladacycle were used to compare against the computational calculations. We collaborate with the Spencer group at Sussex and have used the catalytic activity results from Dr G. W. Roffe.¹⁸⁷ Roffe tested the activity of several unsymmetrical pincer palladacycles PdYCY' in the Suzuki-Miyaura coupling reaction (Scheme 6.23).



Scheme 6.23. Suzuki-Miyaura cross-coupling reaction tested in order to compare with the calculation data.

The experimental catalytic activities were studied under the base-condition in the non-polar solvent *o*-xylene. In order to rationalise these reactivities using simple pincer palladacycles (**1-6**), the presence of the base in toluene is chosen for comparing with experimental data (toluene solvent was chosen since it has a dielectric constant similar to *o*-xylene; ϵ for toluene is 2.374 and ϵ for *o*-xylene is 2.545).

Table 6.4 provides the results from these calculations and the Gibbs free energy profile is shown in Figure 6.23. In consideration of symmetrical pincer palladacycles, the active Pd(0) from PdNCN and PdSCS have lower energy barrier and total Gibbs free energy than PdPCP (PdPCP has the highest energy barrier and total Gibbs free energy). When Pd(0) formation from the unsymmetrical pincer palladacycle PdNCS is considered, the results show that the Gibbs free energy barrier increases compared to PdNCN and PdSCS, but its total Gibbs free energy has only a small change. If the N donor ligand arm of PdNCS is changed to P, providing PdSCP, it was found that the Gibbs free energy barrier barely changes, but the total Gibbs free energy increases dramatically. We have also found that when the S donor ligand arm of PdNCS is changed to P, giving PdNCP, the Gibbs free energy barrier remains similar, but the total Gibbs free energy increases significantly. These results indicate that the P donor ligand arm in the unsymmetric palladacycles causes an increase in the total Gibbs free energy.

Before using the simple pincer palladacycles (**1-6**) to rationalise the catalytic activity, we will highlight the experimental catalytic activity results of unsymmetric palladacycles and provide the key steps (TM and RE) and total Gibbs free energy from computational studies by Roffe (Table 6.5).¹⁸⁷ The experimental data reveals that the pre-catalysts PdNCN' (**8-9**) and PdNCP (**10-11**) provide the highest GC percentage conversion of product **I**, while the PdNCS (**7d-7e**) achieve the lowest GC percentage conversion. The results from calculations show that PdNCN' (**8-9**) has a higher TM and RE energy barrier compared to PdNCS (**7d-7e**). Comparing PdNCP (**10-11**) and PdNCS (**7d-7e**), the total Gibbs free energy of PdNCP (**10-11**) has a significantly greater value than PdNCS (**7d-7e**).

To rationalise the catalytic activity using simple pincer palladacycles (**1-6**), the catalytic activities of PdNCS (**7a-7c**), PdNCP(**10-11**), PdSCP (**12**) and PdNCN (**13**) in Table 6.4 are used to compare.

The experimental data of PdSCS (**14**) and the calculation results of PdSCS (**2**) are considered (although it should be noted that this is for an alkyl substituted thioether arm rather than phenyl substituted). The experimental result shows that the PdSCS (**14**) achieves a low percentage conversion (47 %). In consideration of the computational result, it was found that TM and RE energy barriers of PdSCS

(**2**) have the lowest value and its total Gibbs free energy also has the smallest value. These results agree with Roffe's work and show that the lowest percentage conversion has the lowest both Gibbs free energy barrier and total Gibbs free energy. The results suggest that formation of the active Pd(0) species is easier when there is a low energy barrier and a low total Gibbs free energy, but this does not result in a higher yield.

The unsymmetric palladacycles PdNCP (**10-11**) provides a good catalytic activity with 94 and 97 % conversion. In the calculated result, PdNCP (**6**) has a high energy barrier and total Gibbs free energy. This agrees well with the calculated results for PdNCP (**10-11**). The experimental observation can be explained as the high energy barrier can control the active Pd(0) species generation by a slower release and retards the agglomeration of palladium nano-particles to form inactive palladium black, acting as an inactive catalyst.¹⁷⁰ In addition, PdNCN (**1**) shows both a high TM and RE transition state with low total Gibbs free energy, but it shows a high percentage conversion (98 %) for PdNCN (**13**). However it is unclear the effect of the Br ligand in PdNCN (**13**) and so a Pd(0) formation from PdNCN (**1**) calculation cannot be used to provide an explanation of the catalytic activity of PdNCN (**13**).

The PdNCS (**7a-7c**) and PdSCP (**12**) have been found to have an intermediate catalytic activity with a percentage conversion of around 64 - 85 %. The calculations from the PdNCS (**4**) and PdSCP (**5**) reactions show that their energy barriers are similar to PdNCP (**6**) but they have a lower total Gibbs free energy than PdNCP (**6**). This result implies that the total Gibbs free energy is an important factor for the high catalytic activity case. The evidence for supporting this is by comparison between PdNCS (**4**) and PdSCP (**5**), where PdSCP (**5**) has a higher total Gibbs free energy than PdNCS (**4**), which shows the catalytic activity of PdSCP (**12**) is better than PdNCS (**7a-7c**).

Additionally, the energetic span model (see section 5.4.4) has been used to determine the rate-determining state for the reaction of pincer palladacycles **1** to **6**. The TS_{\max} appears before I_{\min} (see Figure 6.23) and thus the energetic span δE can be calculated using $TS_{\max} - I_{\min} + \Delta G_r$.¹⁴⁴ Table 6.6 provides δE for the formation of Pd(0) using **1** to **6**. The trend in δE follows the trend in catalytic activity discussed above, i.e. PdNCP (**6**) has the highest δE , and PdNCP (**10-11**)

have good activity (94 - 97 %). PdNCS (**4**) and PdSCP (**5**) have intermediate δE , and PdNCS (**7a-7c**) and PdSCP (**12**) have intermediate activity. PdSCS (**2**) has the smallest δE and PdSCS (**14**) has the worst activity.

In summary, the results show that the active Pd(0) formation reaction originating from simple pincer palladacycles (**1-6**) can be used to rationalise the catalytic activity. The calculations suggest that a good catalyst should have the ability to allow a slow release of active Pd(0) species, which is controlled by a higher energy barrier and total Gibbs free energy.

Table 6.4. Gibbs free energy barrier (ΔG^\ddagger) and total Gibbs free energy ΔG_r from calculations in this work (with base and toluene solvent). Gibbs free energy values are in kJ mol^{-1} .

Compound	Computational data				
	Y	Y'	$\Delta G^\ddagger(\text{TM})$	$\Delta G^\ddagger(\text{RE})$	ΔG_r
PdNCN (1)	Me_2NCH_2	Me_2NCH_2	107.9	114.7	43.6
PdSCS (2)	MeSCH_2	MeSCH_2	98.7	98.8	57.1
PdPCP (3)	Me_2PCH_2	Me_2PCH_2	163.1	62.3	169.4
PdNCS (4)	Me_2NCH_2	MeSCH_2	122.3	91.9	52.8
PdSCP (5)	MeSCH_2	Me_2PCH_2	119.0	89.9	110.9
PdNCP (6)	Me_2NCH_2	Me_2PCH_2	127.9	85.4	124.2

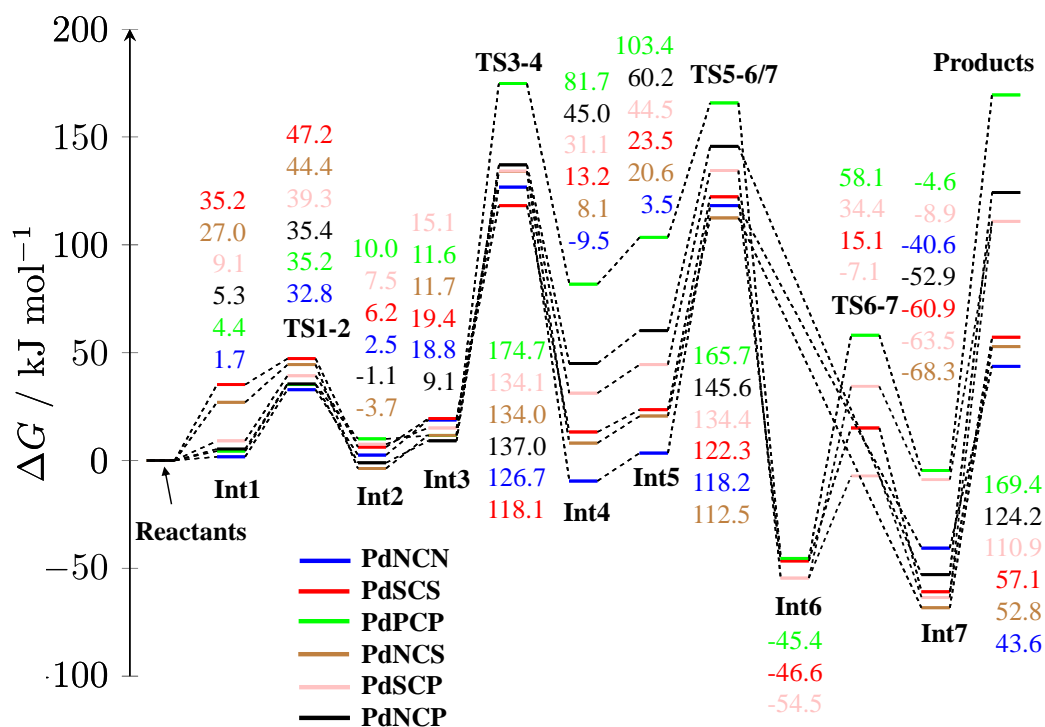


Figure 6.23. The Gibbs free energy profile of symmetrical and unsymmetrical pincer palladacycles to generate catalytically active Pd(0) species in the presence of the base in toluene solvent.

Table 6.5. Gibbs free energy barrier from calculations in the *o*-xylene solvent and percentage conversion from experiments. ¹⁸⁷ Gibbs free energy values are in kJ mol⁻¹. The structure data for **7a** to **14** are shown in Figure 6.24.

PdYCY'	Y	Y'	ΔG^\ddagger (TM)	ΔG^\ddagger (RE)	ΔG_r	Conversion of product I /%
PdNCS 7a	2-NC ₅ H ₄	MeSCH ₂	99.7	95.4	72.4	79
PdNCS 7b	2-NC ₅ H ₄	EtSCH ₂	97.4	83.8	83.0	64
PdNCS 7c	2-NC ₅ H ₄	PrSCH ₂	101.3	88.2	84.1	79
PdNCS 7d	2-NC ₅ H ₄	(<i>p</i> -MeC ₆ H ₄)SCH ₂	104.3	91.7	59.9	39
PdNCS 7e	2-NC ₅ H ₄	(<i>p</i> -MeOC ₆ H ₄)SCH ₂	98.1	96.6	61.1	37
PdNCN' 8	2-NC ₅ H ₄	Et ₂ NCH ₂	129.1	112.0	88.3	98
PdNCN' 9	2-NC ₅ H ₄	OC ₄ H ₈ NCH ₂	127.0	111.9	71.5	99
PdNCP 10	2-NC ₅ H ₄	(C ₆ H ₄) ₂ PO	95.7	73.0	148.5	94
PdNCP 11	2-NC ₅ H ₄	(C ₆ H ₄) ₂ POCH ₂	117.4	66.3	152.3	97
PdSCP 12	MeSC ₆ H ₄	(^{<i>i</i>} Pr) ₂ PO	99.2 ^a	55.4 ^a	73.5 ^a	85
PdNCN 13	Me ₂ NCH ₂	Me ₂ NCH ₂	-	-	-	98
PdSCS 14	PhSCH ₂	PhSCH ₂	-	-	-	47

^aThe ^{*i*}Pr groups in **12** were replaced with hydrogen (**12***) in the calculation.

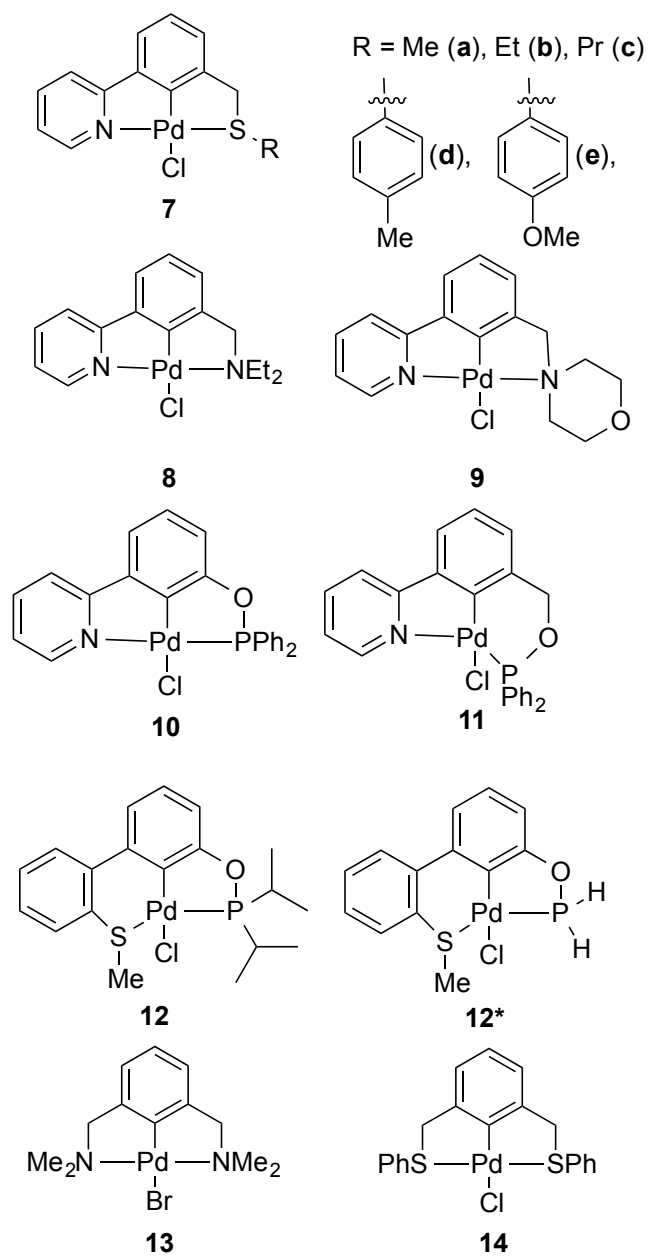


Figure 6.24. Pincer palladacycles investigated by Roffe.¹⁸⁷

Table 6.6. Energetic spans (δE) of Pd(0) formation from pincer palladacycle in the presence of the base in toluene solvent. Energy values are in kJ mol^{-1} .

PdYCY'	TS_{\max}	I_{\min}	ΔG_r	δE
PdNCN (1)	126.7	-40.6	43.6	125.0
PdSCS (2)	122.3	-60.9	57.1	116.1
PdPCP (3)	122.3	-45.4	169.4	117.9
PdNCS (4)	134.0	-68.3	52.8	122.3
PdSCP (5)	134.4	-63.5	110.9	126.9
PdNCP (6)	145.6	-52.9	124.2	146.7

6.5 Conclusion

The formation of Pd(0) has been investigated using symmetrical and unsymmetrical pincer palladacycles with PhB(OH)_2 in the absence and presence of a base. In the Pd(0) formation mechanism, there are two main steps: transmetallation and reductive elimination and it was found that all pincer palladacycles of symmetric and unsymmetric nature favour a non-spontaneous process under both conditions. In the absence of a base, the transmetallation step has a Gibbs free energy barrier higher than the reductive elimination step indicating that the transmetallation step is rate-determining. When the base was introduced in the reaction, it was shown that the Gibbs free energy barrier of the transmetallation step and the total Gibbs free energy of the reaction decreased dramatically. In addition, the inclusion of solvent corrections causes an increase or decrease of the elementary transition energy barrier and this is dependent on the absence or presence of a base. Furthermore, on the inclusion of solvent effects with increasing dielectric constant, the total Gibbs free energy became greater in the base-free reaction, while it decreased in the presence of the base. In comparison with the experimental data, the computational results suggest that a good pre-catalyst should have either a higher Gibbs free energy barrier or a larger total Gibbs free energy, or both, leading to a slow release of the active Pd(0)-catalyst. A fast release would result in Pd-black formation which stops the reaction. Finally, our investigation showed that the symmetrical and unsymmetrical pincer palladacycles show no significant difference in catalytic activity, but the pincer donor ligands play a significant role.

Chapter 7

The Functionalisation of Benzodiazepines Using Pd(II)/Ru(II) Catalysts: a DFT Study

In this chapter, density functional theory (DFT) calculations are performed on the mechanism for the functionalisation of benzodiazepines via C-H bond activation. The effects of catalyst have been studied. Three conditions have been investigated, which are i) functionalisation reaction using Pd(II)/Ru(II)-catalysts, ii) functionalisation reaction using a Pd(II)-catalyst and iii) functionalisation reaction without catalyst.

7.1 Introduction

7.1.1 Benzodiazepine chemistry

A benzodiazepine is a heterocyclic molecule, where the core structure consists of a benzene ring attached to a diazepine ring (Figure 7.1) and there are two nitrogen atoms in the diazepine ring.¹⁹⁹ Benzodiazepines have been used for patients who have psychological disorders such as sleep, anxiety, seizure disorder, etc.²⁰⁰ No one understood how benzodiazepines worked until Haefely *et al.* found the mechanism of benzodiazepines acting on specific sites.^{201,202} They concluded that an inhibitory

neurotransmitter γ -aminobutyric acid (GABA) in the brain is important for the benzodiazepine to work. If there is no GABA, the benzodiazepine has no function.²⁰¹ Additionally, Okada *et al.*²⁰³ and Braestrup *et al.*²⁰⁴ studied a mechanism of the benzodiazepines in the central nervous system and showed that the benzodiazepine binds to specific sites in the central nervous system.

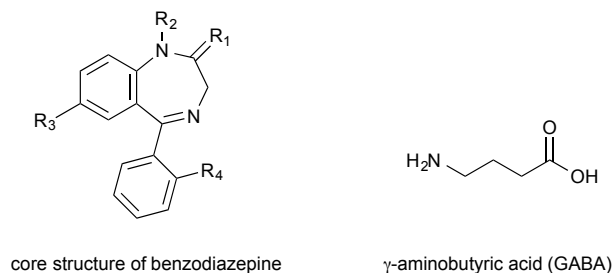


Figure 7.1. Core structure of benzodiazepines where R represents substitutions or side chains on the core structure and γ -aminobutyric acid (GABA), a neurotransmitter.²⁰⁵

A good review explaining the mechanism of benzodiazepine binding to receptors was written by Rudolph and Knoflach.¹⁹⁹ They showed an example of a GABA_A receptor mechanism, which is a ligand-gated chloride channel. The GABA_A receptor is a channel for allowing Cl⁻ specifically to pass through postsynaptic membranes.

The most common GABA_A receptor type has five subunits that consist of two α -subunits, two β -subunits and one γ -subunit (Figure 7.2). The GABA_A active site is located at the interface between the α and β -subunits, while binding sites of benzodiazepines occur between the γ and α -subunits. Normally, the brain will produce more GABA, when we have more stress than normal. When GABA binds to the GABA_A receptor, the conformation of the GABA_A receptor is changed to permit Cl⁻ ions to pass through. Cl⁻ can hyperpolarise the cell, which means a change in the membrane potential to a more negative charge; and this process can lower stress in humans. In terms of benzodiazepine, it enhances the activity of GABA by binding at a benzodiazepine active site on a GABA_A receptor, and increases Cl⁻ influx *via* the postsynaptic membrane.^{204,205}

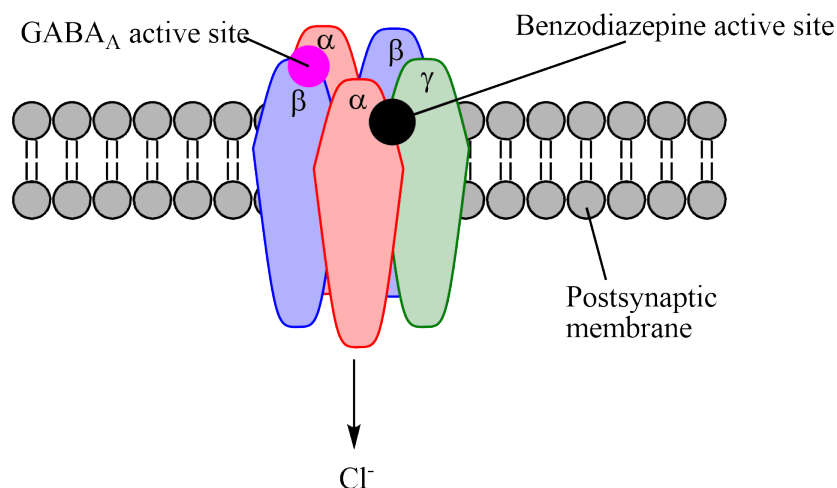


Figure 7.2. GABA_A and benzodiazepine receptors on postsynaptic membrane.

Benzodiazepines are not only prescribed for psychological issues but have also been found to possess a wide range of biological activities such as anti-HIV,²⁰⁶ antibiotic activity,^{207,208} antiarrhythmics,²⁰⁹ enzyme inhibitors²¹⁰ and anticancer agents.²¹⁰

Sternbach *et al.*²¹¹ synthesised a chlorodiazepoxide (Figure 7.3a)). The authors reported that the compound showed sedative and anticonvulsant properties when tested on unanesthetised cats. Chemists then have tried to synthesise different types of benzodiazepines for increasing activity and efficiency. Figure 7.3 shows some common drugs prescribed for patients, in each case their structure consists of N at positions 1 and 4 in the core seven-membered ring, and this is referred to as a 1,4-benzodiazepine.²⁰⁵ For example in organic synthesis, three principal ways for 1,4-benzodiazepine to be synthesised are shown in Scheme 7.1.^{205,212,213} Route i) and ii) were proposed by Sternbach *et al.*²¹² For route i), 1,4-benzodiazepine was synthesised *via* only one step, by mixing *o*-aminobenzophenone with excess glycine ethyl ester in HCl and pyridine. In route ii), it starts from *o*-aminobenzophenone reacting with XCH₂COX to produce haloacetamido compound, then cyclisation reaction occurred in liquid ammonia to produce 1,4-benzodiazepine. Route iii) was proposed by Stempel *et al.*²¹³ In the first step, *o*-aminobenzophenone reacted with carbobenzoxyglycine to generate carbobenzoxyglycylamidobenzophenone where carbobenzoxy acts as protecting group. Glycylamidobenzophenone was produced by a deprotecting group using Pd-charcoal in acid or HBr with acetic acid. The final step was the cyclisation of the glycylamidobenzophenone.

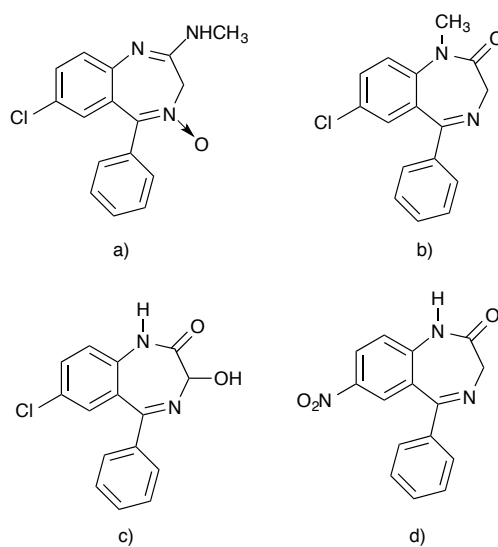
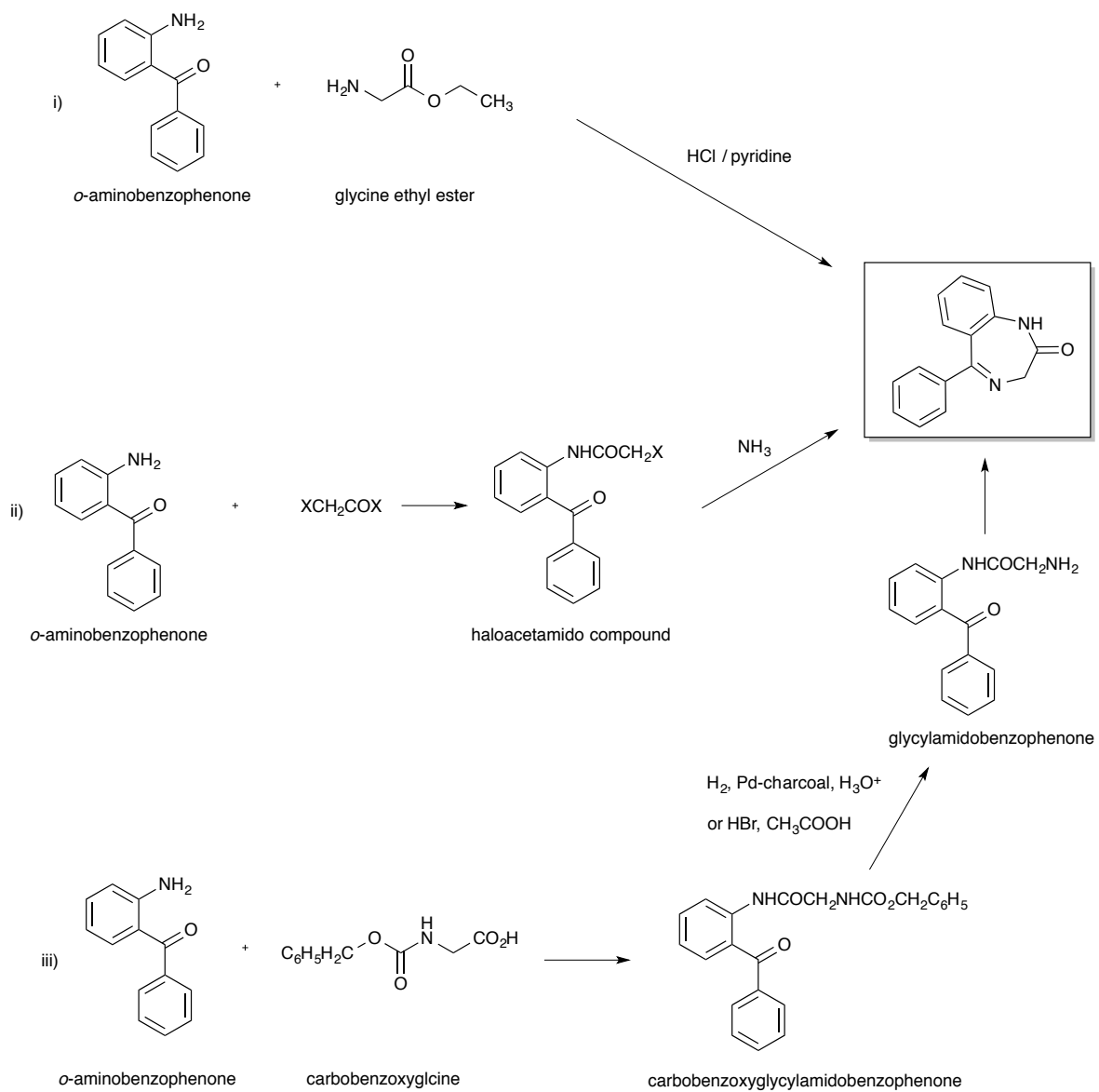
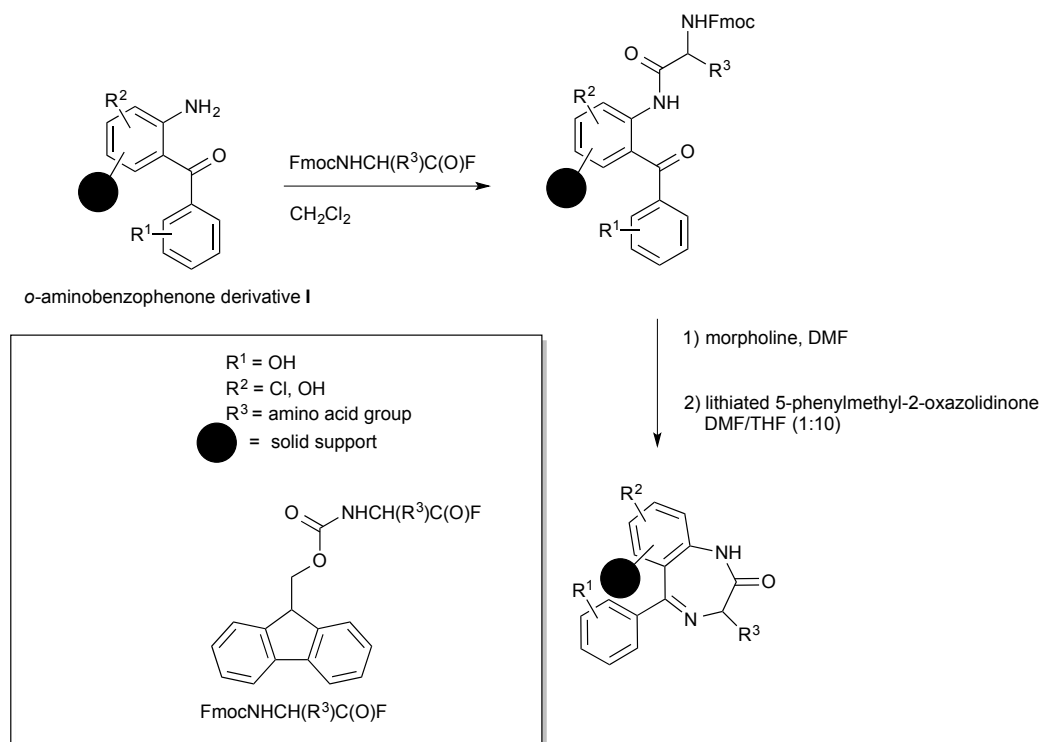


Figure 7.3. Benzodiazepine compounds used for psychosedative and tranquilising agents: a) chlorodiazepoxide, b) diazepam, c) oxazepam and d) nitrazepam.²⁰⁵



Scheme 7.1. Three principal ways for 1,4-benzodiazepine synthesis.^{205,212,213}

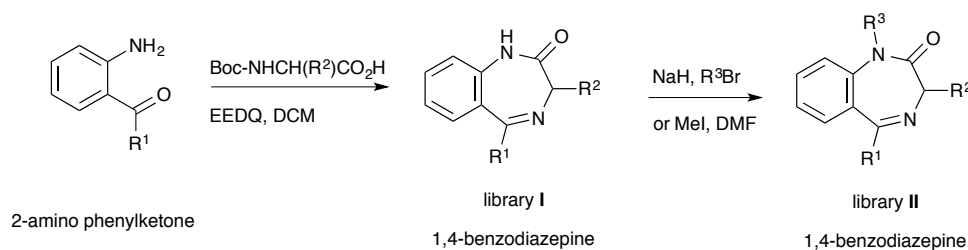
To synthesise of a number of analogous compounds for testing for widespread biological activities, large combinatorial libraries of 1,4-benzodiazepines are required. An example of a library of 1,4-benzodiazepine synthesis was reported by Ellman *et al.* (Scheme 7.2).²¹⁴ It could be synthesised using 9-fluorenylmethoxycarbonyl (Fmoc)-NHCH(R³)C(O)F (R³ is an amino acid group). Initially, *o*-aminobenzophenone derivative **I** reacted with Fmoc-amino acid fluoride in CH₂Cl₂, resulting in Fmoc-protected anilines. This step provided the anilide compound. Then, the 1,4-benzodiazepine library was formed by removing Fmoc protecting group using morpholine in dimethylformamide (DMF) followed by adding lithiated 5-phenylmethyl-2-oxazolidinone in DMF:THF (1:10), where THF is tetrahydrofuran.



Scheme 7.2. Libraries of 1,4-benzodiazepine proposed by Ellman *et al.*²¹⁴

Another example of library synthesis is shown in Scheme 7.3. A 1,4-benzodiazepine library **I** was synthesised from 2-amino phenylketone using *tert*-butyloxycarbonyl (Boc)-NHCH(R²CO₂H) where R² is H, isopropyl (*i*Pr), benzyl (Bn) or CH₂OBn with 2-ethoxy-1-ethoxycarbonyl-1,2-dihydroquinoline (EEDQ) in dichloromethane (DCM), then adding TFA in DCM followed by CH₃COONH₄ with CH₃COOH. A 1,4-benzodiazepine library **II** was synthesis from the 1,4-benzodiazepine library **I** by using the substitution reactions. Hydrogen at nitrogen in 1,4-benzodiazepine library

I was substituted by alkyl or benzyl when it was treated by sodium hydride with alkyl halides.²¹⁵



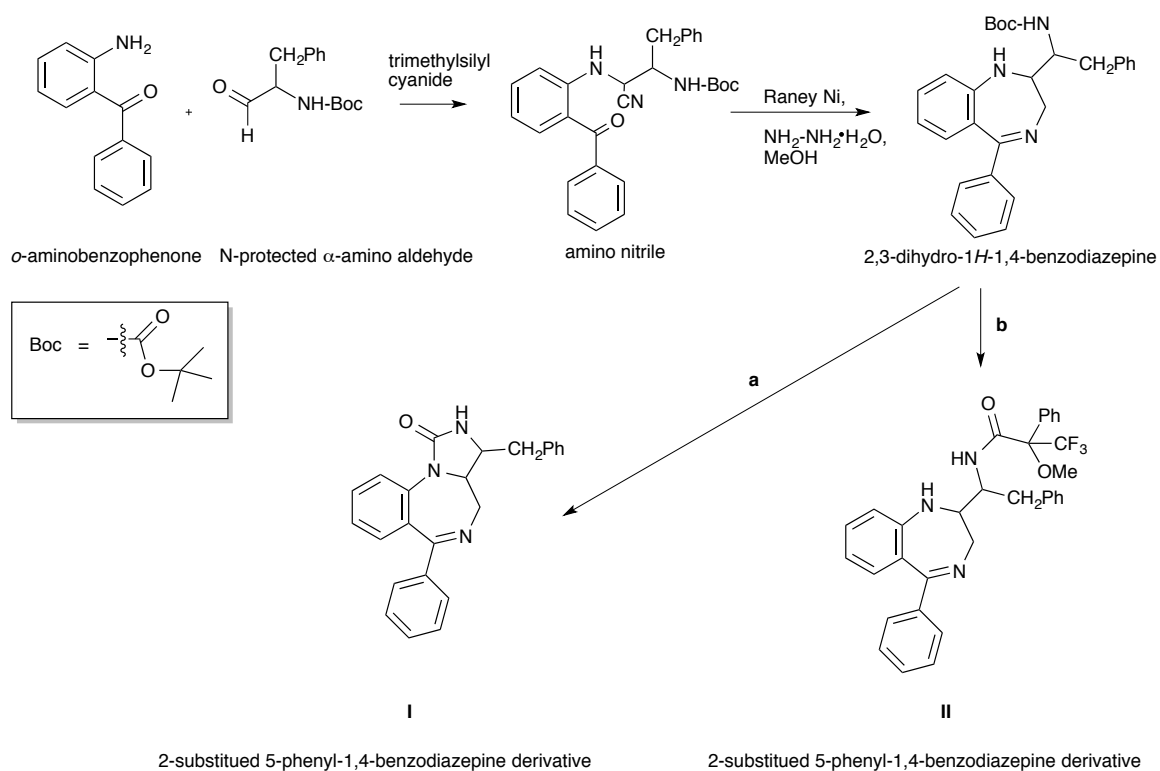
R¹ = phenyl, isopropyl, 2-pyridine, cyclohexyl

R² = H, *i*Pr, benzyl (Bn) and CH₂OBn

R³ = H, methyl, Bn, 2-methylbiphenyl, 8-methylquinoline, CH₂CN, CH₂COOBn and CH₂COOH

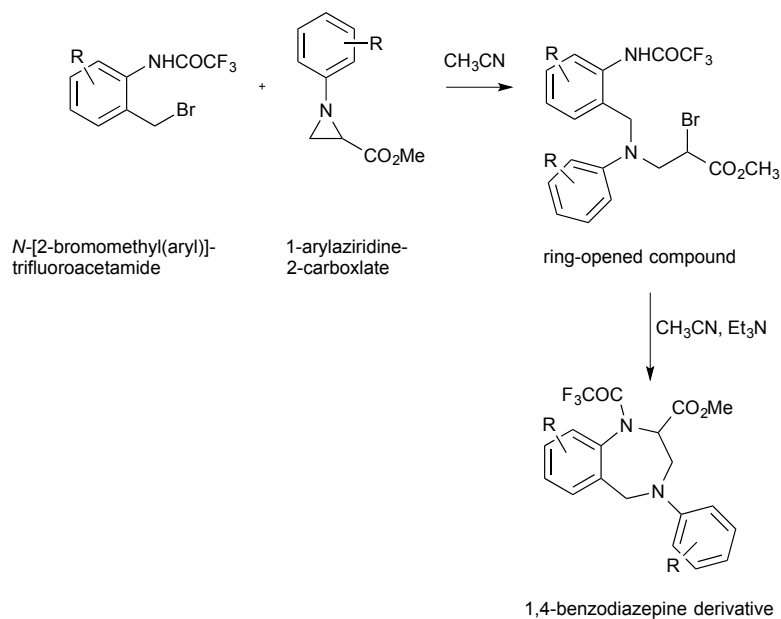
Scheme 7.3. Libraries of 1,4-benzodiazepine proposed by Spencer *et al.*²¹⁵

Reducing the number of steps in a synthesis is key for saving time and reagents for characterisation, therefore, a one-pot procedure is a good technique for 1,4-benzodiazepine synthesis. For instance, in 2003, 2-substituted 5-phenyl-1,4-benzodiazepine derivatives **I** and **II** were synthesised *via* cyano reduction and reductive cyclisation reactions (Scheme 7.4).²¹⁶ Amino nitrile was synthesised from the reaction of *o*-aminobenzophenone, N-protected α -amino aldehyde and trimethylsilyl cyanide. To form 2,3-dihydro-1*H*-1,4-benzodiazepine, when Raney nickel catalyst was added, the cyanide group was reduced to an amino group and then a seven-membered ring was formed. 2-substituted 5-phenyl-1,4-benzodiazepine derivative **I** was formed by removing the Boc-protecting group using HCl in EtOAc and then bis(trichloromethyl)carbonate ((Cl₃CO)₂CO) was added. For 2-substituted 5-phenyl-1,4-benzodiazepine derivative **II**, HCl in EtOAc was added for removing the protecting group, followed by adding the Mosher acid amide (α -methoxy- α -(trifluoromethyl)phenylacetic acid chloride).



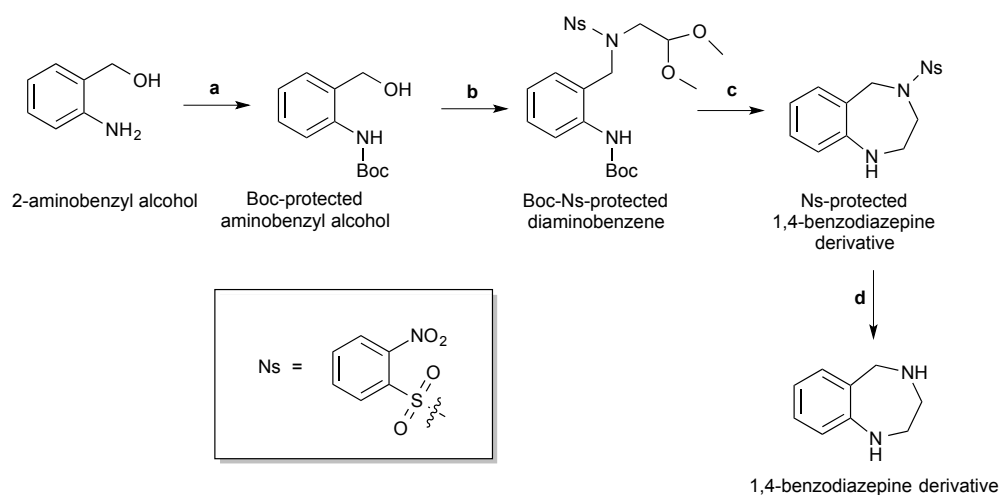
Scheme 7.4. 2-Substituted 5-phenyl-1,4-benzodiazepine derivatives synthesis by Herrero co-workers. **a:** 1) HCl, EtOAc followed by 2) $(\text{Cl}_3\text{CO})_2\text{CO}$, Et_3N , CH_2Cl_2 ; **b:** 1) HCl, EtOAc followed by 2) α -methoxy- α -(trifluoromethyl)phenylacetic acid chloride.²¹⁶

Wang *et al.*²¹⁷ proposed a new method for 1,4-benzodiazepine derivative synthesis *via* a one-pot method. Initially, *N*-[2-bromomethyl(aryl)]trifluoroacetamide was reacted with 1-arylaziridine-2-carboxylate in acetonitrile (Scheme 7.5). This reaction produced the ring-opened compound. The 1,4-benzodiazepine derivative was found *via* intramolecular nucleophilic displacement using acetonitrile in triethylamine as a base.



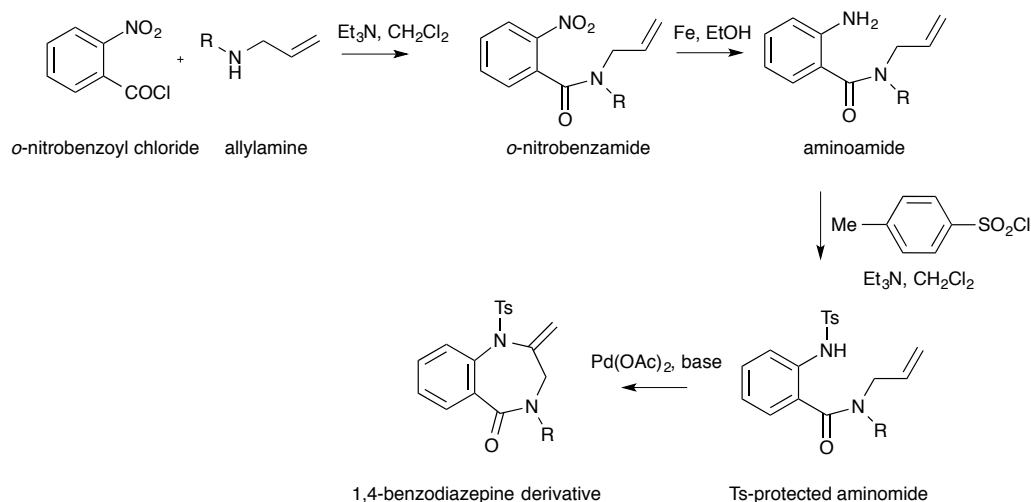
Scheme 7.5. One-pot synthesis of 1,4-benzodiazepine derivative by Wang *et al.*²¹⁷

Recently, Popp *et al.*²¹⁸ synthesised 1,4-benzodiazepine *via* a cyclisation reaction in a one-pot synthesis (Scheme 7.6). The starting 2-aminobenzyl alcohol reacted with di-*tert*-butyl dicarbonate, a N-protecting agent, in THF to form Boc-protected aminobenzyl alcohol. Then, PPh_3 , diisopropyl azodicarboxylate and *N*-(2,2-dimethoxyethyl)-2-nitrobenzenesulfonamide in THF were added, and Boc-Ns-protected diaminobenzene was formed where Ns is 2-nitrobenzene-1-sulfonyl (nosyl) protecting group. The Boc-protecting group was removed and cyclisation occurred when trifluoroacetic acid and triethylsilane in dichloromethane were added in the reaction. Finally, the Ns-protecting group was removed using thiophenol and K_2CO_3 in MeCN.

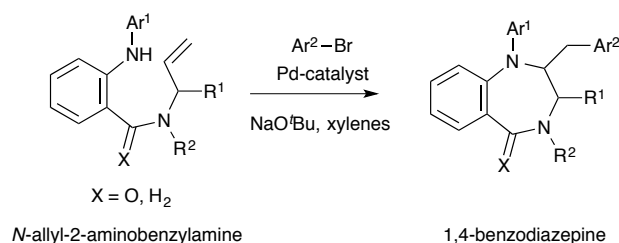


Scheme 7.6. One-pot N-deprotection and cyclisation of a 1,4-benzodiazepine derivative by Popp *et al.* **a:** di-*tert*-butyl dicarbonate, THF; **b:** PPh₃, diisopropyl azodicarboxylate, *N*-(2,2-dimethoxyethyl)-2-nitrobenzenesulfonamide, THF; **c:** trifluoroacetic acid, triethylsilane, dichloromethane; **d:** thiophenol, K₂CO₃, MeCN.²¹⁸

Among the metal-catalysts used in organic reactions, Pd-catalysts have been found to be effective at increasing the rate of the reaction. It has been reported in reviews that Pd-catalysts were used in intramolecular cyclisation reaction for heterocyclic compounds.^{219,220} Pd-catalysts were also used to synthesise heterocyclic benzodiazepine compounds. For example, Beccalli *et al.*²²¹ synthesised the 1,4-benzodiazepine derivative *via* intramolecular Pd-catalyst amination of *N*-allyl-antranilamide (Scheme 7.7). The reaction started from mixing *o*-nitrobenzoyl chloride and allylamine to produce *o*-nitrobenzamide, which was then reduced by Fe/EtOH to produce aminoamide. The amino group in aminoamide was blocked *via* tosylation. Finally, the 1,4-benzodiazepine product was produced by adding Pd(OAc)₂ in base *via* intramolecular cyclisation. In another example, Neukom *et al.* (2011)²²² discovered a process for the synthesis of the 1,4-benzodiazepine using Pd-catalyst. 1,4-benzodiazepine product was prepared by Pd-catalysed coupling between *N*-allyl-2-aminobenzylamine and aryl bromide (Scheme 7.8).

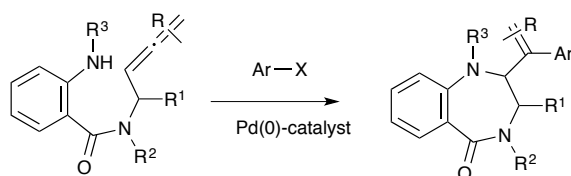


Scheme 7.7. 1,4-benzodiazepine derivative synthesis *via* cyclisation using Pd-catalysis.²²¹



Scheme 7.8. Carboamination reaction of saturated 1,4-benzodiazepines using a Pd-catalyst.²²²

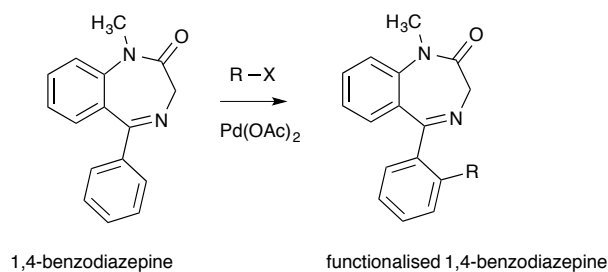
In 2014, Rigamonti and co-workers²²³ proposed a method for the preparation of a saturated 1,4-benzodiazepine (Scheme 7.9). The latter was synthesised using the Pd(0) catalyst formed by reaction of $\text{Pd}(\text{CH}_3\text{CN})_2\text{Cl}_2$, BuLi and base in DMSO (Scheme 7.9).



Scheme 7.9. Pd-catalysed synthesis of saturated 1,4-benzodiazepines by Rigamonti and co-workers.²²³

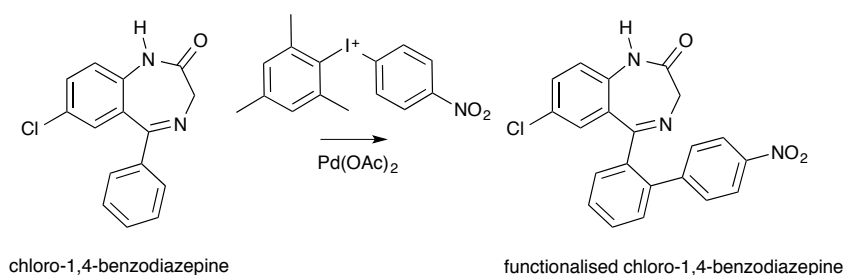
It has been found that 1,4-benzodiazepine structures (core structures) have been studied widely, while the introduction of different R groups into benzodiazepine structures is inefficient. (Scheme 7.10) The functionalisation *via* C-H bond activation using $\text{Pd}(\text{OAc})_2$, proceeding *via* palladacycle intermediate was reported by Spencer *et al.*²²⁴

in 2008 and showed percentage conversion for the functionalised-1,4-benzodiazepine product of around 60 % (R is only phenyl group). Recently, Khan *et al.* under the supervision of Spencer²²⁵ studied functionalisation on benzodiazepine (Scheme 7.10). They successfully studied the functionalisation of different R group on the aryl group at position 5 (R = C₆H₅, *o* or *m*-FC₆H₄, *o* or *m*-CF₃C₆H₄, and when methyl at N was substituted by H, R = C₆H₄, *o* or *m*-FC₆H₄, *o* or *m*-CF₃C₆H₄, *p*-CH₃OC₆H₄) and *p*-NO₂C₆H₄). The 1,4-benzodiazepine structures were synthesised once, then functionalised R groups were introduced *via* C-H bond activation either using Pd(OAc)₂ alone or using Pd(OAc)₂ with the photocatalyst tris-2,2'-bipyridylruthenium(II) ion ([Ru(bpy)₃]²⁺).



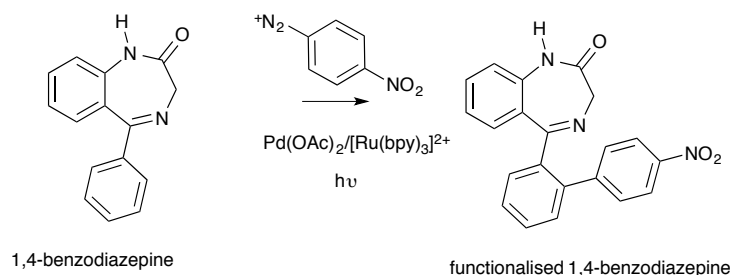
Scheme 7.10. Pd-catalyst synthesis of functionalised 1,4-benzodiazepines by Spencer group.²²⁵

The functionalised chloro-1,4-benzodiazepine which is shown in Scheme 7.11 for R-X = (4-nitrophenyl)-(2,4,6-trimethylphenyl)iodonium triflate was synthesised using Pd(OAc)₂ in acetic acid, resulting in a yield of 55 %.²²⁵



Scheme 7.11. Functionalised chloro-1,4-benzodiazepine using Pd(OAc)₂ by Spencer group.²²⁵

This yield was increased to 71 % when the functionalised 1,4-benzodiazepine was synthesised by using *p*-nitrobenzenediazonium with Pd(OAc)₂ and the photocatalyst [Ru(bpy)₃]²⁺ in methanol (Scheme 7.12).



Scheme 7.12. Functionalised 1,4-benzodiazepine using $\text{Pd}(\text{OAc})_2$ and photocatalyst $[\text{Ru}(\text{bpy})_3]^{2+}$ by Spencer group.

The aim of this chapter is to investigate the functionalisation of 1,4-benzodiazepines using *p*-nitrobenzenediazonium (see Scheme 7.12) to elucidate the effect of the catalyst $\text{Pd}(\text{OAc})_2$ with and without the photocatalyst $[\text{Ru}(\text{bpy})_3]^{2+}$.

7.1.2 $[\text{Ru}(\text{bpy})_3]^{2+}$ chemistry

$[\text{Ru}(\text{bpy})_3]^{2+}$ (tris-2,2'-bipyridylruthenium(II) ion) has played an important role since Tokel-Takvoryan *et al.*²²⁶ studied its chemiluminescence behaviour. $[\text{Ru}(\text{bpy})_3]^{2+}$ is a coordination complex, where the ruthenium centre coordinates with three 2,2'-bipyridine bidentate ligands (Figure 7.4). The spectroscopy, photochemical properties and redox properties of $[\text{Ru}(\text{bpy})_3]^{2+}$ have been studied extensively.²²⁷

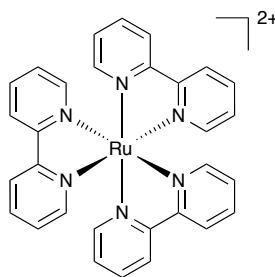
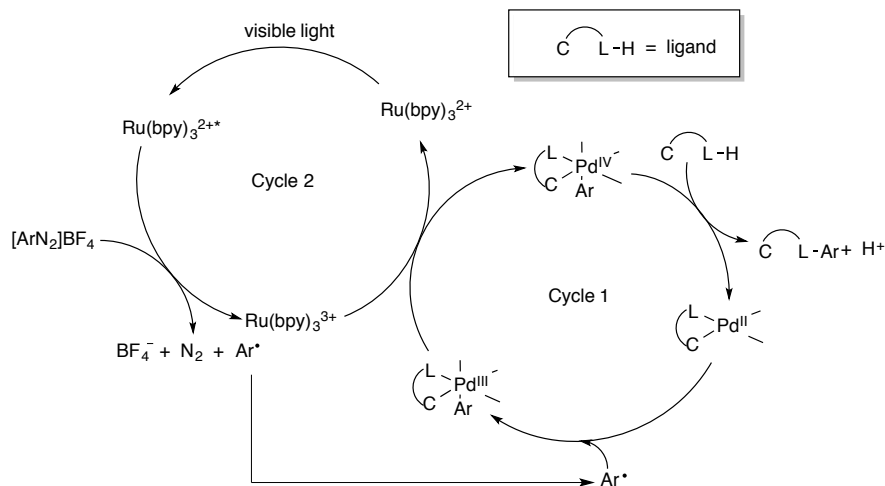


Figure 7.4. Tris-2,2'-bipyridylruthenium(II) ion.

One of the most important applications of $[\text{Ru}(\text{bpy})_3]^{2+}$ is as a photocatalyst.^{228–230} The exciting application of combining the Pd-catalyst and Ru-photocatalyst allows for C-H activation at room-temperature.²²⁹ A possible reaction mechanism for Pd(II)/Ru(II)-catalysed C-H activation is shown in Scheme 7.13 proposed by Kalyani *et al.*²²⁹ in 2011. The key steps for this reaction are i) photoexcitation of Ru(II)-photocatalyst, ii) oxidative quenching by $[\text{ArN}_2]\text{BF}_4$, an electron-accepting quencher, and Ar-radical generated, iii) coordination of Ar-radical with Pd(II)-complex that was

generated by Pd-catalyst coordination with the ligand (C-LH), iv) a single electron transfer between Pd(III)-complex and $[\text{Ru}(\text{bpy})_3]^{3+}$ to form the Pd(IV)-complex and v) C-C formation reaction leading to the product.²²⁹



Scheme 7.13. Possible reaction mechanism of functionalisation using Pd(II)/Ru(II)-catalysts.²²⁹

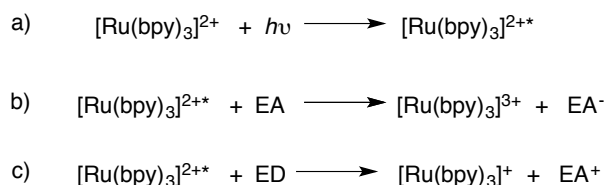
This reaction mechanism will form the basis of the present study. The next section will describe how we will calculate the electron transfer process.

7.1.3 Electron transfer theory

a) Description of the method for determining the excited state redox potential

An electron transfer quenching process was first studied by Gafney and Adamson.²³¹ They studied this process using the reaction between a $[\text{Ru}(\text{bpy})_3]^{2+}$ donor and $[\text{Co}(\text{NH}_3)_5\text{Br}]^{2+}$ acceptor, where the $[\text{Ru}(\text{bpy})_3]^{2+}$ is excited by ultraviolet (UV) and visible light. The excited-state $[\text{Ru}(\text{bpy})_3]^{2+*}$ can be quenched through two processes; i) oxidative quenching or ii) reductive quenching, by an electron-accepting (EA) or an electron-donating (ED) quencher, respectively (Scheme 7.14).²³²

Redox properties of the $[\text{Ru}(\text{bpy})_3]^{2+}$ ground-state and lowest excited-state can be determined by applying a Latimer diagram.²³³ The Latimer diagram for the excited state redox potential calculation is shown in Figure 7.5.



Scheme 7.14. a) Electron excited-state of tris-2,2'-bipyridylruthenium(II) ion by UV and visible light, b) oxidative quenching and c) reductive quenching.²³²

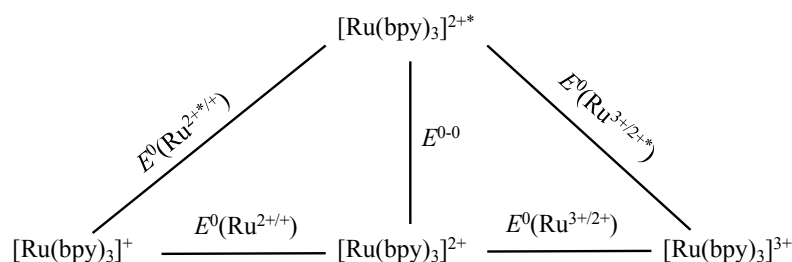


Figure 7.5. The Latimer diagram for calculation of excited state redox potential.²³³

The excited-state reduction potential $E^0(\text{Ru}^{2+*/+})$ can be calculated by:

$$E^0(\text{Ru}^{2+*/+}) = E^0(\text{Ru}^{2+/+}) + E^{0-0}, \quad (7.1)$$

while the excited-state oxidation potential $E^0(\text{Ru}^{3+/2+*})$ is determined using:

$$E^0(\text{Ru}^{3+/2+*}) = E^0(\text{Ru}^{3+/2+}) - E^{0-0} \quad (7.2)$$

where E^{0-0} is the 0-0 transition energy and $E^0(\text{Ru}^{2+/+})$ and $E^0(\text{Ru}^{3+/2+})$ are the ground-state redox potentials.²³³

Based on the simplified Jablonski diagram (Figure 7.6), E^{0-0} can be determined by the difference in energy of the excited-state (E^{ES}) and the energy of the ground state (E^{GS}), which gives the adiabatic energy (E^{adia}). This value is then corrected for the zero-point vibrational energy (ZPVE):^{234,235}

$$E^{0-0} = (E^{\text{ES}} - E^{\text{GS}}) + (E^{\text{ZPVE-ES}} - E^{\text{ZPVE-GS}}) = E^{\text{adia}} + \Delta E^{\text{ZPVE}}. \quad (7.3)$$

where $E^{\text{ZPVE-ES}}$ is the ZPVE of the excited-state structure and $E^{\text{ZPVE-GS}}$ is the ZPVE of the ground-state structure.

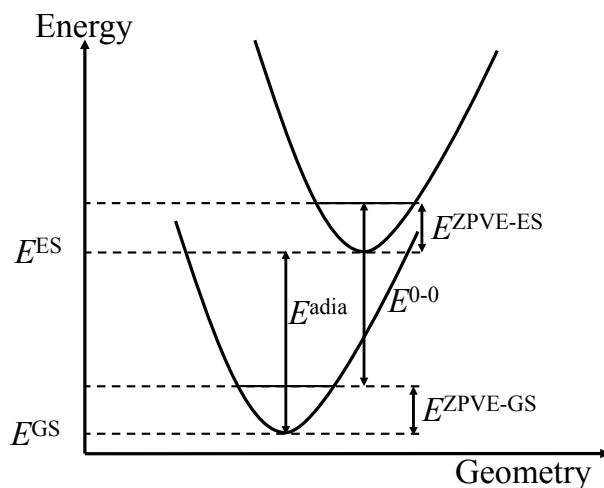


Figure 7.6. Simplified Jablonski diagram.²³⁴

b) Electron transfer between complexes

Electron transfer (ET) is a chemical process that can be found in biological and chemical processes such as ET in protein,²³⁶ or dye sensitised solar cells.²³⁷ In this thesis chapter, we have focused on inorganic chemical reactions that can be divided into two mechanisms.²³⁸ The first is the outer-sphere ET mechanism. In this mechanism, an electron is transferred when two complexes contact each other, which occurs when the coordination sphere of the donor molecule contacts the coordination sphere of the acceptor molecule, giving rise to ET between the molecules. For this process, there is only a small change in the bond distance between the metal and ligand (Figure 7.7a). The second process is an inner-sphere ET mechanism, which involves a bridging ligand transferring electrons between complexes. When the complexes contact each other, a ligand substitution will create the bridge between the complexes, and the coordination spheres of both complexes are changed. This leads to a change in the oxidation state of the complexes (Figure 7.7b). Examples of good bridging ligands for inner-sphere reaction are Cl^- , SCN^- , N_3^- and CN^- . In this work, only the outer-sphere electron transfer mechanism is considered.

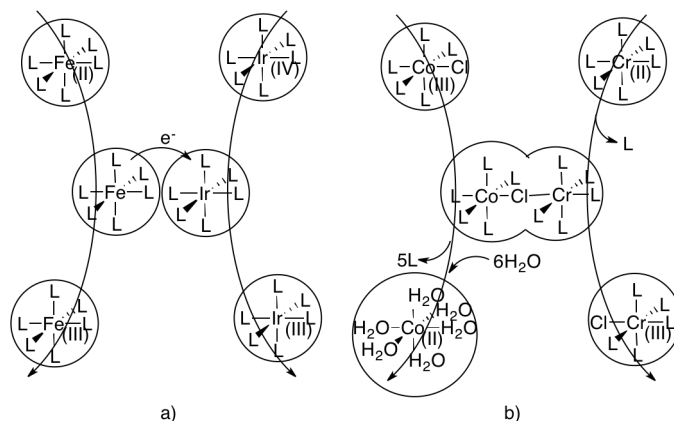


Figure 7.7. Electron transfer process diagram of inorganic reaction; a) outer-sphere and b) inner-sphere redox reactions.

c) Marcus theory

Marcus^{239–243} developed a theory to explain electron transfer. We can use two parabolic curves for representing the structures along the reaction coordinate (Figure 7.8).

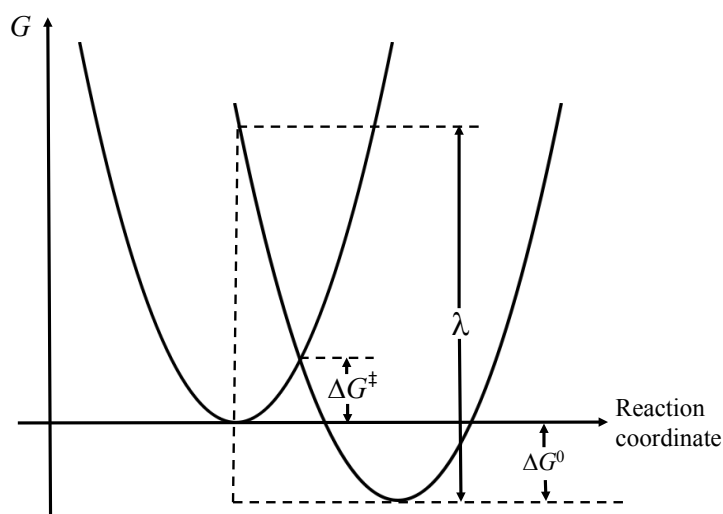


Figure 7.8. Parabolic curves to represent electron transfer from reactant to product.²⁴⁴

There are two parameters to control the ET reaction that are i) the driving force and ii) the reorganisation energy.²⁴⁴ The driving force is $-\Delta G^0$, while the reorganisation energy (λ) is the energy change when a molecule is rearranged. From the relationship of two parabolas, Marcus provided the equation (7.4) to find the

Gibbs free activation energy (ΔG^\ddagger).

$$\Delta G^\ddagger = \frac{(\lambda + \Delta G^0)^2}{4\lambda} = \frac{\lambda}{4} \left[1 + \frac{\Delta G^0}{\lambda} \right]^2 \quad (7.4)$$

When the driving force is zero i.e. $\Delta G^0 = 0$, the equation (7.4) reduces to:

$$\Delta G^\ddagger = \Delta G_0^\ddagger = \frac{\lambda}{4}. \quad (7.5)$$

λ consists of the inner reorganisation energy of the reactants (λ_i) and the solvent reorganisation energy (λ_o):

$$\lambda = \lambda_i + \lambda_o \quad (7.6)$$

Marcus defined these parameters for a homogeneous ET process. λ_i is described by the following equation:

$$\lambda_i = \frac{k_j^R k_j^P}{k_j^R + k_j^P} (q_j^R - q_j^P)^2 \quad (7.7)$$

where k_j^R and k_j^P are the normal mode constants at the vibrational coordinates of reactant and product, respectively and $q_j^R - q_j^P$ are the changes in the bond lengths and bond angles of the reactant and product. λ_o can be calculated by the following equation:

$$\lambda_o = \frac{N_A e^2}{4\pi \varepsilon_0} \left(\frac{1}{\varepsilon_{op}} - \frac{1}{\varepsilon_s} \right) \left(\frac{1}{2r_1} + \frac{1}{2r_2} - \frac{1}{R} \right) \quad (7.8)$$

where, N_A is the Avogadro constant ($6.022 \times 10^{23} \text{ mol}^{-1}$), e is the electronic charge ($1.602 \times 10^{-19} \text{ C}$), ε_0 is the vacuum permittivity ($8.854 \times 10^{-12} \text{ J}^{-1} \text{ C}^2 \text{ m}^{-1}$) and, ε_{op} and ε_s are the optical and static dielectric constant for the solvent, respectively. r_1 , r_2 and R are the hard sphere radii of donor, acceptor and sum of hard sphere radii donor and acceptor, respectively. The optical dielectric constant can be calculated from the square of the reflective index.²⁴⁵

d) Marcus theory with outer-sphere electron transfer

Savéant²⁴⁶ stated that the redox reaction in liquid phase does not involve a bond breaking or a bond forming. In this situation, a quadratic activation free energy-driving force relationship can be used to calculate the Gibbs free energy of activation, which was developed by Marcus²³⁹⁻²⁴³ and Hush.²⁴⁷ In the case of the outer-sphere

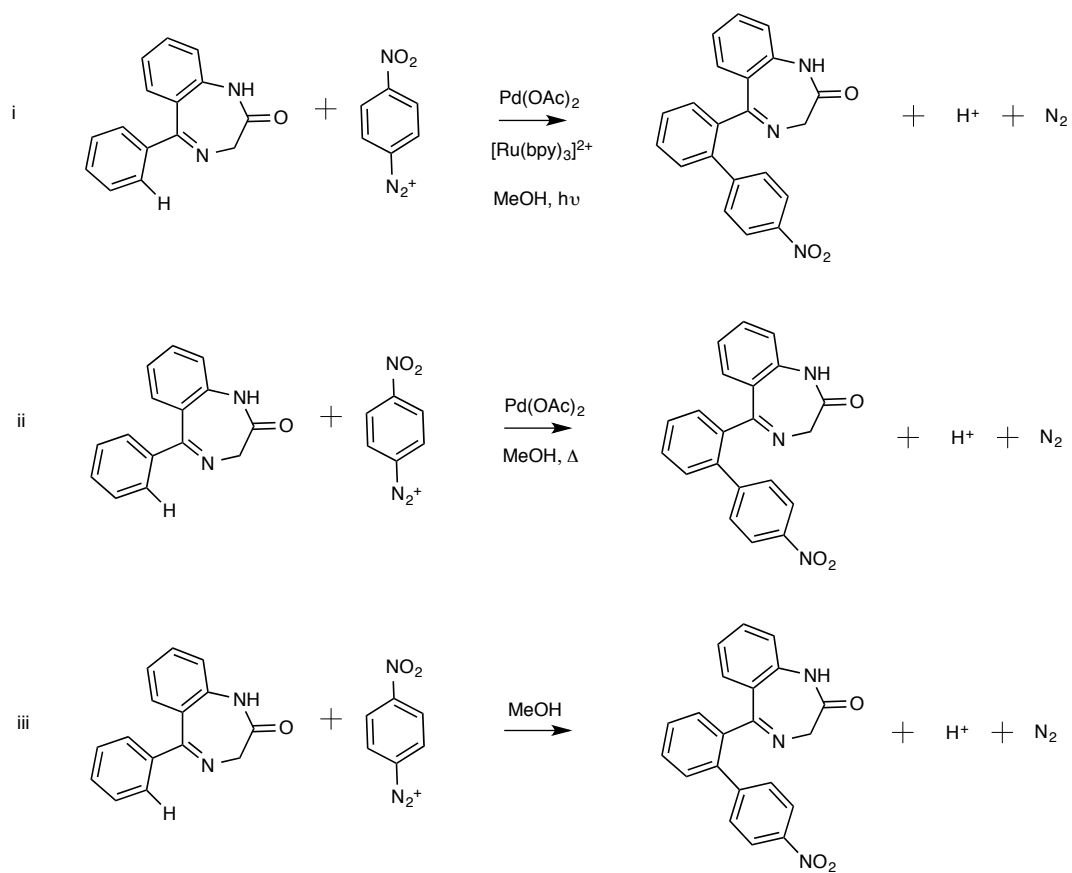
ET, it is also not involving the bond breaking or bond formation and this reaction occurs at zero driving force. We can determine the Gibbs free energy barrier for outer-sphere ET $\Delta G_{\text{ET}}^\ddagger$ by using:

$$\Delta G_{\text{ET}}^\ddagger = \Delta G_0^\ddagger \left[1 + \frac{\Delta G_r}{4\Delta G_0^\ddagger} \right]^2 \quad (7.9)$$

where ΔG_r is the reaction energy and ΔG_0^\ddagger is the intrinsic barrier (i.e. the Gibbs free energy barrier at zero driving force).^{248,249}

7.2 Aim of this work

We have used density functional theory calculations to study the feasibility of mechanisms for functionalisation *via* C-H bond activation at the 5-position on 1,4-benzodiazepines. In this work, reactant 1,4-benzodiazepines are called unfunctionalised-benzodiazepines (unf-BZD) and product 1,4-benzodiazepines are called functionalised-benzodiazepines (func-BZD). We have examined the role of the catalyst by calculating: i) the reaction with $\text{Pd}(\text{OAc})_2/[\text{Ru}(\text{bpy})_3]^{2+}$ -catalysts (Pd(II)/Ru(II)-catalysts), ii) the reaction using only $\text{Pd}(\text{OAc})_2$ (Pd(II)-catalyst) and iii) the reaction without any catalyst (Scheme 7.15).



Scheme 7.15. Model reactions investigated in this study, calculated in methanol solvent.

7.3 Computational details

All calculations were performed using the Gaussian09 program.⁸⁷ All optimisation of structures were carried out with the same procedure as our pincer palladacycle study since this method provides accurate bond distances around the palladium atom, i.e. the PBE^{45,46} functional with the effective core potential of Stuttgart/Dresden ECP (SDD)⁵⁷ for describing Pd and Ru, and 6-31+G(d,p) basis set for other atoms (PBE/6-31+G(d,p)[SDD]) to find the stationary state structures. Single-point energy calculations were carried out at the PBE optimised geometries using both the PBE and the ω B97XD⁵³ functional, with implicit solvent corrections. The SDD ECP was used for Pd and Ru, while the large basis set 6-311++G(2df,2p) was used for other atoms.

Firstly, we studied the effect of solvation and cavity models on the ground-state redox potential of $[\text{Ru}(\text{bpy})_3]^{2+}$ in its low spin state (singlet) and high spin state (quintet). $[\text{Ru}(\text{bpy})_3]^+$ and $[\text{Ru}(\text{bpy})_3]^{3+}$ were also calculated in the low-spin and high-spin states; the low-spin and high-spin states of $[\text{Ru}(\text{bpy})_3]^+$ are doublet and quartet, respectively; low-spin and high-spin states of $[\text{Ru}(\text{bpy})_3]^{3+}$ are doublet and sextet, respectively. Solvent effect on both the high-spin and low-spin states $[\text{Ru}(\text{bpy})_3]^{n+}$ ($n = 1, 2, 3$) structures were taken into account through two models: i) the polarisable continuum model (PCM) using the integral equation formalism model (IEFPCM)⁶⁰ and ii) conductor-like polarisable continuum model (CPCM).^{250,251} Three types of molecular cavity, which is the atomic radii of sphere around each solute atom, were considered: i) UFF,²⁵² ii) UAKS⁸⁷ and iii) Bondi models.²⁵³ The UAKS uses the radii of the United Atom Topological Model (UA), optimised for DFT method (Kohn-Sham energy, KS), the UFF uses the radii of Universal Force Field and Bondi uses Bondi's radii.⁸⁷ The standard absolute redox potential ($E^0(\text{abs})$) was calculated by the following:

$$E^0(\text{abs}) = \frac{-\Delta G^0(\text{soln, redox})}{ZF} \quad (7.10)$$

where F is the Faraday constant (23.061 kcalV⁻¹ g⁻¹), $Z = 1$ as we are considering a one-electron redox process and $\Delta G(\text{soln, redox})$ is the redox Gibbs free energy change in solution. $\Delta G(\text{soln, redox})$ was calculated using a Born-Haber cycle (Figure 7.9).

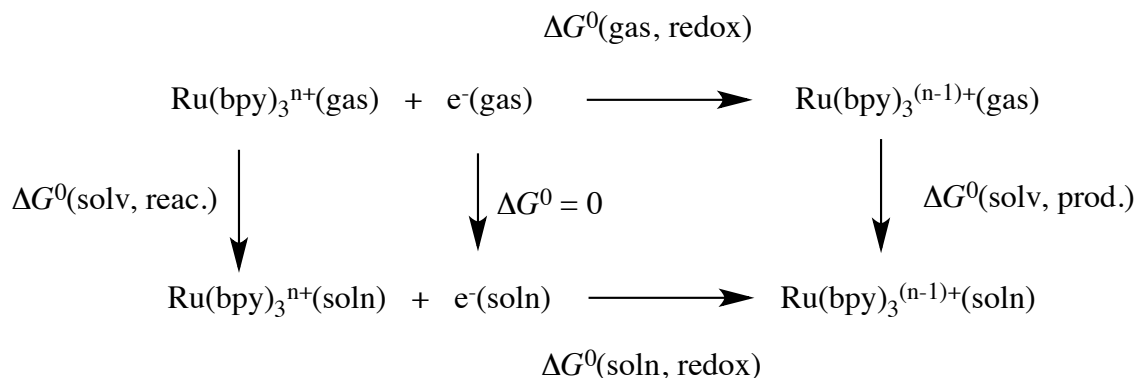


Figure 7.9. Born-Haber cycle for calculating the redox Gibbs free energy change.

From the Born-Haber cycle, the $\Delta G(\text{soln, redox})$ can be calculated by:

$$\Delta G^0(\text{soln, redox}) = \Delta G^0(\text{gas, redox}) + \Delta G^0(\text{solv, prod.}) - \Delta G^0(\text{solv, reac.}) \quad (7.11)$$

where, $\Delta G^0(\text{gas, redox})$ is free energy change in the gas phase, $\Delta G^0(\text{solv, prod.})$ is free energy change of the product and $\Delta G^0(\text{solv, reac.})$ is free energy change of the reactant. To compare the theoretical and experimental redox potential, the absolute potential calculation, $E^0(\text{cal, SCE})$ using saturated calomel electrode as reference (SCE) was carried out using the following:²⁵⁴

$$E^0(\text{cal, SCE}) = E^0(\text{abs}) - E^0(\text{abs, SCE}) \quad (7.12)$$

and

$$E^0(\text{abs, SCE}) = E^0(\text{ref, SCE}) - E_{LJ} \quad (7.13)$$

where, $E^0(\text{abs, SCE})$ is an absolute redox potential ($E^0(\text{abs, SCE}) = 4.429 \text{ V}$), which is calculated by difference between a reference absolute potential, $E^0(\text{ref, SCE})$ and the liquid junction potential, E_{LJ} .²⁵⁵ The reported experimental values of $E^0(\text{ref, SCE})$ and E_{LJ} , used for calculating $E^0(\text{abs, SCE})$, were $E^0(\text{ref, SCE})$ is 4.522 V ²⁵⁵ and E_{LJ} in MeCN is 0.093 V .²⁵⁶ In order to compare the calculated and experimental data, $E^0(\text{abs})$ was corrected by $E^0(\text{abs, SCE})$, providing $E^0(\text{cal, SCE})$ that was used for comparing to the absolute potential experimental value, $E^0(\text{expt})$. The $E^0(\text{expt})$ in MeCN for $[\text{Ru}(\text{bpy})_3]^{2+} + e^- \rightarrow [\text{Ru}(\text{bpy})_3]^+$ is -1.33 V and for $[\text{Ru}(\text{bpy})_3]^{3+} + e^- \rightarrow [\text{Ru}(\text{bpy})_3]^{2+}$ is 1.29 V .²⁵⁷

However, methanol (rather than MeCN) was used as the solvent in the exper-

imental functionalisation reaction. Therefore, we performed single-point energy calculation on the reacting species in methanol ($\epsilon = 32.613$). For calculating $E^0(\text{cal, SCE})$ in MeOH solvent, $E^0(\text{abs, SCE}) = 4.497$ V was used for correcting $E^0(\text{abs})$ ($E^0(\text{ref, SCE}) = 4.522$ V and $E^0(\text{abs}) E_{LJ}$ for MeOH = 0.025 V²⁵⁶).

All optimisation structures at minima and transition states of reaction mechanism determinations were verified by vibrational frequency analysis, where transition state structures were characterised by one imaginary frequency, while the frequencies of minimum structures were real. Every transition state was confirmed by eigenvector following to confirm that the transition state connected to the right intermediates.

Determination of 0-0 energies (E^{0-0}) were performed using time-dependent density functional theory (TDDFT). CAM-B3LYP²⁵⁸/6-31+G(d,p)[SDD] with methanol solvent was used for optimisation of both ground-state and excited-state structures of $[\text{Ru}(\text{bpy})_3]^{2+}$. For the excited-state optimisation, the tight keyword (tight convergence criteria) was used, recommended by Jacquemin *et al.*^{234,259}

7.4 Results and discussion

7.4.1 Reduction potential

The results in Table 7.1 show the comparison of the calculated redox potential with experiment. The two continuum solvation models used in this study are CPCM and PCM with different solute cavity models, UFF, UAKS and Bondi. Firstly, two sets of calculations, which are i) PBE/6-311++G(2df,2p)[SDD]//PBE/6-31+G(d,p)[SDD] and ii) ω B97XD/6-311++G(2df,2p)[SDD]//PBE/6-31+G(d,p)[SDD], were examined with fixed solute cavity model using UFF. Within the CPCM with UFF results, the data shows that the reduction potential ($E^0(\text{cal, SCE})$) of $[\text{Ru}(\text{bpy})_3]^{2+}$ using ω B97XD functional has an absolute deviation (0.35 V) lower than using PBE (0.44 V). The $E^0(\text{cal, SCE})$ of $[\text{Ru}(\text{bpy})_3]^{3+}$ follows the same trend. Moreover, in the PCM solvation and UFF solute cavity models, the $E^0(\text{cal, SCE})$ of both $[\text{Ru}(\text{bpy})_3]^{2+}$ and $[\text{Ru}(\text{bpy})_3]^{2+}$ obtained using ω B97XD functional is found to have a smaller absolute deviation, compared to that obtained using the PBE functional. This suggests that the single-point energy calculation using ω B97XD method is more accurate than the PBE method.

Cavity effects in the CPCM and PCM approaches are studied using the different solute cavity models, UFF, UAKS and Bondi. Our results show that when the cavity models are changed (fixing solvation model), the deviation between calculation and experiment changes (ΔE^0 changes). Thus, PCM and CPCM correction are dependent on the choice of cavity model. These results are in agreement with Dinescu and Clark²⁶⁰ who investigated ΔG^0 values and they stated that “PCM correction are highly dependent on the choice of cavity model”. In the present work, we calculate $E^0(\text{cal, SCE})$ values which are derived from ΔG^0 values.

To gain insight into the effect of solvation and cavity models, we have analysed them. At CPCM, the $E^0(\text{cal, SCE})$ of $[\text{Ru}(\text{bpy})_3]^{2+}$ using UFF, UAKS and Bondi calculations underestimates the experimental value, while the $E^0(\text{cal, SCE})$ of $[\text{Ru}(\text{bpy})_3]^{3+}$ using UFF overestimates. When UAKS and Bondi are used, the results show an underestimation. Using PCM provides results that are similar to the CPCM results, i.e. underestimation of $E^0(\text{cal, SCE})$ for both $[\text{Ru}(\text{bpy})_3]^{2+}$ and $[\text{Ru}(\text{bpy})_3]^{3+}$ except for the $E^0(\text{cal, SCE})$ of $[\text{Ru}(\text{bpy})_3]^{3+}$ which is overestimated. Moreover, this calculation also shows that, when we use the same cavity model, we found very little difference between PCM and CPCM (< 0.01 V). However, the CPCM is slightly better than PCM.

When taking into account the cavity model for $E^0(\text{cal, SCE})$ using CPCM, the deviation between calculation and experiment for the $E^0(\text{cal, SCE})$ of $[\text{Ru}(\text{bpy})_3]^{2+}$ are 0.35, 0.57 and 0.59 V using UFF, UAKS and Bondi cavities, respectively, and for the $E^0(\text{cal, SCE})$ of $[\text{Ru}(\text{bpy})_3]^{3+}$ are -0.05, 0.39 and 0.51 V using UFF, UAKS and Bondi cavities, respectively. Therefore, the results for the calculation with a UFF cavity agree most closely with the experimental data. Thus, the ωB97XD functional with the CPCM solvation model and UFF solute cavity model for $E^0(\text{cal, SCE})$ determination was used in subsequent calculations.

To determine the effect of spin multiplicity, we have also calculated the high-spin $[\text{Ru}(\text{bpy})_3]^{2+}$ and $[\text{Ru}(\text{bpy})_3]^{3+}$ complexes. The $E^0(\text{cal, SCE})$ calculations with CPCM and PCM corrections with UFF cavity for both $[\text{Ru}(\text{bpy})_3]^{2+}$ and $[\text{Ru}(\text{bpy})_3]^{3+}$ complexes are shown in Table 7.2. The ωB97XD functional predicts the $E^0(\text{cal, SCE})$ of $[\text{Ru}(\text{bpy})_3]^{2+}$ better than PBE, while PBE predicts the $E^0(\text{cal, SCE})$ of $[\text{Ru}(\text{bpy})_3]^{3+}$ better. However, PBE gets the sign wrong for $[\text{Ru}(\text{bpy})_3]^{2+} + \text{e}^- \rightarrow$

$[\text{Ru}(\text{bpy})_3]^+$. The calculated results reveal that all ωB97XD calculations overestimate $E^0(\text{cal, SCE})$ and are significantly different from experimental value (the deviation between calculation and experiment is more than 1.00 V for one-electron transfer (96.5 kJ mol⁻¹)).

As discussed above, our results for $E^0(\text{cal,SCE})$ of $[\text{Ru}(\text{bpy})_3]^{2+}$ are not consistent with the experimental data, but the reaction mechanism in this study involves the reduction of $[\text{Ru}(\text{bpy})_3]^{3+}$ low-spin complex ($[\text{Ru}(\text{bpy})_3]^{3+} + e^- \rightarrow [\text{Ru}(\text{bpy})_3]^{2+}$), with the smallest error (0.05 V), which is in agreement with the ligand type that the 2,2'-bipyridine ligand exerts a strong ligand field leading to form low-spin complexes.²³⁸ It indicates that the best agreement with the experimental value in MeCN can be achieved using the $\omega\text{B97XD}/6\text{-}311\text{++G}(2\text{df},2\text{p})[\text{SDD}]$ combined with the CPCM solvation and UFF solute cavity model approach after $\text{PBE}/6\text{-}31\text{+G}(\text{d},\text{p})[\text{SDD}]$ optimisation (Gaussian 09 implementation). Therefore, all reaction mechanisms in this study performed in MeOH will use these methods, basis sets, solvation model and solute cavity model.

Using this methodology, i.e. $\omega\text{B97XD}/6\text{-}311\text{++G}(2\text{df},2\text{p})[\text{SDD}]/\text{PBE}/6\text{-}31\text{+G}(\text{d},\text{p})[\text{SDD}]$ with the CPCM solvation and UFF solute cavity model, the absolute potential of the reaction $[\text{Ru}(\text{bpy})_3]^{3+} + e^- \rightarrow [\text{Ru}(\text{bpy})_3]^{2+}$ in MeOH (rather than MeCN used for this validation) is 1.26 eV.

Table 7.1. Comparison of the calculated and experimental data of redox potential for low spin complex $[\text{Ru}(\text{bpy})_3]^{n+}$ in MeCN solvent with different solvation model and molecular cavity.

Half reaction	Method	Solvation model / Molecular cavity	$E^0(\text{cal, SCE}) / \text{V}$	${}^a E^0(\text{expt}) / \text{V}$	ΔE^0
$[\text{Ru}(\text{bpy})_3]^{2+} + e^- \rightarrow [\text{Ru}(\text{bpy})_3]^+$	ωB97XD	CPCM / UFF	-1.68	-1.33	-0.35
$[\text{Ru}(\text{bpy})_3]^{2+} + e^- \rightarrow [\text{Ru}(\text{bpy})_3]^+$	PBE	CPCM / UFF	-0.89	-1.33	0.44
$[\text{Ru}(\text{bpy})_3]^{2+} + e^- \rightarrow [\text{Ru}(\text{bpy})_3]^+$	ωB97XD	CPCM / UAKS	-1.90	-1.33	-0.57
$[\text{Ru}(\text{bpy})_3]^{2+} + e^- \rightarrow [\text{Ru}(\text{bpy})_3]^+$	ωB97XD	CPCM / Bondi	-1.92	-1.33	-0.59
$[\text{Ru}(\text{bpy})_3]^{3+} + e^- \rightarrow [\text{Ru}(\text{bpy})_3]^{2+}$	ωB97XD	CPCM / UFF	1.34	1.29	0.05
$[\text{Ru}(\text{bpy})_3]^{3+} + e^- \rightarrow [\text{Ru}(\text{bpy})_3]^{2+}$	PBE	CPCM / UFF	1.49	1.29	0.20
$[\text{Ru}(\text{bpy})_3]^{3+} + e^- \rightarrow [\text{Ru}(\text{bpy})_3]^{2+}$	ωB97XD	CPCM / UAKS	0.90	1.29	-0.39
$[\text{Ru}(\text{bpy})_3]^{3+} + e^- \rightarrow [\text{Ru}(\text{bpy})_3]^{2+}$	ωB97XD	CPCM / Bondi	0.78	1.29	-0.51
$[\text{Ru}(\text{bpy})_3]^{2+} + e^- \rightarrow [\text{Ru}(\text{bpy})_3]^+$	ωB97XD	PCM / UFF	-1.69	-1.33	-0.36
$[\text{Ru}(\text{bpy})_3]^{2+} + e^- \rightarrow [\text{Ru}(\text{bpy})_3]^+$	PBE	PCM / UFF	-0.89	-1.33	0.44
$[\text{Ru}(\text{bpy})_3]^{2+} + e^- \rightarrow [\text{Ru}(\text{bpy})_3]^+$	ωB97XD	PCM / UAKS	-1.91	-1.33	-0.58
$[\text{Ru}(\text{bpy})_3]^{2+} + e^- \rightarrow [\text{Ru}(\text{bpy})_3]^+$	ωB97XD	PCM / Bondi	-1.93	-1.33	-0.60
$[\text{Ru}(\text{bpy})_3]^{3+} + e^- \rightarrow [\text{Ru}(\text{bpy})_3]^{2+}$	ωB97XD	PCM / UFF	1.34	1.29	0.05
$[\text{Ru}(\text{bpy})_3]^{3+} + e^- \rightarrow [\text{Ru}(\text{bpy})_3]^{2+}$	PBE	PCM / UFF	1.49	1.29	0.20
$[\text{Ru}(\text{bpy})_3]^{3+} + e^- \rightarrow [\text{Ru}(\text{bpy})_3]^{2+}$	ωB97XD	PCM / UAKS	0.90	1.29	-0.39
$[\text{Ru}(\text{bpy})_3]^{3+} + e^- \rightarrow [\text{Ru}(\text{bpy})_3]^{2+}$	ωB97XD	PCM / Bondi	0.77	1.29	-0.52

^a $E^0(\text{expt})$ values were taken from Bock *et al.*²⁵⁷

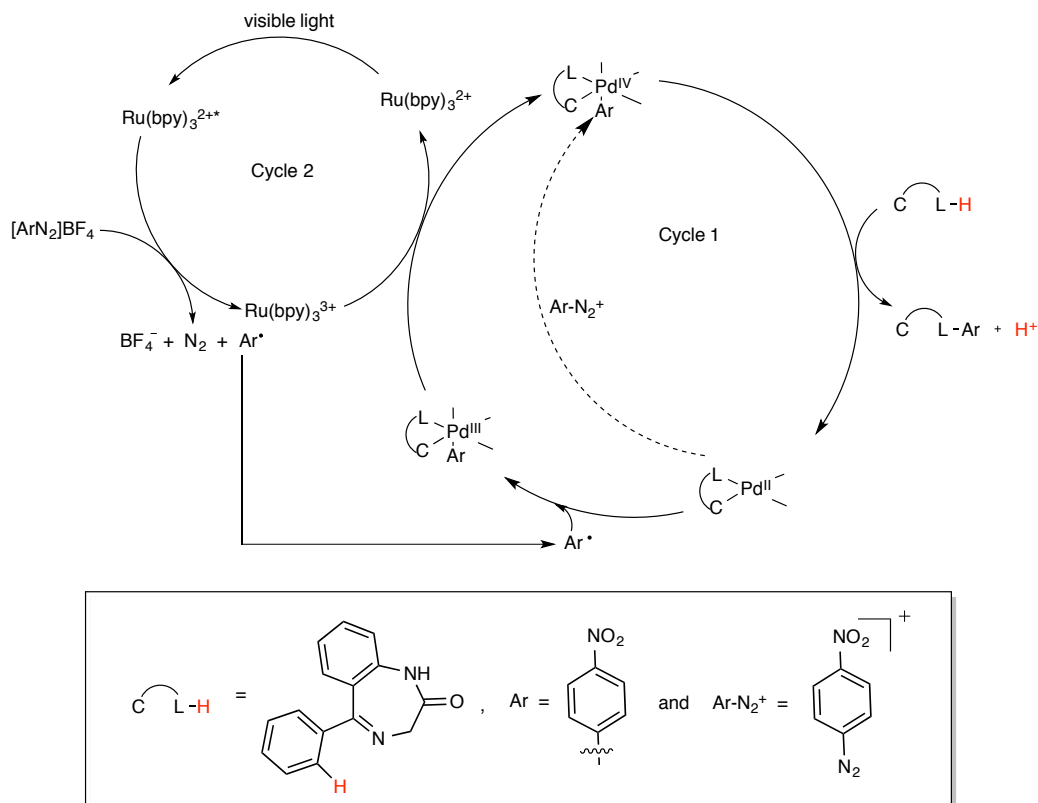
Table 7.2. Comparison of the calculated and experimental data of redox potential for high spin complex $[\text{Ru}(\text{bpy})_3]^{n+}$ in MeCN solvent with different solvation model and molecular cavity.

Half reaction	Method	Solvation model / Molecular cavity	$E^0(\text{cal, SCE}) / \text{V}$	${}^a E^0(\text{expt}) / \text{V}$	ΔE^0
$[\text{Ru}(\text{bpy})_3]^{2+} + e^- \rightarrow [\text{Ru}(\text{bpy})_3]^+$	ω B97XD	CPCM / UFF	-0.28	-1.33	1.05
$[\text{Ru}(\text{bpy})_3]^{2+} + e^- \rightarrow [\text{Ru}(\text{bpy})_3]^+$	PBE	CPCM / UFF	1.51	-1.33	2.84
$[\text{Ru}(\text{bpy})_3]^{2+} + e^- \rightarrow [\text{Ru}(\text{bpy})_3]^+$	ω B97XD	CPCM / UAKS	-0.29	-1.33	1.04
$[\text{Ru}(\text{bpy})_3]^{2+} + e^- \rightarrow [\text{Ru}(\text{bpy})_3]^+$	ω B97XD	CPCM / Bondi	-0.27	-1.33	1.06
$[\text{Ru}(\text{bpy})_3]^{3+} + e^- \rightarrow [\text{Ru}(\text{bpy})_3]^{2+}$	ω B97XD	CPCM / UFF	4.17	1.29	2.88
$[\text{Ru}(\text{bpy})_3]^{3+} + e^- \rightarrow [\text{Ru}(\text{bpy})_3]^{2+}$	PBE	CPCM / UFF	2.54	1.29	1.25
$[\text{Ru}(\text{bpy})_3]^{3+} + e^- \rightarrow [\text{Ru}(\text{bpy})_3]^{2+}$	ω B97XD	CPCM / UAKS	3.83	1.29	2.54
$[\text{Ru}(\text{bpy})_3]^{3+} + e^- \rightarrow [\text{Ru}(\text{bpy})_3]^{2+}$	ω B97XD	CPCM / Bondi	3.74	1.29	2.45
$[\text{Ru}(\text{bpy})_3]^{2+} + e^- \rightarrow [\text{Ru}(\text{bpy})_3]^+$	ω B97XD	PCM / UFF	0.01	-1.33	1.34
$[\text{Ru}(\text{bpy})_3]^{2+} + e^- \rightarrow [\text{Ru}(\text{bpy})_3]^+$	PBE	PCM / UFF	1.49	-1.33	2.82
$[\text{Ru}(\text{bpy})_3]^{2+} + e^- \rightarrow [\text{Ru}(\text{bpy})_3]^+$	ω B97XD	PCM / UAKS	-0.29	-1.33	1.04
$[\text{Ru}(\text{bpy})_3]^{2+} + e^- \rightarrow [\text{Ru}(\text{bpy})_3]^+$	ω B97XD	PCM / Bondi	-0.27	-1.33	1.06
$[\text{Ru}(\text{bpy})_3]^{3+} + e^- \rightarrow [\text{Ru}(\text{bpy})_3]^{2+}$	ω B97XD	PCM / UFF	4.08	1.29	2.79
$[\text{Ru}(\text{bpy})_3]^{3+} + e^- \rightarrow [\text{Ru}(\text{bpy})_3]^{2+}$	PBE	PCM / UFF	2.55	1.29	1.26
$[\text{Ru}(\text{bpy})_3]^{3+} + e^- \rightarrow [\text{Ru}(\text{bpy})_3]^{2+}$	ω B97XD	PCM / UAKS	3.82	1.29	2.53
$[\text{Ru}(\text{bpy})_3]^{3+} + e^- \rightarrow [\text{Ru}(\text{bpy})_3]^{2+}$	ω B97XD	PCM / Bondi	3.72	1.29	2.43

^a $E^0(\text{expt})$ values were taken from Bock *et al.*²⁵⁷

7.4.2 Mechanism of functionalisation using Pd(II)/Ru(II)-catalysts

A possible reaction mechanism for functionalisation of a benzodiazepine using Pd(II)/Ru(II)-catalysts for the entire catalytic cycle is shown in Scheme 7.16, based on Scheme 7.13. Cycle 1 involves a Pd(II)-catalyst and cycle 2 involves the Ru(II)-catalyst.



Scheme 7.16. Possible reaction cycle of functionalisation using Pd(II)/Ru(II)-catalysts used in this work. The dotted line indicates the role of Pd(II) in the absence of the Ru(II)-photocatalyst.

First, we have studied reaction i in Scheme 7.15. The Gibbs free energy profile for functionalisation of benzodiazepine is given in Figure 7.10. The Gibbs free energies are calculated relative to the Gibbs free energy of $\text{Pd}(\text{OAc})_2 + [\text{Ru}(\text{bpy})_3]^{2+} + p\text{-nitrobenzenediazonium} + \text{unf-BZD} + \text{H}_2\text{O}$. To take account of the proton (H^+) energy, H_3O^+ is calculated and H_2O is used to balance the chemical equation in Scheme 7.15i.

C-H bond activation process: This process involves three steps and occurs *via* an agostic complex (**Int2**). The first step is the coordination between unf-BZD

and the Pd-centre of Pd(OAc)₂ to form **Int1** where the N1 atom of the unf-BZD coordinates to the Pd-centre (Scheme 7.17). The Pd coordination sphere in **Int1** is square planar. This process is exogenic by -34.1 kJ mol⁻¹ (Figure 7.10).

The second step occurs *via* **TS1-2** with Gibbs free energy barrier 36.6 kJ mol⁻¹, leading to agostic complex (**Int2**). The agostic interaction in **Int2** is confirmed by the shortening of the Pd···H bond (1.903 Å) and the elongation of C-H distance (1.147 Å), compared to **Int1** and these bond lengths of **Int2** are in good agreement with Davies *et al.*¹¹⁶ who calculated the mechanism of cyclometalation by palladium acetate (Pd···H distance = 1.91 Å and C-H bond = 1.15 Å). In addition, the bond distances of Pd···C (2.262 Å) and Pd···H (1.903 Å) of the agostic complex **Int2** are in excellent agreement with the Rh···C (2.273 Å) and Rh···H (1.950 Å) in an agostic rhodium arene complex.²⁶¹

The third step involves the C-H bond activation **TS2-3** and leads to **Int3** which involves two η¹-acetate ligands coordinated to the Pd-centre. The **TS2-3** occurs *via* a six-membered ring by transferring a H atom from C1 to O2 with Gibbs free energy barrier of 41.4 kJ mol⁻¹ and the total Gibbs free energy of **Int2** to **Int3** is -64.7 kJ mol⁻¹, indicating that this step is a spontaneous process. This step is similar to the calculation of cyclometallation of Pd(OAc)₂ with dimethylbenzylamine¹¹⁶ and cyclisation of phenyl-*tert*-butanol using Pd(OAc)₂.²⁶²

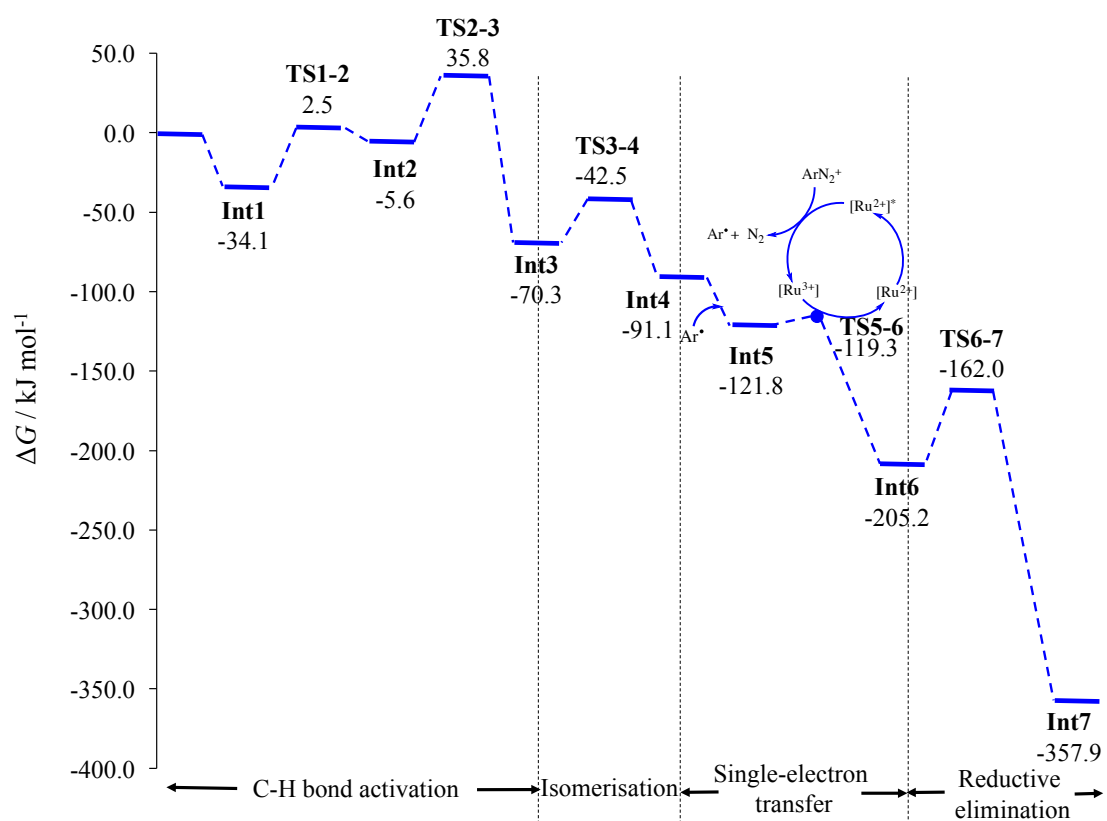
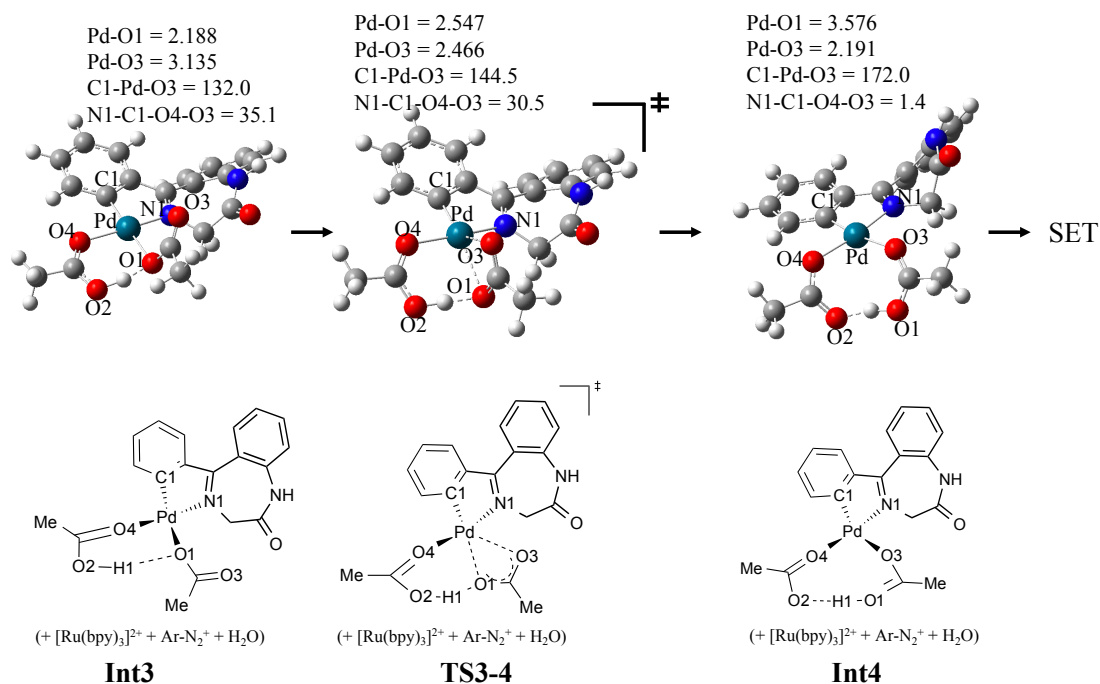


Figure 7.10. Gibbs free energy profile of the functionalisation of the benzodiazepine mechanism using Pd(II)/Ru(II)-catalysts. In the reaction mechanism cycle, $[\text{Ru}^{2+}]$ and $[\text{Ru}^{3+}]$ represent $[\text{Ru}(\text{bpy})_3]^{2+}$ and $[\text{Ru}(\text{bpy})_3]^{3+}$, respectively.

Isomerisation process: This step involves the orientation of the C1-Pd-O3 angle, which changes from 132.0 to 172.0° from **Int3** to **Int4**. Scheme 7.18 reveals the geometrical structures of this isomerisation step. **Int4** involves O3 atom coordinating and O1 atom de-coordinating, where O1 atom and O3 atom are part of the same acetate ion, from the Pd *via* **TS3-4**, with Gibbs free energy barrier of 27.8 kJ mol⁻¹. In addition, the torsion angle of N1-C1-O4-O3 (35.1°) changes to square planar (N1-C1-O4-O3 = 1.4°).



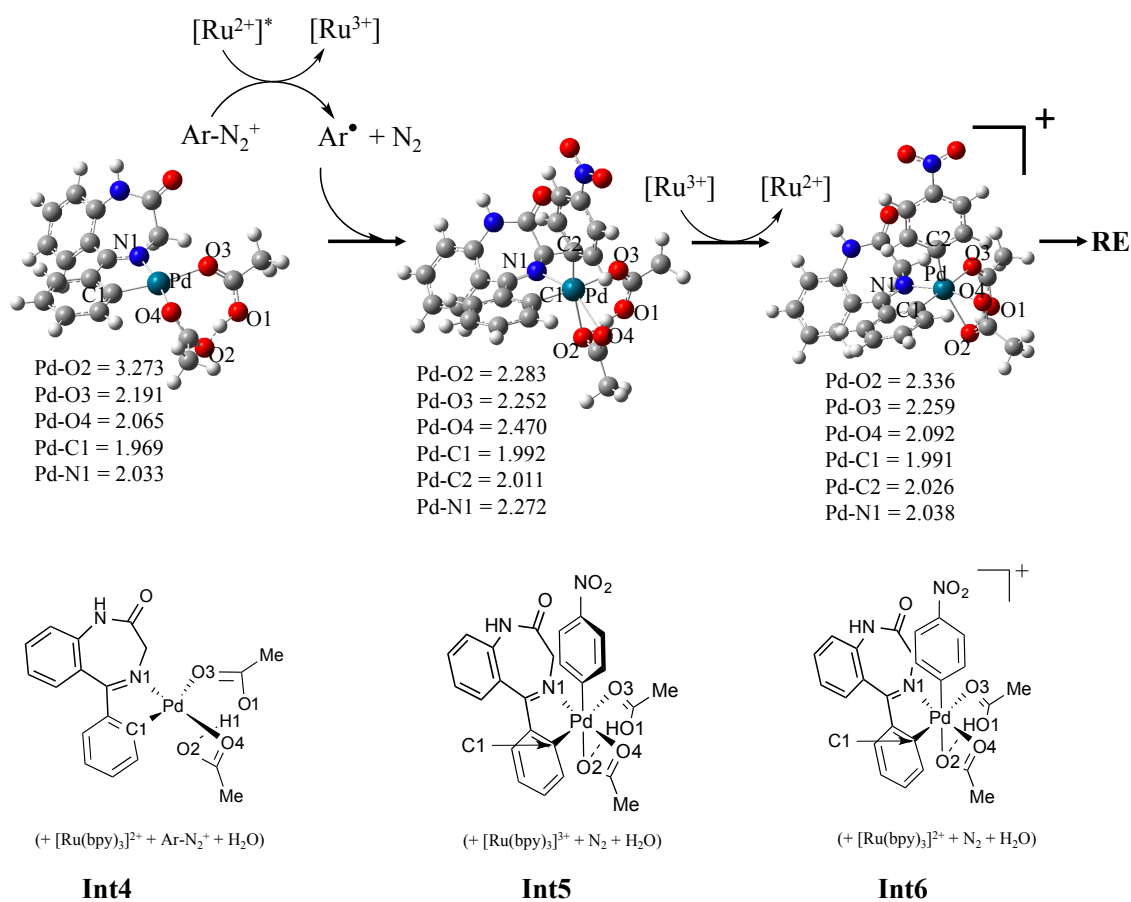
Scheme 7.18. Calculated geometries for isomerisation process. The bond distances are shown in Å and bond angles are in degree.

Single-electron transfer (SET) process: Scheme 7.19 shows the reaction mechanism of the SET. In experimental observation, [Ru(bpy)₃]²⁺ absorbs the visible light then [Ru(bpy)₃]^{2+*} is generated.²⁶³ [Ru(bpy)₃]^{2+*} is oxidatively quenched by *p*-nitrobenzenediazonium to give nitrobenzene radical.²⁶³ The isomerisation in the previous process occurs to avoid steric hindrance with the nitrobenzene radical. Now, the nitrobenzene radical can bind at the Pd-centre of **Int4** to form **Int5** and the Gibbs free energy decreases to -121.8 kJ mol⁻¹, indicating a spontaneous process. We have not found the transition structure between **Int4** and **Int5**. It appears to be a barrierless process, confirmed by calculating the energy whilst varying the Pd...C2 atomic distances of **Int5** which increases monotonically. This SET step involves a change in the oxidation state of the Pd-centre from Pd(II) to Pd(III). The

geometry around Pd coordination sphere changes from a square planar (**Int4**) to a distorted-octahedral Pd complex (**Int5**). **Int5** geometry is consistent with the X-ray structure of Pd(III)-complexes reported by Khusnutdinova *et al.*,^{264,265} where the Pd complexes were six-coordinate structures. In **Int5**, O2 moves to bind with the Pd-centre, changing the Pd...O2 distance from 3.273 Å in **Int4** to 2.283 Å in **Int5** and Pd-O4 bond increases from 2.065 Å in **Int4** to 2.470 Å in **Int5**, indicating that the interaction of Pd-O4 bond in **Int5** is weaker than Pd-O4 in **Int4**.

Applying Marcus and Savéant theory, we can calculate the SET Gibbs free energy barrier, $\Delta G_{\text{ET}}^\ddagger$, using equation (7.9). ΔG_r is the energy difference between **Int5** and **Int6** where **Int5** corresponds to the energy of Pd(III)-complex + [Ru(bpy)₃]³⁺ + N₂ + H₂O and **Int6** corresponds to the energy of Pd(IV)-complex + [Ru(bpy)₃]²⁺ + N₂ + H₂O. This has a value of -83.4 kJ mol⁻¹. To calculate ΔG_0^\ddagger (equation (7.5)), we need to calculate $\lambda = \lambda_i + \lambda_0$ (equation (7.6)). In this work, as in previous work,^{249,266} it is assumed the inner reorganisation energy of the reactants is zero ($\lambda_i = 0$). Therefore, λ is equal to λ_0 which is calculated using equation (7.8). The hard sphere radii approximation of [Ru(bpy)₃]³⁺ and the Pd(III)-complex (**Int5**) were calculated using keyword VOLUME in Gaussian09. We have found that the hard sphere radii of [Ru(bpy)₃]³⁺ is 6.18 Å and for the Pd(III)-complex (**Int5**) is 6.47 Å. The optical dielectric constant can be approximated from a refractive index squares.²⁶⁷ The optical dielectric constant of methanol is 1.76²⁶⁸ and the static dielectric constant of methanol is 32.613. Therefore, $\lambda = \lambda_0 = 59.1$ kJ mol⁻¹. Now, we can calculate ΔG_0^\ddagger , the intrinsic barrier at zero driving force for the outer-sphere electron transfer, i.e. $\Delta G_0^\ddagger = \lambda/4 = 14.8$ kJ mol⁻¹. Substituting the values of ΔG_0^\ddagger and ΔG_r in equation (7.9), the SET Gibbs free energy barrier, $\Delta G_{\text{ET}}^\ddagger = 2.5$ kJ mol⁻¹. This value is a similar magnitude to that obtained for the Au/Ru-complexes SET process by Zhang *et al.*²⁶⁹ These authors found that $\Delta G_{\text{ET}}^\ddagger$ ranged from 0.4 to 15.1 kJ mol⁻¹ depending on the ligand.

As shown in Scheme 7.19, **Int5** is oxidised by [Ru(bpy)₃]³⁺ to generate **Int6** (Pd(III) → Pd(IV) complex). **Int6** is still a six-coordinate structure, commonly occurring for Pd(IV) geometry,²⁷⁰ while bond distances around the Pd-centre change compared to **Int5**.



Scheme 7.19. Calculated geometries for single-electron transfer (SET) process. The bond distances are in Å.

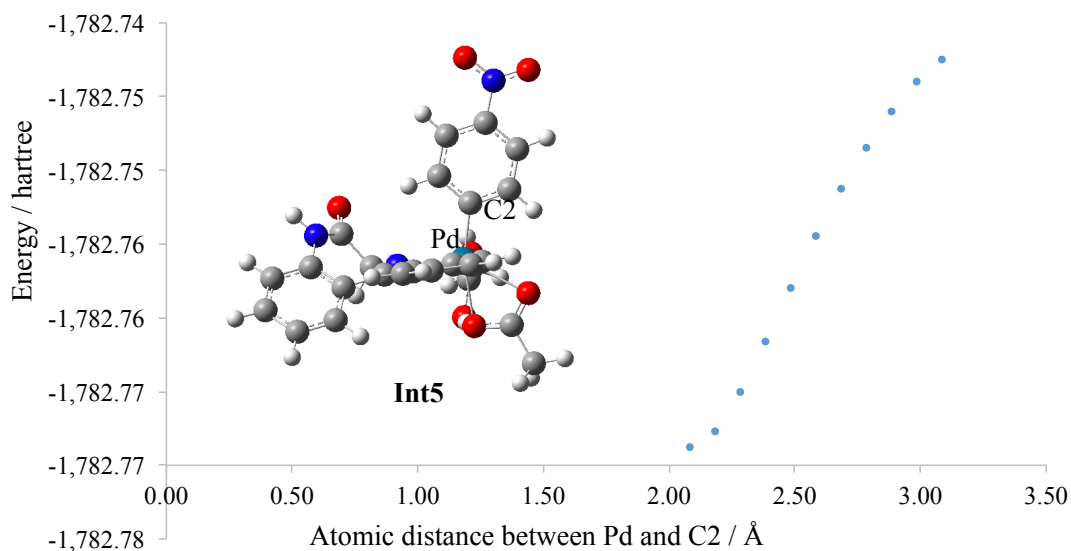
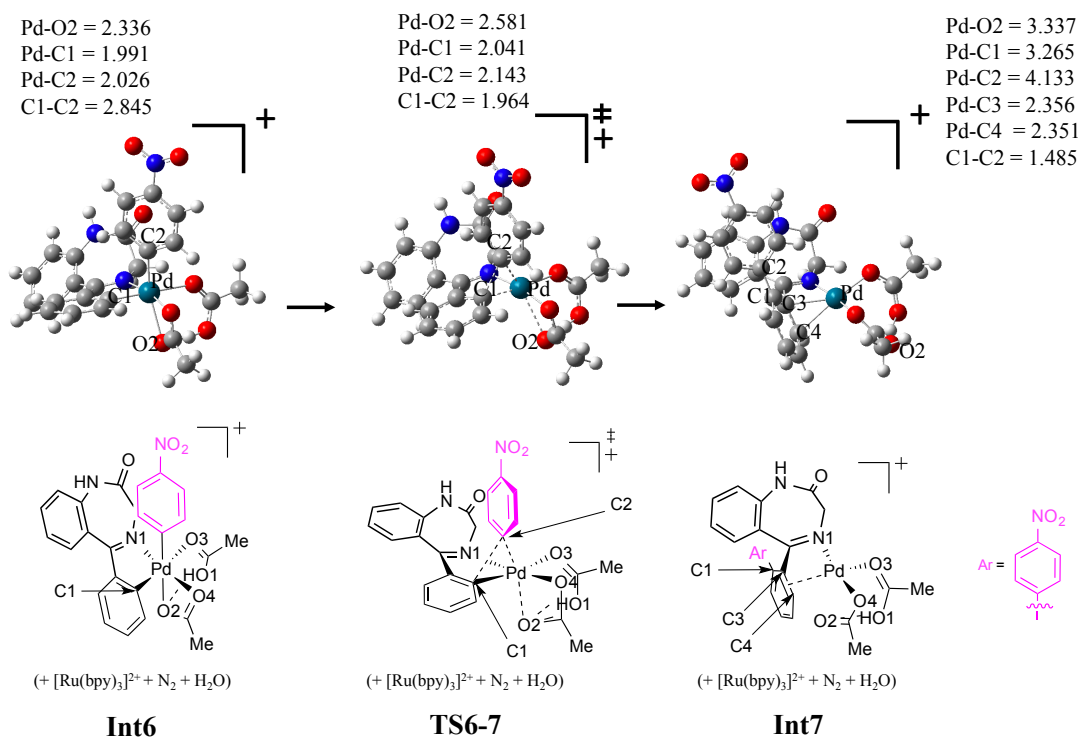


Figure 7.11. The energy plot by varying the bond distance between Pd and C2 to confirm no transition state between **Int4** and **Int5** (assuming Pd-C2 is the reaction coordinate). The energies are shown in hartrees.

Reductive elimination process: The C1-C2 bond is formed through a reductive elimination step (Scheme 7.20). The oxidation state of the Pd-complex changes from Pd(IV) to Pd(II). C2 migrates from the Pd-centre to C1 *via* **TS6-7** with Gibbs free energy barrier of 43.2 kJ mol⁻¹; C1...C2 in **Int7** shortens to 1.485 Å, indicating a bond forming between C1 and C2. In **Int7**, we have found $\eta^2(\text{C}=\text{C})$ interacting with Pd; Pd...C3 is 2.356 Å and Pd...C4 is 2.351 Å. This structure is supported by investigation of the reductive elimination mechanism from bimetallic palladium complex by Ariaifard *et al.*²⁷¹ and Canty *et al.*²⁷² work. They found the η^2 -coordination with Pd...C after the reductive elimination step in their DFT calculations.



Scheme 7.20. Calculated geometries for reductive elimination process. The bond distances are in Å.

For cycle 2, the excited-state redox potential is determined. The excited-state was calculated using TDDFT with the CAM-B3LYP functional. The Latimer diagram is performed for excited-state redox potential calculations. We found that the redox ground state $[\text{Ru}(\text{bpy})_3]^{3+} + e^- \rightarrow [\text{Ru}(\text{bpy})_3]^{2+}$ is accurate enough for calculation of excited-state redox potential, with an error of only 0.05 V (see Table 7.1).

For saving CPU time, we calculated this step using CAM-B3LYP/6-31+G(d,p)[SDD] with methanol solvation CPCM and UFF cavity models, and hence only get the E^{adia} . We have found that the frequency calculation of the excited state is hard to converge. Jacquemin *et al.*²³⁴ mentioned that 90% of the time for determining the excitation optimisation came from the vibration frequency calculation. In our calculation, CPU time for optimisation of the excited-state was ca. 51 days (single core), therefore the vibration frequency for determination of this structure is estimated to be ca. 459 days. Therefore, we firstly approximate $E^{0-0} \approx E^{\text{adia}}$. This may introduce an error, but in the absence of experiment, this cannot be confirmed. The HOMO-LUMO transition, chosen to study the E^{0-0} , involves a metal-to-ligand charge transfer (MLCT) complex (Figure 7.12). Our calculation reveals that the E^{adia} is 2.98 eV.

We do not have a E^{0-0} experimental data of $[\text{Ru}(\text{bpy})_3]^{2+}$ in methanol. This is a limitation of our benchmark set for checking the calculation. Therefore, we have used a vertical excitation energy (E^{ver}) for checking our calculation. In theory, E^{ver} should be more than or equal to E^{adia} . Our calculation shows that E^{ver} is 3.36 eV with oscillator strength of 0.0013, which is greater than our calculated E^{adia} .

Using Latimer diagram for excited state redox potential (equation (7.2)), the excited-state redox potential of $[\text{Ru}(\text{bpy})_3]^{2+}$ is -1.72 eV calculated as the difference between reduction potential $E^0(\text{SCE}) = 1.26$ eV (see section 7.4.1 for reduction reaction: $[\text{Ru}(\text{bpy})_3]^{3+} + e^- \rightarrow [\text{Ru}(\text{bpy})_3]^{2+}$) and $E^{0-0} \approx E^{\text{adia}} = 2.98$ eV which is the excitation energy of $[\text{Ru}(\text{bpy})_3]^{2+}$ in MeOH.

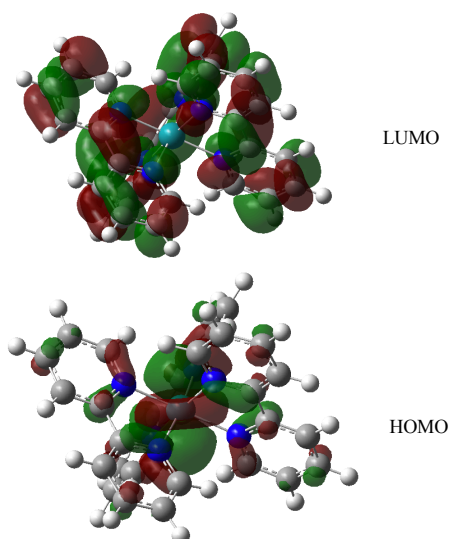


Figure 7.12. Molecular plot of HOMO and LUMO of $[\text{Ru}(\text{bpy})_3]^{2+}$.

In summary, the overall reaction of the functionalisation of benzodiazepine using a Pd(II)-catalyst with a Ru(II)-photocatalyst is -189.3 kJ mol^{-1} . The energy barrier of C-H bond activation step (**TS2-3**) differs from the reductive elimination step by only 1.8 kJ mol^{-1} , indicating that they are the rate-determining steps in this reaction. In the SET step, the Gibbs free energy barrier is just 2.5 kJ mol^{-1} .

7.4.3 Mechanism of functionalisation using Pd(II)-catalyst

It is assumed that the mechanism for functionalisation using a Pd(II)-catalyst involves the following main processes: i) C-H bond activation, ii) isomerisation, iii) oxidative

addition and iv) reductive elimination. The processes i), ii) and iv) are the same as those discussed in the previous section for the reaction using Pd(II)/Ru(II)-catalysts. Therefore, in this section, we have discussed only the oxidative addition process.

To compare between Pd(II)-catalyst and Pd(II)/Ru(II)-catalysts, we have studied the Pd(II)-catalysed reaction at room temperature. The Gibbs free energy profile of the mechanism is provided in Figure 7.13. The zero energy is set to be energy of Pd(OAc)₂ + *p*-nitrobenzenediazonium + unf-BZD + H₂O.

To model the oxidative addition process, we have adapted a transition structure based on the transition state found by Canty *et al.*²⁷² who studied Ar-Ar bond formation *via* binuclear Pd(II)-complexes. The results show that in **Int5**, nitrobenzenediazonium is bound to the Pd-complex species. Then, in **TS5-6**, phenyl migrates from N to the Pd-centre; the C2-N2 bond is broken and the C2-Pd bond is formed. An oxidation state change of the Pd-centre to Pd(IV) involves a changing ligand coordination sphere. The Gibbs free energy barrier of the oxidative addition transition state is 127.1 kJ mol⁻¹. This value is significantly higher than the other Gibbs free energy barriers in the mechanism indicating that this step is the rate-determining step. The Gibbs free energy process of this step (**Int5** to **Int6**) is a thermodynamically favourable process ($\Delta G = -110.6$ kJ mol⁻¹).

In the next step, N₂ is eliminated from the Pd-complex. The removal of N₂ from **Int6** → **Int7** is a thermodynamically favourable process, with a Gibbs free energy change of -20.5 kJ mol⁻¹. The calculation of **Int6** → **Int7** is an endothermic reaction, with enthalpy change of +3.0 kJ mol⁻¹, since N₂ needs to absorb energy to break the interaction between N₂ and the Pd(IV)-complex.

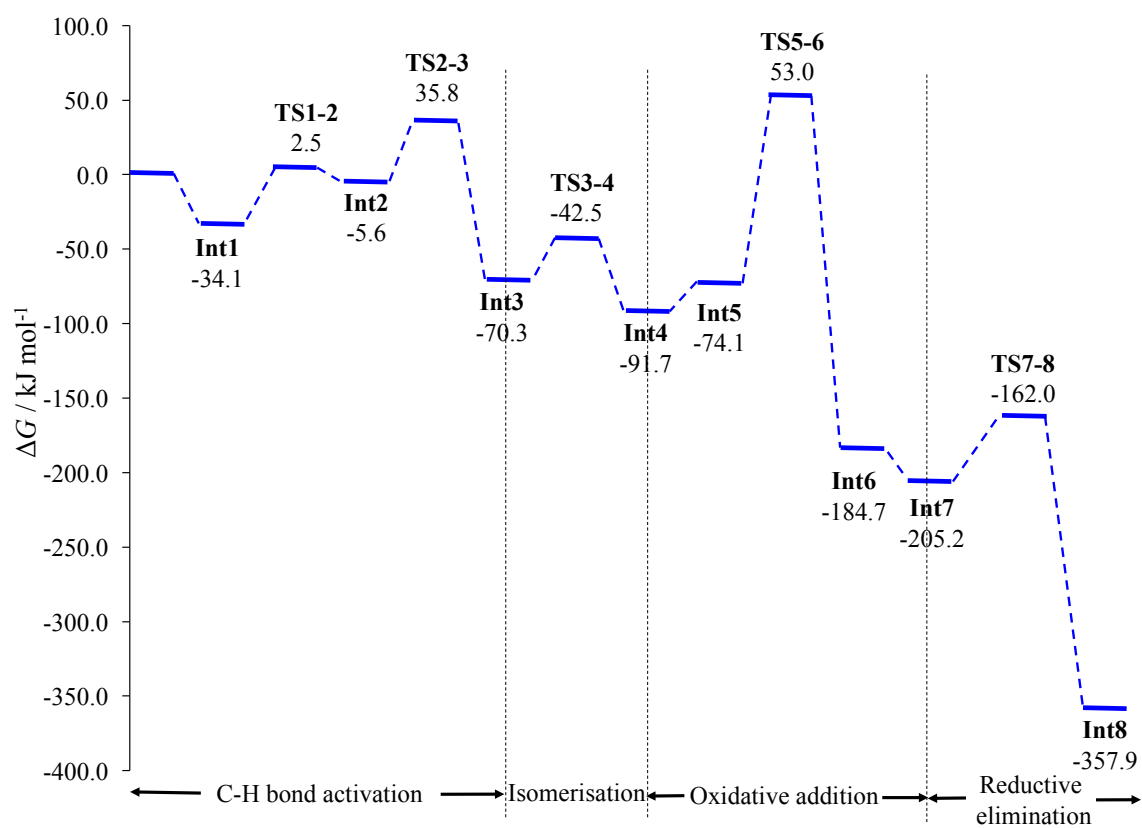
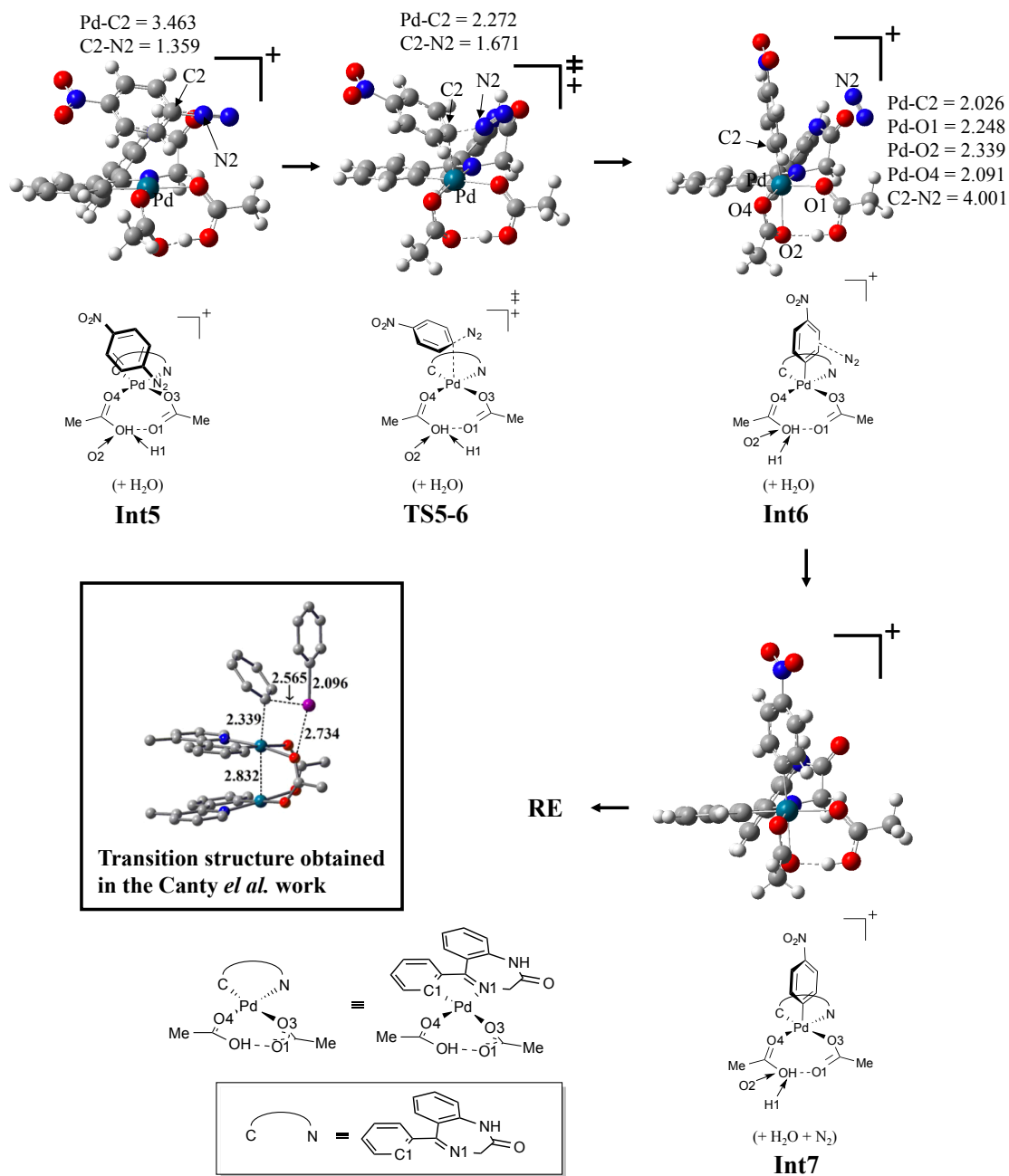


Figure 7.13. Gibbs free energy profile of functionalisation using Pd(II)-catalyst.



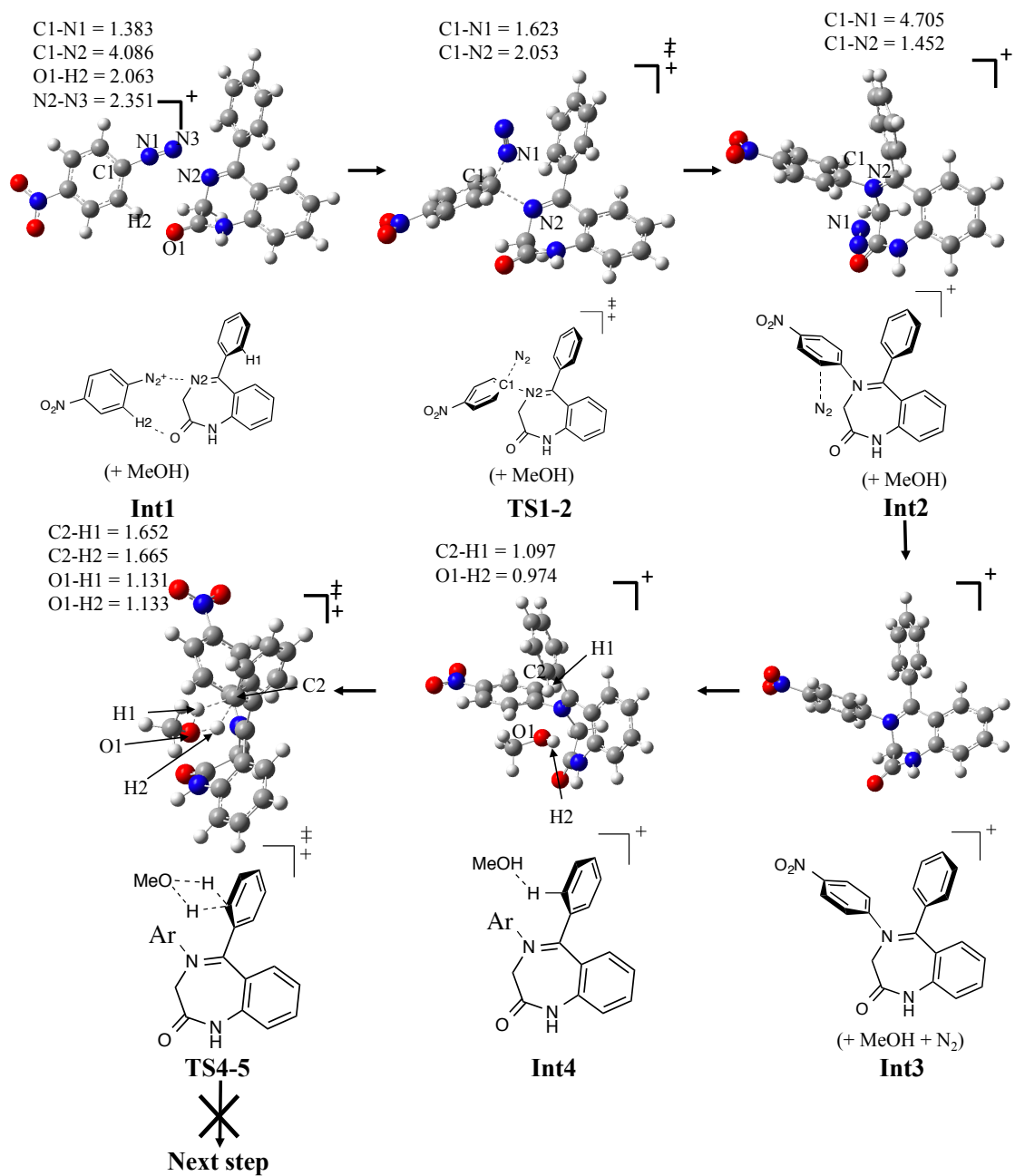
Scheme 7.21. Calculated geometries of oxidative addition process of the reaction with Pd(II)-catalyst. The model transition, **TS5-6**, is based on the transition structure obtained in the Canty *et al.* study.²⁷²

In summary, the overall Gibbs free energy reaction is the same as for mechanism involving photocatalyst, however it is shown that in the reaction mechanism involving only a Pd(II)-catalyst the oxidative addition is the rate-determining step.

7.4.4 Mechanism of functionalisation without catalyst

Scheme 7.15iii involves the reaction of the *p*-nitrobenzenediazonium with unf-BZD in the absence of a catalyst. It was not possible to abstract the H1 on benzene at position 5 in the proposed reaction mechanism using a simple dielectric model for the solvent (Scheme 7.22). Therefore, an explicit MeOH molecule to model the solvent was introduced to abstract the H1 and facilitate the migration of the nitrobenzene to the carbon to form the C-C bond. Figure 7.14 shows the Gibbs free energy profile where the energy is relative to *p*-nitrobenzenediazonium + unf-BZD + MeOH (explicit solvent). At the first step, the structure of *p*-nitrobenzenediazonium binds to unf-BZD (Scheme 7.22). We have found that this step is a thermodynamically unfavourable process with ΔG of 40.4 kJ mol⁻¹. In the **TS1-2** transition, the mechanism is a S_N2 reaction where the N2 in the diazepine ring acts as a nucleophile which attacks the C1 of electrophilic *p*-nitrobenzenediazonium to generate **Int2**. Following **Int2**, **Int3** involves the removal of N₂, and this step is spontaneous. In the next step, H1 needs to be abstracted to facilitate the migration of the nitrogen to the carbon, forming the product. An explicit MeOH molecule was used to try and abstract H1 *via* **TS4-5** but given that H1 is not acidic and MeOH is not sufficiently basic to abstract this H, the reaction could not proceed.

In the absence of a catalyst to facilitate the H1 abstraction, we conclude that this reaction will not proceed.



Scheme 7.22. Calculated geometries of functionalisation reaction without catalyst with an explicit MeOH molecule.

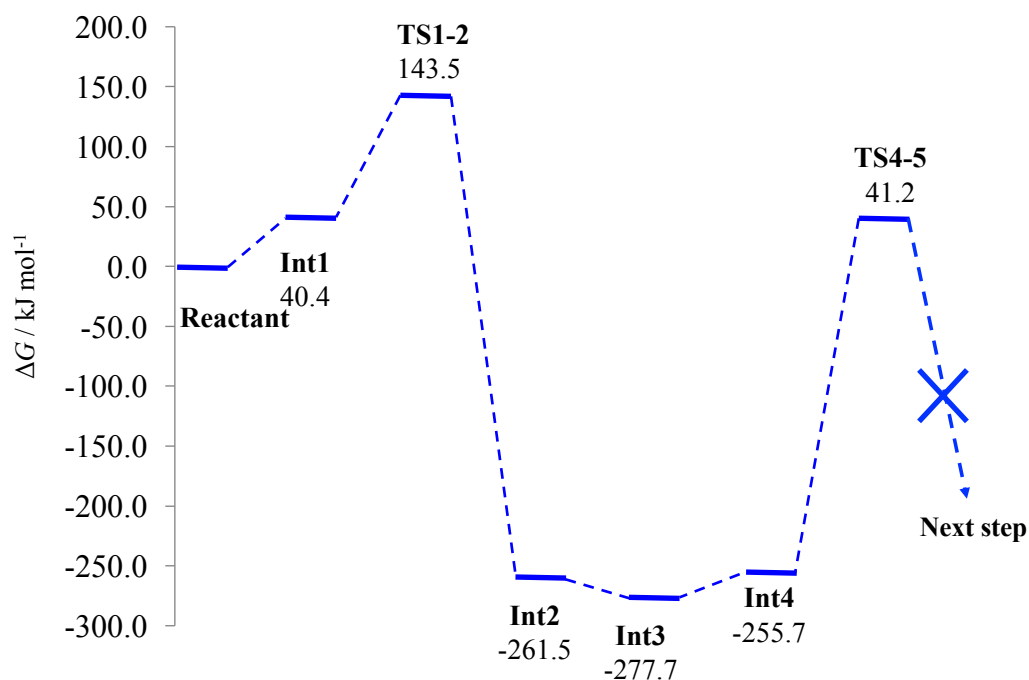


Figure 7.14. Gibbs free energy profile of functionalisation without catalyst with an explicit MeOH molecule.

7.4.5 Consideration of the role of the catalyst

The calculations show that the catalyst has a major effect on the functionalisation reaction. If no catalyst is loaded in the reaction, the functionalisation of benzodiazepine does not occur in experiments, supported by computational investigation of the reaction without a catalyst. In the reaction with the Pd(II)/Ru(II)-catalysts, it is shown that the **TS2-3** of C-H bond activation step and **TS6-7** of reductive elimination step have very similar Gibbs free energy barrier where they differ by 1.8 kJ mol⁻¹ and the SET barrier was just 2.5 kJ mol⁻¹. Therefore, both **TS2-3** and **TS6-7** were rate-determining steps. In the reaction with just the Pd(II)-catalyst, the rate-determining step was the oxidative addition, which had a barrier of 127.1 kJ mol⁻¹. Thus it has been shown that the Pd(II)/Ru(II)-catalytic condition has an energy barrier lower than the Pd(II)-catalytic condition by 83.9 kJ mol⁻¹. In the overall reaction mechanism studied, it suggests that the best condition for functionalisation of benzodiazepine is the reaction using the Pd(II)-catalyst with the Ru(II)-photocatalyst.

7.5 Conclusion

In this chapter, the functionalisation reaction of a benzodiazepine under three conditions i) Pd(II)/Ru(II)-catalysts, ii) Pd(II)-catalyst and ii) without catalyst was investigated. First, we investigated an effective and a reliable solvation and cavity model to calculate the reduction potential of tris-2,2'-bipyridylruthenium(m) ion ($m = \text{II}$ and III) ($[\text{Ru}(\text{bpy})_3]^{n+}$, $n = 2, 3$). The reduction potential calculation of $[\text{Ru}(\text{bpy})_3]^{2+}$ and $[\text{Ru}(\text{bpy})_3]^{3+}$ using $\omega\text{B97XD}/6\text{-311++G}(2\text{df},2\text{p})[\text{SDD}]/\text{PBE}/6\text{-31+G}(\text{d},\text{p})[\text{SDD}]$ with solvent correction using either CPCM or PCM solvation models, with UFF solute cavity provided the best results. The results were in good agreement with experiment with the deviation of ≈ 0.36 eV for the reduction potential of $[\text{Ru}(\text{bpy})_3]^{2+}$ and 0.05 eV for $[\text{Ru}(\text{bpy})_3]^{2+}$. These results imply that the solute cavity model is important for studying the Gibbs free energy.

Through theoretical study of functionalisation on benzodiazepines, we have found that for the Pd(II)/Ru(II)-catalyst calculations, the reaction occurred *via* C-H bond activation, isomerisation, single-electron transfer, reductive elimination and catalytic recovery. The C-H bond activation and reductive elimination are the rate-determining steps, but in consideration of thermodynamic properties, the reductive elimination is a more thermodynamically favourable process than C-H bond activation. The calculation results show good agreement with the proposed reaction mechanism by Kalyani *et al.*²²⁹

In the mechanism with just the Pd(II)-catalyst, there are five steps; C-H bond activation, isomerisation, oxidative addition, reductive elimination and catalytic recovery. We have found that in this condition the oxidative addition is the rate-determining step and is also a thermodynamically favourable process. For the condition without catalyst, no product was found.

In summary, these calculation have shown that in the absence of the photocatalyst, the reaction proceeds *via* oxidative addition and this is the rate-determining step. When the photocatalyst is introduced the rate-determining oxidative addition step is circumvented as the reaction proceeds *via* a SET process. The barrier to SET is considerably smaller, at just 2.5 kJ mol^{-1} , compared with oxidative addition which is $127.1 \text{ kJ mol}^{-1}$ explaining the increased yield in the presence of the photocatalyst.

Chapter 8

Concluding Remarks, Future Direction and Thesis Outcome

8.1 Concluding remarks

In this thesis, we have used quantum chemistry to elucidate the reactivity and mechanism of some palladium catalysts. It was shown in Chapters 3 and 4 that density functional theory is a suitable methodology for studying the electronic and geometric pincer palladacycle structures. DFT provides a good performance for accurate prediction of pincer palladacycle structures⁸⁶ and all pincer palladacycle structures both symmetric and unsymmetric require a single-reference method.

The main focus has been the catalytic behaviour of palladium complexes. In this thesis, we have demonstrated that the donor atoms of the pincer palladacycles play a crucial role in the stability, pincer palladacycle formation reaction (Chapter 5) and catalytic activity of the pincer palladacycle pre-catalysts (Chapter 6). For forming pincer compounds, the C-H bond activation step was key, and its energy barrier depends on the type of donor atom coordinating to the palladium atom.^{32,86} The strength and nature of dative bonds of pincer palladacycles can be investigated using the Quantum Theory of Atoms In Molecules and there was an interesting point in the case of the unsymmetric palladacycles which are the strength of the dative bond depended on the *trans* influence (Chapter 5).¹⁵⁹ In the catalytic activity (Chapter 6), it was shown that good pincer palladacycle pre-catalysts should have a large TM, RE or overall reaction energies to control the release of catalytically active Pd(0).

The magnitude of the barriers were again found to depend on the donor atoms, and which donor ligand arm de-coordinated first.¹⁸⁸

In Chapter 7, Pd(II)-catalysis was considered. It was found that the reaction can be enhanced when the Pd(II)-catalyst is used in conjunction with a Ru(II)-photocatalyst. When photocatalyst ruthenium complex was introduced in the reaction, the single electron transfer (SET) reaction occurred instead of the rate-determining oxidative addition and the SET barrier was considerably smaller, explaining the increased yield.

8.2 Future direction

R. Raysa in the Spencer group has conducted functionalisation of benzodiazepine using different starting reagents using the palladium complex catalyst and photocatalyst ruthenium complex. The percentage yield of functionalised-benzodiazepine products was found to vary when substitution in the aryldiazonium salt was changed (Figure 8.1).

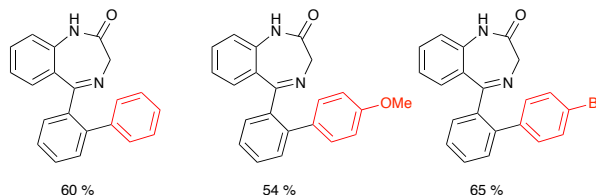


Figure 8.1. Percentage yield for functionalised-benzodiazepine products using different aryldiazonium salt.

It would be beneficial to investigate the effect of substitution in the aryldiazonium salt for functionalisation on benzodiazepine. It will be interesting to determine the reaction mechanism and thermodynamic properties using DFT to observe the effect of substitution in the aryldiazonium salt for rationalising and explaining the experimental data hence and determine the key physical and chemical properties for production of high yield.

8.3 Thesis outcomes

Various parts of this thesis have been published in journals and presented at UK and international conferences. The following is a summary of these publications and events:

Publications:

1. S. Boonseng, G. W. Roffe, J. Spencer and H. Cox “The nature of the bonding in symmetrical pincer palladacycle”, *Dalton Trans.*, 2015, **44**, 7570-7577. DOI: 10.1039/C5DT00031A
2. G. W. Roffe, S. Boonseng, C. B. Baltus, S. J. Coles, I. J. Day, R. N. Jones, N. J. Press, M. Ruiz, G. J. Tizzard, H. Cox and J. Spencer “A synthetic, catalytic and theoretical investigation of an unsymmetrical SCN pincer palladacycle”, *Royal Soc. Open Sci.*, 2016, **3**, 150656. DOI:10.1098/rsos.150656
3. S. Boonseng, G. W. Roffe, R. Jones, G. Tizzard, S. Coles, J. Spencer and H. Cox “The *trans* influence in unsymmetrical pincer palladacycles: an experimental and computational study”, *Inorganics*, 2016, **4**, 25. DOI:10.3390/inorganics4030025
4. S. Boonseng, G. W. Roffe, M. Targema, J. Spencer and H. Cox, “Rationalization of the mechanism of *in situ* Pd(0) formation for cross-coupling reactions from novel unsymmetrical pincer palladacycles using DFT calculations”, *J. Organomet. Chem.*, In Press. DOI:<http://dx.doi.org/10.1016/j.jorganchem.2017.02.040>
5. R. Khan, S. Boonseng, P. D. Kemmitt, R. Felix, S. J. Coles, G. J. Tizzard, G. Williams, O. Simmonds, J. Harvey-Cox, J. Atack, H. Cox and J. Spencer “Combining Sanford arylations on benzodiazepines with the nuisance effect”, In preparation.

Book chapter:

1. G. W. Roffe, S. Boonseng, H. Cox and J. Spencer “Pincer Compounds: Chemistry and Applications, Chapter: Synthesis and uses of unsymmetrical pincer palladacycles in catalysis.”, Elsevier, In press.

Poster presentations:

1. Sarote Boonseng and Hazel Cox “Symmetric pincer palladacycles and the reactivity of their ligands: a DFT study”, NSCCS User Meeting 2013 on 11 December 2013, Imperial College, London, UK.
2. Sarote Boonseng, Gavin W. Roffe, John Spencer and Hazel Cox “The formation of Pd(0) from pincer palladacycles”, ISTCP IX 2016 Conference on 17–22 July 2016, Grand Forks, North Dakota, USA.

Poster presentations (with flash/oral presentation):

1. Sarote Boonseng, Gavin W. Roffe, John Spencer and Hazel Cox “The nature of the bonding in symmetrical pincer palladacycles”, Young Modellers’ Forum 2014 on 28 November 2014, School of Oriental & African Studies (SOAS), London, UK.
2. Sarote Boonseng, Gavin W. Roffe, John Spencer and Hazel Cox “The nature of the bonding in symmetrical pincer palladacycles”, NSCCS User Meeting 14/15 on 18 February 2015, Imperial College, London, UK.
3. Sarote Boonseng, Gavin W. Roffe, John Spencer and Hazel Cox “The theoretical investigation of Pd(0) formation from pincer palladacycles”, Postgraduate Research Colloquium 2015 on 7-8 September 2015, University of Sussex, Brighton, UK.

Oral presentation:

1. Sarote Boonseng, Gavin W. Roffe, John Spencer and Hazel Cox “Pincer palladacycles as a source of catalytically active Pd(0): a computational study”, Postgraduate Research Colloquium 2016 on 5-6 September 2016, University of Sussex, Brighton, UK.

Virtual conference:

1. Sarote Boonseng, Gavin W. Roffe, John Spencer and Hazel Cox “The reactivity of unsymmetrical pincer ligands and the nature of the bonding in unsymmetrical pincer palladacycles”, Virtual conference on computational chemistry VCCC-2015 on 1-31 August 2015.

Transferable skills training:

1. NSCCS Gaussian Workshop for Beginners on 17-18 September 2013, Imperial College, London, UK.
2. NSCCS Gaussian Workshop on Computing Molecular Excited States on 12-13 December 2013, University of Sussex, Brighton, UK.
3. NSCCS ADF Workshop 2014 on 8-9 April 2014, Imperial College, London, UK.
4. Virtual winter school for computational chemistry on 3-9 February 2016.

References

- [1] A. C. Cope, R. W. Siekman, *J. Am. Chem. Soc.* **1965**, *87*, 3272–3273.
- [2] N. Selander, K. J. Szabó, *Chem. Rev.* **2011**, *111*, 2048–2076.
- [3] J. Dupont, C. S. Consorti, J. Spencer, *Chem. Rev.* **2005**, *105*, 2527–2571.
- [4] M. Albrecht, G. van Koten, *Angew. Chem. Int. Ed. Engl.* **2001**, *40*, 3750–3781.
- [5] F. Zamora, V. M. González, J. M. Pérez, J. R. Masaguer, C. Alonso, C. Navarro-Ranninger, *Appl. Organomet. Chem.* **1997**, *11*, 659–666.
- [6] J. Dupont, M. Pfeffer, *Palladacycles: Synthesis, Characterization and Applications*, John Wiley & Sons, **2008**, pp. 15–20.
- [7] D. J. de Geest, B. J. O’Keefe, P. J. Steel, *J. Organomet. Chem.* **1999**, *579*, 97–105.
- [8] J.-F. Gong, Y.-H. Zhang, M.-P. Song, C. Xu, *Organometallics* **2007**, *26*, 6487–6492.
- [9] D. Morales-morales, *Rev. Soc. Quim. Mex* **2004**, *48*, 338–346.
- [10] M. Ohff, A. Ohff, M. E. Van der Boom, D. Milstein, *J. Am. Chem. Soc.* **1997**, *119*, 11687–11688.
- [11] M. Beller, A. Zapf, *Synlett* **1998**, *1998*, 792–793.
- [12] D. Morales-Morales, C. Grause, K. Kasaoka, R. Redón, R. E. Cramer, C. M. Jensen, *Inorganica Chim. Acta* **2000**, *300-302*, 958–963.
- [13] D. Duncan, E. G. Hope, K. Singh, A. M. Stuart, *Dalton Trans.* **2011**, *40*, 1998–2005.

- [14] D. E. Bergbreiter, P. L. Osburn, Y.-S. Liu, *J. Am. Chem. Soc.* **1999**, *121*, 9531–9538.
- [15] K. Yu, W. Sommer, J. M. Richardson, M. Weck, C. W. Jones, *Adv. Synth. Catal.* **2005**, *347*, 161–171.
- [16] A. Corma, H. García, A. Leyva, *J. Catal.* **2006**, *240*, 87–99.
- [17] E. Alacid, C. Nájera, *European J. Org. Chem.* **2008**, 3102–3106.
- [18] K. Karami, Z. K. Moghadam, M. Hosseini-Kharat, *Catal. Commun.* **2014**, *43*, 25–28.
- [19] R. B. Bedford, S. M. Draper, P. Noelle Scully, S. L. Welch, *New J. Chem.* **2000**, *24*, 745–747.
- [20] S. Gibson, D. F. Foster, D. J. Cole-Hamilton, G. R. Eastham, R. P. Tooze, *Chem. Commun.* **2001**, *8*, 779–780.
- [21] D. Zim, A. S. Gruber, G. Ebeling, J. Dupont, A. L. Monteiro, *Org. Lett.* **2000**, *2*, 2881–2884.
- [22] T. Takemoto, S. Iwasa, H. Hamada, K. Shibatomi, M. Kameyama, Y. Motoyama, H. Nishiyama, *Tetrahedron Lett.* **2007**, *48*, 3397–3401.
- [23] R. B. Bedford, C. S. J. Cazin, *Chem. Commun.* **2001**, 1540–1541.
- [24] H. H. Zhang, W. Peng, J. Dong, Q. S. Hu, *ACS Macro Lett.* **2016**, *5*, 656–660.
- [25] K. Karami, M. Hosseini-Kharat, Z. Shirani-Sarmazeh, R. Zahedi-Nasab, C. Rizzoli, J. Lipkowski, *J. Coord. Chem.* **2016**, *69*, 763–778.
- [26] R. B. Bedford, C. S. J. Cazin, M. B. Hursthouse, M. E. Light, V. J. M. Scordia, *Dalton Trans.* **2004**, 3864.
- [27] D. A. Alonso, C. Nájera, M. C. Pacheco, *J. Org. Chem.* **2002**, *67*, 5588–5594.
- [28] Y.-C. Yang, P. H. Toy, *Synlett* **2014**, 1319–1324.
- [29] M. Mondal, U. Bora, *New J. Chem.* **2016**, *40*, 3119–3123.

- [30] W. Susanto, C.-Y. Chu, W. J. Ang, T.-C. Chou, L.-C. Lo, Y. Lam, *Green Chem.* **2012**, *14*, 77.
- [31] S. J. Sabounchei, M. Hosseinzadeh, M. Panahimehr, D. Nematollahi, H. R. Khavasi, S. Khazalpour, *Transit. Met. Chem.* **2015**, *40*, 657–663.
- [32] G. W. Roffe, S. Boonseng, C. B. Baltus, S. J. Coles, I. J. Day, R. N. Jones, N. J. Press, M. Ruiz, G. J. Tizzard, H. Cox, J. Spencer, *Royal Soc. Open Sci.* **2016**, *3*, 150656.
- [33] G. W. Roffe, G. J. Tizzard, S. J. Coles, H. Cox, J. Spencer, *Org. Chem. Front.* **2016**, *3*, 957–965.
- [34] J. Albert, S. García, J. Granell, A. Llorca, M. V. Lovelle, V. Moreno, A. Presa, L. Rodríguez, J. Quirante, C. Calvis, R. Messeguer, J. Badía, L. Baldomá, *J. Organomet. Chem.* **2013**, *724*, 289–296.
- [35] A. R. Kapdi, I. J. S. Fairlamb, *Chem. Soc. Rev.* **2014**, *43*, 4751–4777.
- [36] C. J. Cramer, *Essentials of computational chemistry: theories and models*, John Wiley & Sons, 2nd ed., **2013**.
- [37] D. Young, *Computational chemistry: a practical guide for applying techniques to real world problems.*, John Wiley & Sons, **2004**.
- [38] W. Koch, C. H. Max, *A chemist's guide to density functional theory*, John Wiley & Sons, 2nd ed., **2015**.
- [39] P. Atkins, J. De Paula, F. Ronald, *Physical Chemistry: Quanta, Matter, and Change*, Oxford University Press, USA, 2nd ed., **2013**, p. 22.
- [40] E. G. Lewars, *Computational Chemistry: Introduction to the Theory and Applications of Molecular and Quantum Mechanics*, Springer Netherlands, Dordrecht, 2nd ed., **2011**.
- [41] F. Jensen, *Introduction to computational chemistry*, John Wiley & Sons, Ltd, Chichester, UK, 2nd ed., **2013**.

- [42] P. W. Atkins, R. S. Friedman, *Molecular quantum mechanics*, Oxford University Press, Oxford, UK, 5th ed., **2011**.
- [43] I. N. Levine, *Quantum chemistry*, Pearson Education, Inc. Upper Saddle River, NJ, 6th ed., **2009**.
- [44] J. P. Perdew, *AIP Conf. Proc.* **2001**, *577*, 1–20.
- [45] J. P. Perdew, K. Burke, M. Ernzerhof, *Phys. Rev. Lett.* **1996**, *77*, 3865–3868.
- [46] J. P. Perdew, K. Burke, M. Ernzerhof, *Phys. Rev. Lett.* **1997**, *78*, 1396.
- [47] A. D. Becke, *Phys. Rev. A* **1988**, *38*, 3098–3100.
- [48] J. P. Perdew, *Phys. Rev. B* **1986**, *33*, 8822–8824.
- [49] A. D. Becke, *J. Chem. Phys.* **1997**, *107*, 8554.
- [50] J. Tao, J. Perdew, V. Staroverov, G. Scuseria, *Phys. Rev. Lett.* **2003**, *91*, 146401.
- [51] Y. Zhao, D. G. Truhlar, *J. Chem. Phys.* **2006**, *125*, 194101.
- [52] Y. Zhao, D. G. Truhlar, *Theor. Chem. Acc.* **2007**, *120*, 215–241.
- [53] J.-D. Chai, M. Head-Gordon, *Phys. Chem. Chem. Phys.* **2008**, *10*, 6615–6620.
- [54] W. G. Richards, D. L. Cooper, *Ab initio molecular orbital calculations for Chemists*, Oxford University Press, USA, **1983**.
- [55] R. Ditchfield, W. J. Hehre, J. A. Pople, *J. Chem. Phys.* **1971**, *54*, 724.
- [56] H. Hellmann, *J. Chem. Phys.* **1935**, *3*, 61.
- [57] D. Andrae, U. Häußermann, M. Dolg, H. Preuß, *Theor. Chim. Acta* **1990**, *77*, 123–141.
- [58] P. J. Hay, W. R. Wadt, *J. Chem. Phys.* **1985**, *82*, 299–310.
- [59] P. J. Hay, W. R. Wadt, *J. Chem. Phys.* **1985**, *82*, 270–283.
- [60] J. Tomasi, B. Mennucci, R. Cammi, *Chem. Rev.* **2005**, *105*, 2999–3093.

- [61] E. Cancès, B. Mennucci, *J. Math. Chem.* **1998**, *23*, 309–326.
- [62] E. Cancès, B. Mennucci, J. Tomasi, *J. Chem. Phys.* **1997**, *107*, 3032.
- [63] B. Mennucci, E. Cancès, J. Tomasi, *J. Phys. Chem. B* **1997**, *101*, 10506–10517.
- [64] R. E. Skyner, J. L. McDonagh, C. R. Groom, M. T. Van, J. B. O. Mitchell, *Phys Chem Chem Phys* **2015**, *17*, 6174–6191.
- [65] B. Mennucci, J. Tomasi, R. Cammi, J. R. Cheeseman, M. J. Frisch, F. J. Devlin, S. Gabriel, P. J. Stephens, *J. Phys. Chem. A* **2002**, *106*, 6102–6113.
- [66] R. F. W. Bader, *Acc. Chem. Res.* **1985**, *18*, 9–15.
- [67] R. F. W. Bader, *Atoms in Molecules: A Quantum Theory*, Oxford University Press, Oxford, UK, **1990**.
- [68] C. F. Matta, R. J. Boyd, *The Quantum Theory of Atoms in Molecules*, Wiley-VCH Verlag GmbH & Co. KGaA, Weinheim, Germany, **2007**, pp. 1–34.
- [69] R. F. W. Bader, *J. Phys. Chem. A* **2009**, *113*, 10391–10396.
- [70] B. D. Cremer, E. Kraka, *Angew. Chem. Int. Ed. Engl* **1984**, *23*, 627–628.
- [71] E. D. Glendening, A. E. Reed, J. E. Carpenter, F. Weinhold, *NBO 3.0 program manual*, Theoretical Chemistry Institute, University of Wisconsin, Madison, Wisconsin, **1996**.
- [72] J. P. Foster, F. Weinhold, *J. Am. Chem. Soc.* **1980**, *102*, 7211–7218.
- [73] M. Bühl, C. Reimann, D. A. Pantazis, T. Bredow, F. Neese, *J. Chem. Theory Comput.* **2008**, *4*, 1449–1459.
- [74] A. C. Tsipis, *Coord. Chem. Rev.* **2014**, *272*, 1–29.
- [75] C. J. Cramer, D. G. Truhlar, *Phys. Chem. Chem. Phys.* **2009**, *11*, 10757–10816.
- [76] F. Furche, J. P. Perdew, *J. Chem. Phys.* **2006**, *124*, 1–28.
- [77] V. Barone, C. Adamo, *Int. J. Quantum Chem.* **1997**, *61*, 443–451.

- [78] M. P. Waller, H. Braun, N. Hojdis, M. Buhl, *J. Chem. Theory Comput.* **2007**, *3*, 2234–2242.
- [79] N. Sieffert, M. Bühl, *Inorg. Chem.* **2009**, *48*, 4622–4624.
- [80] P. Rydberg, L. Olsen, *J. Phys. Chem. A* **2009**, *113*, 11949–11953.
- [81] N. Marom, A. Tkatchenko, M. Scheffler, L. Kronik, *J. Chem. Theory Comput.* **2010**, *6*, 81–90.
- [82] Y. Minenkov, A. Singstad, G. Occhipinti, V. R. Jensen, *Dalton Trans.* **2012**, *41*, 5526–5541.
- [83] J. Zhao, Y. Zhang, Y. Kan, L. Zhu, *Spectrochim. Acta Part A Mol. Biomol. Spectrosc.* **2004**, *60*, 679–688.
- [84] G. Yang, C. Jin, J. Hong, Z. Guo, L. Zhu, *Spectrochim. Acta. A. Mol. Biomol. Spectrosc.* **2004**, *60*, 3187–3195.
- [85] Z. Li, L. Liu, Y. Fu, Q. X. Guo, *J. Mol. Struct. THEOCHEM* **2005**, *757*, 69–76.
- [86] S. Boonseng, G. W. Roffe, J. Spencer, H. Cox, *Dalton Trans.* **2015**, *44*, 7570–7577.
- [87] M. J. Frisch, G. W. Trucks, H. B. Schlegel, G. E. Scuseria, M. A. Robb, J. R. Cheeseman, G. Scalmani, V. Barone, B. Mennucci, G. A. Petersson, H. Nakatsuji, M. Caricato, X. Li, H. P. Hratchian, A. F. Izmaylov, J. Bloino, G. Zheng, J. L. Sonnenberg, M. Hada, M. Ehara, K. Toyota, R. Fukuda, J. Hasegawa, M. Ishida, T. Nakajima, Y. Honda, O. Kitao, H. Nakai, T. Vreven, J. A. Montgomery, J. E. Peralta, F. Ogliaro, M. Bearpark, J. J. Heyd, E. Brothers, K. N. Kudin, V. N. Staroverov, R. Kobayashi, J. Normand, K. Raghavachari, A. Rendell, J. C. Burant, S. S. Iyengar, J. Tomasi, M. Cossi, N. Rega, J. M. Millam, M. Klene, J. E. Knox, J. B. Cross, V. Bakken, C. Adamo, J. Jaramillo, R. Gomperts, R. E. Stratmann, O. Yazyev, A. J. Austin, R. Cammi, C. Pomelli, J. W. Ochterski, R. L. Martin, K. Morokuma, V. G. Zakrzewski, G. A. Voth, P. Salvador, J. J. Dannenberg, S. Dapprich, A. D. Daniels, Farkas,

- J. B. Foresman, J. V. Ortiz, J. Cioslowski, D. J. Fox, *Gaussian 09, Revision B.01*, **2009**.
- [88] S. Grimme, *J. Comput. Chem.* **2006**, *27*, 1787–1799.
- [89] A. D. Becke, *J. Chem. Phys.* **1996**, *104*, 1040–1046.
- [90] B.-B. Liu, X.-R. Wang, Z.-F. Guo, Z.-L. Lu, *Inorg. Chem. Commun.* **2010**, *13*, 814–817.
- [91] C. A. Kruithof, H. P. Dijkstra, M. Lutz, A. L. Spek, R. J. M. K. Gebbink, G. van Koten, *Organometallics* **2008**, *27*, 4928–4937.
- [92] D. J. Heisterberg, *The Quatfit Program, the CCL archive*, **2009**.
- [93] J. R. Khusnutdinova, D. Milstein, *Angew. Chemie Int. Ed.* **2015**, *54*, 12236–12273.
- [94] C. A. Jiménez-Hoyos, B. G. Janesko, G. E. Scuseria, *J. Phys. Chem. A* **2009**, *113*, 11742–11749.
- [95] P. Surawatanawong, M. B. Hall, *Organometallics* **2008**, *27*, 6222–6232.
- [96] P. Surawatanawong, Y. Fan, M. B. Hall, *J. Organomet. Chem.* **2008**, *693*, 1552–1563.
- [97] B. O. Roos, *Chem. Phys. Lett.* **1972**, *15*, 153–159.
- [98] S. Yamamoto, H. Kashiwagi, *Chem. Phys. Lett.* **1993**, *205*, 306–312.
- [99] K. P. Jensen, *J. Phys. Chem. B* **2005**, *109*, 10505–10512.
- [100] N. Kumar, M. Alfonso-Prieto, C. Rovira, P. Lodowski, M. Jaworska, P. M. Kozłowski, *J. Chem. Theory Comput.* **2011**, *7*, 1541–1551.
- [101] H. Nakano, *J. Chem. Phys.* **1993**, *99*, 7983–7992.
- [102] T. Takatani, J. S. Sears, C. D. Sherrill, *J. Phys. Chem. A* **2009**, *113*, 9231–9236.
- [103] V. Veryazov, P. A. Malmqvist, B. O. Roos, *Int. J. Quantum Chem.* **2011**, *111*, 3329–3338.

- [104] A. Milet, A. Dedieu, *J. Am. Chem. Soc.* **1995**, *2*, 361–367.
- [105] K. Pierloot, A. Ceulemans, M. Merchán, L. Serrano-Andrés, *J. Phys. Chem. A* **2000**, *104*, 4374–4382.
- [106] T. Matsushita, T. Asada, S. Koseki, *J. Phys. Chem. C* **2007**, *111*, 6897–6903.
- [107] L. Freitag, S. Knecht, S. F. Keller, M. G. Delcey, F. Aquilante, T. Bondo Pedersen, R. Lindh, M. Reiher, L. González, *Phys. Chem. Chem. Phys.* **2015**, 14383–14392.
- [108] R. H. A. Eade, M. A. Robb, *Chem. Phys. Lett.* **1981**, *83*, 362–368.
- [109] H. B. Schlegel, M. A. Robb, *Chem. Phys. Lett.* **1982**, *93*, 43–46.
- [110] F. Bernardi, A. Bottoni, J. J. W. McDouall, M. A. Robb, H. B. Schlegel, *Faraday Symp. Chem. Soc.* **1984**, *19*, 137.
- [111] I. N. Ragazos, M. A. Robb, H. B. Schlegel, *Chem. Phys. Lett.* **1992**, *189*, 524–528.
- [112] N. Yamamoto, T. Vreven, M. A. Robb, M. J. Frisch, H. Bernhard Schlegel, *Chem. Phys. Lett.* **1996**, *250*, 373–378.
- [113] J.-L. Niu, X.-Q. Hao, J.-F. Gong, M.-P. Song, *Dalton Trans.* **2011**, *40*, 5135–5150.
- [114] A. D. Ryabov, *Chem. Rev.* **1990**, *90*, 403–424.
- [115] H. Takahashi, J. Tsuji, *J. Organomet. Chem.* **1967**, *10*, 511–517.
- [116] D. L. Davies, S. M. A. Donald, S. A. Macgregor, *J. Am. Chem. Soc.* **2005**, *127*, 13754–13755.
- [117] S. Pascual, P. de Mendoza, A. A. C. Braga, F. Maseras, A. M. Echavarren, *Tetrahedron* **2008**, *64*, 6021–6029.
- [118] D. García-Cuadrado, P. de Mendoza, A. A. C. Braga, F. Maseras, A. M. Echavarren, *J. Am. Chem. Soc.* **2007**, *129*, 6880–6886.

- [119] P. Steenwinkel, R. A. Gossage, T. Maunula, D. M. Grove, G. van Koten, *Chem. - A Eur. J.* **1998**, *4*, 763–768.
- [120] D. Babić, M. Čurić, D. M. Smith, *J. Organomet. Chem.* **2011**, *696*, 661–669.
- [121] P. E. M. Siegbahn, *Theor. Chim. Acta* **1994**, *88*, 413–424.
- [122] M. Steinmetz, S. Grimme, *ChemistryOpen* **2013**, *2*, 115–124.
- [123] A. Pidcock, R. E. Richards, L. M. Venanzi, *J. Chem. Soc. A Inorganic Phys. Theor.* **1966**, 1707–1710.
- [124] J. E. Huheey, E. A. Keiter, R. L. Keiter, O. K. Medhi, *Inorganic chemistry: principles of structure and reactivity*, Pearson Education India, **2006**.
- [125] L. Rigamonti, M. Rusconi, C. Manassero, M. Manassero, A. Pasini, *Inorganica Chim. Acta* **2010**, *363*, 3498–3505.
- [126] L. Randaccio, N. Bresciani-Pahor, P. J. Toscano, L. G. Marzilli, *Inorg. Chem.* **1981**, *20*, 2722–2724.
- [127] S. Otto, M. H. Johansson, *Inorganica Chim. Acta* **2002**, *329*, 135–140.
- [128] S. Pérez, R. Bosque, C. López, X. Solans, M. Font-Bardia, *J. Organomet. Chem.* **2001**, *625*, 67–76.
- [129] N. Kaltsoyannis, P. Mountford, *J. Chem. Soc. Dalt. Trans.* **1999**, 781–790.
- [130] P. D. Lyne, D. P. Mingos, *J. Organomet. Chem.* **1994**, *478*, 141–151.
- [131] H. Jacobsen, H. Berke, *J. Chem. Soc. Dalt. Trans.* **2002**, 3117–3122.
- [132] R. J. Deeth, *J. Chem. Soc. Dalt. Trans.* **1993**, 3711–3713.
- [133] J. K. Burdett, T. A. Albright, *Inorg. Chem.* **1979**, *18*, 2112–2120.
- [134] Y. Minenkov, G. Occhipinti, V. R. Jensen, *J. Phys. Chem. A* **2009**, *113*, 11833–11844.
- [135] M. L. Laury, A. K. Wilson, *J. Chem. Theory Comput.* **2013**, *9*, 3939–3946.
- [136] Y. Zhao, D. G. Truhlar, *J. Chem. Theory Comput.* **2011**, *7*, 669–676.

- [137] P. K. Sajith, C. H. Suresh, *Inorg. Chem.* **2011**, *50*, 8085–8093.
- [138] T. Lu, F. Chen, *J. Comput. Chem.* **2012**, *33*, 580–592.
- [139] A. G. Orpen, N. G. Connelly, *Organometallics* **1990**, *9*, 1206–1210.
- [140] C. Kölmel, C. Oehsenfeld, R. Ahlrichs, *Theor. Chim. Acta* **1991**, 271–284.
- [141] C. D. Montgomery, *J. Chem. Educ.* **2013**, *90*, 661–664.
- [142] M. Brookhart, M. L. H. Green, G. Parkin, *Proc. Natl. Acad. Sci.* **2007**, *104*, 6908–6914.
- [143] D. A. McQuarrie, J. D. Simon, *Physical Chemistry: A Molecular Approach*, Viva Books, Sausalito, CA: University science books, 1st ed., **1997**.
- [144] S. Kozuch, J. M. L. Martin, *ChemPhysChem* **2011**, *12*, 1413–1418.
- [145] P. Atkins, J. D. Paula, *Atkins' physical chemistry*, Oxford University Press, Oxford, UK, 9th ed., **2010**.
- [146] W. Nakanishi, S. Hayashi, *Curr. Org. Chem.* **2010**, *14*, 181–197.
- [147] E. Espinosa, I. Alkorta, J. Elguero, E. Molins, *J. Chem. Phys.* **2002**, *117*, 5529–5542.
- [148] M. Niskanen, P. Hirva, M. Haukka, *J. Chem. Theory Comput.* **2009**, *5*, 1084–1090.
- [149] M. Montag, I. Efremenko, G. Leitus, Y. Ben-David, J. M. L. Martin, D. Milstein, *Organometallics* **2013**, *32*, 7163–7180.
- [150] S. K. Brayshaw, J. C. Green, G. Kociok-Köhn, E. L. Sceats, A. S. Weller, *Angew. Chemie Int. Ed.* **2006**, *45*, 452–456.
- [151] X. Li, J. Sun, Z. Sun, Y. Zeng, S. Zheng, L. Meng, *Organometallics* **2012**, *31*, 6582–6588.
- [152] J. A. Cabeza, J. F. Van der Maelen, S. García-Granda, *Organometallics* **2009**, *28*, 3666–3672.

- [153] P. Macchi, A. Sironi, *Coord. Chem. Rev.* **2003**, *238-239*, 383–412.
- [154] P. L. Popelier, *Atoms in Molecules: An Introduction*, Pearson Education Limited, 1st ed., **2000**.
- [155] P. K. Sajith, C. H. Suresh, *J. Organomet. Chem.* **2011**, *696*, 2086–2092.
- [156] P. K. Sajith, C. H. Suresh, *Dalton Trans.* **2010**, *39*, 815–822.
- [157] J. Zhu, Z. Lin, T. B. Marder, *Inorg. Chem.* **2005**, *44*, 9384–9390.
- [158] P. N. Kapoor, R. Kakkar, *J. Mol. Struct. THEOCHEM* **2004**, *679*, 149–156.
- [159] S. Boonseng, G. Roffe, R. Jones, G. Tizzard, S. Coles, J. Spencer, H. Cox, *Inorganics* **2016**, *4*, 25.
- [160] R. F. Heck, *J. Am. Chem. Soc.* **1968**, *90*, 5526–5531.
- [161] T. G. Crisp, *Chem. Soc. Rev.* **1998**, *27*, 427–436.
- [162] N. T. S. Phan, M. Van Der Sluys, C. W. Jones, *Adv. Synth. Catal.* **2006**, *348*, 609–679.
- [163] C. Amatore, A. Jutand, *Acc. Chem. Res.* **2000**, *33*, 314–321.
- [164] C. Amatore, A. Jutand, M. A. M'Barki, *Organometallics* **1992**, *11*, 3009–3013.
- [165] C. Amatore, E. Carré, A. Jutand, M. A. M'Barki, *Organometallics* **1995**, *14*, 1818–1826.
- [166] C. Amatore, A. Jutand, A. Suarez, *J. Am. Chem. Soc.* **1993**, *115*, 9531–9541.
- [167] L. Kürti, B. Czakó, *Strategic applications of named reactions in organic synthesis*, Elsevier Academic Press, 1st ed., **2005**, p. 448.
- [168] N. Miyaura, K. Yamada, H. Suginome, A. Suzuki, *J. Am. Chem. Soc.* **1985**, *107*, 972–980.
- [169] N. A. Bumagin, P. G. More, I. P. Beletskaya, *J. Organomet. Chem.* **1989**, *371*, 397–401.

- [170] A. H. M. de Vries, J. M. C. A. Mulders, J. H. M. Mommers, H. J. W. Henderickx, J. G. de Vries, *Org. Lett.* **2003**, *5*, 3285–3288.
- [171] D. V. Aleksanyan, V. A. Kozlov, N. E. Shevchenko, V. G. Nenajdenko, A. A. Vasilev, Y. V. Nelyubina, I. V. Ananyev, P. V. Petrovskii, I. L. Odinetz, *J. Organomet. Chem.* **2012**, *711*, 52–61.
- [172] M. R. Eberhard, *Org. Lett.* **2004**, *6*, 2125–2128.
- [173] P. Nilsson, O. F. Wendt, *J. Organomet. Chem.* **2005**, *690*, 4197–4202.
- [174] R. C. da Costa, M. Jurisch, J. A. Gladysz, *Inorganica Chim. Acta* **2008**, *361*, 3205–3214.
- [175] R. B. Bedford, C. S. J. Cazin, M. B. Hursthouse, M. E. Light, K. J. Pike, S. Wimperis, *J. Organomet. Chem.* **2001**, *633*, 173–181.
- [176] J. L. Serrano, L. García, J. Pérez, E. Pérez, J. García, G. Sánchez, P. Sehnal, S. De Ornellas, T. J. Williams, I. J. S. Fairlamb, *Organometallics* **2011**, *30*, 5095–5109.
- [177] A. R. Kapdi, G. Dhangar, J. L. Serrano, J. Pérez, L. García, I. J. S. Fairlamb, *Chem. Commun. (Camb)*. **2014**, *50*, 9859–61.
- [178] J. E. Marcone, K. G. Moloy, *J. Am. Chem. Soc.* **1998**, *120*, 8527–8528.
- [179] J. L. Klinkenberg, J. F. Hartwig, *J. Am. Chem. Soc.* **2012**, *134*, 5758–5761.
- [180] L. J. Goossen, D. Koley, H. L. Hermann, W. Thiel, *Organometallics* **2005**, *24*, 2398–2410.
- [181] A. A. C. Braga, G. Ujaque, F. Maseras, *Organometallics* **2006**, *25*, 3647–3658.
- [182] Y. L. Huang, C. M. Weng, F. E. Hong, *Chem. - A Eur. J.* **2008**, *14*, 4426–4434.
- [183] K. J. Szabó, *J. Mol. Catal. A Chem.* **2010**, *324*, 56–63.
- [184] M. Gagliardo, N. Selander, N. C. Mehendale, G. Van Koten, R. J. M. Klein Gebbink, K. J. Szabó, *Chem. - A Eur. J.* **2008**, *14*, 4800–4809.

- [185] B.-S. Zhang, C. Wang, J.-F. Gong, M.-P. Song, *J. Organomet. Chem.* **2009**, *694*, 2555–2561.
- [186] I. Moreno, R. SanMartin, B. Ines, M. T. Herrero, E. Domínguez, *Curr. Org. Chem.* **2009**, *13*, 878–895.
- [187] G. W. Roffe, PhD thesis, University of Sussex, **2016**.
- [188] S. Boonseng, G. W. Roffe, M. Targema, J. Spencer, H. Cox, *J. Organomet. Chem.* **2017**, *In press*, xxx.
- [189] G. B. Smith, G. C. Dezeny, D. L. Hughes, A. O. King, T. R. Verhoeven, *J. Org. Chem.* **1994**, *59*, 8151–8156.
- [190] C. A. Hunter, J. K. M. Sanders, *J. Am. Chem. Soc.* **1990**, *112*, 5525–5534.
- [191] M. O. Sinnokrot, C. D. Sherrill, *J. Am. Chem. Soc.* **2004**, *126*, 7690–7697.
- [192] A. A. C. Braga, N. H. Morgon, G. Ujaque, A. Lledós, F. Maseras, *J. Organomet. Chem.* **2006**, *691*, 4459–4466.
- [193] L. Estévez, L. W. Tuxworth, J.-M. Sotiropoulos, P. W. Dyer, K. Miqueu, *Dalton Trans.* **2014**, *43*, 11165–79.
- [194] J. L. Klinkenberg, J. F. Hartwig, *J. Am. Chem. Soc.* **2012**, *134*, 5758–61.
- [195] H. Ossor, M. Pfeffer, J. T. B. H. Jastrzebski, C. H. Stam, *Inorg. Chem.* **1987**, *26*, 1169–1171.
- [196] N. Miyaura, *J. Organomet. Chem.* **2002**, *653*, 54–57.
- [197] A. A. C. Braga, N. H. Morgon, G. Ujaque, F. Maseras, *J. Am. Chem. Soc.* **2005**, *127*, 9298–9307.
- [198] C. Sicre, A. A. C. Braga, F. Maseras, M. M. Cid, *Tetrahedron* **2008**, *64*, 7437–7443.
- [199] U. Rudolph, F. Knoflach, *Nat. Rev. Drug Discov.* **2011**, *10*, 685–97.
- [200] T. Mehdi, *Br. J. Med. Pract.* **2012**, *5*, a501.

- [201] P. Polc, H. Möhler, W. Haefely, *Naunyn. Schmiedebergs. Arch. Pharmacol.* **1974**, *284*, 319–337.
- [202] W. E. Haefely, *Br. J. Psychiatry* **1978**, *133*, 231–238.
- [203] H. Möhler, T. Okada, *Science* **1977**, *198*, 849–851.
- [204] C. Braestrup, R. Schmiechen, G. Neef, M. Nielsen, E. N. Petersen, *Science* **1982**, *216*, 1241–1243.
- [205] G. A. Archer, L. H. Sternbach, *Chem. Rev.* **1968**, *68*, 747–784.
- [206] M.-C. Hsu, A. Schutt, M. Holly, L. Slice, M. Sherman, D. Richman, M. Potash, D. Volsky, *Science* **1991**, *254*, 1799–1802.
- [207] P. G. Baraldi, G. Balboni, B. Cacciari, A. Guiotto, S. Manfredini, R. Romagnoli, G. Spalluto, D. E. Thurston, P. W. Howard, N. Bianchi, C. Rutigliano, C. Mischianti, R. Gambari, *J. Med. Chem.* **1999**, *42*, 5131–5141.
- [208] K. Ishimoto, T. Nagata, M. Murabayashi, T. Ikemoto, *Tetrahedron* **2015**, *71*, 407–418.
- [209] H. G. Selnick, N. J. Liverton, J. J. Baldwin, J. W. Butcher, D. A. Claremon, J. M. Elliott, R. M. Freidinger, S. A. King, B. E. Libby, C. J. McIntyre, D. A. Pribush, D. C. Remy, G. R. Smith, A. J. Tebben, N. K. Jurkiewicz, J. J. Lynch, J. J. Salata, M. C. Sanguinetti, P. K. S. Siegl, *Communications* **1997**, *2623*, 3865–3868.
- [210] J. Spencer, R. Rathnam, B. Chowdhry, *Future Med. Chem.* **2010**, *2*, 1441–1449.
- [211] L. H. Sternbach, *J. Med. Chem.* **1979**, *22*, 1–7.
- [212] L. H. Sternbach, R. I. Fryer, W. Metlesics, E. Reeder, G. Sach, G. Saucy, A. Stempel, *J. Org. Chem.* **1962**, *27*, 3788–3796.
- [213] A. Stempel, F. W. Landgraf, *J. Org. Chem.* **1962**, *27*, 4675–4677.
- [214] B. A. Bunin, M. J. Plunkett, J. A. Ellman, *Proc. Natl. Acad. Sci. U. S. A.* **1994**, *91*, 4708–4712.

- [215] J. Spencer, R. P. Rathnam, A. L. Harvey, C. J. Clements, R. L. Clark, M. P. Barrett, P. E. Wong, L. Male, S. J. Coles, S. P. MacKay, *Bioorganic Med. Chem.* **2011**, *19*, 1802–1815.
- [216] S. Herrero, M. T. García-López, R. Herranz, *J. Org. Chem.* **2003**, *68*, 4582–4585.
- [217] J.-Y. Wang, X.-F. Guo, D.-X. Wang, Z.-T. Huang, M.-X. Wang, *J. Org. Chem.* **2008**, *73*, 1979–1982.
- [218] T. A. Popp, E. Uhl, D. N. Ong, S. Dittrich, F. Bracher, *Tetrahedron* **2016**, *72*, 1668–1674.
- [219] I. Nakamura, Y. Yamamoto, *Chem. Rev.* **2004**, *104*, 2127–2198.
- [220] G. Zeni, R. C. Larock, *Chem. Rev.* **2004**, *104*, 2285–2309.
- [221] E. M. Beccalli, G. Broggin, G. Paladino, A. Penoni, C. Zoni, *J. Org. Chem.* **2004**, *69*, 5627–5630.
- [222] J. D. Neukom, A. S. Aquino, J. P. Wolfe, *Org. Lett.* **2011**, *13*, 2196–2199.
- [223] M. Rigamonti, G. Prestat, G. Broggin, G. Poli, *J. Organomet. Chem.* **2014**, *760*, 149–155.
- [224] J. Spencer, B. Z. Chowdhry, A. I. Mallet, R. P. Rathnam, T. Adatia, A. Bashall, F. Rominger, *Tetrahedron* **2008**, *64*, 6082–6089.
- [225] R. Khan, R. Felix, P. D. Kemmitt, S. J. Coles, I. J. Day, G. J. Tizzard, J. Spencer, *Adv. Synth. Catal.* **2016**, *358*, 98–109.
- [226] N. E. Tokel-Takvoryan, R. E. Hemingway, A. J. Bard, *J. Am. Chem. Soc.* **1973**, *95*, 6582–6589.
- [227] A. Juris, V. Balzani, F. Barigelletti, S. Campagna, P. Belser, A. von Zelewsky, *Coord. Chem. Rev.* **1988**, *84*, 85–277.
- [228] M. A. Ischay, M. E. Anzovino, J. Du, T. P. Yoon, *J. Am. Chem. Soc.* **2008**, *130*, 12886–12887.

- [229] D. Kalyani, K. B. McMurtrey, S. R. Neufeldt, M. S. Sanford, *J. Am. Chem. Soc.* **2011**, *133*, 18566–18569.
- [230] R. Ananthkrishnan, S. Gazi, *Catal. Sci. Technol.* **2012**, *2*, 1463.
- [231] H. Gafney, A. Adamson, *J. Am. Chem. Soc.* **1972**, *94*, 8238–8239.
- [232] T. A. White, S. M. Arachchige, B. Sedai, K. J. Brewer, *Materials (Basel)*. **2010**, *3*, 4328–4354.
- [233] H. B. Gray, A. W. Maverick, *Science* **1981**, *214*, 1201–1205.
- [234] D. Jacquemin, C. Adamo, B. Mennucci, *J. Chem. Theory Comput.* **2012**, *8*, 2359–2372.
- [235] C. Adamo, D. Jacquemin, *Chem. Soc. Rev.* **2013**, *42*, 845–856.
- [236] H. B. Gray, J. R. Winkler, *Annu. Rev. Biochem.* **1996**, *65*, 537–561.
- [237] A. Hagfeldt, G. Boschloo, L. Sun, L. Kloo, H. Pettersson, *Chem. Rev.* **2010**, *110*, 6595–6663.
- [238] P. W. Atkins, T. Overton, J. Rourke, M. Weller, A. Fraser, *Shriver and Atkins' inorganic chemistry*, Oxford University Press, Oxford, UK, 5th ed., **2010**.
- [239] R. A. Marcus, *Annu. Rev. Phys. Chem.* **1964**, *15*, 155–196.
- [240] R. A. Marcus, *J. Chem. Phys.* **1956**, *24*, 966–978.
- [241] R. A. Marcus, *J. Chem. Phys.* **1956**, *24*, 979–989.
- [242] R. A. Marcus, *J. Chem. Phys.* **1957**, *26*, 872–877.
- [243] R. Marcus, N. Sutin, *Biochim. Biophys. Acta - Rev. Bioenerg.* **1985**, *811*, 265–322.
- [244] Q. Wu, T. Van Voorhis, *J. Phys. Chem. A* **2006**, *110*, 9212–9218.
- [245] W. Mönch, *Semiconductor surfaces and interfaces*, Springer Science & Business Media, **2013**.
- [246] J. M. Saveant, *J. Am. Chem. Soc.* **1987**, *109*, 6788–6795.

- [247] N. S. Hush, *J. Chem. Phys.* **1958**, *28*, 962–972.
- [248] A. Houmam, *Chem. Rev.* **2008**, *108*, 2180–2237.
- [249] G. O. Jones, P. Liu, K. N. Houk, S. L. Buchwald, *J. Am. Chem. Soc.* **2010**, *132*, 6205–6213.
- [250] V. Barone, M. Cossi, *J. Phys. Chem. A* **1998**, *102*, 1995–2001.
- [251] M. Cossi, N. Rega, G. Scalmani, V. Barone, *J. Comput. Chem.* **2003**, *24*, 669–681.
- [252] A. K. Rappé, C. J. Casewit, K. S. Colwell, W. Goddard III, W. Skiff, *J. Am. Chem. Soc.* **1992**, *114*, 10024–10035.
- [253] A. Bondi, *J. Phys. Chem.* **1964**, *68*, 441–451.
- [254] A. V. Marenich, J. Ho, M. L. Coote, C. J. Cramer, D. G. Truhlar, *Phys. Chem. Chem. Phys.* **2014**, *16*, 15068.
- [255] T. B. Demissie, K. Ruud, J. H. Hansen, *Organometallics* **2015**, *34*, 4218–4228.
- [256] K. Izutsu, *Anal. Sci.* **2011**, *27*, 685.
- [257] C. R. Bock, J. A. Connor, A. R. Gutierrez, T. J. Meyer, D. G. Whitten, B. P. Sullivan, J. K. Nagle, *J. Am. Chem. Soc.* **1979**, *101*, 4815–4824.
- [258] T. Yanai, D. P. Tew, N. C. Handy, *Chem. Phys. Lett.* **2004**, *393*, 51–57.
- [259] A. Chantzis, J. Cerezo, A. Perrier, F. Santoro, D. Jacquemin, *J. Chem. Theory Comput.* **2014**, *10*, 3944–3957.
- [260] A. Dinescu, A. E. Clark, *J. Phys. Chem. A* **2008**, *112*, 11198–11206.
- [261] A. Vigalok, O. Uzan, L. J. W. Shimon, Y. Ben-David, J. M. L. Martin, D. Milstein, *J. Am. Chem. Soc.* **1998**, *120*, 12539–12544.
- [262] B. Lian, L. Zhang, G. A. Chass, D.-C. Fang, *J. Org. Chem.* **2013**, *78*, 8376–85.
- [263] F. Teplý, *Collect. Czechoslov. Chem. Commun.* **2011**, *76*, 859–917.

- [264] J. R. Khusnutdinova, N. P. Rath, L. M. Mirica, *J. Am. Chem. Soc.* **2010**, *132*, 7303–7305.
- [265] J. R. Khusnutdinova, N. P. Rath, L. M. Mirica, *J. Am. Chem. Soc.* **2012**, *134*, 2414–2422.
- [266] Y. L. Ching, M. L. Coote, A. Gennaro, K. Matyjaszewski, *J. Am. Chem. Soc.* **2008**, *130*, 12762–12774.
- [267] W. Mönch, *Semiconductor surfaces and interfaces*, Springer Science & Business Media, 3rd ed., **2013**, p. 479.
- [268] L. Solymar, D. Walsh, *Electrical properties of materials*, OUP Oxford, Oxford, 9th ed., **2009**, p. 232.
- [269] Q. Zhang, Z.-Q. Zhang, Y. Fu, H. Yu, *ACS Catal.* **2016**, *6*, 798–808.
- [270] K. Muñoz, *Angew. Chem. Int. Ed. Engl.* **2009**, *48*, 9412–23.
- [271] A. Ariafard, C. J. T. Hyland, A. J. Canty, M. Sharma, B. F. Yates, *Inorg. Chem.* **2011**, *50*, 6449–6457.
- [272] A. J. Canty, A. Ariafard, M. S. Sanford, B. F. Yates, *Organometallics* **2013**, *32*, 544–555.

Appendices

Appendix A

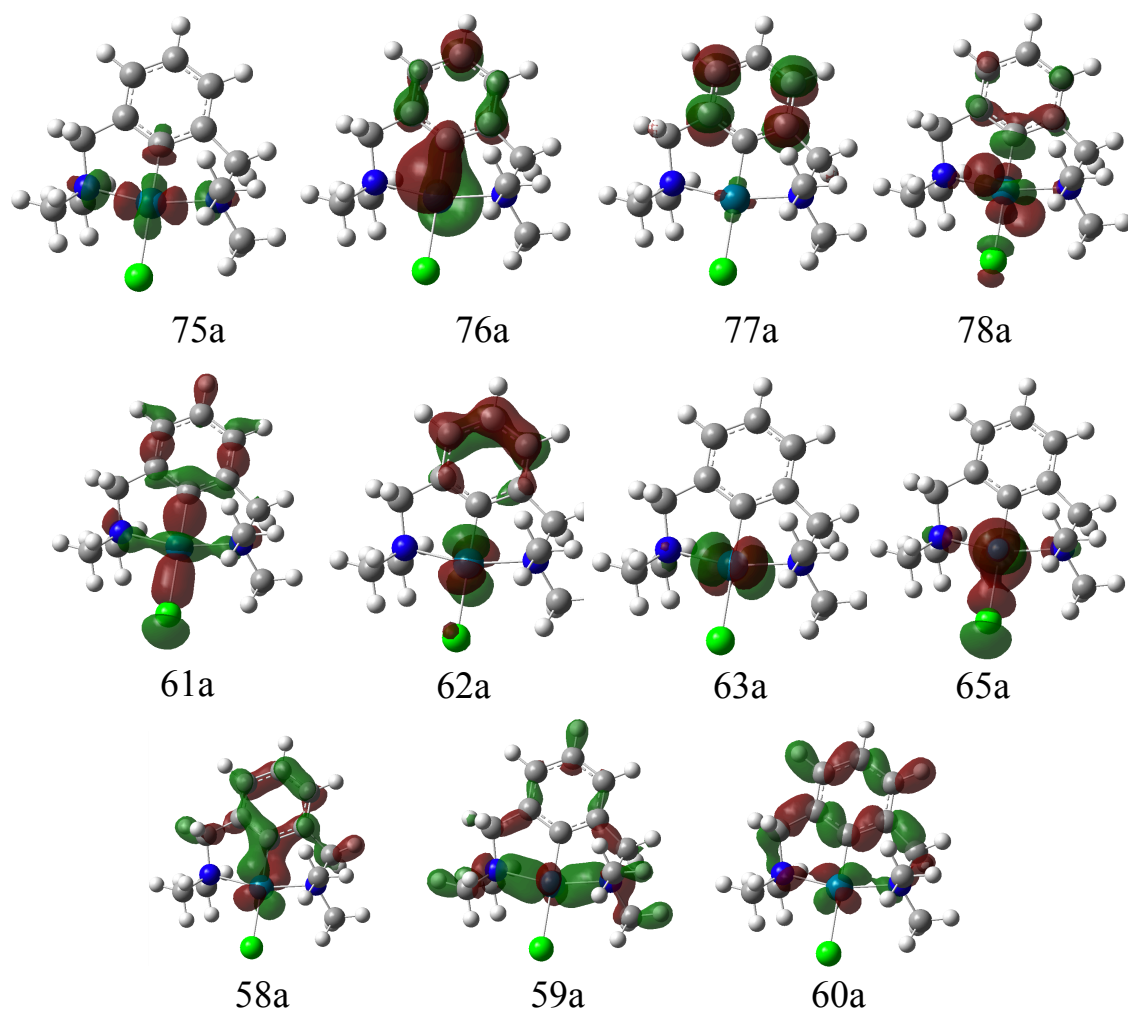


Figure A.1. Representation of canonical molecular orbitals of a symmetrical NCN pincer palladacycle resulting from the HF calculation.

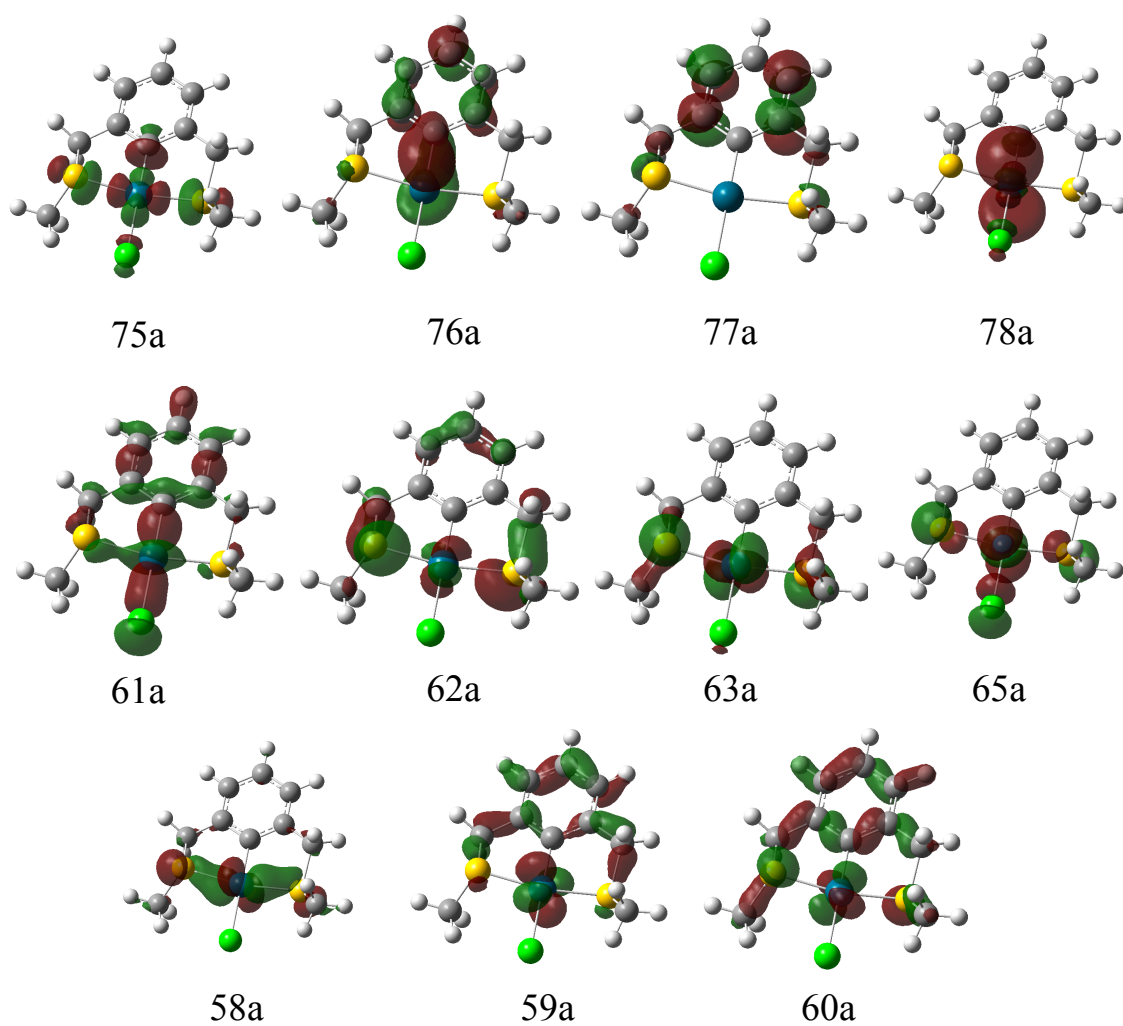


Figure A.2. Representation of canonical molecular orbitals of a symmetrical SCS pincer palladacycle resulting from the HF calculation.

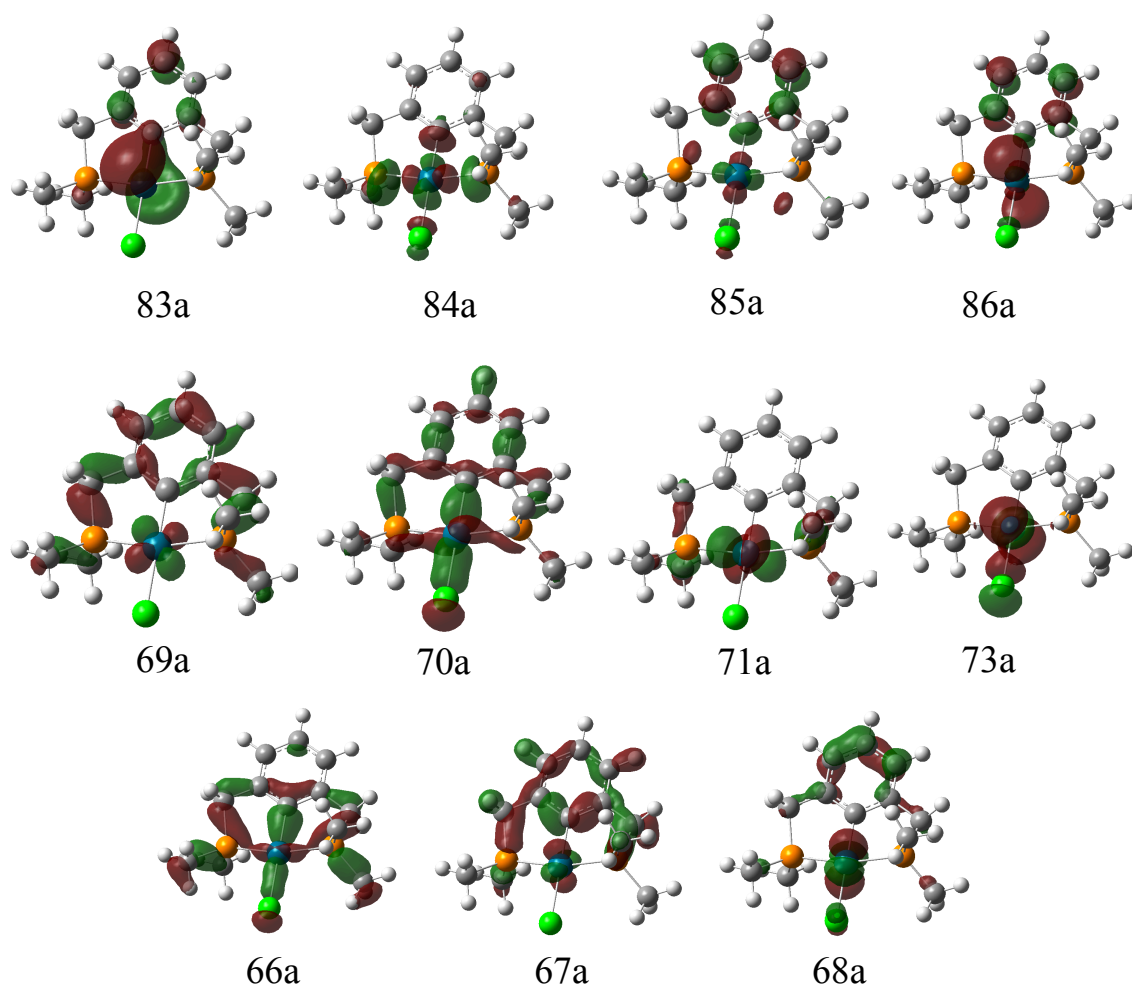


Figure A.3. Representation of canonical molecular orbitals of a symmetrical PCP pincer palladacycle resulting from the HF calculation.

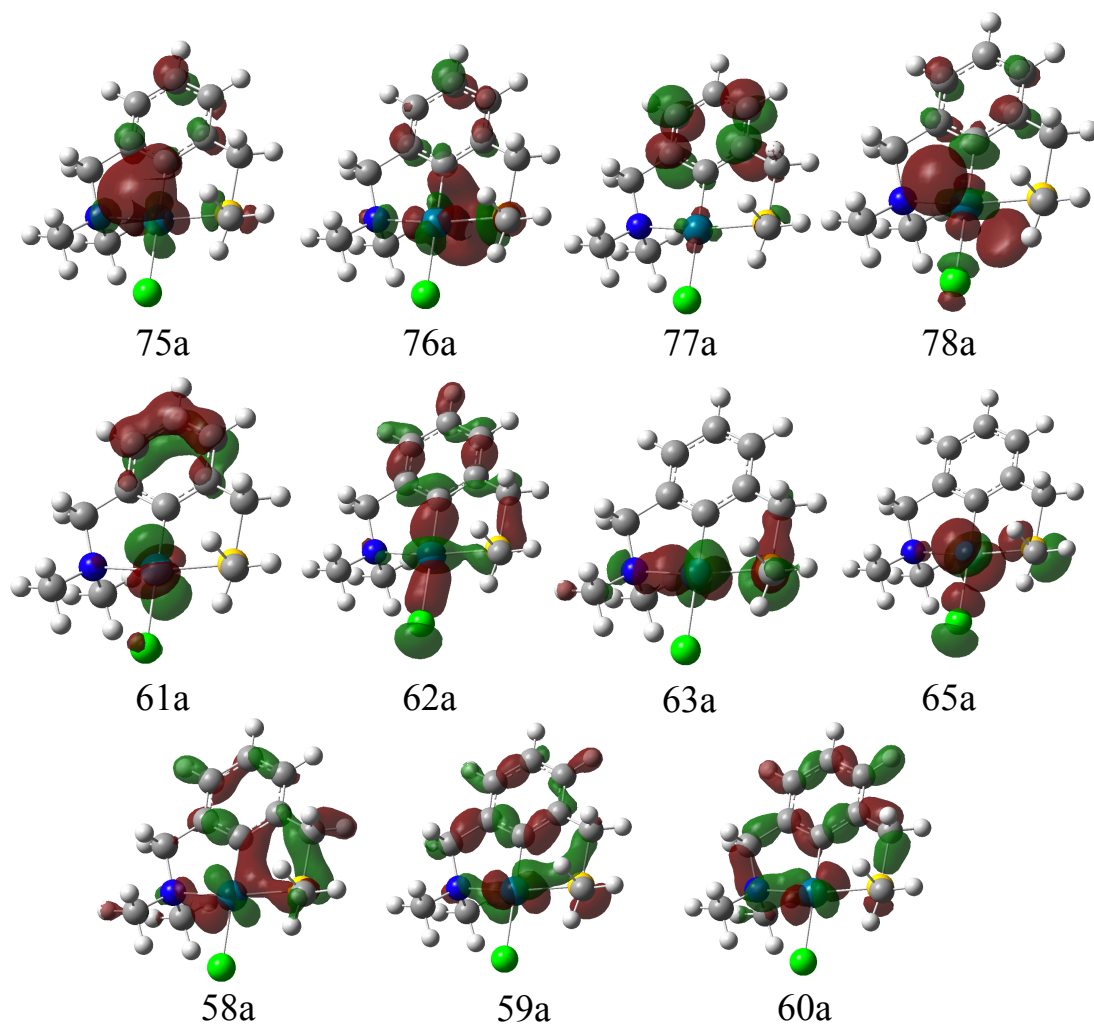


Figure A.4. Representation of canonical molecular orbitals of an unsymmetrical NCS pincer palladacycle resulting from the HF calculation.

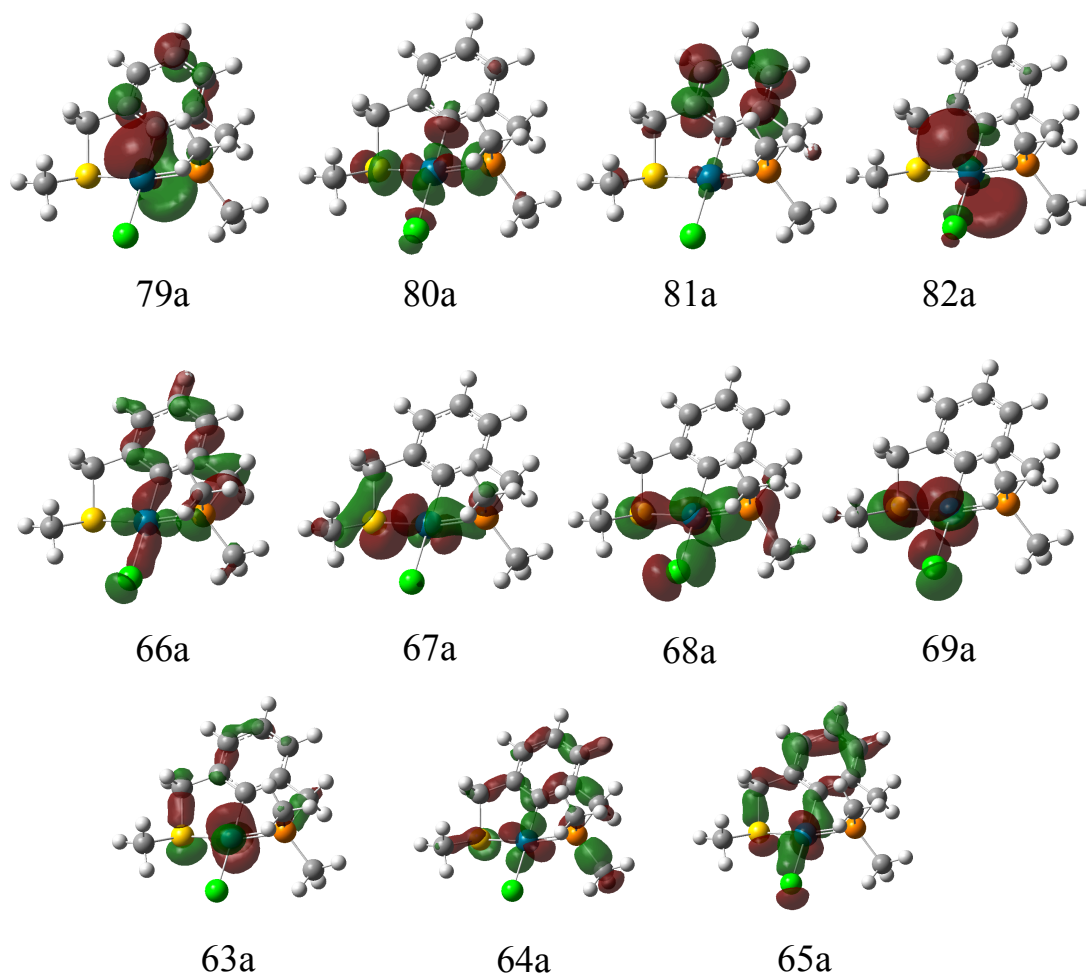


Figure A.5. Representation of canonical molecular orbitals of an unsymmetrical SCP pincer palladacycle resulting from the HF calculation.

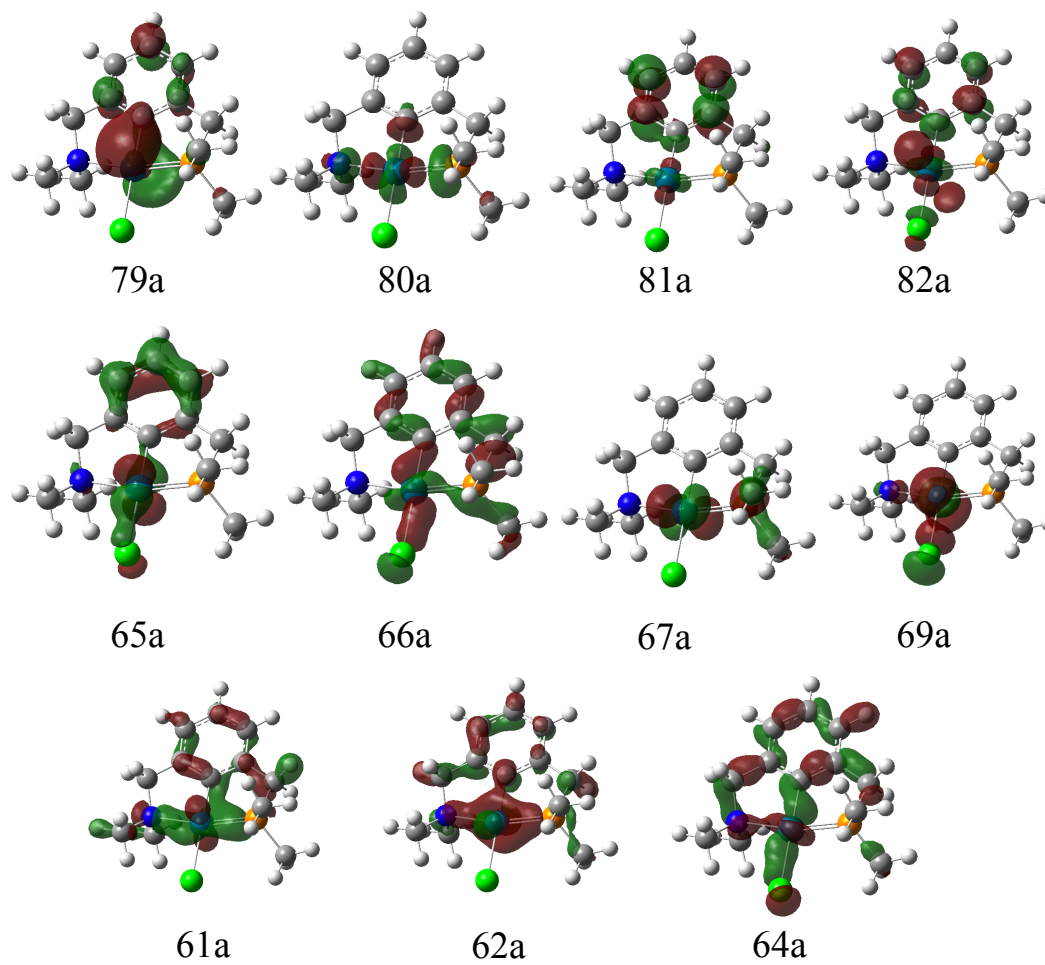


Figure A.6. Representation of canonical molecular orbitals of an unsymmetrical NCP pincer palladacycle resulting from the HF calculation.

Appendix B

Table B.1. The relative Gibbs free energy of reaction for PdYCY in gas phase and solvent under the base-free condition.

Reaction process for PdYCY	Relative Gibbs free energy/kJ mol ⁻¹			
	Gas	Toluene	THF	Acetonitrile
PdNCN				
Reactants A	0.0	0.0	0.0	0.0
Int1A	2.3	7.9	11.8	13.4
TS1-2A	204.5	215.7	223.4	226.6
Int2A	130.1	145.0	155.7	160.4
Int3A	141.3	144.9	145.3	144.1
TS3-5A	250.0	259.5	266.3	269.2
Int5A	87.0	100.8	111.0	115.7
Product A	171.0	185.0	196.3	201.5
PdSCS				
Reactants A	0.0	0.0	0.0	0.0
Int1A	2.7	7.2	10.3	11.6
TS1-2A	211.5	224.4	233.6	237.6
Int2A	130.1	148.4	162	168.3
Int3A	146.7	153.1	156.3	157.0
TS3-4A	238.5	252.0	261.8	266.3
Int4A	65.8	83.1	95.5	101.1
TS4-5A	128.8	144.7	156.4	161.7
Int5A	52.3	68.7	81.1	87.0
Products A	173.0	186.7	197.7	203.0
PdPCP				
Reactants A	0.0	0.0	0.0	0.0
Int1A	-12.7	-4.1	1.8	4.3
TS1-2A	276.7	293.5	305.4	311.0
Int2A	219.8	238.9	252.6	259.0
Int3A	226.4	233.0	236.5	237.5
TS3-4A	282.1	295.4	304.3	308.0
Int4A	66.6	84.3	96.6	101.9
TS4-5A	172.5	187.8	198.3	202.8
Int5A	108.6	125.1	136.9	142.4
Products A	284.9	299.0	309.9	315.0

Table B.2. The relative Gibbs free energy of reaction for PdNCS in gas phase and solvent under the base-free condition.

Reaction process for PdNCS	Relative Gibbs free energy/kJ mol ⁻¹			
	Gas	Toluene	THF	Acetonitrile
Path a: (<i>via</i> N de-coordination first)				
Reactants B	0.0	0.0	0.0	0.0
Int1B	-2.4	2.5	6.1	7.7
TS1-2B	224.0	235.8	244.2	247.9
Int2B	139.4	156.8	169.7	175.6
Int3B	156.4	162.0	164.7	165.1
TS3-5B	242.4	253.9	262.2	266.0
Int5B	57.0	73.1	85.5	91.3
Products B	181.0	194.2	204.9	210.0
Path b: (<i>via</i> S de-coordination first)				
Reactants B	0.0	0.0	0.0	0.0
Int1B	5.1	10.0	13.1	14.2
TS1-2B	209.1	220.1	227.6	230.5
Int2B	126.8	142.2	153.3	158.0
Int3B	146.4	149.5	149.7	148.6
TS3-4B	261.1	272.5	280.8	284.4
Int4B	121.1	136.9	148.7	154.0
TS4-5B,I / TS4-5B,II	139.0 / 164.5	154.3 / 178.8	165.4 / 189.4	170.3 / 194.2
Int5B,I / Int5B,II	57.0 / 98.8	73.1 / 111.4	85.5 / 120.6	91.3 / 124.7
Products B	181.0	194.2	204.9	210.0

Table B.3. The relative Gibbs free energy of reaction for PdSCP in gas phase and solvent under the base-free condition.

Reaction process for PdSCP	Relative Gibbs free energy/kJ mol ⁻¹			
	Gas	Toluene	THF	Acetonitrile
Path a: phenyl orientated over S (S de-coordination)				
Reactants C	0.0	0.0	0.0	0.0
Int1C	5.3	10.3	13.7	15.1
TS1-2C	225.9	238.4	247.4	251.3
Int2C	161.4	176.6	187.8	192.7
Int3C	181.6	185.2	186.3	186.0
TS3-4C	262.4	275.0	284.3	288.5
Int4C	70.0	86.1	97.8	102.8
TS4-5C,I / TS4-5C,II	119.5 / 165.8	133.5 / 175.1	143.1 / 181.2	147.0 / 183.6
Int5C,I / Int5C,II	62.1 / 116.4	77.1 / 131.7	88.3 / 143.4	93.4 / 149.0
Products C	238.9	251.6	261.8	266.7
Path b: phenyl orientated over P (S de-coordination)				
Reactants C	0.0	0.0	0.0	0.0
Int1C	-14.8	-6.6	-0.1	3.0
TS1-2C	244.2	256.2	264.5	267.9
Int2C	166.6	182.1	193.4	198.5
Int3C	181.6	185.2	186.3	186.0
TS3-4C	269.9	281.7	290.1	293.9
Int4C	70.0	86.1	97.8	102.8
TS4-5C,I / TS4-5C,II	119.5 / 165.8	133.5 / 175.1	143.1 / 181.2	147.0 / 183.6
Int5C,I / Int5C,II	62.1 / 116.4	77.1 / 131.7	88.3 / 143.4	93.4 / 149.0
Products C	238.9	251.6	261.8	266.7

Table B.4. The relative Gibbs free energy of reaction for PdNCP in gas phase and solvent under the base-free condition.

Reaction process for PdNCP	Relative Gibbs free energy/kJ mol ⁻¹			
	Gas	Toluene	THF	Acetonitrile
Path a: <i>via</i> N de-coordination first				
Reactants D	0.0	0.0	0.0	0.0
Int1D	1.2	7.1	11.1	12.9
TS1-2D	238.9	252.0	261.4	265.5
Int2D	173.6	190.1	202.0	207.3
Int4D	196.4	201.5	203.6	203.7
TS4-6D	274.6	286.9	295.7	299.6
Int6D	72.0	88.5	100.7	106.4
Products D	251.6	265.5	276.6	281.8
Path b: <i>via</i> P de-coordination first				
Reactants D	0.0	0.0	0.0	0.0
Int1D	0.6	7.3	11.7	13.6
TS1-2D	278.1	290.1	298.1	301.4
Int2D	207.0	222.9	234.5	239.7
Int3D	215.6	220.3	222.0	221.7
TS3-4D	256.6	264.9	269.5	270.7
Int4D	196.5	201.6	203.7	203.7
TS4-5D	291.3	303.2	311.5	315.1
Int5D	125.1	140.8	151.7	156.2
TS5-6D,I / TS5-6D,II	138.1 / 222.4	152.9 / 236.2	162.8 / 246.3	166.7 / 250.9
Int6D	72.1 / 168.8	88.5 / 182.2	100.7 / 191.9	106.4 / 196.3
Products D	251.6	265.6	276.6	281.9

Table B.5. The relative Gibbs free energy of reaction for PdYCY in gas phase and solvent under the presence of the base.

Reaction process for PdYCY	Relative Gibbs free energy/kJ mol ⁻¹			
	Gas	Toluene	THF	Acetonitrile
PdNCN				
Reactants E	0.0	0.0	0.0	0.0
Int1E	-29.1	1.7	15.7	19.9
TS1-2E	2.5	32.8	47.0	51.8
Int2E	-18.4	2.5	10.5	12.5
Int3E	65.7	18.8	2.3	-1.7
TS3-4E	171.2	126.7	109.8	104.3
Int4E	32.9	-9.5	-24.1	-27.9
Int5E	55.6	3.5	-19.5	-28.0
TS5-7E	164.2	118.2	101.4	97.1
Int7E	-53.9	-40.6	-53.9	-56.5
Products E	85.3	43.6	31.4	29.4
PdSCS				
Reactants E	0.0	0.0	0.0	0.0
Int1E	10.3	35.2	44.5	46.0
TS1-2E	20.9	47.2	56.9	58.2
Int2E	-25.8	6.2	21.2	26.1
Int3E	65.2	19.4	2.3	-2.5
TS3-4E	158.7	118.1	105.4	102.7
Int4E	56.6	13.2	-1.9	-5.6
Int5E	77.8	23.5	-1.6	-10.8
TS5-6E	169.6	122.3	103.8	98.5
Int6E	-3.1	-46.6	-62.5	-66.8
TS6-7E	59.9	15.1	-1.6	-6.1
Int7E	-16.6	-60.9	-76.8	-80.8
Products E	104.1	57.1	39.8	35.1
PdPCP				
Reactants E	0.0	0.0	0.0	0
Int1E	-27.3	4.4	17.9	21.5
TS1-2E	1.2	35.2	50.4	54.8
Int2E	-19.0	10.0	22.0	25.0
Int3E	53.7	11.6	-2.8	-6.1
TS3-4E	215.7	174.7	160.8	157.6
Int4E	119.7	81.7	70.7	69.0
Int5E	157.5	103.4	78.5	69.6
TS5-6E	213.2	165.7	146.3	140.2
Int6E	-2.3	-45.4	-61.4	-66.0
TS6-7E	103.6	58.1	40.3	34.9
Int7E	39.7	-4.6	-21.0	-25.4
Products E	216.0	169.4	151.9	147.2

Table B.6. The relative Gibbs free energy of reaction for PdNCS in gas phase and solvent under the presence of the base.

Reaction process for PdNCS	Relative Gibbs free energy/kJ mol ⁻¹			
	Gas	Toluene	THF	Acetonitrile
Reactants F	0.0	0.0	0.0	0.0
Int1F	2.2	27.0	36.7	39.0
TS1-2F	15.7	44.4	55.5	57.9
Int2F	-29.5	-3.7	7.7	11.3
Int3F	55.8	11.7	-3.6	-7.3
TS3-4F	182.0	134.0	115.5	110.2
Int4F	47.9	8.1	-3.9	-6.2
Int5F	70.7	20.6	-0.2	-7.1
TS5-7F	156.7	112.5	97.4	93.9
Int7F	-28.8	-68.3	-79.5	-80.8
Products F	95.3	52.8	40.0	37.8

Table B.7. The relative Gibbs free energy of reaction for PdSCP in gas phase and solvent under the presence of the base.

Reaction process for PdSCP	Relative Gibbs free energy/kJ mol ⁻¹			
	Gas	Toluene	THF	Acetonitrile
Reactants G	0.0	0.0	0.0	0.0
Int1G	-20.4	9.1	21.8	25.0
TS1-2G	6.4	39.3	53.5	57.2
Int2G	-23.0	7.5	20.8	24.6
Int3G	56.8	15.1	1.4	-1.7
TS3-4G	178.8	134.1	117.3	112.4
Int4G	69.5	31.2	20.3	18.8
Int5G	94.3	44.5	42.6	16.5
TS5-6G	175.1	134.4	121.5	119.0
Int6G	-17.3	-54.5	-65	-66.7
TS6-7G	32.2 / 78.5	-7.1 / 34.4	-19.6 / 18.4	-22.5 / 14.1
Int7G	-25.2 / 29.1	-63.5 / -8.9	-74.5 / -19.4	-76.1 / -20.5
Products G	151.6	110.9	99.0	97.2

Table B.8. The relative Gibbs free energy of reaction for PdNCP in gas phase and solvent under the presence of the base.

Reaction process for PdNCP	Relative Gibbs free energy/kJ mol ⁻¹			
	Gas	Toluene	THF	Acetonitrile
Reactants H	0.0	0.0	0.0	0.0
Int1H	-25.1	5.3	18.7	22.7
TS1-2H	1.6	35.4	51.3	56.7
Int2H	-27.6	-1.1	10.7	14.3
Int3H	52.8	9.1	-6.2	-9.8
TS3-4H	182.9	137.0	119.7	114.9
Int4H	85.8	45.0	31.8	28.9
Int5H	110.7	60.2	38.8	31.6
TS5-7H	188.9	145.6	130.9	127.6
Int7H	-13.7	-52.9	-64.1	-65.7
Products H	165.9	124.2	111.8	109.8